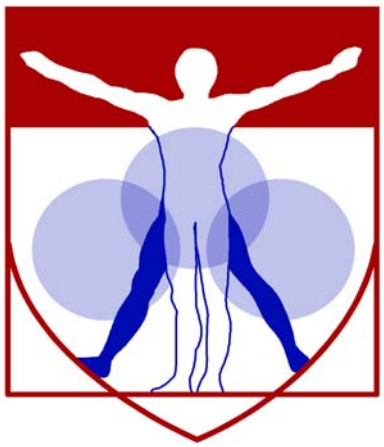

PENN
CENTER for
MUSCULOSKELETAL
DISORDERS

12th Annual Scientific Symposium/Retreat

Thursday, November 19, 2015
BRB II/III Auditorium and Lobby
9:30am-5:30pm
www.med.upenn.edu/pcmd

Table of Contents

We gratefully acknowledge the financial support provided by the National Institute of Arthritis, Musculoskeletal and Skin Diseases of the National Institutes of Health and the University of Pennsylvania Perelman School of Medicine for our Center.

Penn Center for Musculoskeletal Disorders
Scientific Symposium Agenda

November 19, 2015

BRB II/III Auditorium/Lobby ♦ University of Pennsylvania

9:30 – 10:15am **Registration and Poster Set-up**

10:15 – 10:30am **Welcome and Overview**
Louis J. Soslowsky, Ph.D.

10:30 – 11:15am **Session I: Affiliate Member Session** (Moderator: Louis Soslowsky, Ph.D.)

- *Ani Ural, Ph.D., Villanova University - "A Multiscale Computational Assessment of Bone Fracture"*
- *Theresa Freeman, Ph.D., Thomas Jefferson University - Cold-Plasma a New Tool for Skeletal Tissue Engineering, Repair and Regeneration*
- *Sue Shapses, Ph.D., R.D., Rutgers University - "Obese Bones and the Response to Energy Restriction"*

11:15 – 12:00pm **Session II: Recent New Member Session** (Moderator: Robert Mauck, Ph.D.)

- *Songtao Shi, D.D.S, M.S., Ph.D. - "Mesenchymal stem cell-based regeneration and immune therapies"*
- *Eric Granquist, DM.D., M.D. – "A non-invasive model of temporomandibular joint pain with tunable outcomes of acute and chronic pain in the rat"*
- *George Hajishengallis, D.D.S., Ph.D. – "DEL-1 restrains osteoclastogenesis and inhibits inflammatory bone loss in nonhuman primates"*

12:00 – 1:45pm **Poster Session and Lunch (provided) in BRB Lobby**

- 12:45 – 1:15pm Poster Session (Odd Numbered)
- 1:15 – 1:45pm Poster Session (Even Numbered)

1:45 – 2:45pm **Session III: Pilot Grantee Session** (Moderator: Maurizio Pacifici, Ph.D.)

- *Arjun Raj, Ph.D. – "Marker gene expression at the single cell level does not correlate with functional chondrogenic potential"*
- *Lachlan Smith, Ph.D. – "Mechanisms of failed bone formation in mucopolysaccharidosis VII"*
- *Hansell Stedman, M.D. – "Lessons from muscle injury and muscular dystrophy about the evolution of animal locomotion - and vice versa"*

2:45 – 3:45pm **Keynote Speaker** (Moderator: Robert Pignolo, M.D., Ph.D.)

Nancy Lane, M.D.
Director for the Center for Musculoskeletal Health
University of California at Davis
"Treatment of musculoskeletal diseases with a little help from your own stem cells"

3:45 – 4:00pm **Final Comments Preceding Poster Session and Reception**

4:00 – 5:30pm **Poster Session, Presentation of Poster Awards and Reception in BRB Lobby**

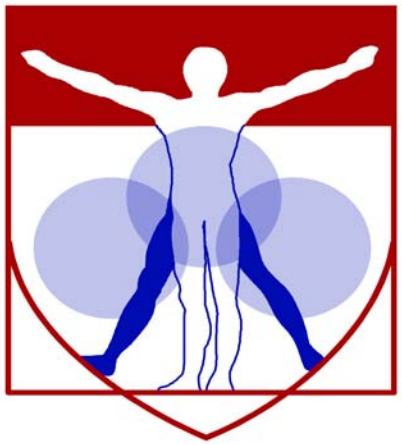

PENN

CENTER for

MUSCULOSKELETAL

DISORDERS

Center

Components

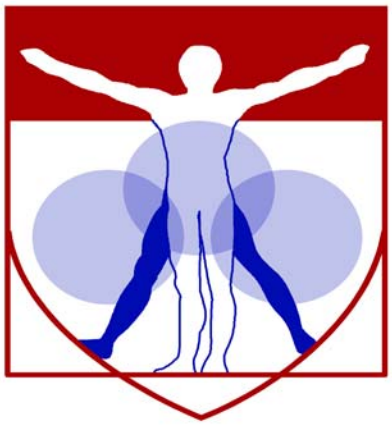

PENN

CENTER for

MUSCULOSKELETAL

DISORDERS

Center Overview

OVERVIEW OF THE PENN CENTER FOR MUSCULOSKELETAL DISORDERS

Director: Louis J. Soslowsky, PhD (soslowsk@upenn.edu)
Associate Director: Maurizio Pacifici, PhD (PacificiM@email.chop.edu)

Musculoskeletal-related conditions in the United States account for 132 million visits to physicians' offices, 29 million visits to emergency rooms, 15 million hospital outpatient visits, and cost over $850 billion each year. Further, musculoskeletal injuries in the United States cause workers to miss more than 440 million days of work annually. In fact, more than one in four Americans has a musculoskeletal impairment. With the widespread increase in athletic and recreational activities, and the increase of the elderly population at large, these numbers are expected to rise substantially. Musculoskeletal injuries represent a critical health concern which must be better understood and better treated. To do so, a dedicated and focused strategic effort is required that optimizes research translation from the bench to the bedside in an efficient and effective manner.

The Penn Center for Musculoskeletal Disorders (PCMD) will continue to enhance the research productivity and provide critical resources and programs to investigators, with a wide variety of expertise, to address multidisciplinary research strategies for musculoskeletal problems. The overall goal of this Center is to promote a cooperative interaction among investigators to enhance the effectiveness of ongoing research and promote new research. The theme of our Center is "Musculoskeletal Tissue Injury and Repair". This theme is both broad (as it includes all musculoskeletal tissue types, such as bone, cartilage, disc, ligament, meniscus, muscle, and tendon), focused (as it includes similarities of approaches across all tissue types, with particular emphasis on applications using small animal models), and clinically significant (as it fosters development of assays, procedures and new knowledge with direct translational relevance). It is important to note that our PCMD is not a "bone center", nor is it a "muscle center". Indeed, one of the major strengths that differentiates our efforts is our inclusive home for all musculoskeletal researchers at Penn.

One focus of the Core Center will be to apply research themes, approaches, and paradigms that are consistent across different tissues. Musculoskeletal tissues have much in common, as they are primarily comprised of collagen and proteoglycan and largely serve a biomechanical function. Notably, their similarities are often overlooked when focusing upon only a single tissue type. For example, the role of inflammatory cytokines is well studied in several tissue injury and repair scenarios; yet specific findings in one tissue-type are not always known and applied to other tissues. Similarly, the role and availability of technologies for imaging new blood vessel formation *in vivo* in order to monitor healing in a single tissue are not always known to researchers in other tissues. In general, approaches used to evaluate mechanisms present in one tissue are not always known and applied by researchers in other tissues.

While forming research groups "within" tissue types has benefits, this approach also has some limitations. Currently, many investigators consider themselves "bone researchers" or "cartilage researchers" and are often not aware of advances made on other tissues that may be relevant to their own. This issue is exacerbated by the fact that many scientific conferences do not construct their programs based on themes, approaches, and paradigms. Programs are generally constructed as "tissue specific" (e.g., typical sessions at the Orthopaedic Research Society meeting are on Tendon Injury, Bone Mechanics, Intervertebral Disc, etc.). In fact, some conferences are focused on a single area (e.g., Sun Valley Hard Tissue Workshop, International Symposium on Tendons and Ligaments).While these specialty meetings have high scientific value and are important venues for exchange of information, they are usually only attended by investigators active in these particular areas. Bringing multidisciplinary researchers together, focusing not on a specific tissue, but on research approaches or paradigms, will enhance and advance the research programs for all investigators and serve to foster collaborative research efforts. An example of this

concept is the Gordon Conferences where meetings on “Proteoglycans” or “Musculoskeletal Science” cross tissue types and can address higher level paradigms.

To provide a further focus for our Center, we will develop programs with an emphasis on small animal models of human musculoskeletal disorders. Although both large and small animal models for various human diseases currently exist and continue to be developed, the use of small animals (e.g., mouse and rat) has become increasingly preferred for many reasons. These reasons include the availability of transgenic and knockout animals, the ease of procuring consistent animals in large numbers, animal cost, handling, housing, and other practical management issues. More importantly, the sequencing of their genomes and the varieties of molecular analyses currently available have made the mouse and rat increasingly preferred. However, some technical difficulties remain in performing certain assays and experiments simply because of the small size of the mouse and rat, and these difficulties can often not be overcome in single investigator laboratories.

Thus, the primary aims of this Center are to enhance and advance the research productivity of investigators in musculoskeletal tissue injury and repair by:

Aim 1: Developing critical research core facilities in fundamental areas that cross disciplines and hierarchies. These core facilities are Molecular Profiling, Imaging, biomechanics, and Histology.

Aim 2: Developing a pilot and feasibility grant program for new and established investigators whereby new approaches, ideas, and collaborations can be developed prior to seeking extramural funding, and,

Aim 3: Developing educational, training, and research enrichment programs for the musculoskeletal community spanning multiple tissue types, research approaches, and paradigms, through which investigators can learn from each other, and from national leaders, in areas where they are not expert.

High quality musculoskeletal research is currently being conducted by many groups using molecular, cellular, tissue, and/or organ-level approaches. Examples include genetic analyses using microarrays, structural assays using sophisticated imaging modalities, and evaluation of the stiffness and strength of tissues using biomechanical analyses. While these and many other modalities are commonly brought to bear on musculoskeletal problems, very few research groups have the required expertise and specialized facilities to perform high quality work in all of these areas in their own labs. Furthermore, most investigators are not aware of approaches utilized and results obtained in other tissues that may have direct relevance on their primary research questions. This PCMD provides an environment and a forum for such expertise and exchanges.

Ultimately, close cooperation, communication, and collaboration among researchers across all musculoskeletal tissue types and from a wide variety of disciplines will significantly enhance the musculoskeletal research opportunities at the University of Pennsylvania. The Center will provide opportunities to integrate multi-disciplinary techniques to determine mechanisms for tissue function, injury, and repair, with an ultimate goal to advance the ability to diagnose, treat, and prevent diseases and injuries of the musculoskeletal system and its component tissues.

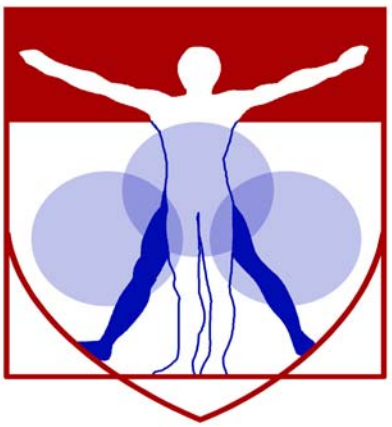

PENN

CENTER for
MUSCULOSKELETAL
DISORDERS

Core I

Molecular Profiling

Molecular Profiling Core

Faculty Director: Tapan Ganguly, Ph.D. (gangulyt@mail.med.upenn.edu)
Bioinformatics Technical Director: John Tobias, Ph.D. (jtobias@upenn.edu)

The musculoskeletal disease research field continues to expand its use of studies at the molecular level. In particular, a variety of evaluation tools are now available that allow investigators to study the molecular systems in which biological processes occur. These tools enable a low as well as high-throughput evaluation of an organism's DNA and RNA biomarkers. Specifically, gene and miRNA expression analysis, DNA variant genotyping, gene copy number detection, and methylation analysis can be used on samples obtained from a variety of sources. Microarray technologies have revolutionized molecular profiling and allow researchers to interrogate hundreds of thousands of DNA or RNA markers in a high-throughput fashion. Array-based and genomic technologies are advancing rapidly in scope and power.

The mission of the PCMD Molecular Profiling Core, located in the Penn Genomic Analysis Core, is to support molecular profiling research for members of the PCMD by providing quality services conducted on a variety of genomic platforms for low or high throughput analysis as well as bioinformatics support. The scope of services provided includes assistance with experimental design and resource assessment, sample preparation, assay performance, and data management and analysis. Several pilot grants are funded each year by the Core to encourage use of the facility by PCMD members.

The Specific Aims are:

Aim 1: To provide guidance and training on the capabilities, advantages, and disadvantages of various genomic protocols and analyses for musculoskeletal research through formal educational enrichment programs and one-on-one interactions.

Aim 2: To provide expertise and service for whole-genome and targeted RNA profiling assays of musculoskeletal tissues.

Aim 3: To provide expertise and service for whole-genome and targeted DNA profiling assays of musculoskeletal tissues.

Aim 4: To provide bioinformatics services and training appropriate for analyzing the data produced in Aims 2 and 3.

These Aims are supported through Core expertise and equipment for Affymetrix, Sequenom, Fluidigm, and Luminex. The facility also offers TaqMan quantitative PCR, robotic DNA/RNA extraction and handling, and bioinformatics hardware and software.

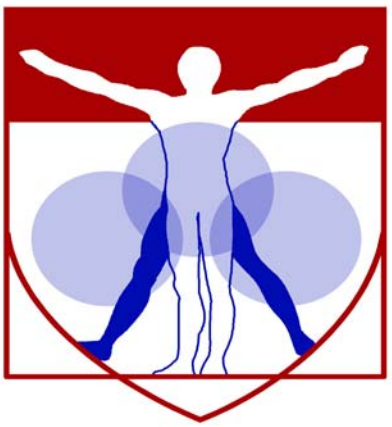

PENN

CENTER for

MUSCULOSKELETAL

DISORDERS

Core II

Imaging

Imaging Core

Director: Felix Wehrli, Ph.D. (wehrli@mail.med.upenn.edu)
Associate Director: X. Sherry Liu, Ph.D. (xiaoweil@mail.med.upenn.edu)

Imaging is a critically important technology for clinical, translational, cadaveric, and *in vivo* studies of animal and human disease. Whether the ability to characterize tissue structure or visualize molecular markers in a non-invasive manner, advanced imaging methods have proven to be powerful tools specifically for musculoskeletal applications. Research employing imaging that addresses problems in musculoskeletal injury and repair in humans has a long track record. Further, imaging is recognized to be vital as new evaluation and treatment modalities are developed and used for some of the major degenerative disorders such as osteoporosis and osteoarthritis or traumatic injuries such as fractures.

A key objective of the Penn Center for Musculoskeletal Disorders (PCMD) therefore is to provide an on-campus Imaging Core (IC) to musculoskeletal researchers for imaging of both humans and large and small animals. The overall objective of the IC is to develop and utilize a wide range of imaging techniques directed toward problems of musculoskeletal tissue injury and repair.

The Specific Aims are:

Aim 1: To provide guidance and expertise on the use of imaging for musculoskeletal research through educational enrichment programs and one-on-one interactions.

Aim 2: To provide a range of imaging resources for the study of structure, function and physiology of the musculoskeletal system in laboratory animals and humans.

Aim 3: To provide pilot funding for development of new projects and collaborations and for investigators to generate preliminary data.

Successful completion of these Aims will significantly enhance the environment and capabilities of researchers at the University of Pennsylvania, leading to novel and innovative approaches to address musculoskeletal disorders and to new collaborations between Core faculty who may not have previously included human and/or animal imaging in their musculoskeletal research programs.

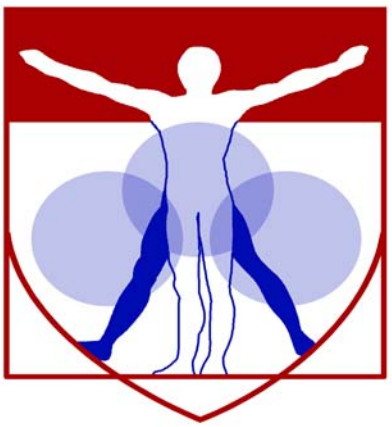

PENN

CENTER for

MUSCULOSKELETAL

DISORDERS

Core III

Biomechanics

Biomechanics Core

Core Director: Robert Mauck, Ph.D. (lemauck@mail.med.upenn.edu)
Technical Director: Snehal Shetye, Ph.D. (shetye@upenn.edu)

The overall objective of this Biomechanics Core (BC) is to develop and utilize a wide range of biomechanical approaches to evaluate musculoskeletal tissue damage and repair, and to provide training and funding for new projects and collaborations utilizing these assays. Succinctly, our overarching aims are:

- To provide guidance and training on the capabilities, advantages, and disadvantages of the various methodologies to assess musculoskeletal tissue biomechanical function through formal educational enrichment programs and one-on-one interactions.
- To provide expertise and service for biomechanical assays of musculoskeletal tissues.
- To develop new biomechanical testing techniques that will be applicable to musculoskeletal research.
- To provide funding for development of new projects and collaborations and to develop preliminary and/or feasibility data for investigators.

Successful completion of these aims will significantly enhance the environment and the capabilities of researchers at the University of Pennsylvania, leading to new approaches to address musculoskeletal disorders and new collaborations between Center faculties who may have not previously included biomechanical function approaches in their musculoskeletal research programs.

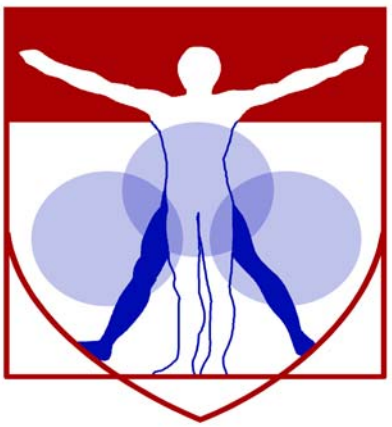

PENN

CENTER for

MUSCULOSKELETAL

DISORDERS

Core IV

Histology

Histology Core

Director: Robert Pignolo, M.D., Ph.D. (pignolo@mail.med.upenn.edu)

The structure and composition of musculoskeletal tissues are tailored to meet their demanding functions. With injury, the structure and composition of these tissues deteriorate, resulting in a decline or loss of mechanical function. Musculoskeletal tissues each have a wide array of compositional and structural variety with respect to collagen and proteoglycan types, as well as other extracellular matrix constituents and factors. Careful description and quantification of tissue structural organization and composition, as well as localization and identification of growth factors and cytokines, are necessary requirements for elucidation of the biologic mechanisms underlying musculoskeletal integrity, injury, and repair. The overall objective of this Histology Core (HC) is to develop and utilize a wide range of histological and histomorphometric approaches to evaluate musculoskeletal tissue injury and repair, and to provide training and funding for new projects and collaborations utilizing these assays.

The Specific Aims are:

Aim 1: To provide guidance and training on the capabilities, advantages, and disadvantages of the various methodologies to assess musculoskeletal tissue structure and composition through formal educational enrichment programs and one-on-one interactions.

Aim 2: To provide expertise and service for histological and histomorphometric assays of musculoskeletal tissues.

Aim 3: To develop new histologically-based techniques that will be applicable to musculoskeletal research.

Aim 4: To provide funding for development of new projects and collaborations and to develop preliminary and/or feasibility data for investigators.

Successful completion of these aims will significantly enhance the environment and the capabilities of researchers in the Penn Center for Musculoskeletal Disorders at the University of Pennsylvania (Penn), leading to new approaches to address musculoskeletal disorders and new collaborations between Center faculty who may have not previously included structural and compositional approaches through histological examination in their musculoskeletal research programs.

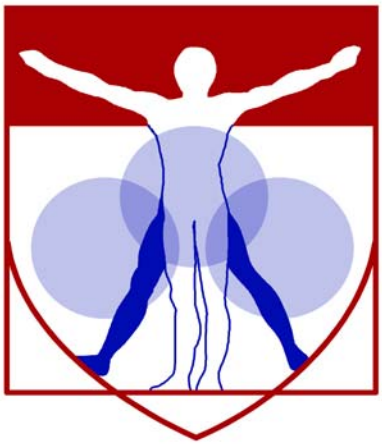

PENN

CENTER for

MUSCULOSKELETAL

DISORDERS

Pilot Grant Program

PENN CENTER FOR MUSCULOSKELETAL DISORDERS
PILOT AND FEASIBILITY GRANT PROGRAM

The Penn Center for Musculoskeletal Disorders has an ongoing Pilot and Feasibility Grant Program. Submissions should be related to musculoskeletal tissue injury and repair which is the broad focus of the Center and Grants are only eligible for Center members (if you are not a member but would like to become one, please contact pcmd@mail.med.upenn.edu. For more information on our Cores and Center in general, please see our web site at http://www.med.upenn.edu/pcmd. We are anticipating that the next Center grant submission deadline will be in early Spring 2016.

Eligibility

- Only Full Center members are eligible. If you are not currently a member, please go to the link: http://www.med.upenn.edu/pcmd/memberinfo.shtml
- Categories of applicants include: 1) Established investigators with a proposal to test the feasibility of a new or innovative idea in musculoskeletal tissue injury and repair representing a clear and distinct departure from their ongoing research, 2) Established investigators with no previous work in musculoskeletal tissue injury and repair interested in testing the applicability of their expertise on a problem in this area, and 3) New investigators without significant extramural grant support as a Principal Investigator to develop a new project.
- Pilot and Feasibility Grants must use at least one of the Center's Research Cores.
- Pilot project awardees are eligible for one year, with a second year to be considered (budgets will be for $20-50,000 per year and timelines should be for one or two years). The second year of funding, the dollar amount of which would only be for up to half the year one budget, will be considered based on the progress report submitted after the first year of funding and funding availability in the Center. Please note that second year funding will often not be awarded, and when awarded, will be done so primarily to new investigators; second year funding to senior investigators will be quite rare.
- It is expected that these Pilot grants will lead to funding through other independent, extramural mechanisms. Therefore, the likelihood of future extramural funding will enter into the evaluation of these proposals.

Format

- Applications should be formatted loosely in the style of an NIH R03 grant (http://grants.nih.gov/grants/guide/pa-files/PA-13-304.html). The main body of the application (Specific Aims through Research Design and Methods-sections 4-7 below) is limited to five pages. The application should be in a single pdf file. The format should be:

  1) Cover Page (not NIH face page) with grant title, PI name (and co-PI name if applicable), affiliation, contact information
  2) Budget and brief justification (note that equipment is not allowed)
  3) NIH Biosketch of PI (and co-PI if applicable)
  4) Specific Aims
  5) Significance
  6) Innovation
  7) Approach
  8) Brief Statement of Category of Investigator per guidelines above
  9) Brief Statement of how this Funding will lead to other Extramural Funding
  10) Human Subjects and/or Vertebrate Animal Subjects (if applicable)
  11) Consultants (if applicable)
  12) Literature Cited
  13) Certification of Patient Oriented Research (if applicable)

Please do not hesitate to email pcmd@mail.med.upenn.edu with any questions or comments.

Penn Center for Musculoskeletal Disorders Pilot & Feasibility Grants
(All grants awarded since inception of Center)

Awarded 2015-2016

Yejia Zhang, MD, PhD, Department of Physical Medicine and Rehabilitation, "Inhibition of ADAM-8 to reduce intervertebral disc degeneration" *(supported in part from the IRM Program in Musculoskeletal Regeneration)*

Oren Friedman, MD, Department of Otorhinolaryngology, "Effect of injury to cartilage and recovery treatment with FGF-18" *(supported in part from the IRM Program in Musculoskeletal Regeneration)*

Harvey Smith, MD, Department of Orthopaedic Surgery, "Impact of Pre-Culture and In Vivo Remobilization on Engineered Disc Replacement" *(supported in part from the IRM Program in Musculoskeletal Regeneration)*

Tejvir Khurana, MD, PhD, Department of Physiology, "Role of the IL-15 / IL-15Rα axis in modulating muscle-tendon-bone adaptation and repair" *(supported in part from the IRM Program in Musculoskeletal Regeneration)*

Awarded 2014-2015

Joshua F. Baker, MD, MSCE, Department of Rheumatology & Epidemiology/Perelman School of Medicine: *"Assessment of Intramyocellular Fat Accumulation in Rheumatoid Arthritis Using MR Spectroscopy*"

Russ P. Carstens, MD, Department of Renal-Electrolyte and Hypertension Division, Perelman School of Medicine: "Roles of Epithelial Splicing Regulatory Proteins in Craniofacial Development" *(awarded extramural funding from the NIH 1R56DE024749 and awarded R01 NIDCR)*

Foteini Mourkioti, PhD, Department of Orthopaedic Surgery/Perelman School of Medicine: "A Novel Molecular Mechanism in Chronic Skeletal Muscle Injury" *(supported in part from the IRM)*

Chamith Rajapakse, PhD, Department of Radiology/Perelman School of Medicine: "Biomechanics of Hip Fracture Assessed by MRI"

Awarded 2013-2014

X. Sherry Liu, PhD, Department of Orthopaedic Surgery, Perelman School of Medicine: "Structure and Strength Recovery in Post-Lactation Bone" *(awarded extramural funding from the NIH R03 AR065145)*

Ling Qin, Ph.D., Department of Orthopaedic Surgery, Perelman School of Medicine: "Novel Anabolic Treatment for Radiation-Induced Osteoporosis" *(awarded extramural funding from the NIH R01AR066098)*

Lachlan Smith, Ph.D. Department of Orthopaedic Surgery, Perelman School of Medicine: "Molecular Mechanisms of Failed Vertebral Bone Formation in Mucopolysaccharidosis VII" *(awarded extramural funding from the NIH R03 AR065142 and the MPS Society)*

Hansell H. Stedman, MD, Department of Surgery, Perelman School of Medicine: "Molecular Pattern Recognition in Acute and Chronic Injury to Muscle and Myotendinous Junction" *(awarded extramural funding from the NIH R01NS094705)*

Awarded 2012-2013

Jason Burdick, PhD, Department of Bioengineering, School of Engineering and Applied Science: "Acelluar Fibrous Scaffolds for Stem Cell Recruitment and Cartilage Repair" *(awarded extramural funding from the NIH R01 EB008722)*

James L. Carey, MD, MPH, Department of Orthopaedic Surgery, Perelman School of Medicine: "Development of a Large Animal Model of Osteochondritis Dissecans" *(awarded extramural funding from the NIH R01 EB008722)*

Andrew Kuntz, MD, Department of Orthopaedic Surgery, Perelman School of Medicine: "Effects of Intra-Articular Glenohumeral Injection of a Nonsteroidal Anti-Inflammatory Drug on Shoulder Joint Mechanics in a Rat Model"

Arjun Raj, PhD, Department of Bioengineering, School of Engineering and Applied Science: "Single Cell Analysis of Molecular and Micromechanical Heterogeneity in Mesenchymal Stem Cells and Engineered Tissues"

Awarded 2011-2012

Struan F.A. Grant, PhD, Department of Pediatrics, Children's Hospital of Philadelphia and Perelman School of Medicine: "Utilization of ChIP-seq to Identify Genes Regulated by Osterix"

Motomi Enomoto-Iwamoto, DDS, PhD, Department of Orthopaedic Surgery, Children's Hospital of Philadelphia and Perelman School of Medicine: "Tendon Repair by Retinoic Acid Receptor Agonists" *(awarded extramural funding from the NIH R21 AR062193)*

Ian N. Jacobs, MD, Department of Otorhinolaryngology: Head and Neck Surgery, Children's Hospital of Philadelphia and Perelman School of Medicine: "A Pilot Study for the Development of a Rabbit In-Vivo Tissue- Engineered Cartilage Graft for Pediatric Laryngotracheal Reconstruction" *(awarded extramural funding from The Triological Society)*

Awarded 2010-2011

Susan W. Volk, VMD, PhD, Dipl ACVC, Department of Small Animal Surgery, School of Veterinary Medicine: "The Role of Type III Collagen in Bone Repair and Regeneration"

Jaimo Ahn, MD, PhD, Department of Orthopaedic Surgery, Perelman School of Medicine: "Toward the Identification of Molecular Pathway Alterations in Aged Fracture Healing: A Pilot Study Utilizing a Genetic Model of Senescence" *(awarded extramural funding from the NIH R03 AG040670)*

Shannon Fisher, MD, PhD, Department of Cell and Developmental Biology, Perelman School of Medicine: "Requirement for Osterix in Skull Formation and Maintenance of Adult Bone in Zebrafish" *(awarded extramural funding from the NIH R21 DE021509)*

Awarded 2010-2011 (Jointly with IOA)

Olena Jacenko, PhD, Department of Animal Biology, School of Veterinary Medicine: "Aging of the hematopoietic niche" *(awarded extramural funding from the NIH R01 DK088334)*

Eileen M. Shore, PhD, Departments of Orthopaedic Surgery and Genetics, Perelman School of Medicine: "Modulation of Progenitor Cell Differentiation through BMP Signaling" *(awarded extramural funding from the NIH R01 AR041916)*

Kurt D. Hankenson, DVM, PhD, Department of Animal Biology, School of Veterinary Medicine: "Notch Signaling in Bone Regeneration" *(awarded extramural funding from the DOD CDMRP)*

Awarded 2009-2010

Ling Qin, PhD, Department of Orthopaedic Surgery, School of Medicine: "Mechanisms of EGFR Action on Bone" *(awarded extramural funding from the NIH R01 DK095803)*

Steven Scherer, MD, PhD, Department of Neurology, Perelman School of Medicine: "Are N-cadherin and L1 Adhesion Molecules Required for Recovery of Muscle Strength after Nerve Injury?"

Nader M. Hebela, MD, Department of Orthopaedic Surgery, Perelman School of Medicine: "A Pre-Clinical Rodent Model of Intervertebral Disc Autograft Transplant" *(awarded extramural funding from the DOD/CDMRP/PROP OR090090)*

Awarded 2008-2009

Sunday O. Akintoye, BDS, DDS, MS, Department of Oral Medicine, School of Dental Medicine: "Orofacial Bone Marrow Stromal Cells Promote Bisphosphonate-Associated Jaw Osteonecrosis" *(awarded extramural funding from the NIDCR R21 DE022826)*

Margaret M. Chou, PhD, Departments of Cell and Developmental Biology, Perelman School of Medicine: "Mechanisms of TRE17/USP6 Function in the Etiology of Aneurysmal Bone Cyst" *(awarded extramural funding from the NIH-NCI R01 CA168452 and R21-CA18601)*

Kenneth W. Leichty, MD, Department of Surgery, Perelman School of Medicine: "The Role of Inflammation in Regenerative Fetal Tendon Wound Healing" *(awarded extramural funding from the NIH DP2 DK083085)*

Kathleen M. Loomes, MD, Department of Pediatrics, Children's Hospital of Philadelphia: "The Role of Jag1 in Osteogenesis"

Eileen M. Shore, PhD, Departments of Orthopaedic Surgery and Genetics, Perelman School of Medicine: "Analysis of an ACVR1 Knock-in Mouse Model for FOP*" (awarded extramural funding from the NIH R01 AR041916)*

Awarded 2007-2008

Sherrill L. Adams, PhD, Department of Biochemistry, School of Dental Medicine: "Collagen III-deficient Mice as a Model for Musculoskeletal Wound Repair"

Kurt D. Hankenson, DVM, PhD, Department of Animal Biology, School of Veterinary Medicine: "Regulation of Bone Formation by Novel Activators of Canonical Wnt Signaling"

Awarded 2006-2007

Robert J. Pignolo, MD, PhD, Department of Medicine, Perelman School of Medicine: "Stem Cell Rescue of the Osteoporotic Phenotype in a Mouse Model of Accelerated Aging" *(awarded extramural funding from the NIH R01 AG028873)*

Robert L. Mauck, PhD, Department of Orthopaedic Surgery, Perelman School of Medicine "Meniscus Repair with a Novel Aligned Nanofiber Scaffold" *(awarded extramural funding from the NIH R01 AR056624 and the VA RR & D)*

Christopher S. Chen, MD PhD, Department of Bioengineering, School of Engineering and Applied Science: "Mechanotransduction in Mesenchymal Stem Cells" *(awarded partial funding as Co-Investigator on NIH P41 EB001046)*

Pedro K. Beredjiklian, MD, Department of Orthopaedic Surgery, Perelman School of Medicine: "Role of Hyaluronic Acid Receptors in Tendon Healing" (*awarded extramural funding from the NIH R21 AR052393*)

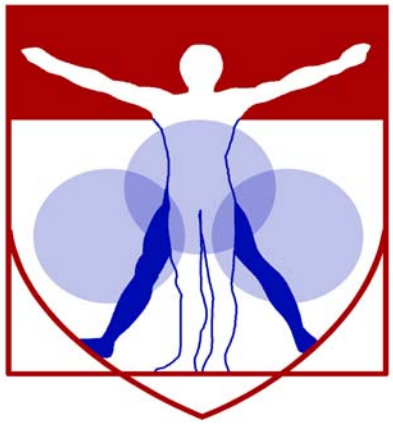

PENN

CENTER for

MUSCULOSKELETAL

DISORDERS

Visiting Professorship Series

PENN
CENTER for
MUSCULOSKELETAL
DISORDERS

Visiting Professorship Series-Academic Year 2015-2016

Tuesday, May 17, 2016, 1:30-2:30/TBD
TBD
David J. Glass, MD
Novartis Institutes for Biomedical Research

Tuesday, April 19, 2016, 1:30-2:30pm/TBD
Genome and Epigenome editing for Gene Therapy and Programming Cell Fate
Charles Gersbach, Ph.D.
Associate Professor of Biomedical Engineering
Assistant Professor of Orthopaedic Surgery
Duke University

Tuesday, March 2016 TBD

Tuesday, February 16, 2016, 1:30-2:30pm/TBD
Unravelling the neurobiology of osteoarthritis pain
Anna-Marie Malfait, MD, PhD
Associate Professor of Medicine and Biochemistry
Rush University Medical Center

Tuesday, January 19, 2016, 1:30-2:30pm/TBD
Role of Connexin43 in Cortical Bone Adaptation to Mechanical Load
Roberto Civitelli, MD, PhD
Associate Professor of Chemical & Biological Engineering
BioFrontiers Institute

Tuesday, December 15, 2015, 1:30-2:30pm/CRB Auditorium
TGF-beta Integration of Physical and Biochemical Cues in the Skeleton
Tamara Alliston, PhD
Associate Professor, Department of Orthopaedic Surgery
University of California, San Francisco

ANNUAL SCIENTIFIC SYMPOSIUM (all day event)
Thursday, November 19, 2015, 9:30-5:30pm/BRB Auditorium
Title: "Treatment of Musculoskeletal Diseases with a little help from your own Stem Cells"
Nancy Lane, MD
Director, Center for Musculoskeletal Health
UC Davis Health System

Tuesday, October 20, 2015, 1:30-2:30pm/8-146 SCTR
Title: "A Runted Tale of Skeletal Homeostasis and Repair"
M. Hicham Drissi, PhD
Profess of Orthopaedic Surgery
UConn Health

Tuesday, September 8, 2015, 1:30-2:30pm/8-146 SCTR
Title: Evolving roles of Prolyl Hydroxylases in Intervertebral Disc Health and Disease
Markarand V. Risbud, PhD
Professor of Orthopaedic Surgery; Director, Spine Research Program
Sidney Kimmel Medical College, Thomas Jefferson University

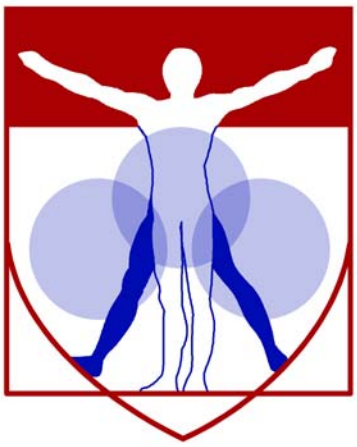

PENN
CENTER for
MUSCULOSKELETAL
DISORDERS

Symposium Participants

Last Name	First Name	Email	Affiliation
Akins	Jon	jsakins@widener.edu	Widener Univ Biomedical Engineering
Alavi	Abass	abass.alavi@uphs.upenn.edu	Penn Radiology
Alharbi	Mohammed	malharbi@dental.upenn.edu	Penn Endodontics
Arany	Zolt	zarany@mail.med.upenn.edu	Penn Cardiology
Baker	Joshua	bakerjo@uphs.upenn.edu	Penn Rheumatology/Epidemiology
Bansal	Sonia	soniab@seas.upenn.edu	Penn Bioengineering
Barbe	Mary	mary.barbe@temple.edu	Temple Anatomy/Cell Biology
Barnum	Carrie	cbarnum@mail.med.upenn.edu	Penn Ortho
Bendigo	Justin	jbendigo@med.mail.upenn.edu	Penn Ortho
Bhatt	Pankti	bhattpankti14@gmail.com	Penn Ortho
Billings	Paul	billingsp@email.cho.edu	CHOP Ortho
Borges	Kelly	kborges@mail.med.upenn.edu	Penn Radiology
Brewer	Niambi	nbrewer@mail.med.upenn.edu	Penn Ortho
Brody	Robert	robert.brody@uphs.upenn.edu	Penn Otorhinolaryngology
Burdick	Jason	burdick2@seas.upenn.edu	Penn Bioengineering
Caron	Bob	rcaron@mail.med.upenn.edu	Penn Ortho
Casey	Ellen	ecasey@drexelmed.edu	Drexel Univ College of Medicine
Chakkalakal	Salin	salin@mail.med.upenn.edu	Penn Ortho
Chandra	Abhishek	abhic@mail.med.upenn.edu	Penn Ortho
Chang	Ting-Han	cth0616@hotmail.com	Taiwan Adventist Hospital
Chang	Chih-Chiang	changc4@seas.upenn.edu	Penn Bioengineering
Chen	Chider	chenc10@dental.upenn.edu	Penn Anatomy/Cell Biology
Chen	Meiqi	chenmei@mail.med.upenn.edu	Penn Cardiology
Chen	Minna	minnac@seas.upenn.edu	Penn Bioengineering
Chen	Chider	chenc10@dental.upenn.edu	Penn Anatomy/Cell Biology
Chernets	Natalie	chernetsn@gmail.com	Thomas Jefferson Univ Ortho
Chesi	Alessandra	chesia@email.chop.edu	CHOP Human Genetics
Coldren	Faith	fcoldren@upenn.edu	ITMAT Bioinformatics
Convente	Michael	convente@mail.med.upenn.edu	Penn Ortho
Cosgrove	Brian	bdcosgro@gmail.com	Penn Bioengineering
Cote	Allison	allcote@mail.med.upenn.edu	Penn Cell/Molecular Biology
Cottingham	Naiga	cottinghan@email.chop.edu	CHOP Ortho
Cousminer	Diana	cousminerd@email.chop.edu	CHOP Genetics
de Bakker	Chantal	chantald@seas.upenn.edu	Penn Bioengineering

Decker	Rebekah	DeckerR@chop.edu	CHOP Ortho
Deie	Suzu	b124250@hiroshima-u.ac.jp	CHOP Ortho
Dinella	Susan	sdinella@upenn.edu	Penn Ortho
Doyran	Basak	bd386@drexel.edu	Drexel Univ Biomedical Sciences
Esterhai	John	john.esterhai@uphs.upenn.edu	Penn Ortho
Farber	Daniel	daniel.farber@uphs.upenn.edu	Penn Ortho
Farrar	John	jfarrar@upenn.edu	Penn CCEB
Fong	John	fongdung@mail.med.upenn.edu	Penn Ortho
Francois	Noelle	francoisn@email.chop.edu	CHOP Ortho
Frara	Nagat	tuc36797@temple.edu	Temple Univ Anatomy/Cell Biology
Freedman	Benjamin	freedman.br@gmail.com	Penn Bioengineering
Freeman	Theresa	theresa.freeman@jefferson.edu	Thomas Jefferson Univ Ortho
Friedman	James	james.friedman@uphs.upenn.edu	Penn Ortho
Fryhofer	George	fryhofer@mail.med.upenn.edu	Penn Ortho
Gandiga	Prateek	prateek.gandiga@uphs.upenn.edu	Penn Rheumatology
Ganguly	Tapan	gangulyt@mail.med.upenn.edu	Penn Genetics
Glaser	David	david.glaser@uphs.upenn.edu	Penn Ortho
Graves	Dana	dtgraves@dental.upenn.edu	Penn Periodontics
Greer	Christopher	greerc@mail.med.upenn.edu	Penn Ortho
Grice	Elizabeth	egrice@upenn.edu	Penn Dermatology
Gullbrand	Sarah	selinley516@gmail.com	Penn Ortho
Guo	Jianman	jianmanguo@gmail.com	Penn Ortho
Guo	Pneg	james249540408@gmail.com	Penn Ortho
Han	Lin	lh535@drexel.edu	Drexel Univ Biomedical Engineering
Han	Biao	bh462@drexel.edu	Drexel Univ Biomedical Engineering
Hanifi	Arash	a.hanifi@gmail.com	Temple Univ Bioengineering
Hast	Michael	hast@upenn.edu	Penn Ortho
Henning	Elizabeth	ehenning@mail.med.upenn.edu	Penn Ortho
Hillin	Cody	cody.hillin@uphs.upenn.edu	Penn Ortho
Holsgrove	Timothy	thols@seas.upenn.edu	Penn Bioengineering
Huegel	Julianne	jhuegel08@gmail.com	Penn Ortho
Ibrahim	Mazen	mazenabdallah79@gmail.com	CHOP Ortho
Ihida-Stansbury	Kaori	ikaori@mail.med.upenn.edu	Penn Pathology & Lab Medicine
Ita	Meagan	meita@seas.upenn.edu	Penn Bioengineering
Iwamoto	Motomi	iwamotom1@email.chop.edu	CHOP Ortho

Iwamoto	Masahiro	iwamotom@email.chop.edu	CHOP Ortho
Jacenko	Olena	jacenko@vet.upenn.edu	Penn Vet Biomedical Sciences
Jia	Haoruo	horror7haoruo@gmail.com	Penn Ortho
Kang	Jennifer	jenkang@sas.upenn.edu	Penn Ortho
Kaplan	Frederick	Frederick.Kaplan@uphs.upenn.edu	Penn
Kartha	Sonia	skartha@seas.upenn.edu	Penn Bioengineering
Keah	Niobra	niobra.keah@gmail.com	Penn Ortho
Kelly	John	john.kelly@uphs.upenn.edu	Penn Ortho
Khan	Amna	amna.khan@uphs.upenn.edu	Penn Medicine/Philadelphia VAMC
Khurana	Tejvir	tsk@mail.med.upenn.edu	Penn Physiology/Penn Muscle Institute
Kim	Minwook	kimminw@mail.med.upenn.edu	Penn Ortho
Kobe	Elizabeth	ekobe@seas.upenn.edu	Penn Bioengineering
Kolasinski	Sharon	sharon.kolasinski@uphs.upenn.edu	Penn Medicine/Rheumatology
Kou	Xiaoxing	xiaoxing@dental.upenn.edu	Penn Anatomy/Cell Biology
Kuntz	Andrew	andrew.kuntz@uphs.upenn.edu	Penn Ortho
Kwon	Mi	miykwon@seas.upenn.edu	Penn Bioengineering
Lane	Nancy	nelane@ucdavis.edu	University of California Davis
Lang Sala	Renata	renata.lang89@gmail.com	Penn Bioengineering
Langham	Michael	langhamc@mail.med.upenn.edu	Penn Radiology
Lee	Wonsae	wonsae@seas.upenn.edu	Penn Biotechnology
Leung	Thomas	thl@upenn.edu	Penn Dermatology
Lewis	Gregory	glewis1@hmc.psu.edu	Pennsylvania State Univ Ortho
Li	Qing	ql55@drexel.edu	Drexel Univ Biomedical Engineering
Li	Yihan	yihanl@seas.upenn.edu	Penn Ortho
Liu	Jin	ljamelia@163.com	Penn Dental Anatomy/Cell Biology
Liu	Dawei	daweiliu@upenn.edu	Penn Dental Anatomy/Cell Biology
Liu	Min	lium4@email.chop.edu	CHOP Ortho
Liu	Minglin	lium1@mail.med.upenn.edu	Penn Dermatology
Liu	X. Sherry	xiaoweil@mail.med.upenn.edu	Penn Ortho
Loro	Emanuele	eloro@mail.med.upenn.edu	Penn Physiology
Lounev	Vitali	vlounev@mail.med.upenn.edu	Penn Ortho
Lu	Ming	luming200708@126.com	Penn Ortho
Ma	Xiaoyuan	asdmxywin@gmail.com	Penn Ortho
Malhotra	Neil	nrm@uphs.upenn.edu	Penn Neurgosurgery
Mao	Qin	maoqin1025@163.com	Penn Anatomy/Cell Biology

Mascareno	Rachel	mascarenor@email.chop.edu	CHOP Ortho
Mauck	Robert	lemauck@mail.med.upenn.edu	Penn Ortho
McCarrick-Walmsley	Ruth	mcc.walmsley@gmail.com	Penn Ortho
McGill	Neilia-Kay	Neilia.Mcgill@uphs.upenn.edu	Penn Rheumatology
McLeod	Claire	cm.mcleod@gmail.com	Penn Bioengineering
Meloni	Gregory	gmeloni@mail.med.upenn.edu	Penn Ortho
Mitchell	Jonathan	mitchellj2@email.chop.edu	CHOP Pediatrics
Mohanraj	Bhavana	mohanraj.bhavana@gmail.com	Penn Ortho
Morales	Leon	leonmorales89@gmail.com	Penn Physiology
Morris	Tyler	tylerrohintonmorris@gmail.com	Penn Ortho
Mourkioti	Foteini	fmour@upenn.edu	Penn Ortho
Mundy	Christina	matticolac@email.chop.edu	CHOP Ortho
Mupparapu	Mel	mmd@dental.upenn.edu	Penn Oral Medicine
Naha	Pratap	pratapnaha@gmail.com	Penn Radiology
Najem	Catherine	catherine.najem@uphs.upenn.edu	Penn Rheumatology
Nanga	Ravi	nravi@mail.med.upenn.edu	Penn Radiology
Oyster	Nick	oyster@upenn.edu	Penn Ortho
Pacifici	Maurizio	PacificiM@email.chop.edu	CHOP Ortho
Padalkar	Mugdha	tub84972@temple.edu	Temple University Bioengineering
Pardes	Adam	adampardes@gmail.com	Penn Bioengineering
Pardi	Norbert	pnorbert@mail.med.upenn.edu	Penn Microbiology
Peck	Sun	sunchung@mail.med.upenn.edu	Penn Ortho
Peng	Chao	pengchao0160@gmail.com	Penn Pathology & Lab Medicine
Pignolo	Robert	pignolo@mail.med.upenn.edu	Penn Medicine
Pleshko	Nancy	npleshko@temple.edu	Temple Univ Bioengineering
Pullman-Mooar	Sally	sally.pullman-mooar@va.gov	PVAMC Med Rheumatology
Qin	Ling	qinling@mail.med.upenn.edu	Penn Ortho
Qu	Feini	feini@vet.upenn.edu	Penn Bioengineering
Qu	Haibo	hqu@seas.upenn.edu	Penn Bioengineering
Raffiani	Greg	raffiani@princeton.edu	Princeton Univ Athletics
Rajapakse	Chamith	chamith@mail.med.upenn.edu	Penn Radiology
Ramaswamy	Girish	rgirish@mail.med.upenn.edu	Penn Ortho
Riggin	Corinne	criggin@seas.upenn.edu	Penn Bioengineering
Roberts	Douglas	douglas2@vet.upenn.edu	Penn Biomedical Sciences

Rosenblum	Shira	shira.rosenblum@gmail.com	Penn Surgery
Rostami	Susan	susan.rostami@uphs.upenn.edu	Penn Surgery
Rozans	Sam	sjr64@drexel.edu	Drexel Univ Biomedical Engineering
Salka	Nabeel	nabeelsalka@gmail.com	Penn Ortho
Salzberg	Brian	bmsalzbe@mail.med.upenn.edu	Penn Neuroscience / Physiology
Sambamurthy	Nisha	nishasam@mail.med.upenn.edu	Penn Rheumatology
Schumm	Samantha	schumms@seas.upenn.edu	Penn Bioengineering
Seiber	Breanna	bseiber@mail.med.upenn.edu	Penn Ortho
Sennett	Mackenzie	sennett@mail.med.upenn.edu	Penn Ortho
Seravello	Donna	donnaser@exchange.upenn.edu	Penn Ortho
Sgariglia	Federica	fsgariglia@gmail.com	CHOP Ortho
Shaker	Hend	hendraafat710@yahoo.com	Ministry of Health, Egypt
Shapiro	Irving	irvng.shapiro@jefferson.edu	Thomas Jefferson Univ Ortho
Shapses	Sue	shapses@aesop.rutgers.edu	Rutgers Univ Nutritional Sciences
Sharifi-Sanjani	Maryam	msharif@upenn.edu	Penn Ortho
Shetye	Snehal	shetye@upenn.edu	Penn Ortho
Shore	Eileen	shore@mail.med.upenn.edu	Penn Ortho
Sinha	Sayantani	sinhas@email.chop.edu	CHOP TRP Pediatric Ortho
Smalley	Ryan	rynsmalley@gmail.com	Penn Ortho
Smith	Lachlan	lachlans@mail.med.upenn.edu	Penn Neurosurgery
Smith	Harvey	Harveysmith27@gmail.com	Penn Ortho
Song	Yafeng	yafeng.song@uphs.upenn.edu	Penn Surgery
Song	Hee Kwon	hsong@uphs.upenn.edu	Penn Radiology
Soslowsky	Lou	soslowsk@upenn.edu	Penn Ortho
Sperry	Megan	sperrym@seas.upenn.edu	Penn Bioengineering
Stanley	Alexandra	astanle@mail.med.upenn.edu	Penn Ortho
Stedman	Hansell	hstedman@mail.med.upenn.edu	Penn Surgery
Steinberg	David	david.steinberg@uphs.upenn.edu	Penn Ortho
Stewart	Holly	hstew@vet.upenn.edu	Penn New Bolton Center
Szczesny	Spencer	esy@mail.med.upenn.edu	Penn Ortho
Thornton	Angelique	thorntona1@email.chop.edu	CHOP Ortho
Tichy	Elisia	etichy@mail.med.upenn.edu	Penn Ortho
Tobias	John	jtobias@upenn.edu	Penn Genetics
Tong	Wei	tongwei312@gmail.com	Penn Ortho
Towler	Oscar	otowler@mail.med.upenn.edu	Penn Ortho

Tseng	Wei-Ju	weits@mail.med.upenn.edu	Penn Ortho
Tsinman	Tonia	ttsinman@seas.upenn.edu	Penn Bioengineering
Ural	Ani	ani.ural@villanova.edu	Villanova Univ Mechanical Engineering
Usami	Yu	usamiy@email.chop.edu	CHOP Surgery
Vega	Sebastian	sebv@seas.upenn.edu	Penn Bioengineering
Volk	Susan	swvolk@vet.upenn.edu	Penn Vet Clinical Studies
Wang	Luqiang	wangluqiang1988@gmail.com	Penn Ortho
Wang	Bin	bin.wang@jefferson.edu	Thomas Jefferson Univ Medicine
Wang	Hong	whon@mail.med.upenn.edu	Penn Pathology
Wang	Haitao	whaitao@mail.med.upenn.edu	Penn Ortho
Weisshaar	Christine	weissha@seas.upenn.edu	Penn Bioengineering
Werhli	Felix	wehrli@mail.med.upenn.edu	Penn Radiology
Winkelstein	Beth	winkelst@seas.upenn.edu	Penn Bioengineering
Wong	Sarah	sarabw@mail.med.upenn.edu	Penn Neurology
Wu	Lily	wul4@email.chop.edu	CHOP Ortho
Xu	Meiqi	mqx@mail.med.upenn.edu	Penn Ortho
Yang	Hee Jin	tuf78061@temple.edu	Temple Univ Bioengineering
Yang	Li	yangli762@gmail.com	Penn Neurology
Yang	Yanmei	yanmei.yang@jefferson.edu	Thomas Jefferson Univ Medicine
Yang	Feikun	feikun@vet.upenn.edu	Penn New Bolton Center
Yousefi	Farzad	tuf16650@temple.edu	Temple Univ Bioengineering
Yu	Ming	mingyu@mail.med.upenn.edu	Penn Surgery
Yu	Wenjing	wenjingy@dental.upenn.edu	Penn Anatomy/Cell Biology
Yu	Ming	mingyu@mail.med.upenn.edu	Penn Surgery
Yuh	Da-Yo	yuhda@dental.upenn.edu	Penn Periodontology
Zemel	Babette	zemel@email.chop.edu	CHOP Pediatrics
Zhang	Rong	zhrong@upenn.edu.cn	Penn Anatomy/Cell Biology
Zhang	Sijia	sijiaz@seas.upenn.edu	Penn Bioengineering
Zhang	Qian	qian2@mail.med.upenn.edu	Penn Pathology
Zhang	Deyu	deyuz@mail.med.upenn.edu	Penn Ortho
Zhang	Yejia	yejia.zhang@uphs.upenn.edu	Penn Ortho & PM&R
Zhao	Hongbo	zhhongbo@mail.med.upenn.edu	Penn Ortho
Zolkipli Cunningham	Zarazuela	zolkipliz@email.chop.edu	CHOP Neurology

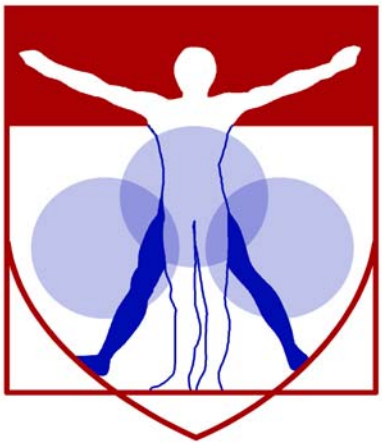

PENN

CENTER for

MUSCULOSKELETAL

DISORDERS

Speaker Abstracts

A Multiscale Computational Assessment of Bone Fracture

Ani Ural, PhD
Department of Mechanical Engineering, Villanova University

Abstract:

Osteoporotic and age-related fractures are a significant public health problem. The current standard of fracture assessment based on bone mineral density has been shown to be inadequate for fracture risk predictions. Recent studies demonstrated the importance of bone quality and hierarchical structure of bone in determining the propensity of bone to fracture and highlighted the potential to improve fracture risk assessment based on these new measures.

In this talk, components of a noninvasive patient-specific fracture risk assessment framework based on computational modeling will be presented. Specifically, the talk will focus on a new fracture mechanics-based finite element modeling approach for assessing distal forearm fracture which is one of the most frequently observed osteoporotic fractures. In addition, microscale finite element modeling of bone that elucidates the role of heterogeneity and individual microstructural components of bone in the fracture process will be presented. The results of these computational modeling efforts provide a new understanding of the fracture mechanisms at different scales and provide the foundation for a non-invasive fracture risk assessment framework.

Theresa Freeman, Ph,D
Thomas Jefferson University

Cold-Plasma a New Tool for Skeletal Tissue Engineering, Repair and Regeneration

The medical application of hot (thermal) plasma (ionized gas) has been used for decades as a surgical tool for cutting tissue (plasma knife) and to pretreat implant material like silicone and titanium before implantation for sterilization and to enhance cell attachment. More recently, the development of cold (non-thermal) plasma allows the application of plasma directly or indirectly to cells and tissues without thermal damage. This has led to the use of plasma for medical applications including: wound healing, blood coagulation, cancer and regeneration [1-5]. The basis for the multiple biological activities that are stimulated by plasma treatment are not completely understood, but the generation of reactive oxygen species (ROS) and reactive nitrogen species (RNS) by cold plasma is thought to be the primary causative agent. The cold plasma energy and species generated can be tuned for each biomedical application by changing the frequency, voltage, pulse width, electrode characteristics and/or gas mixture to create a variety of different plasma geometries with very specific characteristics. My laboratory focuses on understanding plasma and its effect on cells and tissues to promote the development of cold plasma for orthopaedic applications.

Our research using cold plasma has focused on atmospheric dielectric barrier discharge (DBD); a filamentous plasma that comes in physical contact with the cells or tissues. Our laboratory has shown that short plasma treatment (10 sec) of mesenchymal cells with microsecond pulsed DBD increases intracellular ROS and ROS-associated signaling to enhance chondrogenesis and osteogenesis [3]. We have also shown that this same treatment of murine limb autopods accelerates development, survival and growth/elongation in culture [5]. As parallels exist between autopod development and regeneration, we are currently investigating the use of cold plasma treatment to enhance regeneration on a hole punched in the mouse ear. DBD treated mouse ears had significantly higher closure rates on day 32, as compared to control ears ($n=10$, $p<0.001$). Additionally, plasma can be applied to extracellular matrix (ECM) or tissue engineering materials to alter the cell/ECM interactions. Plasma treatment of these materials can induce a wide range of cellular responses including improved cellular adhesion, proliferation and mesenchymal cell differentiation [6-8]. In our recent work we show plasma treatment of Matrigel can modulated to either enhance or inhibit bone formation in the murine model of endochondral ossification. In the future we hope to test plasma *in vivo* in a tibial bone defect model to enhance healing.

1. Wu, A.S., et al., J Surg Res, 2013. **179**(1): p. e1-e12.
2. Arjunan, K.P., et al., J R Soc Interface, 2012. **9**(66): p. 147-57.
3. Steinbeck, M.J., et al., PLoS One, 2013. **8**(12): p. e82143.
4. Chernets, N., et al., Plasma Processes and Polymers, 2015.
5. Chernets, N., et al., Tissue Engineering, 2014(ja).
6. Alves, C.M., et al., J Biomed Mater Res B Appl Biomater, 2008. **87**(1): p. 59-66.
7. Nakagawa, M., et al., J Biomed Mater Res A, 2006. **77**(1): p. 112-8.
8. Reyes, C.D., et al., Biomaterials, 2007. **28**(21): p. 3228-35.

Obese bones and the response to energy restriction.

Sue Shapses, PhD
Professor, Department of Nutritional Sciences
Acting Chair, Department of Exercise Science and Sport Studies

Lean individuals have low bone mineral density (BMD) and are at greatest risk of fracture. Obesity is associated with higher BMD, yet bone quality is compromised. Bone quality and biomechanical properties are altered due to diet induced obesity in growing mice. This may be due to both direct and indirect effects of obesity. An increased sedentary behavior, compromised nutrient intake, secondary hyperparathyroidism, and low serum 25-hydroxyvitamin D are a few factors that may be contributing to altered cortical bone properties in the obese. Moreover, studies indicate that fractures occur at non-traditional sites in the obese (upper and lower limbs).

Weight loss intervention is an important means to reduce co-morbidities in the obese, yet it can lead to bone loss and increased fracture risk, especially at central anatomical sites. Indeed, weight-loss induced reduction in bone mass is more than double what is expected for weight-stable postmenopausal women over one year, and BMD loss continues at a faster rate after weight loss ends, even with weight regain. Our controlled intervention trials (OWLE: AG12161) show a 1-2% loss of BMD at the hip and lumbar spine with about 10% weight reduction in older, but not younger women. However, the response to this same level of moderate weight loss is attenuated or null in older men. A few mechanisms appear to be regulating the rise in bone turnover during energy restriction such as reduced Ca absorption and lower serum estradiol. Overall, there will be a discussion of bone properties in the obese and factors regulating bone and fracture risk due to dietary energy restriction.

Mesenchymal stem cell-based regeneration and immune therapies

Songtao Shi, DDS, Ph.D.
University of Penn School of Dental Medicine

Mesenchymal stem cells (MSCs) are a population of hierarchical postnatal stem cells with the potential to multiple differentiations and thus serve as a promising cell source for regenerative medicine in terms of forming mineralized tissues to replace damaged and diseased tissues. MSCs have been successfully used for mineralized and soft tissue regeneration in animal models and clinics. Also, MSCs display profound immunomodulatory properties by inhibiting proliferation and function of several major immune cells, such as dendritic cells, T and B lymphocytes, and natural killer (NK) cells. In fact, MSC-based therapy has been successfully applied in various human diseases, including graft versus host disease (GvHD), systemic lupus erythematosus (SLE), rheumatoid arthritis, autoimmune encephalomyelitis, inflammatory bowel disease, and multiple sclerosis. We found that MSC transplantation (MSCT) induced transient T-cell apoptosis *via* the Fas ligand (FasL)-dependent Fas pathway and could ameliorate disease phenotypes in fibrillin-1 mutated systemic sclerosis (SS) and dextran sulfate sodium-induced experimental colitis. Mechanistic analysis revealed that Fas-regulated monocyte chemotactic protein 1 (MCP-1) secretion by MSCs recruited T-cells for FasL-mediated apoptosis. The apoptotic T-cells subsequently triggered macrophages to produce high levels of TGF□□which in turn led to the upregulation of Tregs and, ultimately, to immune tolerance. Additionally, MSCT is able to release exosomes to rescue recipient MSCs via miRNA transfer and cellular component reuse. These data therefore demonstrate previously unrecognized mechanisms underlying MSC-based immunotherapy involving coupling *via* Fas/FasL to induce T-cell apoptosis and epigenetic regulation.

A novel non-invasive model of temporomandibular joint pain in the tat with tunable outcomes of acute and chronic pain.

Eric J. Granquist, DMD, MD
Director, Center for Temporomandibular Joint Disease

TMJ pain presents many clinical challenges due to inability to predict which cases will resolve and which will become chronic. Existing animal models use invasive approaches to induce pathology and/or pain but do not replicate all disease states. This study aimed to develop a non-invasive rat model that induces either resolving or sustained TMJ pain. Separate groups of female Holtzman rats underwent repeated mouth opening for 1 hour daily for 7 days using a load of 2N (n=4), 3.5N (n=4), or no opening (sham; n=2). Orofacial sensitivity was assessed daily during and after the loading phase in the TMJ region using von Frey filaments to measure the threshold for eliciting a response. The mechanical threshold decreased from baseline immediately from 37.5±3.9g to 6.6±1.4g for 3.5N and 9.1±3.4g for 2N; both were significantly lower ($p<0.0001$) than sham responses during the period of loading. Thresholds in the 2N group returned to sham and baseline levels by day 13. However, TMJ sensitivity was sustained ($p<0.0001$) in the 3.5N loading group for at least another 14 days. Additional studies are needed to define when sensitivity resolves. However, this work provides a useful platform for understanding those mechanisms which may be contributing to pain maintenance as well as identify imaging biomarkers for clinical translation.

DEL-1 restrains osteoclastogenesis and inhibits inflammatory bone loss in nonhuman primates.

George Hajishengallis, DDS, PhD
Penn Dental Medicine, Department of Microbiology

We have previously shown that an endothelial cell-secreted protein designated DEL-1 regulates LFA-1-integrin–dependent leukocyte recruitment and inflammation in various tissues. We have now identified a novel regulatory mechanism of DEL-1 in osteoclast biology. Specifically, we showed that DEL-1 is expressed by human and mouse osteoclasts and regulates their differentiation and resorptive function. Mechanistically, DEL-1 inhibits the expression of NFATc1, a master regulator of osteoclastogenesis, in a Mac-1-integrin–dependent manner. In vivo mechanistic analysis has dissociated the anti-inflammatory from the anti-bone resorptive action of DEL-1 and identified structural components thereof mediating these distinct functions. Importantly, locally administered human DEL-1 blocks inflammatory periodontal bone loss in nonhuman primates—a relevant model of human periodontitis. The ability of DEL-1 to regulate both upstream (inflammatory cell recruitment) and downstream (osteoclastogenesis) events that lead to inflammatory bone loss paves the way to a new class of endogenous therapeutics for treating periodontitis and perhaps other bone loss disorders, such as rheumatoid arthritis and osteoporosis.

Marker gene expression at the single cell level does not correlate with functional chondrogenic potential.

Arjun Raj, Ph.D.
Assistant Professor of Bioengineering

Mesenchymal stem cell (MSC) populations display substantial cell-to-cell heterogeneity that complicates their use in regenerative applications. However, most conventional assays measure MSC properties in bulk and as a consequence mask this cell-to-cell variation. Here, we used single molecule RNA FISH to query the mRNA expression levels of conventional differentiation markers at the single cell level, and found that both primary chondrocytes and chondrogenically-induced MSCs demonstrated substantial mRNA expression heterogeneity. Even small MSC colonies and sister cell pairs showed high cell-to-cell variation in transcript abundance, suggesting that marker mRNA expression was not heritable through cell division. Moreover, this variation in marker transcript levels only weakly associated with cartilage-like matrix production at the single cell level. Together, these quantitative analyses suggest that efforts to sort chondrogenically "superior" MSC subpopulations based on these markers would only marginally enrich the progenitor population. Our results suggest that, although canonical markers have very clear functional roles in differentiation and matrix formation, their instantaneous mRNA abundance is only tenuously linked to the chondrogenic phenotype and matrix elaboration at the single cell level.

Mechanisms of Bone Disease in Mucopolysaccharidosis VII

Lachlan Smith, PhD
Research Assistant Professor of Neurosurgery

The mucopolysaccharidoses (MPS) are a family of lysosomal storage disorders characterized by deficiencies in enzymes that degrade glycosaminoglycans (GAGs). These GAGs accumulate in cells and tissues resulting in progressive, multi-organ disease manifestations. While the clinical phenotype varies between subtypes, skeletal disease is prevalent and unresponsive to current treatment modalities. The molecular mechanisms linking GAG accumulation, cellular dysfunction and skeletal disease in MPS are poorly understood, impeding development of improved therapeutic strategies. MPS VII is caused by deficient activity of the enzyme beta-glucuronidase leading to accumulation of chondroitin, heparan and dermatan sulfate GAGs. MPS VII patients exhibit progressive kyphoscoliotic deformity and spinal cord compression resulting in increased mortality and reduced quality of life. Our laboratory uses naturally-occurring canine models of MPS VII that closely mimic the progression of skeletal disease that occurs in human patients. In previous work we demonstrated that MPS VII dogs have large, cartilaginous lesions in the vertebral bodies that compromise the mechanics of the intervertebral joint. These lesions, also present in human MPS VII, other MPS subtypes and in long bones, are caused by failed conversion of cartilage to bone during postnatal growth. The overall objective of this work was to establish the molecular mechanisms of failed bone formation in MPS VII. Our overall hypothesis was that progressive, abnormal accumulation of GAGs in MPS VII epiphyseal cartilage disrupts the distribution and activity of secreted signaling molecules, preventing chondrocyte differentiation and subsequent bone formation at the appropriate developmental stage.

Using longitudinal x-rays, microCT and mRNA analyses, we identified the critical developmental window (between 9 and 14 days-of-age) when secondary ossification commences in normal dogs but in MPS VII dogs does not. We established that MPS VII dogs exhibit abnormally high intra and extracellular GAG accumulation as early as 9 days-of-age. By measuring expression of chondrocyte differentiation markers across this developmental window, we discovered that failed bone formation could be traced to the impaired ability of epiphyseal chondrocytes to transition from proliferation to hypertrophy. We then used whole transcriptome sequencing (RNA-Seq) to investigate the molecular mechanisms contributing to impaired chondrocyte differentiation, with Wnt/β-catenin signaling found to be the top dysregulated bone formation pathway. Wnt molecules are critical regulators of both the timing and rate of chondrocyte hypertrophic differentiation, and secreted Wnts are highly dependent on GAGs for proper distribution and activity. Finally, using cartilage explants cultures, we showed that MPS VII chondrocytes exhibit impaired responses to exogenous Wnt treatment, further implicating this pathway in the disease pathogenesis. The long-term goal of this work is to identify improved strategies for treating skeletal disease in patients with MPS and other musculoskeletal diseases involving abnormal GAG metabolism.

Lessons from Muscle Injury and Muscular Dystrophy about the Evolution of Animal Locomotion

Hansell Stedman, MD
Associate Professor of Surgery

Deletional frameshift or loss of coding exons in DMD complicates therapy with recombinant dystrophin, as "non-self" peptide epitopes put patients at risk for chronic immune recognition. The paralogous protein utrophin may confer central immunological tolerance to its peptide sequence through early developmental expression in the thymus, but utrophin is expressed in dystrophic muscle at levels insufficient to protect the sarcolemma during forceful deformation. To maximize the therapeutic index of recombinant utrophin vectors we have used a comparative phylogenomic approach to map the evolution of ancestral domains of dystrophin and utrophin relative to inferred increases in myosin-powered contractility. This analysis provides evidence that the spectrin-like repeats of the rod underwent massive tandem replication before the entire domain was co-opted for its role in a dystrophin ortholog. Both expansion and co-option predated the emergence of sarcomeres, suggesting that length may be physiologically less important than strength in dystrophin and utrophin. In blinded studies of systemic AAV9 administration to neonatal mdx mice, we find that a best-in-class 3.5 kb synthetic utrophin transgene (μU) *completely* prevents histological signs of myonecrosis throughout growth to skeletal maturity. AAV9μU completely prevented centronucleation and saturated global recovery of the sarcoglycan complex, despite a post-administration tenfold increase in striated muscle mass. In dystrophic puppies, intravenous injection of a 30-fold lower relative dose of AAV9μU fully restored sarcoglycan levels and normalized the myofiber size-distribution following a threefold increase in muscle mass. Interferon-gamma ELISpot assays using utrophin-derived peptides revealed no reactivity in injected dogs, consistent with central immunological tolerance. These findings suggest a rationale for neonatal gene therapy using utrophin as an internally deleted “self” protein in DMD to minimize the risk of chronic immunotoxicity. We outline a rigorous translational approach using escalating vector doses in GSHPMD dogs harboring a newly defined 5 megabase deletion encompassing the dystrophin ORF.

Abstract: A majority of the sporadic mutations causing Duchenne muscular dystrophy (DMD) result in a deletional frameshift and absence of the giant cytoskeletal protein dystrophin. To optimize the function of a non-immunogenic substitute for dystrophin small enough for systemic delivery, we used a phylogenomic approach to reconstruct the evolutionary history of dystrophin's orthologs and closest paralog, utrophin. Body-wide transduction of striated muscle with an AAV9 vector encoding a reverse-engineered micro(μ)Utrophin for a first time conferred histologically complete protection against myonecrosis in dystrophin-deficient striated muscles of mdx mice. In dystrophic dogs, AAV9μUtrophin restored normal sarcoglycan levels without provoking a detectable immune response to transgene product. The exceptional functionality and immunological stealth of the optimized AAV9μUtrophin offers the unique combination of efficacy and safety needed for clinical translation.

Treatment of musculoskeletal diseases with a little help from your own stem cells

Nancy E. Lane, M.D.
Director, Center for Musculoskeletal Health

ABSTRACT

One of the many challenges of regenerative medicine for musculoskeletal diseases has been to direct mesenchymal stem cells (MSCs) to the bone surface. We developed a hybrid compound, LLP2A-Ale that can direct the endogenous MSCs to the bone surface. Our proof of concept experiments have determined that both endogenous and exogenous MSCs can be directed to the remodeling bone surface with LLP2A- Ale. This presentation will review studies that demonstrate the efficacy of endogenous MSCs for the treatment of a number of bone related Diseases including osteoporosis, osteonecrosis, fracture and inflammatory arthritis.

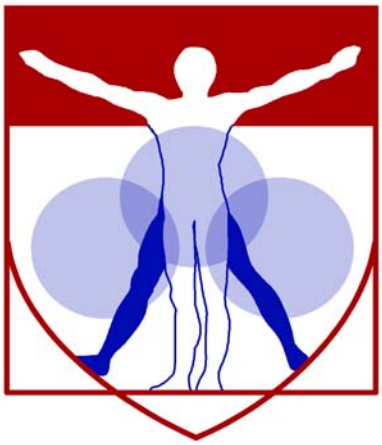

PENN

CENTER for
MUSCULOSKELETAL
DISORDERS

Abstracts

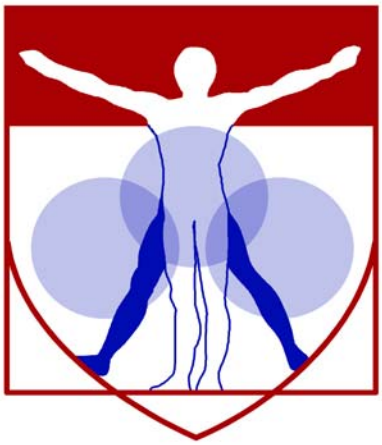

PENN

CENTER for

MUSCULOSKELETAL

DISORDERS

Biomechanics Abstracts

Insight into Meniscus Tie Fiber Function: Disorganized Layers within an Aligned Fibrous Network Preserve Bulk Mechanics and Promote Strain Reconstitution in the Context of a Radial Tear

Sonia Bansal[1], Feini Qu[1,2], Alexander L. Neuwirth[1,2], Niobra M. Keah[1,2], Spencer E. Szczesny[1,2], Robert L. Mauck[1,2], Miltiadis H. Zgonis[1,2]
[1]McKay Orthopaedic Research Laboratory, University of Pennsylvania, Philadelphia, PA
[2]Translational Musculoskeletal Research Center, Philadelphia VA Medical Center, Philadelphia, PA

Disclosures: S. Bansal (N), F. Qu (N), A.L. Neuwirth (N), N.M. Keah (N), S.E. Szczesny (N), R.L. Mauck (N), M.H. Zgonis (N)

INTRODUCTION: Meniscal tears are among the most common orthopedic injuries in the U.S. [1]. Radial tears, which interject perpendicularly and sever the circumferential fibers that make up the bulk of the meniscus, are thought to compromise the mechanical function of the meniscus. As such, these injuries are usually treated by partial meniscectomy (i.e., excision of the damaged region), with the assumption that severed fibers play no mechanical role. While this is the common dogma, a recent study by Bedi suggests that radial tears do not increase contact stresses in the knee until they reach ~90% of meniscus width [2]. To resolve this apparent contradiction, we reconsidered the role of radial elements ('tie fibers') in the meniscus. These fibers (and sheets), which originate at the lateral margin of the meniscus and interdigitate amongst the circumferential fibers, are thought to bind circumferential fibers together [3]. To test the role of these radial elements in an otherwise aligned network, we utilized electrospinning to generate a meniscus analog. Both aligned and disorganized networks can be produced by changing the speed of the nanofiber collecting surface [4]. Here, we used this approach to create scaffolds that were primarily aligned, but contained a subset of disorganized fibers to create 'tie-fiber-like' elements. Through testing of intact scaffolds and those into which a 'radial' defect was introduced, we demonstrate that radial elements play a critical role in preserving mechanical properties when aligned fibers are severed.

METHODS: Nanofibrous poly(ε-caprolactone) (PCL) scaffolds were electrospun as previously described [5]. To create aligned (AL) scaffolds, a mandrel rotating at 10 m/s served as the grounded collector, with fibers aligned in the direction of rotation. To form non-aligned (NA) scaffolds, the mandrel was slowed to ~3 m/s. To replicate radial tie elements, AL scaffolds were produced to include discrete NA layers by alternating the speed of the mandrel for set periods of time during collection. A 'Layered' scaffold included 3 total layers of AL, NA, and AL fibers, with each layer spun for 2 hours. The 'Distributed' scaffold had a similar ratio of AL to NA content, but the NA content was distributed more uniformly across the thickness **(Fig. 1A)**. Namely, the scaffold was fabricated by alternating 60 min fast (AL) and 40 min slow (NA) cycles, resulting in 7 interconnected layers (Figure 1). After fabrication, scaffolds were cut to 30 mm length (in the AL direction) x 5.5 mm width. Two conditions were tested: intact or defect (which contained a radial cut spanning 50% of the width at 50% of the length) (**Fig. 2A**). Cross sectional area was measured with a laser-based device [5] prior to speckle coating. Samples were evaluated in tension in a ramp to failure test (0.5% strain/s), during which they were imaged for strain tracking using the Vic2D image correlation software. Stress vs. strain data were curve-fit using a custom bilinear fitting program in MATLAB to define the 'toe' and 'linear' modulus, as well as the transition strain between the two [6]. Data (n=8/group) was analyzed using one and two-way ANOVA ($p \leq 0.05$), with Tukey's post hoc where applicable, and presented as mean ± SEM.

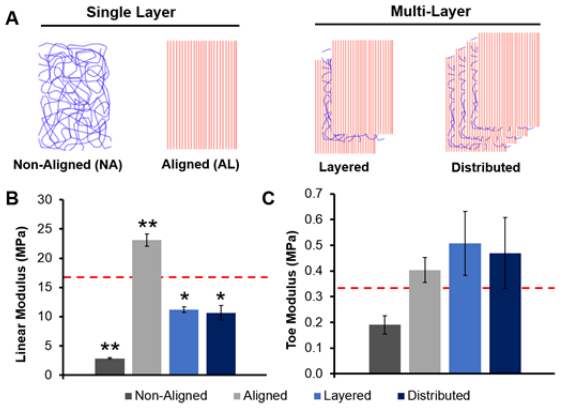

Fig. 1. Radial tie elements influence mechanical properties of aligned scaffolds. (A) Schematic of scaffold groups. (B) Linear and (C) toe modulus of intact scaffolds. Red line indicates prediction from weighted mixture. *=$p \leq 0.05$ vs NA and AL. **= $p \leq 0.05$ vs. all other groups.

RESULTS: The toe and linear modulus of AL scaffolds was ~2 and ~8X higher (0.4 and 23.1 MPa, respectively) than that of NA scaffolds (0.2 and 2.9 MPa, respectively). Interestingly, both the layered and distributed scaffolds, comprised of 2/3 AL and 1/3 NA regions, had a linear modulus that was less than expected based on their component fraction properties (~16.4 MPa in a simple weighted mixture model). Instead, the linear modulus was 11.2 MPa and 10.7 MPa, respectively (**Fig. 1B**). Conversely, the toe modulus of layered and distributed scaffolds was higher than the expected weighted average of the NA and AL scaffolds (**Fig. 1C**), indicating layer interaction. Finally, when comparing the linear modulus of intact versus defect scaffolds, there was a significant difference in the percent change in aligned scaffolds compared to all other groups. That is, AL scaffolds lost ~50% of their effective modulus, as would be expected, while all other groups lost only ~20-25% (**Fig. 2B**), again suggesting contributions from severed fibers to overall scaffold mechanics. This is supported by preliminary data showing more rapid strain reconstitution near a defect in layered scaffolds compared to AL scaffolds (**Fig. 3**).

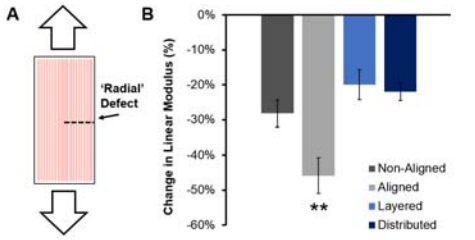

Fig. 2. Radial tie elements contribute to load transfer after introduction of a 'radial' defect. (A) Schematic of tensile evaluation of defect scaffold. (B) % Change in linear modulus after introduction of a defect. **=$p \leq 0.05$ vs. all other groups.

DISCUSSION: This study developed a biomaterial analog of the meniscus radial tie fiber, namely a disorganized fibrous layer interspersed in an otherwise aligned fiber array. The linear and toe moduli of these layered and distributed scaffolds did not match expectations based on simple weighted averaging. This implies that interruption of the fibrous architecture leads to some sacrifice of tensile efficiency in the higher strain domain, but a better than expected response in the low strain regime. When a 50% radial cut was introduced, only aligned scaffolds showed the expected 50% decrease in apparent modulus, whereas the NA, layered, and distributed scaffolds all showed a less marked loss in properties. This suggests that layered and distributed scaffolds, by virtue of the NA inclusions, provide some degree of strain sharing between aligned layers, potentially engaging those aligned fibers that reside in the defect region. This is consistent with our previous studies of the tensile response of non-orthogonally aligned nanofibrous layers [7,8] and with a recently reported shear lag mechanisms in native tendon [6]. Collectively, these data imply that radial tie elements in native meniscus may be essential for enabling efficient load transfer in the context of tears that interrupt the circumferential fibrous architecture.

SIGNIFICANCE: The results of this study indicate that radial tie fibers in the native meniscus may play a heretofore unappreciated role in allowing for load transfer around tears that interrupt the continuity of circumferential fibers. This may explain recent experimental observations and ultimately alter clinical practice with respect to partial meniscectomy, as well as direct tissue engineering strategies aimed at producing functional replacements.

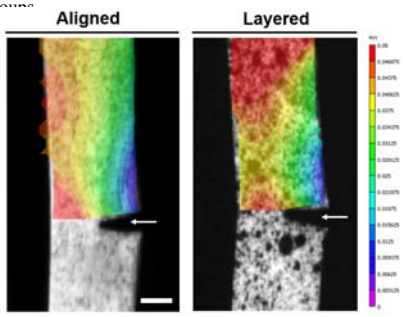

Fig. 3. Local strain tracking of an Aligned and Layered scaffold with defect (arrow) at 5% global strain. Color bar from 0% (purple) to 5% strain (red). Scale = 2 mm.

References: [1] Moran+, Sports Med Arthrosc 2015. [2] Bedi+, J Bone Joint Burg Am 2010. [3] Skaggs+, J Orthop Res 1997. [4] Li+, J Biomech 2007. [5] Baker+, Biomaterials 2007. [6] Szczesny+, Acta Biomater 2014. [7] Nerurkar+, Nat Mater 2009. [8] Fisher+, Acta Biomater 2014.

Acknowledgments: This work was supported by an OREF New Investigator Grant, the NIH, and the Department of Veterans Affairs.

Exploring Differences in the Tensile Mechanical Properties of the Pregnant and Non-pregnant Mouse Cervix

Carrie E. Barnum, Jennifer L. Fey, Brianne K. Connizzo, Snehal S. Shetye, Michal A. Elovitz, and Louis J. Soslowsky

Introduction: The cervix is a unique organ able to dramatically change its shape and function from serving as a barrier to protect the growing fetus to completely dilating and allowing delivery of a term infant. There is an emerging concept that the cervix may change or 'remodel' early in many cases of preterm birth (PTB). While the cervix must have certain biomechanical properties to allow this diverse function, little is known regarding the tensile mechanical properties of the cervix throughout pregnancy. These studies sought to assess the biomechanical properties of the cervix through pregnancy.

Methods: Non-pregnant (NP) and pregnant CD-1 mice at embryonic day 10, 12, 14, 16 and 18 (n=6-21) were sacrificed and frozen. The cervix was harvested and cut along its length to expose the lumen surface and lay the tissue flat. The ends were affixed between two pieces of sandpaper for gripping and a custom laser device was used to measure cross sectional area. Tensile properties were measured after subjecting samples to a protocol consisting of a single ramp to failure at 1mm/minute. Statistical comparisons used one-way AVOVAs with post-hoc Bonferroni tests (significance at $p<0.05$).

Results: Cross-sectional area was significantly reduced in E10 pregnant cervices but gradually returned to NP levels by E14. Maximum load was not different between groups, but stiffness was decreased in pregnant samples. Maximum stress and modulus were also significantly decreased in pregnant samples after E14 compared to NP.

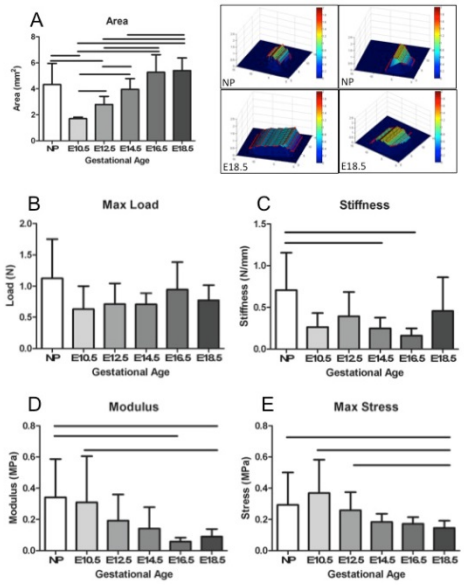

Conclusions: Overall, compared to NP the tensile biomechanical properties of the cervix decrease during pregnancy. These differences in mechanical properties suggest that during gestation, the cervix becomes less stiff and more deformable to allow for delivery. This work lays a foundation for investigating cervical biomechanics and the role of the cervix in PTB. (MOD Prematurity Research Center at PENN)

N-Cadherin presentation alters Rac1 signaling to modulate mesenchymal progenitor cell mechanosensing of soft tissue microenvironments

Brian D. Cosgrove[1], Keeley L. Mui, Ph.D. [1], Tristan P. Driscoll, Ph.D.[1], Richard K. Assoian, Ph.D.[1], Jason A. Burdick, Ph.D.[1], Robert L. Mauck, Ph.D.[1]
[1]University of Pennsylvania, Philadelphia, PA

Progenitor cell behavior is regulated by cues from the microenvironment, including extracellular matrix (ECM) composition and stiffness, as well as cell-cell interactions mediated through cadherins. Here, we develop an engineered hyaluronic acid (HA) hydrogel system that permits independent control of N-Cadherin (HAVDI) and fibronectin (RGD) adhesive domain co-presentation while also allowing for tuning of matrix stiffness through UV polymerization time. Using this system, we elucidated a new mechanism through which mesenchymal stem cells may tune their interpretation of the mechanical microenvironment. Our findings show that on gels of intermediate stiffness, NCad presentation (in the context of constant RGD presentation) decreases the contractile state and YAP/TAZ nuclear localization of mesenchymal progenitors in a Rac1-dependent fashion, resulting in altered interpretations of ECM stiffness. Within this physiologic context, cell-cell signaling mechanically confounds how stem cells are able to probe the underlying matrix, causing them to perceive the microenvironment as being much softer than it actually is, resulting in stem cell behaviors that would normally not occur in that specific mechanical niche. This ECM stiffness “shielding” through N-Cadherin is likely to be an important component of the development of mesenchymal tissues and relevant in pathologies that disrupt the balance of cell-ECM and cell-cell signaling, such as wound healing. Additionally, this new insight into N-Cadherin regulation of cellular mechanobiology may be harnessed towards novel biomaterial design to direct mesenchymal stem cell behavior and tune the cellular response to substrate stiffness cues in regenerative medicine approaches.

Nanomechanical Heterogeneity in Murine Temporomandibular Joint Cartilaginous Tissues

Basak Doyran[1], Prashant Chandrasekaran[1], Qing Li[1], Eiki Koyama[2], Hyun-Duck Nah[2], X. Lucas Lu[3], Lin Han[1]

[1]Drexel University, Philadelphia, PA, USA
[2]The Children's Hospital of Philadelphia, Philadelphia, PA, USA
[3]University of Delaware, Newark, DE, USA

Abstract:

Despite the wide use of murine models in the development and pathology of temporomandibular joint (TMJ), there is little understanding of the mechanical properties of murine TMJ cartilaginous tissues, e.g., the condyle and disc. Knowledge of the local mechanical properties of these tissues will significantly benefit TMJ arthritis research by providing a mechanics-based functional benchmark for various disease models and tissue engineering protocols. In this study, we measured the murine TMJ nanomechanical properties of both the condyle and disc tissues in 12-week old male C57BL/6J mouse ($n \geq 4$) via AFM-based nanoindentation. Nanoindentation was performed on the superficial zone of condyle cartilage, both the tubercle and condyle sides of disc using a colloidal spherical tip (R ~ 5 μm, k ~ 7.4 N/m) at 10 μm/s (> 8 each sample). Indentation modulus E_{ind} was calculated on the loading curves via the Hertz model. We found the E_{ind} in the range of 0.35 ± 0.08 MPa for condyle, 0.21 ± 0.08 MPa for disc (tubercle side) and 0.06 ± 0.01 MPa for disc (condyle side) (mean ± SEM). The significant differences in E_{ind} between these tissues (Mann-Whitney test, $p < 0.05$) are associated with their different biomechanical function in TMJ and different extracellular matrix composition/structure. For the tubercle side of the disc, we also found salient non-Hertzian deformation behaviors, in contrast to the other two tissue regions. This non-Hertzian behavior is likely due to the high concentration of transversely aligned collagen I fibrils on the surface of disc tubercle side that is substantially different from other tissues. In addition, for the disc condyle side, we detected a significant increase in E_{ind} from the central to the lateral peripheral region. This observation again highlighted the presence of heterogeneity in the mechanical behaviors of TMJ tissues. Our ongoing studies are using histology, immunohistochemistry and electron microscopy to further characterize the composition and nanostructure of these tissues. This knowledge will enable us to construct fibril-reinforced finite element models to elucidate the structure-property relationships of these tissues. To our knowledge, this is the first study that investigates the heterogeneous mechanics of murine TMJ cartilaginous tissues. We will be able to use this knowledge to study the onset and progression of TMJ arthritis in various transgenic murine models.

Aggressive Rehabilitation with Nonsurgical Treatment Demonstrates Improved Fatigue Mechanics and Functional Outcomes Following Achilles Tendon Rupture in an Animal Model

Benjamin R. Freedman, Tyler M. Morris, Courtney A. Nuss, Corinne N. Riggin, Nabeel S. Salka, Joshua A. Gordon, Aricia Shen, Daniel C. Farber, Louis J. Soslowsky

McKay Orthopaedic Laboratory, University of Pennsylvania, Philadelphia, PA

Disclosures: Benjamin R. Freedman (N), Tyler M. Morris (N), Courtney N. Nuss (N), Corinne N. Riggin (N), Nabeel S. Salka (N), Joshua A. Gordon (N), Aricia Shen (N), Daniel C. Farber (N), Louis J. Soslowsky (Funding from Orthofix and DJO)

INTRODUCTION: Achilles tendon ruptures are devastating injuries that affect 8.3 in 100,000 people yearly [1]. Despite the higher risk for complications and increased costs, operative treatment has historically been believed to provide superior outcomes compared to non-operative treatment in terms of function and re-rupture rates [2]. However, recent studies have suggested that surgical treatment for Achilles ruptures is not necessarily superior [3, 4]. To elucidate the basic mechanical and structural mechanisms governing these clinical outcomes, it is necessary to evaluate the role of various surgical and rehabilitation strategies on tendon quality and function in a controlled model system. Therefore, the objective of this study was to investigate the effects of surgical repair and limb immobilization on Achilles healing and ankle joint function following complete tendon transection in a rat model. We hypothesized that surgical treatment and aggressive rehabilitation would result in superior Achilles tendon mechanical, structural, and functional properties following injury.

METHODS: Study Design: Sprague Dawley rats (n=108) received 2 weeks of treadmill exercise training (up to 60 minutes at 10m/min) [5] (IACUC approved) prior to surgical removal of the right central plantaris longus tendon and blunt mid-substance transection of the right Achilles tendon. Animals were then randomized into repaired (R) (Modified Kessler approach) (n=54) or non-repaired (NR) (n=54) groups, and all hind limbs were immobilized in plantar flexion. These groups were further divided into aggressive (Agg), moderate (Mod), or conservative (Con) rehabilitation (**Fig.1**). Functional evaluation (n=18/group) of passive ankle joint range of motion (ROM) and stiffness was completed using a custom torque cell and accelerometer-based device on anesthetized animals [5]. All assays were performed after 6 weeks of healing. *Ex vivo* Assays: After sacrifice, the Achilles tendon-foot complex was carefully removed *en bloc*, fine dissected, measured for cross sectional area, and secured in fixtures. Tendons were then loaded at 1N in a PBS bath while a series of sagittal B-mode high frequency ultrasound images (HFUS) were acquired using a 40MHz scanner (Vevo 2100, MS550D; VisualSonics) (n=10-11/group) [6]. Tendons were then mechanically tested and imaged (n=10-11/group) with a protocol consisting of stress relaxation (6% strain), a low-load dynamic frequency sweep (0.1 to 10 Hz), and fatigue testing (~10-75% of ultimate failure load) at 2Hz using a sinusoidal waveform until failure (Instron Electropuls 3000). Analysis: Functional ankle joint properties (i.e., ankle ROM and stiffness) for both dorsiflexion and plantar flexion were evaluated. Achilles tendon percent relaxation, dynamic modulus, tanδ, toe and linear modulus, hysteresis, cycles to failure, and laxity were computed from mechanical and optical testing data. Echogenicity and collagen fiber alignment were evaluated from the HFUS images for the injury region [6]. Two-way ANOVAs with post hoc Fisher's tests were used to evaluate the effects of surgical treatment and rehabilitation on mechanical, functional, and structural properties.

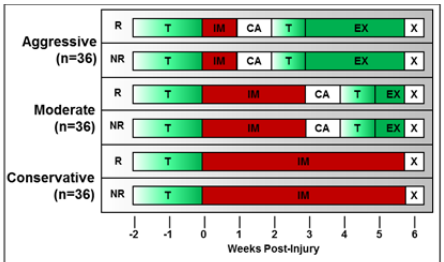

Fig. 1. Study Design. Animals were trained for two weeks prior to injury. Following injury, animals were divided into aggressive, moderate, and conservative rehabilitation groups. Definitions: CA- cage activity; T- treadmill training; IM-immobilization; EX- exercise; R- repaired; NR-non-repaired; X-sacrifice.

RESULTS: After 6 weeks of healing, the plantar- (data not shown) and dorsi-flexion ROM was superior in aggressively rehabilitated animals, closer to pre-injury values **(Fig.2)**. Aggressively rehabilitated animals had dorsiflexion toe stiffness values closer to pre-injury values compared to the moderate rehabilitation group. No changes in plantarflexion toe or linear stiffness, or dorsiflexion linear stiffness were observed. Tendon cross sectional area was higher in repaired tendons, and this effect was exacerbated in animals with aggressive rehabilitation. Mechanical property evaluation revealed an increase in the toe modulus in non-repaired aggressively rehabilitated tendons, but no changes in the percent relaxation or dynamic properties. Marked differences in quasi-static linear modulus and fatigue properties were observed (**Fig.3**) ($p<0.05$). Specifically, non-repaired tendons with aggressive and moderate rehabilitation had an increased linear modulus and number of cycles to failure (**Fig.3**) ($p<0.05$). Additionally, the number of cycles to failure was greatest in the aggressively rehabilitated group. Non-repaired tendons experienced more laxity through 5% fatigue life compared to repaired tendons in aggressive and moderate rehabilitation, and transitioned to the secondary phase of fatigue life earlier ($p<0.05$) (data not shown). Ultrasound evaluation revealed an effect of rehabilitation, but not surgical treatment type, on increased matrix echogenicity, a surrogate measure of fiber density, and alignment ($p<0.05$) (data not shown).

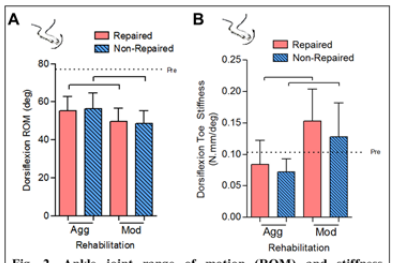

Fig. 2. Ankle joint range of motion (ROM) and stiffness functional outcomes. Rehabilitation was a significant factor ($p<0.05$) on dorsiflexion ROM (A) and toe-stiffness (B) after 6-weeks of healing. Data shown as mean ± standard deviation. Lines indicate significant differences ($p<0.05$). Pre- presurgery values.

DISCUSSION: Achilles tendon healing following a variety of common clinical treatment methods was evaluated after 6 weeks of healing in a rat model. We discovered a mechanism whereby non-repaired tendon fatigue properties had marked improvements in the number of cycles to failure. This work suggests the functional and mechanical benefits of aggressive rehabilitation on Achilles tendon healing following a variety of treatment paradigms [7]. Ultrasound evaluation showed promise to detect changes in healing capacity between groups with different rehabilitation strategies. Although the conservative rehabilitated tendons had higher echogenicity and alignment compared to other groups, they also had lower cross sectional area, which likely limited the capacity of the more aligned tendon to withstand fatigue loading. Future work will relate organizational measures from HFUS to tendon fatigue mechanical properties. Additional ongoing studies will evaluate the long-term effects of these treatment and rehabilitation paradigms.

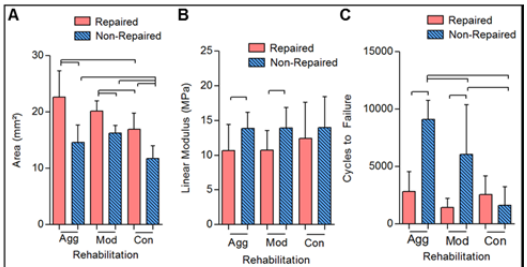

Fig. 3. Mechanical testing results. Surgery was a significant factor in tendon cross sectional area (A), linear modulus (B), and cycles to failure (C) ($p<0.05$). Rehabilitation was a significant factor in tendon cross sectional area and cycles to failure (A,C) ($p<0.05$). Data shown as mean ± standard deviation. Lines indicate significant differences ($p<0.05$).

SIGNIFICANCE: This study demonstrates that aggressive rehabilitation with nonsurgical management leads to improved tendon fatigue mechanics and ankle function after 6 weeks of healing in this rat Achilles tendon injury model. Ultrasound evaluation showed promise to detect changes in healing capacity between groups.

ACKNOWLEDGEMENTS: We acknowledge financial support from NIH/NIAMS R01AR064216, NIH/NIAMS P30AR050950, and the NSF GRFP. We thank Adam Pardes, Jennica Tucker, Bob Zanes, James Cirone, and Joanna Fried for assistance.

REFERENCES: [1] Suchak AA et al., 2005. *FAI*, 26(11) 932-6. [2] Freedman BR et al., 2014. *MLTJ*, 4(2) 245-255. [3] AAOS Guidelines for Achilles Tendon Repair, 2009. [4] Soroceanu et al., 2012. *JBJS* 94(23):2136-43. [5] Peltz CD et al., 2010. *JOR* 28(7): 841-5. [6] Riggin CN et al., 2014. *JBiomech Eng*, 136(2):21-29. [7] Olsson N, et al., 2013. *AJSM*, 41(12):2867-76.

Automated Finite Element Modeling for Preoperative Planning of Fracture Fixation Surgery

Hwabok Wee, J. Spence Reid, Vernon M. Chinchilli, Gregory S. Lewis (glewis1@hmc.psu.edu)
Pennsylvania State University College of Medicine, Hershey, PA, USA

Disclosures: J. Spence Reid (Smith & Nephew; Depuy-Synthes; Zimmer), Gregory S. Lewis (Depuy-Synthes)

Introduction: Internal fixation of fractures using plates and screws is a common orthopaedic procedure [1]. Fracture fixation involves many choices made by the surgeon including type, material, sizes, and geometric configuration of implants. Biomechanical goals of surgery include providing adequate stability to promote healing, while preventing implant mechanical failure. The relationships between the fracture fixation construct and resulting patient-specific 3D biomechanics are complex. The objective of this study was to, for the first time, apply simulation-based design approaches from engineering to orthopaedics, and fit surrogate mathematical models of locked fracture fixation biomechanics based on hundreds of finite element analysis (FEA) simulations. These quadratic polynomial regression equations are useful for clinical insight, quantitative predictions, and fracture fixation optimization. We hypothesized that the working length of the fracture fixation construct would be strongly predictive of fracture gap strains and implant maximum stresses.

Methods: Plated fixation of transverse diaphyseal midshaft fractures were modeled by FEA. A total of 774 unique fracture fixation scenarios were modeled. Long bone was modeled with a hollow cylinder for cortical bone (30 mm outer diameter and 4.3 mm cortical thickness). Simple transverse fracture were modeled with five gap widths (d_{gap}= 0.2-3 cm). Five lengths of plate (4.5 mm Narrow Locking Compression Plate, Depuy Synthes, L_{plate}= 15.2-29.6 cm), and 5 mm locking screws were modeled. Modularized FE models for bone, plate and screw were created using Abaqus (Dassault Systemes) and assembled into full constructs using custom-written Matlab code (Mathworks) (Fig. 1). A transversely isotropic elastic material model was used for bone [2]. Fracture fixation implants were modeled as linear isotropic (stainless steel and titanium), and Coulomb friction (μ=0.3) was assumed for the interaction between plate and bone [3]. Axial compression (400 N) or torsional loading (2 Nm) was applied to the proximal bone end with other translations constrained. Maximum von Mises stresses of the plate (σ_{plate_max}) and screws (σ_{screw_max}), construct stiffness (k_{axial} and $k_{torsion}$), and maximum shear strain at the fracture gap (ε_{shear}) were model outputs. Polynomial regression-based surrogate models (Table 1) were developed for each model output using the statistical software SAS (SAS Institute). The full quadratic models (a total of 26 linear, quadratic, and interaction regressors) and simplified regression models were fit using standard statistical approaches, including a model with the least number of regressors which produced an R^2 value less than 5% different than that of the full quadratic model (R^2-based selection method). Experimental validation was performed on 12 different constructs using PVC bone models and commercial implants.

Results: The full quadratic surrogate models fit FEA results with R^2 ranging from 0.84 to 0.99. Using the R^2-based selection simplified surrogate model, the resulting regressor coefficients were all statistically significant (Table 1) (p<0.0001). Surrogate models with as little as three regressors showed good fitting with R^2 ranging from 0.74 to 0.97 and were expressed with mathematical equations (Table 1). The fit of the response surfaces of these surrogate models are visualized in Fig. 2. The strongest predictor of maximum implant stress and construct stiffness was L_{inner}, and a strong predictor of strain at the healing tissue was d_{gap}. FEA and experimental results showed 6-31% (R^2=0.91) differences in $k_{torsion}$, and 23-53% (R^2=0.31) differences in k_{axial}. An additional 28 simulations using a generic (rectangular cross-section) plate showed good correlation between the commercial and generic locking plate results (R^2=0.90-99), supporting generalizability of our results to other locking plates.

Discussion: This study is the first, to the best of our knowledge, to develop surrogate mathematical models of fracture fixation biomechanics based on large numbers of FE simulations. These surrogate models provide new comprehensive insight and quantitative predictions in how the design of a fracture fixation construct affects implant stresses and mechanical stability at the healing fracture site. Our results are supported by previous literature which looked at these variables more in isolation and generally did not consider interactions between variables. For example working length between screws was previously reported as an important parameter for affecting axial and torsional stiffness [1, 4] and interfragmentary movement at the fracture gap [5]. Limitations of this study include use of simplified models of generic bone and fracture scenarios. Current efforts include modeling variations of subtrochanteric and peritrochanteric proximal femur fractures, and incorporating results into an interactive graphical interface for preoperative planning and resident training.

Significance: These novel surrogate mathematical models fit to large numbers of FE simulations provide a comprehensive overview of fracture fixation biomechanics, in this case for plated diaphyseal fractures. The study provides insight into which surgical variables are important, and provides a new framework for fracture fixation optimization.

Acknowledgement: PA Department of Health (CURE); National Center for Advancing Translational Sciences; Implants donated by Depuy Synthes

References: [1] Stoffel K, et al. (2003) Injury 34, Supplement 2:11–19. [2]Cowin SC, Doty SB. (2007). Tissue mechanics. Springer. [3] Moazen M, et al. (2012). Med. Eng. Phys. 34(8):1041–1048. [4] Nassiri M, et al. (2013) J. Orthop. 10(1):29–37. [5] Märdian S, et al. (2015) Clin. Biomech. 30(4):391–396.

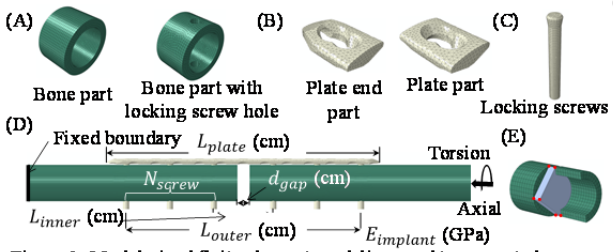

Figure 1. Modularized finite element modeling used to generate large numbers of fracture fixation design configurations. (A) bone with or without screw hole; (B) locking plate parts; (C) locking screw; (D) design variables; (E) virtual hexahedral element at the fracture gap used to compute maximum shear strain in this region.

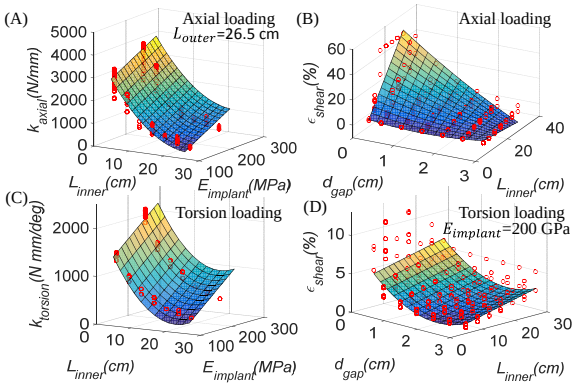

Figure 2. Response surfaces based on R^2-based selection simplified surrogate models. Red dots are the FEA results used to fit the surrogate models.

Table 1. Regression coefficients for the surrogate model using the R^2-based selection. These coefficients combine to form linear equations for predicting each respective output variable.

Axial loading	σ_{plate_max}	R^2=0.88	$-5.68 + 19.82L_{inner} + 0.37E_{implant} - 0.42{L_{inner}}^2 - 0.01L_{outer} \times E_{implant}$
	σ_{screw}	R^2=0.91	$30.02 + 12.86L_{inner} + 2.17{N_{screws}}^2 - 4.28N_{screws} \times L_{inner}$
	k_{axial}	R^2=0.97	$3560.79 - 297.72L_{inner} + 5.42{L_{inner}}^2 + 0.31L_{outer} \times E_{implant}$
	ϵ_{shear}	R^2=0.81	$-10.48 + 2.58L_{inner} + 1.50{d_{gap}}^2 - 0.93d_{gap} \times L_{inner}$

Micromechanical Heterogeneity and Anisotropy of the Meniscus Extracellular Matrix

Qing Li[1]; Feini Qu[2,3]; Biao Han[1]; Robert L. Mauck[2,3]; Lin Han[1].

[1]School of Biomedical Engineering, Science and Health Systems, Drexel University, Philadelphia, PA.
[2]McKay Orthopaedic Research Laboratory, Department of Orthopaedic Surgery, University of Pennsylvania, Philadelphia, PA.
[3]Translational Musculoskeletal Research Center, Philadelphia Veterans Administration Medical Center, Philadelphia, PA.

Abstract:

In this study, we used AFM-based nanoindentation in combination with nano-to-micro scale structural analyses to reveal the region, depth, and direction-dependent micromechanical properties of the bovine meniscus. The outer, middle, and inner zones of juvenile bovine meniscus body were isolated and embedded in OCT media. Each zone was cryosectioned transversely and radially onto glass slides to produce 20 μm thick horizontal and vertical cross-sections. AFM-based nanoindentation was performed on each sample using a colloidal spherical tip ($R \approx 5$ μm), while SEM were acquired to visualize collagen fibril structure. For both the horizontal and vertical cross-sections, we found significant micromechanical heterogeneity in the outer/middle regions, but not in the inner region. In the outer/middle regions, circumferential fiber bundles showed significantly higher E_{ind} than the superficial zone and deep zone radial fibers. For the deep zone circumferential fiber bundles, E_{ind} was significantly higher when indented along the direction of fiber alignment (vertical cross-section, CFc) compared to normal to the direction of fiber alignment (horizontal cross-section, CF). For both the circumferential and radial fibers in the deep zone, collagen appeared to be highly aligned. Collagen crimping was also observed at both the individual fibril and the fiber bundle levels. The observed mechanical heterogeneity is consistent with its known structural heterogeneity. During motion, fiber bundles in the outer/middle regions provide circumferential tensile resistance, while radial fibers in both the superficial and deep zones are responsible for structural stability and integrity. Variations in E_{ind} thus reflect different mechanical functions associated with these structural units. In contrast, the inner region of meniscus primarily resists compression in an isotropic manner. Correspondingly, this region displayed less structural organization and did not exhibit significant mechanical heterogeneity.

Indentation normal to the CF should create tensile stress along fibrils, while indentation along the CFc should lead to fibril compression. The observation that the CFc unit was stiffer than the CF unit seems contradictory to the fact that meniscus is stiffer in tension than compression. However, when collagen crimping is present, local stress induced by nanoindentation normal to fibrils could mainly result in fibril uncrimping and sliding, rather than tensile stretching, until a threshold in tensile strain is reached. Further ongoing investigation of meniscal mechanical heterogeneity and anisotropy associated with regions, length scales, deformation rates, as well variations with age and disease, will provide crucial insights into the developmental and pathological changes seen by this complex tissue. This study highlighted the regional heterogeneity and anisotropy in the micromechanical properties of meniscus. Study of the nanostructural/nanomechanical features of the tissue is essential for understanding meniscus tissue properties across length scales and for designing functional repair strategies.

Focal Chondral Defects Cause Joint-Wide Decreases in Cartilage Mechanics in a Large Animal Model

Gregory R. Meloni[1,2,3], James M. Friedman[1,2], Alexander L. Neuwirth[1,2], Marcelo Bonadio[1,2], George R. Dodge[1,2,3], Robert L. Mauck[1,2,3]
[1]McKay Orthopaedic Research Laboratory, University of Pennsylvania, Philadelphia, PA, USA;
[2]Translational Musculoskeletal Research Center, Philadelphia VA Medical Center, Philadelphia, PA, USA;
[3]Collaborative Research Partner, Acute Cartilage Injury Program, AO Foundation, Davos, Switzerland

DISCLOSURES: No disclosures for any author.

INTRODUCTION: Acute cartilage injuries, including focal defects, typically impact a younger patient population than those suffering from primary degenerative joint disease [1]. However, these localized defects can progress to advanced cartilage damage causing profound deficits in knee function and reductions in quality of life that are comparable to wide-spread joint osteoarthritis [2]. Cartilage remodeling following injury is a progressive process that includes the articular cartilage at the site of injury as well as that beyond the damaged zone [3]. *In vitro* and *ex vivo* impact models, as well as human specimens, have shown that chondrocyte death extends beyond the site of injury within days, and that chondrocytes within and near the zone of injury undergo profound metabolic changes, releasing reactive oxygen species and activating MMPs, while at the same time decreasing their proteoglycan synthesis [4]. The impact of these local events on the overall health and function of cartilage throughout the joint are less well understood. Given that injury-associated arthritis involves the whole joint, focal lesions, even in the short term, may profoundly affect the surrounding articular cartilage. Understanding the extent that focal damage affects regions beyond the initial zone of injury may hold important clues as to the progressive pathophysiology that follows injury. This might also have bearing on the performance and interpretation of cartilage repair studies, where 'normal' cartilage adjacent to experimental defects is often used as a control. To address these issues, this study evaluated, in a large animal model, the mechanical properties of articular cartilage located adjacent to the site of chondral injury, and compared these findings to contralateral joint control cartilage.

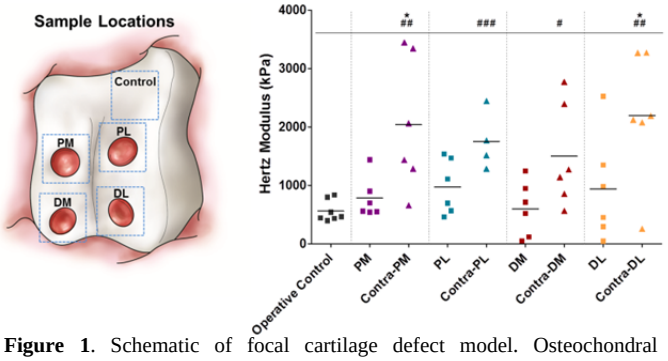

Figure 1. Schematic of focal cartilage defect model. Osteochondral segments at each defect site and a control sample were harvested from each operative joint (proximal medial (PM); proximal lateral (PL); distal medial (DM); distal lateral (DL)). Indentation testing was performed on tissue adjacent (3-4 mm distant) to the defect and at an uninjured control region in the proximal trochlear groove of the operative limb. The contralateral knee served as a positive control, with indentation testing performed at the same locations (Contra-PM/PL/DM/DL). #=p<0.05, ##=p<0.01, ###=p<0.001 vs. Operative Control; *=p<0.05 vs Operative at the same location.

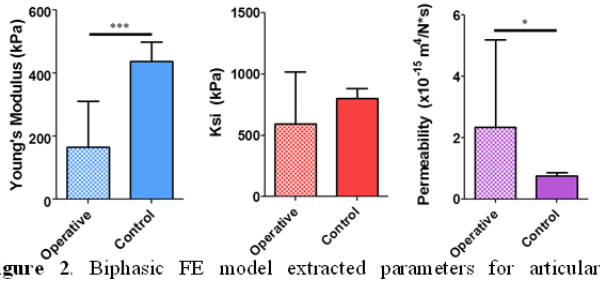

Figure 2. Biphasic FE model extracted parameters for articular cartilage properties in the operative and non-operative (Contralateral) control knees, at sites adjacent to focal defects (operative). *=p<0.05, ***= p<0.001.

METHODS: Full-thickness chondral defects were created in the trochlear groove of the right knee of adult (16-18 month old) male Yucatan minipigs (N=4) as previously described [5], with IACUC approval from the University of Pennsylvania. Defects were created proximal/distal and medial/lateral to create 4 groups. An additional proximal sample was taken as an uninjured control (Fig 1). Animals were euthanized two or three weeks post-surgery, and gross morphology was assessed. Osteochondral segments from the surgical knee and contralateral non-operative knee were harvested, placed in 1X protease inhibitors (Complete, Roche), and frozen at -80°C for mechanical testing. The mechanical properties of cartilage within the injured joint were assessed using an indentation test on intact cartilage located 3-4 mm from the defect boundary, as well as in an uninjured 'control' segment taken from the proximal patellar groove. Mechanical testing consisted of three consecutive stress-relaxation tests of 10% strain applied using a 2 mm diameter impermeable spherical indenter [6]. Young's modulus was calculated from the first ramp using the Hertz model. Additionally, finite element (FE) fiber-reinforced biphasic models of these tests were created in FEBio [7], and cartilage constitutive model parameters including Young's modulus, fiber modulus (ksi), and permeability (k) were determined for each sample by fitting experimental data. Osteochondral segments from the contralateral knee were assessed in an identical fashion. Statistics were performed using 2-way ANOVA and two-tailed Student's t-tests.

RESULTS: There were no gross changes noted in the articular cartilage in the operative joint outside of the defect site, nor were there noticeable differences when compared to the non-operative knee. However, indentation testing and analysis showed that, in two of four locations, the adjacent cartilage in the operative knee had a lower modulus compared to the same location in the non-operative knee (Figure 1, $p<0.05$). Additionally, the modulus at each contralateral location was significantly higher than the operative control ($p<0.05$). Differences in properties ranged from 2.6-fold at the PM location to 1.8-fold at the PL location. FE models were successfully constructed and used to extract constitutive model parameters for each sample (Figure 2). This analysis confirmed that the articular cartilage in the non-operative joint had a significantly higher Young's modulus ($p<0.001$) and a significantly lower permeability ($p<0.05$) than at that same location in the non-operative joint. The fiber modulus term (ksi) also trended towards a lower value in the operative limb, but did not reach statistical significance ($p=0.10$).

DISCUSSION: In this study, we measured the mechanical properties of cartilage both in close proximity and distant to cartilage defects in a Yucatan minipig model of cartilage injury. Cartilage mechanical properties in grossly 'normal' cartilage adjacent to defect sites were significantly lower than articular cartilage in contralateral non-operative knees tested at the same locations. To our knowledge, this is the first *in vivo* description of global mechanical changes to articular cartilage following a localized cartilage injury. This is consistent with previous *in vitro* and *ex vivo* models showing that articular cartilage is affected beyond the local scope of the initial injury. These findings indicate that local damage to cartilage has acute deleterious effects on the cartilage throughout the entire joint, even in uninjured 'control' segments distant to the defects. Presumably, this arises from molecular events, including inflammation and an imbalance of biosynthesis and catabolic events, having a generalized negative effect on joint tissues. Furthermore, cartilage with reduced mechanical properties may be at increased risk for damage under physiologic loading, which may explain the progression of damage to involve the whole joint. These findings also help to better define the most appropriate 'control' to use in studies of cartilage repair and regeneration, where the best option appears to be tissue from outside of the operative joint.

SIGNIFICANCE: This study demonstrates joint-wide changes in articular cartilage mechanics in a large animal model in response to localized chondral injury. These findings may explain how focal defects progress to joint wide arthritis, and importantly, provide insight into the selection of appropriate controls for studies involving articular cartilage injury and repair.

REFERENCES: [1] Green+ Arthritis Rheum 2006; [2] Heir+ AM J Sports Med 2010; [3] Bartell+ J Biomech 2015; [4] Buckwalter+ CORR 2004; [5] Fisher+ Tissue Eng Part A 2015; [6] Meloni+ ORS Annual Meeting 2015; [7] Maas J Biomech Eng 2012.

AKNOWLEDGEMENTS: This study was funded in part by the AO Foundation, the Department of Veterans Affairs, and the NIH.

Loading Induced 'On-Demand' Delivery from Mechanically Activated Microcapsules

Bhavana Mohanraj[1,2], Miju Kim[1], Fuquan Tu[1], Daeyeon Lee[1], George R. Dodge,[1,2], Robert L. Mauck[1,2]
[1]University of Pennsylvania, PA [2]Philadelphia VA Medical Center, Philadelphia, PA

Disclosures: No Disclosures.

INTRODUCTION. Stimuli-responsive drug delivery systems have several advantages, including local delivery, maintenance of drug concentrations within a therapeutic range, and preservation of activity. One desirable feature for these systems is self-regulation, wherein physiology controls release via stimuli-sensitive triggers (e.g. temperature, pH, or enzyme activity [1]). However, to date, few systems exist that take advantage of the mechanical environment to tune release [2]. Tissues within the body experience mechanical perturbation across multiple force magnitudes and length scales, from mechanotransduction at the cellular level [3] to the dynamics of whole joints. These forces provide feedback to regulate cell biology and maintain tissue integrity, but can also, at supra-physiologic levels, initiate degeneration [4]. Current strategies to repair degenerated tissues include combinations of cells, scaffolds, and growth factors; however maturation of such engineered tissues in a demanding mechanical environment may require additional factors. To address this, we developed and characterized of a novel mechano-activated microcapsule (MAMC) technology for "on-demand" drug delivery based on mechanical inputs.

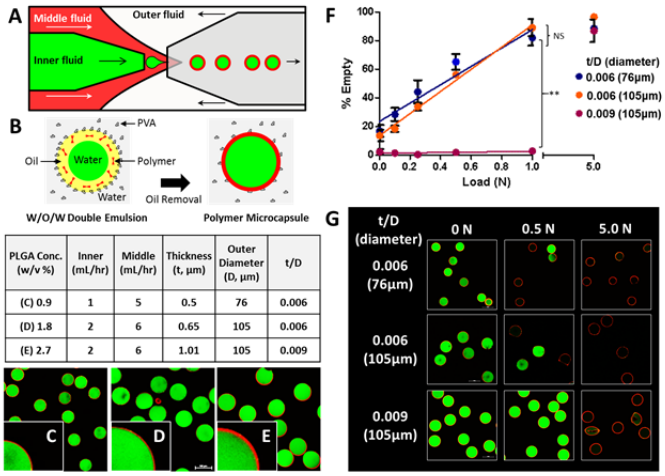

PLGA Conc. (w/v %)	Inner (mL/hr)	Middle (mL/hr)	Thickness (t, μm)	Outer Diameter (D, μm)	t/D
(C) 0.9	1	5	0.5	76	0.006
(D) 1.8	2	6	0.65	105	0.006
(E) 2.7	2	6	1.01	105	0.009

Fig 1. (A-B) Schematic of double emulsion microcapsule generation. (C-E) Fabrication parameters determine MAMC dimensions. (F-G) MAMCs containing dextran (green) with labeled shells (red) deform and fracture under load dependent on the t/D ratio (slopes differ: **p<0.01).

METHODS. MAMCs were fabricated using a glass capillary microfluidic device [5] to form a monodisperse Water/Oil/Water (W/O/W) double emulsion. For proof-of-concept, the inner aqueous phase contained FITC-dextran (2 MDa) and was sheathed by an oil phase consisting of poly(lactic-co-glycolic) acid (PLGA 50:50 + Nile Red 0.001% w/v) to form the microcapsule shell. Shell thickness and outer diameter were tuned by controlling the sheath flow rates and polymer concentration **(Fig 1, A-E)**. To demonstrate mechano-activation, a layer of MAMCs was subjected to increasing load (~500 MAMCs, parallel plate compression test, n=3/load). Intact microcapsules served as negative controls, and microcapsules compressed to 5N served as positive controls. Following compression, MAMCs were imaged by confocal microscopy to determine the empty fraction. The slope of the % empty vs. load curve was determined for each formulation. To determine the impact of degradation on release, MAMCs were incubated at 37C in PBS, and mechano-activation evaluated after 1 (1hr), 3, 7, and 14 days. Confocal 3D volume reconstructions and scanning electron micrographs were also obtained. Mechano-activation was further assessed in 3D analogs by embedding MAMCs in a 30% w/v photo-crosslinked poly(ethylene glycol) diacrylate (PEGDA) hydrogel with a stiffness comparable to cartilage. Using a custom confocal-mounted compression device [6], MAMC-laden hydrogels were compressed in unconfined compression and their deformation tracked (0-20% strain, steps of 4%, followed by compression until hydrogel failure).

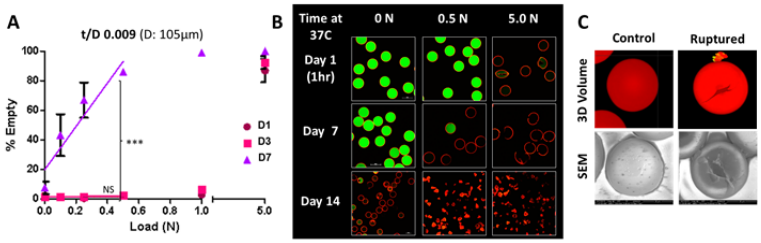

Fig 2. (A-B) Degradation time influences PLGA MAMC mechano-activation profile. (C) Volume reconstructions and SEM of control vs. ruptured MAMCs.

RESULTS. Mechanical testing of MAMCs demonstrated that microcapsule rupture and release depended on the shell thickness to diameter ratio (t/D), with a decreasing ratio resulting in MAMCs with increased sensitivity to load (**Fig 1, F-G**). MAMCs with matched t/D ratios, but different shell thicknesses and diameters, showed similar mechano-activation. In these model microcapsules, PLGA was chosen due to its biocompatibility; however, polymer degradation might impact MAMC response. Indeed, PLGA MAMCs showed increased sensitivity to load after seven days of incubation at 37C (**Fig 2**). Confocal reconstructions and SEM confirmed the spherical, intact shape of naïve MAMCs, with failure in compressed MAMCs illustrated by ruptured shell walls (**Fig 2**). In 3D constructs, MAMCs deformed with increasing gel compression, becoming ellipsoid at 20% and rupturing at 60% strain (hydrogel failure**, Fig 3**).

DISCUSSION. This study demonstrated the production of tunable mechano-activatable microcapsules (MAMCs) whose failure characteristics depend on the shell thickness to diameter ratio. MAMC activation was sensitive to polymer degradation, where degradation of the PLGA shell resulted in an increasing sensitivity with time. While this polymer has a relatively rapid degradation profile, MAMCs can also be fabricated using slower degrading polymer formulations, and with different shell thickness to diameter ratios, creating a suite of MAMCs that are programmed to release within particular physiologic or supra-physiologic loading scenarios. These MAMCs may be applied in acute scenarios of high loading or in the context of tissue engineering, where remobilization and joint loading can be used to control therapeutic release. Ongoing studies are exploring the effect of long-term dynamic loading and MAMC properties to enable sequential release from multiple MAMC populations to stimulate long-term repair in musculoskeletal defects.

SIGNIFICANCE. Mechano-activatable microcapsules (MAMCs) are a novel stimuli-responsive drug delivery platform with the potential for "on-demand" release in a mechanically loaded environment. This work demonstrated the tunability of MAMC release profiles through control of fabrication parameters.

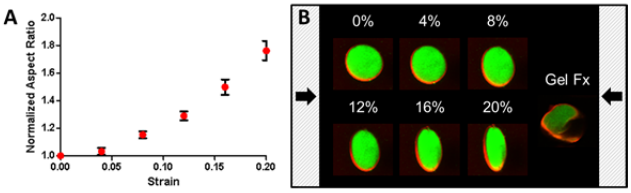

Fig 3. (A-B) MAMC deformation (aspect ratio, AR) with hydrogel deformation; MAMCs ruptured only upon hydrogel fracture (n=11 MAMCs from three separate hydrogels).

REFERENCES. [1] Kost+ Adv Drug Deliv Rev 2001, [2] Korin+ Science 2012, [3] Engler+ Cell 2006, [4] Sun+ Ann NY Acad Sci 2010, [5] Tu+ Langmuir 2012, [6] Farrell+ Eur Cells Mat 2012.

ACKNOWLEDGEMENTS. This work was supported by an NSF Graduate Research Fellowship and an NIH/NIAMS Training Grant (T32 AR007132).

Biomechanical Properties of Regenerating Dystrophic Muscle

AUTHORS: Nick Oyster[1], Claire McLeod[1], Matt Caporizzo[2], Russell Composto[2], Rob Mauck[1], Foteini Mourkioti[1]

[1]*Department of Orthopaedic Surgery, McKay Orthopaedic Research Labs,* [2]*Department of Engineering and Applied Sciences*

ABSTRACT:

Skeletal muscle diseases or myopathies result in loss of muscle mass, degeneration and functional weakness. Duchenne Muscular Dystrophy (DMD) is the most common recessive chronic muscle disorder that results from lack of dystrophin, a cytoskeletal protein that is essential for the stability of the skeletal muscle membrane (Hoffman, 1987). While muscle regeneration is robust in DMD patients, it appears insufficient to match the pace of degeneration. A limitation in therapeutic intervention until now has been that the commonly used mouse model (mdx) exhibit only mild muscle weakness in contrast to patients. We recently developed a new dystrophic mouse model (called G2 hereafter) that exhibits all the pathological hallmarks of human DMD. Therefore, our G2 mouse model offers a useful tool to study tissue dysregulation associated with the disease. The identification of specific biomechanical dysregulation may have therapeutic value for treating both muscular dystrophies as well as other chronic muscle diseases.

For this meeting, we build upon our previous muscle results in combination with new preliminary data of differences in rigidity of G2 muscles, to investigate the influence of matrix elasticity and physical aspects of muscle stem cells (MuSCs) that could impact regeneration. Our experiments are testing the hypothesis that during the progression of the dystrophic phenotype, the altered tissue environment contributes to the rapid functional defects and determine how these parameters influence MuSC fate. Our results provide the first documentation of the specific biomechanical properties of dystrophic muscles using a pre-clinical mouse model that recapitulates the human disease and will investigate the involvement of the microenvironment in directing tissue regeneration. The ultimate goal of this work is to potentiate development of bioengineering therapeutic approaches designed to promote skeletal muscle regeneration.

NIR Spectroscopic Assessment of Ligament Composition Provides Insight into Regional Differences in Mechanical Properties

Mugdha Padalkar[1], Snehal Shetye[2], Michael Hast[2], Louis Soslowsky[2], Nancy Pleshko[1]
[1]Dept. of Bioengineering, Temple University, Philadelphia, PA, 19129
[2] University of Pennsylvania, Philadelphia, PA

Introduction: Knowledge of the mechanical properties of a remodeling ligament graft are of prime importance for optimal rehabilitation. Studies have shown that the mechanical properties of a graft generally do not reach the same level as those in the native ligament (1). Mechanical uniaxial tensile testing has been used as a method of analysis to evaluate ligament properties, but as this method is destructive, it is not applicable to a clinical setting. Infrared spectroscopy is a modality based on molecular vibrations and is sensitive to molecular structure and composition. Near infrared (NIR) spectroscopy, which is based on radiation that can penetrate tissues up to centimeters thick (2), has been emerging as a non-destructive method for musculoskeletal tissue evaluation. NIR spectra have been shown to distinguish normal and enzymatically degraded tissue (3), tissues of varying histological grades (4), and to correlate with mechanical properties of cartilage (5). A non-destructive method such as NIR spectroscopic assessment that correlates to mechanical properties of the ligament and tendon could provide information on the progression of remodeling during an arthroscopic evaluation, which would aid in choosing therapeutic and rehabilitation protocols. Further, spectroscopic assessment of potential allograft or autograft tissues that correlated to mechanical properties could be useful for graft selection. Accordingly, in the current study, we compared compositional information based on NIR spectra of different regions of ligaments to mechanical data from the same regions.

Material: Medial collateral ligaments (MCLs, n = 5) were harvested from Dutch-Belted female rabbits ~ 6 months of age under an IACUC-approved protocol, and stored in PBS and PI at -20°C until NIR data collection. NIR spectra were obtained from the MCLs as described below, and the ligaments were again frozen until mechanical testing studies were performed. Thus, each tissue went through two freeze-thaw cycles.

Near infrared fiber optic probe data collection: NIR spectra were obtained from four regions of each MCL (femoral insertion, tibial insertion, two mid-substance regions) using a 3 mm diameter silica glass diffuse reflectance NIR probe (Art Photonics, Berlin, Germany) coupled to a Matrix-F infrared spectrometer with a TEInGaAs detector (Bruker, MA). NIR data were collected in diffuse reflectance mode from 4000-8000 cm^{-1} at 8 cm^{-1}, and 128 co-added scans. A light pressure was used during data collection to ensure proper contact with the sample.

Mechanical testing: Uuniaxial tensile testing of the MCLs was performed in the McKay Orthopedic Research Laboratory, University of Pennsylvania, using an Instron 5543 Electromechanical Test System (Instron, Norwood MA, USA). Cross-sectional areas of the MCLs were measured using a custom made laser device (6). The tibial and femoral bones that connect the ligament were potted in PMMA and gripped in custom made fixtures. During the testing the MCLs were immersed in a PBS bath. To obtain regional properties of the MCLs, stain lines (Verhoeff's stain) were drawn 4mm apart on the MCL. The stain lines were tracked during mechanical testing by a video analyzer to obtain regional stiffness, which was normalized by cross sectional area to obtain modulus. The specimens were preloaded to 0.1N, followed by preconditioning (0.0 to 0.5 mm, 10 cycles, 10mm/min). This was followed by a hold of 300 seconds prior to a ramp to 45N at a rate of 10mm/min.

Data analysis: Spectral data: NIR spectra were scatter corrected and second derivative (Savitzky Golay, 100pt smoothing) was obtained (Unscrambler software, Camo, Norway). Second derivative peak heights were calculated at 6900 cm^{-1}, which reflects the free water in the tissues, and at 5610 cm^{-1} , which reflects the overall matrix composition. **Mechanical properties:** Mechanical data were analyzed using a custom image processing MATLAB code. For each MCL, optical stiffness and optical modulus were calculated at the femoral and tibial insertion sites, and at mid substance. Paired t-tests was used to establish statistical significance ($p<0.05$) between the tibial and femoral insertion data for stiffness, modulus and NIR peak height values.

Results: The NIR spectra were dominated by water peaks at 5200 and 6900 cm^{-1}, (Fig.1). Qualitatively, differences were apparent in the averaged spectra from tibial insertion sites and femoral insertion sites at 6900 cm^{-1}. When quantified, the second derivative peak heights at 6900 cm^{-1} from the femoral insertion site were significantly greater than the peak heights at the tibial insertion site, indicating a greater water content ($p=0.003$). No differences were apparent in overall NIR-determined matrix content between these two regions.

Uniaxial tensile testing showed regional variations in stiffness of the mid substance and insertion sites of the MCL. The tibial insertion site showed significantly higher values of stiffness ($p=0.007$) as well as modulus ($p=0.006$) when compared with the femoral insertion site parameters (Fig. 2).

Discussion: Previous studies have shown that the composition of the MCL varies along its length, and that water content is greatest at the femoral insertion site, and decreases by ~10% towards the tibial insertion site. Similar changes in water content were found using non-destructive near infrared spectroscopy (7), and these compositional differences may account for difference in stiffness at these two insertion sites. Thus, NIR spectroscopy showed results consistent with differences in mechanical properties of the tissues. **Significance:** Arthroscopic assessment of ligament repair currently relies on visual evaluations to determine remodeling quality. The spectroscopic data presented here allow knowledge of molecular information correlated to mechanical properties to be considered in such evaluations, which could aid in clinical decision making.

References:

1) Beasley, Oper Tech Orthop, 2005. 2) Padalkar, Analyst, 2015. 3) Brown,Phys Med Biol, 2009. 4) McGoverin, Appl. Spectrosc, 2014.
5) Hoffmann, Biomed Tech 57: 1. 2012, 6) Favata, Thesis, University of Pennsylvania, 2006. 7) Padalkar, Ann Biomed Eng 2013

Acknowledgement: Supported by NIH R01AR056145

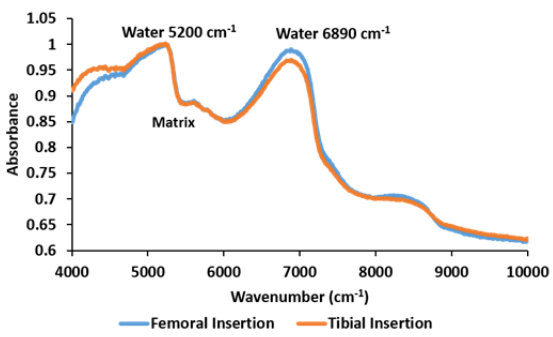

Figure 1: Near infrared spectrum of medial collateral ligament

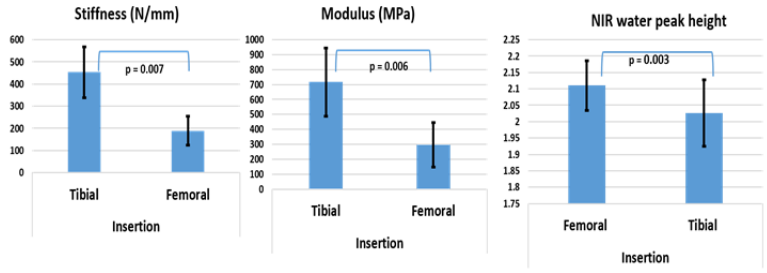

Figure 2: Bar graphs of the stiffness, modulus and NIR water peak height at tibial and femoral insertion sites.

Effect of Varying Levels of Compositional Heterogeneity on Fracture Resistance in Cortical Bone

Ani Ural[1]

[1]Department of Mechanical Engineering, Villanova University, 800 Lancaster Avenue, Villanova, PA

ABSTRACT

The recent reports of atypical femoral fracture and its possible association with prolonged bisphosphonate use highlighted the importance of a thorough understanding of mechanical modifications in bone due to bisphosphonate treatment. The reduced compositional heterogeneity of bone is one of the modifications in bone due to extensive suppression of bone turnover. The goal of the current study is to evaluate the influence of varying levels of compositional heterogeneity on fracture resistance in human cortical bone using finite element modeling.

Transverse microscopy images of cortical bone from the mid-diaphysis of 58-year-old and 70-year-old male donor tibiae were converted to a 3D finite element model which was inserted in a compact tension test specimen to evaluate the fracture resistance of the bone. Crack formation and propagation was modeled by cohesive extended finite element method in the osteons and interstitial bone and by cohesive interface elements at the cement lines. Four models were generated including a model with homogeneous material properties (HM) and four heterogeneous models with 5 (HT5), 10 (HT10), and 20 (HT20) different material property groups in the microstructural region. Heterogeneous material properties were randomly assigned to each element in the microstructural region using a MATLAB script based on values reported in the literature. The average material properties were used for the homogeneous model. The fracture response was assessed through crack growth path and the volume of cracked elements.

The results showed that the fracture resistance increased with increasing heterogeneity, and demonstrated the highest resistance in HT10 case for both models. There was between 6-10% reduction in the crack volume between HM and HT5. On the other hand, the reduction in crack volume in HT10 simulations was between 25-32% compared to the homogeneous material distribution. However, further increasing the heterogeneity demonstrated no significant enhancement in fracture resistance as seen in HT20 case with a reduction in crack volume of 17% with respect to homogenous cases.

In summary, the results showed that although increasing heterogeneity enhanced the fracture resistance of bone, there is a threshold after which its beneficial effects were not as significant. These results provide new information on the relationship between varying levels of tissue heterogeneity and fracture resistance and may improve the understanding of the influence of material level changes due to prolonged bisphosphonate use on the fracture resistance of bone.

Stretch-Induced Network Reconfiguration of Collagen Fibers in the Human Facet Capsular Ligament

Sijia Zhang[1], Danielle S. Bassett[1,2], Beth A Winkelstein[1,3]
[1]Department of Bioengineering, University of Pennsylvania
[2]Department of Electrical and Systems Engineering, University of Pennsylvania
[3]Department of Neurosurgery, University of Pennsylvania

Biomaterials can display complex spatial patterns of cellular response to external forces. Revealing the role of these patterns in material failure requires an understanding of the statistical dependencies between spatially distributed changes in a cell's local biomechanical environment, including altered collagen fiber kinematics in the extracellular matrix. Previous analytic methods detecting anomalous fiber realignment neglect the potential for larger-scale realignment of fiber groups as they adapt to ligament loading. Thus, it is as yet unknown if, and to what extent, local collagen networks display meso-scale organizational changes whose complexity alters ligament mechanics. Here we develop and apply a novel extension of network science methods to investigate how excessive tensile stretch of the human cervical facet capsular ligament (FCL), a common source of chronic neck pain, affects the local reorganization of collagen fibers. We define collagen alignment networks based on similarity in alignment angles measured by quantitative polarized light imaging (QPLI). We quantify the reorganization of these networks following macroscopic loading by describing the dynamic reconfiguration of network communities, regions of the material that display similar fiber alignment angles. Community detection methods revealed differences in the modular structure of the constructed collagen networks before and after tensile loading in regions with previously identified anomalous fiber realignment leading to tissue failure. We also show that alterations in community structure occurred smoothly over time, indicating coordinated adaptation of fibers to loading. Moreover, flexibility, a measure of network reconfiguration, tracked the loss of FCL's mechanical integrity at the onset of anomalous realignment and regions of anomalous realignment displayed altered community structure. These findings utilize novel network-based techniques to explain abnormal collagen fiber reorganization, a dynamic and coordinated multivariate process underlying tissue failure. Our approach provides new insights for understanding how tissue mechanics evolve across time and length scales and can be extended to study other types of collagenous tissues.

Osteoactivin Expression Is Modulated By Anti-Tumor Necrosis Factor Treatment in Bones of Rats Performing Repetitive Reaching Task

Nagat Frara, Steven N. Popoff, Mary F. Barbe
Department of Anatomy and Cell Biology, Temple University School of Medicine, Philadelphia, PA

INTRODUCTION: Bone is a dynamic tissue that undergoes continuous remodeling in response to several factors, including mechanical loading, injury, and local or systemic cytokines whose levels alter with mechanical loading. Although cyclical loading and high force loads are known to i ncrease incidence of hand/wrist osteoarthritis and to reduce bone mass, only a few studies have examined changes occurring in upper extremity bones as a consequence of occupational tasks. Osteoactivin is a type I glycoprotein involved in many biological processes, including cell differentiation, tissue regeneration and inflammation, and plays a significant role in injury and repair of musculoskeletal tissues. In a fracture repair model, osteoactivin was expressed in osteoblasts during bone healing, supporting its role in bone formation and repair. The expression of osteoactivin in association with upper extremity overuse injuries is still under investigation. Barbe and Barr previously developed a voluntary rat model of repetitive reaching and grasping that permits the examination of tissue responses to non-weight bearing muscular loads on bone and other upper limb tissues. Rats performing a high repetition high force (HRHF) reaching and lever pulling task for 2 hours/day, 3 days/week for up to 18 weeks showed transient increases in TNF-α that peaked in serum at 6 weeks. TNF-α is a key pro-inflammatory cytokine known to promote tissue catabolism, and may be one contributor to forelimb bone loss reported in 12-week HRHF rats. We hypothesized that provision of an anti-TNF-α drug for 4 weeks in a time frame that included the 6 week peak of TNF-α, might be an effective intervention for bone loss in this model. Therefore, in this study, we evaluated the morphometry and presence of osteoactivin and inflamamtory cytokines in forelimb bones of 11-week HRHF rats that had undergone treatment with an anti-TNF-α drug provided in task weeks 4-7, compared to saline-treated HRHF rats. We hypothesized that adaptive remodeling in skeletal tissue undergoing prolonged repetitive loading at high force loads is modulated by a superimposed inflammatory response, and that provision of an anti-TNF-α treatment would alter the balance towards anabolic responses, such as increased osteoactivin production and bone volume.

METHODS: All experiments were approved by the Temple University Institutional Animal Care and Use Committee in compliance with NIH guidelines for the humane care and use of laboratory animals. Studies were conducted on 16 young adult (3.5–4 months of age at onset of experiments), female, Sprague-Dawley rats that underwent an initial training period to learn the task (10 min/day, 5 days/wk, for 6 wks), before then performing a HRHF task for 11 weeks (2 hours/day, 3 days/week), and 16 age-matched control (C) rats. At the end of HRHF task week 3, the HRHF rats were divided into two cohorts (n=8 each) that received either five intraperitoneal injections of saline (HRHF+Veh) or anti-rat TNF-α antibody (HRHF+anti-TNF) across 4-7 weeks, as did controls (C+Veh and C+anti-TNF; n=8 each). GraphPad PRISM was used for the statistical analyses. All data are expressed as mean ± SEM. P values of < 0.05 were considered significant. ANOVAs were used to compare results, and Bonferroni post-hoc tests used to determine between group differences.

RESULTS: By task week 11, micro-CT analysis showed that HRHF+anti-TNF rats had increased bone mass (detected as increased trabecular bone volume, thickness, and number and reduced trabecular separation; $p<0.01$ each), compared to the other groups. Histomorphometry showed increased osteoblast numbers in HRHF+anti-TNF rats ($p<0.05$), yet decreased osteoclast numbers ($p<0.05$), compared to HRHF+Veh rats, further indicative of increased bone anabolism in anti-TNF-α treated HRHF rats. ELISA of distal radius and ulna homogenates showed increased TNF-α levels in HRHF+Veh rat bones ($p<0.05$), compared to the other groups including the HRHF+anti-TNF rat bones (showing effectiveness of the drug). ELISA of bone homogenates also showed increased osteoactivin and IL-18 levels in anti-TNF treated HRHF rat bones ($p<0.05$), compared to the other groups, suggesting that loading-induced increases in TNF-α blocked their expression in bones.

DISCUSSION: A modulated effect of the task or treatment on bone morphometry, inflammatory cytokines and osteoactivin levels in forelimb bones was detected at 11 weeks of HRHF task performance. Micro-CT data indicated that saline-treated 11-week HRHF rats showed no morphological changes in the distal radius metaphysis trabeculae, indicative of no bone adaptation to the loading regimen. The increased osteoclast numbers in the HRHF+Veh group of rats is likely due to their increased TNF-α expression since it is known to stimulate osteoclastogenesis and bone resorption. The observed increase of TNF-α in bones of HRHF rats is consistent with prior studies from our lab. However, there were no significant trabecular morphometric changes in saline-treated HRHF rats versus controls. The 11-week end point used in this study may be the onset of catabolic losses previously reported in 12-week HRHF rats.

In contrast, there was an increase in bone mass and osteoblast numbers in rats that had received the anti-TNF-α treatment. This is our first study to identify an intervention that significantly rescued HRHF-induced bone loss. We have previously reported the effects of ibuprofen and ergonomic task reduction interventions; each of which rescued net bone loss but showed no change over to net bone growth. The increase seen in this study is likely due at least partially to the reduction in TNF-α levels for reasons explained above. However, the increased bone mass in anti- TNF-α treated rats may also be linked to their increased osteoactivin levels, since osteoactivin is a known osteogenic factor that enhances bone formation and osteoblast differentiation. We also observed increased IL-18 in the HRHF+anti-TNF rat bones. IL-18 is a cytokine secreted by a variety of cell types, including macrophages, antigen presenting cells, chondrocytes, osteoblasts and fibroblasts. IL-18 has potent immunomodulatory effects which can be pleiotropic, complex, and

paradoxical in various disease processes. Patients with upper extremity soft tissue disorders showed increased serum IL-18 at early stages. It has been reported that IL-18 expression increases in patients with rheumatoid arthritis and osteoarthritis, and that TNF-α can regulate the expression of IL-18 in rheumatoid arthritis synovial fibroblasts. While the increase in IL-18 in our study was unexpected, its increase in bones of anti-TNF-α treated rats supports a role for IL-18 in repair processes in this model. It has been reported that the integrated cytokine response to injury is complex and that tissue responses depend not only on absolute concentrations of TNF-α, but also on the simultaneous presence of naturally occurring cytokine inhibitors and anti-inflammatory cytokines. Perhaps osteoactivin is acting as a feedback regulator of inflammation by upregulating IL-18 production and consequently limiting other pro-inflammatory cytokines and contributing to bone formation and repair.

Limitations of this study include that we did not examine other bony sites of the upper extremity for bone changes. The effectiveness of this intervention should also be repeated in more mature female rats (we studied young adult female rats to the point of musculoskeletal maturity [7 months of age]), and in male rats. Lastly, the effectiveness of this secondary intervention should be repeated in human subjects.

SIGNIFICANCE: This is our first study to identify an intervention that significantly rescued HRHF-induced bone loss. A strong role for task-induced inflammatory processes in bone tissue is supported in our model of repetitive reaching and lever pulling. TNF-α apparently suppresses bone formation as well as osteoactivin, an anabolic bone factor, in our rat model. Since the factors that initiate and modulate different stages of tissue-repair remain to be elucidated, future studies are needed to clarify the interactions between osteoactivin and other repair molecules during inflammatory and repair responses underlying musculoskeletal injuries.

Increased Media Volumes Enhance Viability and Functional Maturation of MSC-Based Engineered Cartilage

Elizabeth A. Henning, MS[1,2], Breanna N. Seiber, BS[1,2], David R. Steinberg, MD[1,2], Robert L. Mauck, PhD[1,2,3]
[1]Dept. of Orthopaedic Surgery, University of Pennsylvania, Philadelphia, PA, USA, [2]Translational Musculoskeletal Research Center, Philadelphia VA Medical Center, Philadelphia, PA, USA, [3]Dept. of Bioengineering, University of Pennsylvania, Philadelphia, PA, USA.

Author Disclosures: E. Henning: None. B.N. Seiber: None. D.R. Steinberg: None. R.L. Mauck: None.

Introduction: The field of cartilage tissue engineering has matured to the point where in vitro tissues, based on chondrocytes or mesenchymal stem cells (MSCs), can be matured to match the bulk mechanical properties and composition of native tissue [1, 2]. With this progress, focus has turned towards the production of larger constructs of anatomic relevance, identifying new limitations [3, 4]. Namely, as construct size increases, diffusional path lengths increase, and so central regions of constructs tend to develop less matrix [5, 6]. These deficiencies in the central regions are particularly evident in MSC-based constructs, where viability, matrix production, and mechanical properties are severely compromised [7]. This is likely a consequence of the fact that chondrogenically differentiated MSCs only approximate the phenotype of native chondrocytes [8]; they can make cartilage-like matrix, but do so in an inefficient manner that rapidly depletes nutrients and may compromise cell health. We recently demonstrated that, for very thin (0.75 mm) MSC-based constructs, increasing the relative media volume led to higher properties and less central cell death [9]. To further this line of inquiry, this study tested the hypothesis that by increasing the media volume provided (and so the pool of nutrients) one could improve cell viability and mechanical properties throughout the depth of thicker (2.25 mm) MSC-seeded constructs, with a particular focus on the construct central region.

Methods: Juvenile bovine MSCs (P2) were encapsulated in 2% agarose ($20x10^6$ cells/ml) to generate constructs (D=4mm) with a thickness of 2.25 mm. Constructs were cultured for 56 days in chemically defined media supplemented with 10 ng/mL TGF-β3. Control constructs (V) were provided the standard volume of 1ml per 2.25 mm construct, replaced in full two times per week, based on our previous work. Additional constructs were 'overfed' using 2 times (2V) or 3 times (3V) the control volume. Care was taken to ensure that constructs did not flip during culture. Prior to testing, the top surface of each construct was marked with Verhoeff's stain to maintain orientation. Bulk properties of constructs (n=4) were assessed in uniaxial unconfined compression and equilibrium (eq.) modulus calculated. Local properties (n=4) were assessed using a microscope-based unconfined compression tester [5]. Constructs were halved diametrically and uniaxial compression was applied in 4% strain increments. Images were acquired at each strain increment and Lagrangian strain calculated. Strain values at 12% were binned into 10 regions of equal size through the depth, with region 1 as the top of the construct and region 10 the bottom, and local eq. modulus calculated from recorded load. Additional construct halves were assessed for cell viability (n=3) with the Live/Dead Viability Kit. Percent viability was determined by imaging the central region of the construct under 10X magnification and using a custom MATLAB script to count the number of cell within the Calcein-AM and ethidium-homodimer-1 channels. Significance ($p \leq 0.05$) was assessed by ANOVA with Tukey's post-hoc correction.

Results: When constructs were provided a greater volume of media, cell viability increased within the central regions for both 2V and 3V constructs at 28 and 56 days compared to controls (Fig. 1). Bulk mechanical analysis of overfed constructs showed improved mechanical outcomes as media volume increased, with eq. modulus of 2V and 3V constructs significantly higher at day 56 compared to day 28, and 3V constructs significantly higher than V constructs at day 56 (Fig 2, $p<0.05$). Analysis of local mechanics showed that increasing media volume resulted in a similar overall depth dependent profile of the constructs. However, a significant improvement was seen in the central region, where the eq. modulus of the 3V constructs was significantly greater than the V constructs on day 56 (Fig 3, $p<0.05$).

Discussion: In this study, we investigated the impact of 'overfeeding' on the viability and functional maturation of MSC-based engineered cartilage, with a primary focus on the construct central region previously shown to have the greatest deficiencies [7, 10]. Based on previous findings that functional maturation of thin 0.75 mm constructs could be improved by providing higher media volumes, we hypothesized that overfeeding of 2.25 mm constructs would lead to improved central viability and mechanical properties that featured less depth dependence. Increasing media volume successfully improved both cell viability in the central region (Fig. 1) and bulk mechanical properties (Fig. 2) for both 2V and 3V constructs at all time points. However, counter our initial hypothesis, the local modulus of the 'overfed' constructs maintained a marked depth dependent profile, similar to control constructs, with the eq. modulus of the central region only showing a slight improvement in the 3V constructs compared to the controls at day 56. Thus, while overfeeding resulted in improved overall mechanics and cell viability in the central region, constructs remained highly heterogeneous through their depth. These findings show that simply increasing the media volume provided does not significantly overcome the challenges of nutrient deprivation in the central regions that stem from nutrient path length. Ongoing and future work will further explore these findings to determine the appropriate media volume that maximizes construct growth potential, producing an engineered MSC-based engineered cartilage with the greatest and most homogeneous properties.

Significance: In this study, increasing media volume led to differences in cell viability and bulk and regional mechanical properties in tissue engineered cartilage of physiologic thickness. These findings will improve *in vitro* culture conditions to optimize MSC seeded construct growth prior to implantation.

References: 1) Lima+ OAC 2009; 2) Erickson+ Acta Biomater 2012; 3) Nims+ Tissue Eng 2015; 4) Cigan+ J Biomech 2014; 5) Buckley+ Tissue Eng 2012; 6) Bian+ OAC 2009; 7) Farrell+ ECM J 2012; 8) Huang+ Tissue Eng 2010; 9) Henning+ ORS 2015; 10) Farrell+ OAC 2014

Acknowledgements: This work was supported by the NIH (R01 EB008722) and the Department of Veterans Affairs (I01 RX000700).

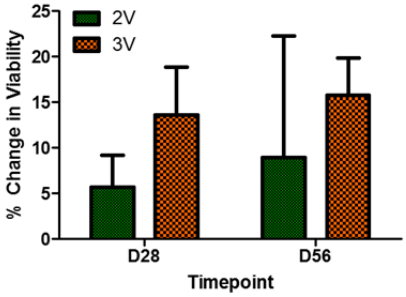

Figure 1. Percent change in cell viability (compared to control) showed an increase in viability in the central region of overfed constructs at day 28 and day 56.

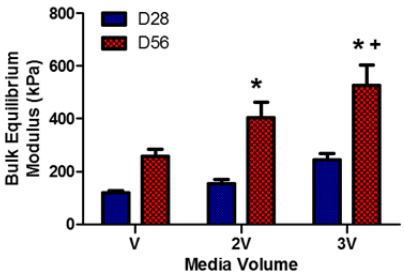

Figure 2. Bulk equilibrium modulus showed increases in modulus with increased media volume (* vs. Day 28; + vs. Day 56 V, $p<0.05$).

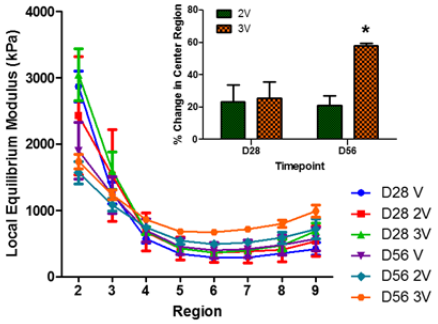

Figure 3. Local equilibrium modulus at day 28 and day 56. Inset: Percent change of modulus of the central regions of constructs showed an increase in overfed constructs compared to control volume (* vs. Day 56 V, $p<0.05$).

Injured Tendons Increase Lactate Synthesis and Pharmacological Inhibition of Lactate Synthesis Improves Tendon Repair.

Motomi Enomoto-Iwamoto[1], Kairui Zhang[1,2], Michael W. Hast[3], Leslie Cantley[1], Masahiro Iwamoto[1], Louis J. Soslowsky[3]
[1]Children's Hospital of Philadelphia, Philadelphia, PA, [23]Southern Medical University, Guangzhou, China, [3]University of Pennsylvania, Philadelphia, PA

Disclosure: Nothing to be disclosed.

INTRODUCTION: Incomplete tendon healing leads to significant mobility restriction, pain and substantial health care costs. To develop novel targeted therapies for tendon injury, it is necessary to define the molecular changes and mechanisms governing the tendon healing process Up-regulation of glycolysis and lactate synthesis occurs in wound, inflammation and cancer. Recently, we have found that IL-1β inhibits tenogenic differentiation of injured-tendon derived progenitors and increases their lactate synthesis and that inhibition of lactate synthesis competed against the IL-1β action on tenogenic differentiation [1]. We also know that inflammatory cytokines are up-regulated in injured tendons [2]. Taken together, we hypothesize that tendons increases lactate synthesis in response to injury and pharmacological inhibition of this alteration is beneficial for tendon repair. We analyzed activities of glycolysis and lactate synthesis in injured tendons with ^{13}C-glucose labeling and examined the effects of dichloroacetat (DCA), an inhibitor of lactate synthesis, on recovery of collagen fiber formation and biomechanical properties in the mouse Achilles tendon injury model.

METHODS: All animal experiment procedures were approved by the Institutional Animal Care and Use Committee of the Children's Hospital of Philadelphia. *Tendon surgery:* A complete transverse incision was made at the midpoint of the right Achilles tendon in 8-week-old female C57/BL6 mice and the gap was left open [3]. Animals were returned to cage activity and euthanized 1 or 4 weeks after surgery, representing the inflammation/proliferation and repair phases, respectively. Harvested tendons were subjected to metabolomics, histological and biomechanical analyses. *^{13}C-glucose labeling*: 13C-glucose (400mg/kg) was peritoneally injected 1 h prior to euthanization. The uninjured or injured tendons (n=4) were snap-frozen in liquid nitrogen and subsequently ground to powder for perchloric acid extraction. ^{13}C-metabolites and intermediates were analyzed by combination of LC-MS and MC-MS [4]. *DCA administration:* Dichloroacetate (DCA) (100 mg/kg, daily) was given to C57/BL6 mice from 1 day to 4 weeks post-surgery. *Mechanical testing:* Achilles tendons with attached calcanei (n=10) were fine dissected and hydrated in PBS. Tendon cross-sectional areas were calculated with a custom laser-based device [5]. For tensile testing to failure, tendons were placed in a custom fixture that grips the calcaneus and tendon ends. Fiber alignment measures were collected during mechanical testing with a cross-polarizing technique.[5 *Statistics:* Student's t-tests or two-way factorial ANOVA followed by Boneferroni post-hoc multiple comparison tests were used to identify differences between groups. Significance for all tests was set as $p<0.05$.

RESULTS: The molar percent enrichment of ^{13}C-latate was strongly increased at 1 week post-injury and remained high after 4 weeks (Fig. 1). In addition, enrichment of ^{13}C-glyceraldehyde, a metabolite in glycolysis pathway, was significantly higher in injured tendons in the 1week group compared to uninjured tendons. Four weeks after injury, ^{13}C-glyceraldehyde enrichment decreased, but was still higher than the uninjured tendon (Fig. 1). DCA-treated samples had smaller cross sectional areas (Fig. 2AAnalysis of axial view of collagen fibers by electron microscopy revealed that the DCA-treated tendon contained thicker fibers. Finally biomechanical assessments demonstrated that modulus and maximum strength were significantly higher in the DCA-treated tendons than the vehicle-treated tendons (Fig. 2B and C). In addition, the DCA-treated tendons had a lower circular variance, which is indicative of better alignment (Fig. 2D).

DISCUSSION: The results indicate that injured tendon acutely increases glycolysis and lactate synthesis and that inhibition of lactate synthesis improves recovery of collagen fiber structure and biomechanical properties. Alterations of glucose metabolism were found not only in an inflammation phase but also in the repair phase, indicating that the responsible cells for the alterations are not only in inflammatory cells and vessels but also the tendon cells and tendon progenitors that contribute to tendon regeneration. Thus, the findings indicate that injured tendons reprogram glucose metabolism and that metabolic drugs can modify this alteration and improve tendon healing. In wounds, lactate accumulates regardless of oxygen concentration and stimulates VEGF in macrophages and collagen synthesis in fibroblasts [6]. Lactate my mediate angiogenesis and fibrous tissue formation (scar) in injured tendons.

SIGNIFICANCE: While a large number of clinical and preclinical approaches have been attempted, none result in complete recovery of mechanical structure and function in injured tendons. This study provides direct evidence that glycolysis and lactate synthesis can be novel therapeutic targets for tendon repair.

REFERENCES: [1] Zhang et al. Biochem Biophys Res Commun (2015); [2]Sugg et al. J Orthop Res 32, 944 (2014); [3] Asai et al. Stem Cells 32, 3266 (2014); [4] Nissim et al. J Biol Chem 289, 9710 (2014); [5] Lake et al. J Orthop Res 27, 12 (2009); [6] Trabold et al. Wound Rep Reg, 11, 504 (2003)
Acknowledgments: We thank Miss A.T. Gunawardena and the Metaboromics Core at CHOP for technical assistance. This study was supported by the Penn Center for Musculoskeletal Disorders Pilot and Feasibility Grant (NIH/NIAMS P30AR050950), the NIH R21AR062193 Grant and the interdepartmental fund of the Children's Hospital of Philadelphia.

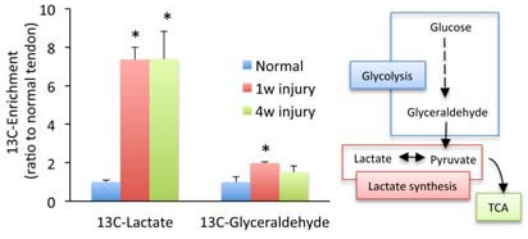

Figure 1. Injured tendons increased an influx of glucose to glycolysis and lactate synthesis pathway. ^{13}C-glucose was injected 1 h in prior to euthanization. The uninjured or injured tendons (1 or 4 weeks postinjury) were harvested and subjected to metaboromics analysis to measure the molar percent enrichment of ^{13}C-metabolites. *, $p<0.05$

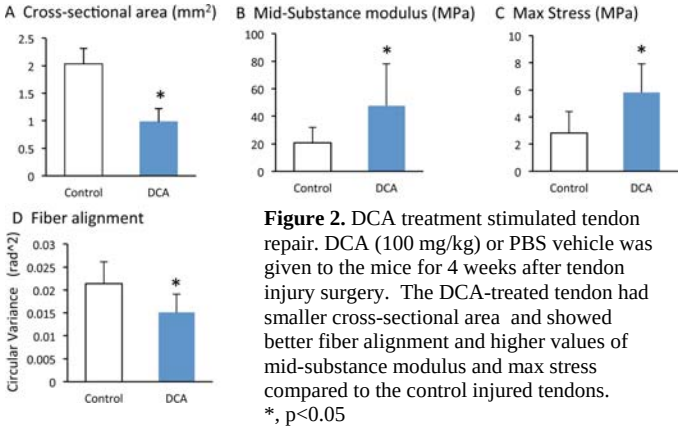

Figure 2. DCA treatment stimulated tendon repair. DCA (100 mg/kg) or PBS vehicle was given to the mice for 4 weeks after tendon injury surgery. The DCA-treated tendon had smaller cross-sectional area and showed better fiber alignment and higher values of mid-substance modulus and max stress compared to the control injured tendons. *, $p<0.05$

Sex Differences Are Present in Uninjured Achilles Tendon and Muscle

Pardes AM, Freedman BR, Fryhofer GW, Salka NS, Bhatt PB, Soslowsky LJ
McKay Orthopaedic Laboratory, University of Pennsylvania, Philadelphia, PA
soslowsk@upenn.edu

Disclosures: Pardes AM (N), Freedman BR (N), Fryhofer GW (N), Salka NS (N), Bhatt PB (N), Soslowsky LJ (5; Orthofix, DJO)

Introduction: Achilles tendon ruptures are common and devastating injuries. Although men and women both experience Achilles tendon ruptures at similar ages and sport participation times, it is surprising that 84% of all ruptures occur in men [1]. Differences in hormone physiology between sexes may influence Achilles tendon and gastrocnemius muscle homeostasis and injury risk [2,3]. However, it is unknown whether the primary effects of hormone differences act specifically on tendon or on its origin muscle [4,5]. Therefore, the objective of this study was to determine mechanical, structural and histological properties of uninjured Achilles tendon and muscle in female, ovariectomized (OVX) female, and male rats. We hypothesized that female and OVX rats would exhibit equal tendon mechanical, structural, and histological properties but decreased muscle fiber size compared to male rats.

Methods: *Experimental design and sample preparation:* Achilles tendon-foot complexes from 54 age-matched adult male (n=16), female (n=16), and OVX (6-weeks after OVX) (n=16) Sprague Dawley rats were harvested (IACUC approved). Tendons were then either fixed for histological analysis or frozen until preparation for high-frequency ultrasound (HFUS) analysis and mechanical testing as described [6]. All tendons were randomized to blind a single dissector at time of fine dissection and subsequent testing and analysis. Additionally, gastrocnemius muscle tissue was excised, embedded in optimal cutting temperature (OCT) compound, and flash frozen for histological analysis. *Tendon histology:* Samples (n=8/group) were processed using standard techniques, sectioned sagitally at 7 µm, and stained with hematoxylin & eosin or safranin-o/fast green. Images were graded on a scale of 1-3 by three blinded investigators for cell shape, cellularity, and proteoglycan staining intensity. *Muscle histology:* Samples (n=8/group) were sectioned axially at 10µm, co-stained with DAPI and laminin, imaged, and analyzed for average fiber cross sectional area (CSA) using the SMASH application [7]. *HFUS:* Tendons (n=12/group) were loaded at 1N in a PBS bath while a series of sagittal images were acquired using a 40MHz scanner (Vevo 2100, MS550D; VisualSonics) and analyzed for fiber alignment. *Mechanical testing:* Tendons (n=8/group) were measured for CSA and underwent a ramp to failure at 0.1%/sec. Tendons used for HFUS were subjected to a separate mechanical testing protocol consisting of stress relaxation at 6% strain, a low-load dynamic frequency sweep (ranging from 0.1 to 10 Hz), and fatigue testing at 2 Hz using a sinusoidal waveform (from ~10-40% of ultimate strength) until failure. From these tests, quasi-static mechanical properties (toe and linear modulus, and percent relaxation) and dynamic mechanical properties (modulus, tan(δ), hysteresis, and laxity) were computed. *Statistics:* One-way ANOVAs were used to compare between groups for all assays except tendon histology. Significant relationships were evaluated using post-hoc tests with Bonferroni corrections (α=0.05/3). Kruskal-Wallis tests were used to evaluate differences in tendon histological properties between groups (α=0.05).

Results: *Tendon histology:* There were no differences between groups in cell shape, cellularity, or proteoglycan content (not shown). *Muscle histology:* The average fiber CSA (Fig1A) was significantly increased in male compared to female muscle samples. There were no differences between OVX muscle samples and the other two groups. *HFUS:* Circular standard deviation of the mean fiber orientation (a measure of collagen alignment) did not differ between groups (not shown). *Mechanical testing:* Tendon CSA (Fig1B) and failure load (Fig2A) were significantly greater in male tendons compared to female and OVX tendons. Failure stress (Fig2B) was not different between groups. Percent relaxation (not shown) and hysteresis (Fig2C) were significantly increased in male compared to female and OVX tendons but there were no differences in tan(δ) between groups (not shown). Toe and linear stiffness, as well as transition strain, were not different between groups (not shown). Conversely, toe modulus was significantly decreased in male compared to female tendons and nearly significant compared to OVX tendons (p=0.02) (Fig2D). Similarly, the linear modulus was significantly decreased in male compared to female and OVX tendons. Dynamic modulus (Fig2E) was significantly decreased in male tendons at all frequencies tested and during fatigue testing (not shown), Tendon laxity (Fig2F) was significantly increased in males.

Discussion: Contrary to our hypothesis, sex differences were found in both uninjured Achilles tendon and muscle. Female and OVX tendons exhibited increased moduli (quasi-static and dynamic) compared to male tendons, which suggests that female and OVX tendons have superior material properties. Further, the decreased percent relaxation and hysteresis in female tendons suggest that they may be more efficient at returning stored elastic energy following deformation. Taken together with the decreased muscle fiber size compared to males, these mechanical differences may, in part, explain the apparent decreased susceptibility to tendon rupture that is observed clinically in women despite their lower failure load. Interestingly, there may be a dose-dependent response with respect to estrogen levels for various mechanical and histological properties (e.g., muscle fiber CSA, tendon modulus, laxity), given that mean values for OVX rats generally fall between those of males and females. Further investigation is required to elucidate the mechanism governing the superior mechanical properties observed in female tendons, especially given that several previous studies implicate estrogen as an inhibitor of collagen production [5]. Future work will study the effect of tendon matrix composition and analysis of protein markers for muscle strength and fiber type, and investigate sex differences in the context of tendon healing.

Significance: This study identified inferior tendon mechanical properties and increased muscle fiber size as a potential explanation for the increased susceptibility for Achilles tendon damage observed clinically in men compared to women.

Acknowledgements: This study was supported by NIH/NIAMS (R01AR064216S1), the NIH/NIAMS supported Penn Center for Musculoskeletal Disorders (P30 AR050950), the NIH/NCATS (TL1TR000138), and the NSF GRFP. The authors thank D. Choi and C. Riggin for their contributions.

References: [1] Vosseller JT et al. Foot Ankle Int, 2013. [2] Torricelli P et al. Age (Dordr), 2013. [3] Romani WA et al. Eur J Appl Physiol, 2013. [4] Kobori M et al. Clin Orthop Relat Res, 1989. [5] Bryant AL et al. J Appl Physiol (1985), 2008. [6] Riggin CN et al. J Biomech Eng, 2014. [7] Smith LR et al. Skelet Muscle, 2014.

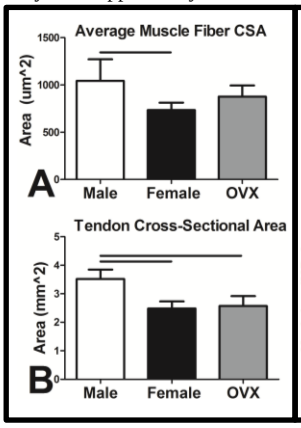

Figure 1 – (A) Achilles muscle fiber area and (B) tendon area were both increased in males. Solid lines indicate significant differences (p<0.017). Data presented as mean and standard deviation.

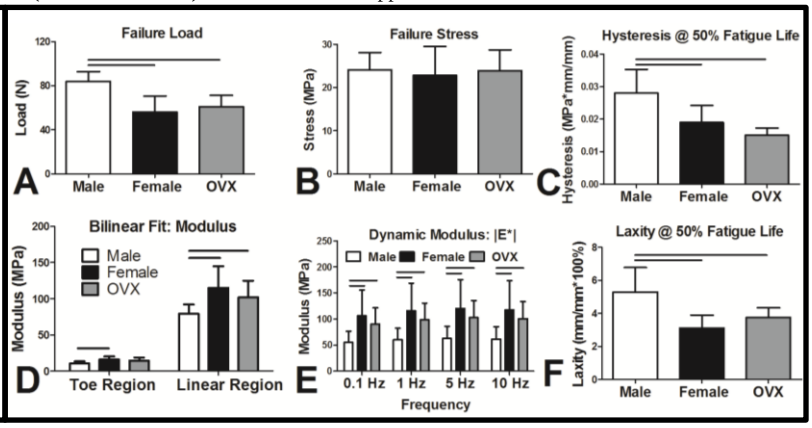

Figure 2 – Achilles tendon mechanical properties. (A) Failure load was increased in males, (B) failure stress was not different between groups, (C) hysteresis was increased in males, (D) toe and linear modulus were both increased in females and OVX, (E) dynamic modulus was increased in females and OVX at 0.1, 1, 5, and 10 Hz, and (F) laxity was increased in males. Solid lines indicate significant differences (p<0.017). Data presented as mean and standard deviation.

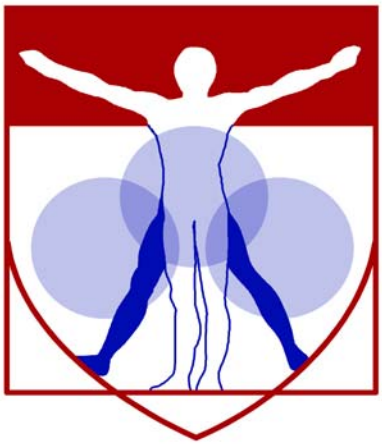

PENN

CENTER for
MUSCULOSKELETAL
DISORDERS

Histology Abstracts

Suppression of Sclerostin Alters and Protects the Fate of Mesenchymal Progenitors to Alleviate the Radiation Induced Osteoporosis

Abhishek Chandra[1], Tiao Lin[1], Tong Wei[1], Tiffany Young[1], Xiaoyuan Ma[1] , Wei-Ju Tseng[1], X. Sherry Liu[1], Keith Cengel[5],Michael Levine[3], and Ling Qin[1]

[1]Departments of Orthopaedic Surgery and [2]Radiation Oncology, Perelman School of Medicine, University of Pennsylvania, Philadelphia, Pennsylvania, USA.[3]Division of Endocrinology and Center for Bone Health Diseases, The Children's Hospital of Philadelphia.

Abstract

Deleterious consequences of clinical radiotherapy on bone architecture are well recognized, but often underscored. We previously reported that regulation by Wnt/β-catenin pathway was essential to overcome the radiation induced DNA damage and apoptosis of the osteolineage cells. Two autosomal recessive genetic diseases associate with high bone mass in humans, Sclerosteosis and van Buchem disease are associated with the depletion of sclerostin gene (SOST-KO). Sclerostin, a negative regulator for bone turnover, also suppresses the Wnt/β-catenin pathway by regulating LRP5/6 receptors. Use of a monoclonal neutralizing antibody against sclerostin (Scl-Ab) completely annulled the effect of radiation on the mouse femur, while femurs of a mouse model with a global deletion of the Sost gene (Sost-KO), were markedly resistant to any scathing attack from radiation. Scl-Ab treatment resulted in a higher bone formation rate, shown by an increased serum osteocalcin, and a reduced resorption rate, shown by serum CTX-I levels. Histomorphometric analysis and TUNEL staining revealed that Scl-Ab reversed the radiation induced reduction of osteoblast and osteocyte numbers, but also negatively regulated the radiation induced adiposity. Utilizing the Col2-cre; R26R-tdTomato reporter, where the cells expressing Col2-cre and their descendants that include cells of different mesenchymal-lineages, were tracked after irradiation. Colony forming assays, progenitor counts in the bone marrow or on the vessel surface and the number of tomato^{+}adipocytes, indicate that Scl-Ab significantly protected mesenchymal progenitor (MP) numbers by blocking their depletion and differentiation into adipocytes. Moreover, radiation induced DNA double strand breaks, as assessed by γH2AX–foci in tomato^{+} osteoblasts, was remarkably reduced by Scl-Ab. Our study provides a mechanistic preview at a cellular level behind the functional protection imparted by Scl-Ab against radiotherapy induced osteoporosis.

Acknowledgement- This work was supported by the National Institute of Health (R01DK095803 to LQ), Penn Center for Musculoskeletal Disorders P30AR050950 (NIAMS/NIH), ASBMR Junior Faculty Osteoporosis Basic Research Award (to LQ) and McCabe Pilot Award (to XSL).

New insights into mouse limb synovial joint morphogenesis using novel cell lineage tracing techniques

Rebekah S. Decker*, Hyo-Bin Um*, Eiki Koyama*, Mark Kronenberg#, Peter Maye#, David Rowe# and Maurizio Pacifici*

*Translational Research Program in Pediatric Orthopaedics, Division of Orthopaedic Surgery, The Children's Hospital of Philadelphia.
#Department of Reconstructive Sciences, University of Connecticut Health Center School of, Dental Medicine

Purpose: There has been great interest in deciphering how the articular cartilage comes to acquire its multiple, distinct zones, including the superficial zone that produces lubricants and contains stem/progenitor cells. We have demonstrated that populations of mesenchymal interzone cells at presumptive limb joint sites give rise to multiple joint tissues. What has remained unknown is whether unique subpopulations of cells exist within the interzone, if these cells selectively participate in development of specific joint tissues, and what roles they may have in postnatal joint phenotype and function. To address these and related questions, we developed and characterized three novel BAC transgenic inducible-Cre mouse lines.

Methods: Female mice from our new Gdf5-Cre*ER-T2, Dkk3CreER-T2 and Prg4CreER-T2* transgenic strains were mated with male ROSA-*tdTomato, ROSA-zsGreen or ROSA-Confetti* reporter mice. Pregnant females received single or multiple injections of tamoxifen at embryonic stages E11.5-E17.5, and offspring were collected at E18.5 or postnatally.

Results: Staged injection of tamoxifen permitted selective labeling of cell populations within developing joints. In one such representative example, *Dkk3CreER-T2; ROSA-tdTomato* mice which received a single tamoxifen injection at E13.5 displayed labeling in the meniscus, synovium, and superficial 3-4 layers of the articular cartilage of the femur at birth. At one month of age, some labeled cells extended throughout all layers of articular cartilage and into the secondary ossification center.

Conclusions: Our data demonstrate the exciting potential of these novel inducible Cre lines for studying spatiotemporal *Gdf-5, Dkk3 and Prg4* activation in developing joints. Though preliminary, these results suggest that sub-populations of progenitor cells emerge within the broadly defined joint interzone, hinting at their diverse joint formation capacity. Lineage tracing has revealed that progeny of these cells participate in postnatal joint morphogenesis, raising the intriguing possibility of their potential role in long-term maintenance and repair of joint tissues.

Epidermal Growth Factor Receptor (EGFR) Signaling in Cartilage Prevents Osteoarthritis Progression

Haoruo Jia[1], Xiaoyuan Ma[1], Basak Doyran[2], Wei Tong[1], Zeyang Sun[1], Xianrong Zhang[3], Motomi Enomoto-Iwamoto[1,4], Lin Han[2], and Ling Qin[1]
[1] Department of Orthopaedic Surgery, School of Medicine, University of Pennsylvania, Philadelphia, Pennsylvania, USA; [2] School of Biomedical Engineering, Science and Health Systems, Drexel University, Philadelphia, Pennsylvania, USA; [3] Department of Physiology, School of Basic Medical Sciences, Wuhan University, Wuhan, China; [4] Department of Surgery, The Children's Hospital of Philadelphia, Pennsylvania, USA

Disclosure: None.

Introduction: Osteoarthritis (OA) is the most common chronic condition of the joints affecting approximately 27 million adults in the United States alone. The consensus is that OA is indeed a disease of mechanics but the molecular mechanism by which normal, healthy articular cartilage maintains its strength to resist mechanical loading and thereby, to prevent OA progression is poorly understood. We recently demonstrated a pivot role of EGFR signaling in growth plate development [1] and endochondral ossification [2], indicating that this is a critical pathway regulating chondrocyte function. To understand the role of EGFR in maintaining articular cartilage and in OA development, we generated cartilage-specific *Egfr* null mice and characterized their knee joint phenotypes under physiological and pathological conditions.

Methods: All animal work was approved by the Institutional Animal Care and Use Committee at the University of Pennsylvania. *Animals and surgery-* Cartilage-specific *Egfr CKO (Col2-Cre Egfr$^{Wa5/f}$)* mice and their *Wa5* (*Egfr$^{Wa5/f}$*) and *wild-type* (*WT*, *Col2-Cre Egfr$^{f/+}$* and *Egfr$^{f/+}$*) siblings were generated by breeding *Col2a1-Cre*, *Egfr$^{Wa5/+}$, and Egfr$^{f/f}$* mice. *Egfr^{Wa5}* codes for a kinase-dead, dominant negative receptor. To induce OA, male mice at 3 months of age were subjected to destabilization of the medial meniscus (DMM) surgery at the right knees and sham surgery at the left knees. *Histology and immunohistochemistry (IHC)-* Mouse knee joints were harvested at indicated times for a serial of 6 μm-thick sagittal sections across the entire medial compartment of the joint for quantification of cartilage thickness, chondrocyte number, subchondral bone plate thickness, and Mankin score, as well as IHC staining for EGFR, phosphorylated-EGFR (p-EGFR), phosphorylated-Erk (p-Erk), osteocalcin, and sclerostin. *μCT-* The distal femurs and proximal tibiae were scanned by μCT 35 (Scanco Medical AG) at a resolution of 6 μm to calculate trabecular bone structural parameters. *Nanoindentation-* Atomic Force Microscopy (AFM)-based nanoindentation was performed on the superficial zone of cartilage using a borosilicate colloidal spherical tip ($R \approx 5$ μm, nominal spring constant $k \approx 7.4$ N/m, AIO-TL tip C) and a Dimension Icon AFM with indentation depth of ~ 1 μm at 1 μm/s and 10 μm/s rates. Effective indentation modulus, E_{ind} (MPa), was calculated from the loading portion of indentation force-depth curves using the Hertz model. *Primary chondrocytes-* Primary epiphyseal chondrocytes were obtained from mouse newborn pups by enzymatic digestions. Cells were cultured in chondrogenic medium (DMEM/F12 medium with 5% fetal bovine serum, 50 μg/ml of L-ascorbic acid, and 1% glutamine). *Statistics-* Data are expressed as means±SEM and analyzed by unpaired, two-tailed Student's t-test.

Results: To delineate the function of cartilage EGFR signaling, qRT-PCR and IHC were first performed with articular cartilage in 2-month-old mice. We observed strong EGFR expression in all mice. p-EGFR and p-Erk were only detected in *WT* and *Wa5* mice but not in *CKO* mice, confirming that *CKO* mice indeed are deficient in EGFR activity in articular cartilage. The most abundant EGFR ligand in cartilage is TGFα, followed by epiregulin and betacellulin. While there was no histological changes in articular cartilage among *WT, Wa5*, and *CKO* mice at this developmental stage (Fig. 1A), cartilage surface E_{ind} was significantly decreased in *Wa5* mice (41.3% of *WT*) and further diminished in *CKO* mice (25.3% of *WT*) (Fig. 1B). Four months later, while the nanomechanical property remained low in *Wa5* and *CKO* mice, *CKO* mice started to show OA symptoms, including partially depleted uncalcified zone, decreased Safarin O staining, and increased chondrocyte hypertrophy (Fig. 1). *Wa5* cartilage had similar alterations but to a much lesser extent. Osteophytes in knee joints were observed in 66.7% of *CKO* mice but never in *WT* or *Wa5*. Primary chondrocyte culture confirmed that activating EGFR stimulates cell proliferation and survival and inhibits their terminal differentiation. DMM was performed in 3-month-old mice to induce OA. Three months later, *WT* developed mild-to-moderate OA (Makin score: 6.0±0.5), *Wa5* exhibited advanced OA (11.5±0.5), and *CKO* had the most severe OA (14.0±0.0) with a complete loss of entire cartilage layer restricted at the medial side (Fig. 2A). Moreover, we observed a local and drastic subchondral bone plate (SBP) thickening (4.5-fold) only under the cartilage damage area (Fig. 2B, C). This was correlated with locally reduced sclerostin amount by osteocytes within SBP (Fig. 3) and increased number of osteoblasts lining SBP surface. Since subchondral and metaphyseal trabecular bone parameters were not altered, we reason that SBP sclerosis was caused by increased mechanical loading and decreased sclerostin amount after cartilage depletion.

Discussion: Our studies clearly demonstrate that chondrogenic EGFR signaling and its cognate ligands, most likely TGFα, is essential for maintaining articular cartilage and is critical for OA development. *Egfr CKO* mice have much weaker articular cartilage and develop spontaneous OA at a much earlier stage compared to *WT*. We also demonstrate that *CKO* mice exhibit much more accelerated OA symptoms in a surgical OA model. The limitation of this study is that articular cartilage of *CKO* mice was already abnormal before surgery. Further investigation using an inducible system (*aggrecan-CreER*) to diminish EGFR activity at the same time of DMM is currently underway to delineate more precisely the role of EGFR in OA development.

Significance: We provide the first direct evidence that chondrogenic EGFR signaling is critical for articular cartilage homeostasis and OA development and that local crosstalk between cartilage and SBP plays an important role in accelerating OA progression.

References: [1] Zhang et al., J Bone Miner Res. 2011, 26(11): 2622-2633. [2] Zhang et al., J Biol Chem. 2013, 288(45): 32229-32240.

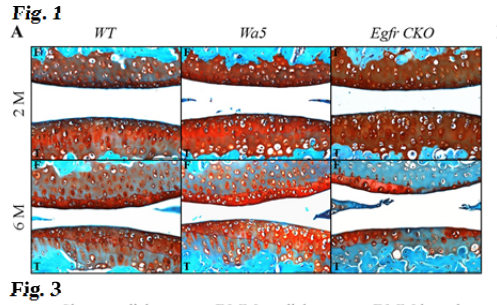

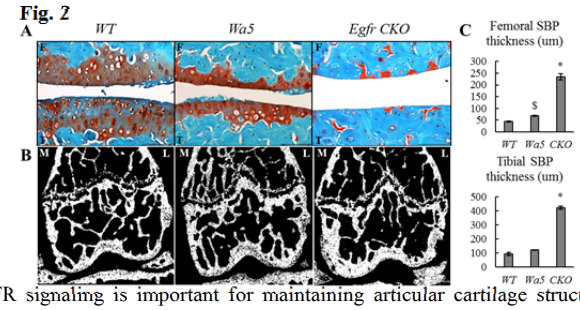

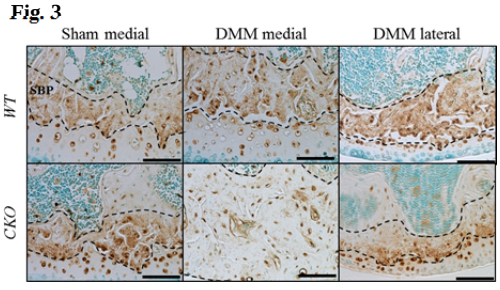

Figure 1. EGFR signaling is important for maintaining articular cartilage structure and mechanical strength. (A) Safranin O staining of knee joints in 2 and 6 month-old mice. F: femur; T: tibia. n=6/genotype/time point. (B) Nanoindentation shows that EGFR deficiency decreases the stiffness of articular cartilage. n=5/genotype/time point. #: $p<0.05$ vs *WT*; $: $p<0.05$ vs *Wa5*.

Figure 2. EGFR chondrogenic deficiency causes severe osteoarthritis after DMM. (A) Safranin O staining of knee joints in mice at 3 months post DMM surgery. (B) μCT images reveal local SBP thickening only at the medial site of *CKO* mouse joint. M: Medial; L: Lateral. (C) Quantification of SBP thickness. n=6/genotype. $: $p<0.01$; *: $p<0.001$ vs *WT*.

Figure 3. Increased bone formation in SBP in *CKO* mice is accompanied by decreased sclerostin amount. Scale = 100um.

Advancing Radial Tie Fiber Quantification in the Knee Meniscus through Second-Harmonic Generation Imaging

Niobra Keah[1,2], Feini Qu[1,2,3], Sonia Bansal[1], Robert L. Mauck[1,2], Miltiadis H. Zgonis[1,2]
[1]McKay Orthopaedic Research Laboratory, University of Pennsylvania, Philadelphia, PA, [2]Translational Musculoskeletal Research Center, Philadelphia VA Medical Center, Philadelphia, PA [3] University of Pennsylvania School of Veterinary Medicine, Philadelphia PA

The menisci are semi-lunar shaped fibrocartilaginous wedges located between the distal femur and the tibial plateau that support the structure and mechanical function of the knee joint. Menisci are primarily composed of circumferentially oriented type I collagen fibers that transfer strain down to the tibial plateau. Interspersed within the extracellular matrix is a smaller population of 'radial tie fibers' (RTFs), which may interact with the circumferential components to help transfer strain [1,2]. With minimal success, a previous study analyzed RTFs using Picrosirius Red stained bovine sections under polarized light [3]. The present study uses second-harmonic generation (SHG) in an attempt to optimize the spatial resolution of RTFs. Due to previous data which show the greatest amount of contact stress centralized in the posterior horn [2], we expect to find a greater density of RTFs in the posterior horn of the meniscus than the anterior and body.

To test our hypothesis, we evaluated RTF density and structure as a function of location (anterior, middle, and posterior horns) and zone (inner, middle, and outer) within the meniscus, which are associated with varying degrees of load bearing. We sectioned a total of twelve juvenile (6 months of age) bovine menisci (6μm thick). We stained six menisci with Picrosirius Red for collagen. We then imaged these samples at 10x magnification under polarized light. We fixed the remaining samples on histological slides and imaged them at 10x magnification using SHG. Two slices from each location in a sample were then evaluated for RTF density using the FIJI software package [4,5,6].

Our findings clearly displayed differences across imaging techniques. For the samples imaged using polarized light, we found a lower density of RTFs in the posterior horn than in the anterior horn and body. In contrast, samples imaged using SHG, showed a greater density of RTFs in the posterior horn than the anterior horns and body. In both polarized light and SHG images, we found a greater density of fibers in the inner zone than the outer zone of the anterior and posterior horns. Lastly, we found that the body contained the lowest average density of RTFs fibers irrespective of zone.

Polarized light imaging has been used in previous research to visualize RTFs [3]; however, we found that this technique was inadequate for drawing quantitative conclusions on RTF architecture. Differences in polarized light and SHG data show that measuring RTF density, which is already highly polarized as a collagenous structure, using pulsed near-infrared lasers produces images with less noise [7]. Thus, SHG allows for a more defined identification of RTFs yielding greater validity and reliability for quantitative analysis. Future work will utilize SHG to explore age differences in RTF structure and distribution.

References: [1] Skaggs+, J Orthop Res 1997. [2] Bedi+, J Bone Joint Burg Am 2010. [3] Xiangkai+, J Orthop Res 2014 [4] Saalfeld, FIJI 2012 [5] Dougherty, FIJI 2006 [6] Schindelin+, Nature Methods 2012. [7] Campagnola+, Nat Biotechnol 2003.

Interstitial Cell Migration in Dense Connective Tissues is Modulated by Matrix Microstructure and Micromechanics

Feini Qu[1,2], Miltiadis H. Zgonis[1], Robert L. Mauck[1,2]

[1]McKay Orthopaedic Research Laboratory, Dept. of Orthopaedic Surgery, University of Pennsylvania, Philadelphia, PA
[2]Translational Musculoskeletal Research Center, Philadelphia VA Medical Center, Philadelphia, PA

Few regenerative approaches exist for the treatment of injuries to adult dense connective tissues. Compared to fetal tissues, these adult connective tissues are hypocellular and show limited endogenous cell-mediated healing after injury. However, it is unknown whether this deficiency in repair is due to the limited cell number itself, by steric constraints to migration imposed by the extracellular matrix (ECM), or by a combination of the two. We hypothesized that robust repair occurs in fetal tissues due to an immature ECM conducive to cell migration and fails in adults due to a dense and stiff ECM that acts as a biophysical impediment. Using the knee meniscus as a test platform, this study evaluated the microstructure and micromechanics of fetal and adult tissues (via atomic force microscopy and second harmonic generation imaging, respectively), with a particular focus on the inter-fibrillar regions through which cells might migrate. Further, we monitored the morphology and interstitial migration of adult meniscal cells through fetal and adult tissue microenvironments. Finally, building from our recent studies showing that local pre-treatment with collagenase improves cellular colonization of the wound interface in the adult meniscus, we measured adult cell migration through a pre-digested adult ECM.

Analysis of fetal and adult meniscus revealed distinct microenvironments. Second harmonic generation (SHG) imaging and atomic force microscopy (AFM) were used to visualize fibrillar collagen and determine the local modulus of tissue cryosections, respectively. Adult ECM (aECM) had thicker and more organized collagen bundles than fetal ECM (fECM), and contained less inter-fibrillar matrix. Further, aECM was approximately 3 times stiffer than fECM. When adult meniscal explants were placed atop fECM and aECM, meniscal cells adhered, spread, and infiltrated into devitalized tissue substrates. Cells on both substrates aligned in the fiber direction of the underlying tissue, although cells on aECM were larger, had a higher aspect ratio, and exhibited lower circularity and solidity compared to cells on fECM. Cells that egressed onto aECM pre-treated with collagenase (aECM-C) were smaller and rounder compared to aECM, better approximating those on fECM. Cells migrating through aECM were visibly more deformed compared to those within fECM and aECM-C, and formed narrow protrusions into the surrounding matrix. Cell infiltration depth was greater for cells on fECM compared to cells on aECM. However, cells on aECM-C migrated to a similar extent as on fECM, with 20% reaching depths of $\geq$25 μm from the surface.

Our findings suggest that cell mobility through dense connective tissues decreases with tissue maturation. Compared to the fetal ECM, adult ECM is denser, stiffer, and more organized, resulting in a physically restrictive microenvironment that limits interstitial cell migration. Meniscal cells on devitalized fetal tissue sections are smaller and more invasive than the same cells on adult tissue, which exhibit enhanced cell spreading on the substrate surface and elongation along the collagen fiber direction. Importantly, infiltration occurred primarily at inter-fibrillar regions, which are more numerous and compliant in immature fetal tissue. In adult tissue, migrating cells must deform through narrow crevices between rigid, aligned collagen bundles, similar to the steric constraints imposed by decreasing pore size in Transwell assays. These age-related, biophysical changes to the microenvironment likely contribute to the dearth of reparative cells at the wound site and subsequent poor repair in the adult meniscus. Recently, we showed that 'reprogramming' the meniscal wound interface with collagenase reduces ECM density and stiffness, increases interfacial cellularity, and facilitates repair. Here, we provide further evidence that expedited migration to the injury site is responsible for this superior healing response. By clarifying the role of local matrix properties in wound repair, these studies may establish new clinical strategies to promote endogenous regeneration of the meniscus and other dense connective tissues.

CCR7 deficiency delays development of early structural degeneration and functional deficits in a murine model of osteoarthritis

Nisha Sambamurthy[1, 2], Vu Nguyen[1, 2], Justin Gan[4], George Dodge[2, 3] Carla R. Scanzello[1, 2, 3]
[1]University of Pennsylvania Perelman School of Medicine, Division of Rheumatology, Philadelphia, PA
[2] Philadelphia Veterans Administration Medical Center, Translational Musculoskeletal Research Center, Philadelphia, PA; [3] University of Pennsylvania Perelman School of Medicine, Department of Orthopedic Surgery, Philadelphia, PA; [4] Rush University Medical Center, Division of Rheumatology, Chicago, IL

Purpose: Synovial inflammation has been associated with progressive loss of articular cartilage and joint pain in osteoarthritis (OA). High throughput analyses have led to the identification of chemokine receptor-7 (CCR7) expression being associated with synovial inflammation and severity of symptoms in patients with meniscal tears or early knee OA (1-3). CCR7, in addition to its well-characterized function in normal leukocyte trafficking, can contribute to chronic inflammation. This study seeks to understand the mechanistic role of CCR7 towards the development and progression of OA-related structural and functional manifestations in a murine model of OA. **Methods:** To confirm expression of CCR7 in human disease, knee synovial biopsies from 14 patients with meniscal tears, 13 patients with advanced OA and 8 asymptomatic organ donors were collected through IRB-approved biorepositories. Immunoperoxidase staining for CCR7 was evaluated by microscopy and automated image analysis. Effects of CCR7 deficiency were investigated *in vivo* using mice lacking expression of CCR7 ($CCR7^{-/-}$), backcrossed onto the C57BL/6 background, obtained from Jackson Laboratory. 10-12 week old male $CCR7^{-/-}$ and C57BL/6 (WT) controls were subjected to the destabilization of the medial meniscus (DMM) surgery. At 6 and 19 weeks post-surgery, groups of 5 mice were sacrificed and knee joints harvested, formalin fixed and paraffin embedded. Cartilage erosion, osteophytosis and synovial hyperplasia were evaluated using published histologic scoring methods (4-7). Changes in spontaneous activity were investigated longitudinally (every 4 weeks, up to 16 weeks) after DMM surgery in the two strains, using the LABORAS® Laboratory animal behavior observation registration and analysis system (Metris B.V., Hoofdorp, The Netherlands). **Results:** Histopathologic analysis at 6 weeks post-DMM surgery indicated significantly reduced cartilage degeneration in CCR7-/- mice (Mean±SEM=1.60±0.81) as compared to their WT controls (5.20±1.07, $p<0.0001$ 1-way ANOVA). These early changes to the cartilage were limited largely to the medial side (WT: 4.60±0.60; CCR7-/-: 0.40±0.40, $p<0.0001$) in comparison to the lateral (WT: 0.60±0.60; CCR7-/-: 1.20±0.74, $p=0.24$). However by 19 weeks post-DMM surgery the CCR7-/- mice displayed similar degrees of cartilage loss throughout the joint (18.75±4.64) as their WT controls (16.22±3.61, $p=0.40$). Analysis of osteophyte size on the medial side indicated that CCR7-/- mice had smaller osteophytes at 6 weeks post-DMM (mean measure (μm) ± SEM= 80.00±21.68 vs. 162.00±21.54 in WT, $p=0.028$), which by 19 weeks became comparable (83.75±35.55) to their WT counterparts (104.44±23.16, $p=0.63$). Synovial hyperplasia (evaluated at the medial femoral and peri-patellar regions) indicated modest increases in synovial lining hyperplasia scores at 6 weeks post-DMM, which were similar in both strains, compared to un-operated controls. At the later stage (19 weeks) we found no marked differences in hyperplasia scores between strains or treatments. Analysis of spontaneous activity indicated significant reduction in time spent climbing in WT post-DMM starting at 4 weeks, and decreases were maximal at 8 weeks post-DMM surgery (46.87% lower than baseline). In contrast, $CCR7^{-/-}$ mice maintained pre-operative climbing activity by 4 weeks post-DMM, and even increased climbing activity by 8 weeks post-DMM (25.64% higher than baseline). At 8 weeks, time spent climbing was significantly reduced in WT DMM mice compared to sham ($p=0.015$) and naïve ($p=0.002$) controls, while differences between DMM-operated, sham and naïve $CCR7^{-/-}$ mice were not significant. Climbing activity returned to baseline levels in both strains of mice by 16 weeks post-DMM surgery. **Conclusions:** The results in this study indicate a role for CCR7 in the early development phase of cartilage and bone abnormalities and altered functional deficits in the murine DMM model of OA. While mild in this model, synovial hyperplasia was not reduced in CCR7 deficient mice. Current efforts are directed at better understanding the differences in inflammatory cell recruitment and activation profiles in both WT and $CCR7^{-/-}$ mice at the early stages of disease development in this model. Further, understanding the role of CCR7 receptor signaling in the initiation of joint pathology can aid in developing better therapeutics to blunt OA progression.

References:
(1) Scanzello et al. *Arthritis & Rheum 2011*
(2) Scanzello et al. *OA & Cartilage 2013*
(3) Nair et al. *OA & Cartilage 2015*
(4) *Bendele AM. J. Musculoskel Neuron Interact 2001*
(5) *Gerwin N et al.,* Osteoarthritis Cartilage 2010
(6) *Glasson SS et al.*, Osteoarthritis Cartilage 2010
(7) *Jackson MT et al*., Arthritis and Rheum 2014

Cranial base defects in a mouse model of Hereditary Multiple Exostoses are associated with ectopic hedgehog signaling

Federica Sgariglia[1], Paul Billings[1], Kevin B. Jones[2], Eiki Koyama[1] and Maurizio Pacifici[1]

Division of Orthopaedic Surgery, The Children's Hospital of Philadelphia, PA 19104, USA[1]; Department of Orthopaedics, Huntsman Cancer Institute, University of Utah, Salt Lake City, UT 84112, USA [2]

Hereditary Multiple Exososte s (HME) is a pediatric autosomal-dominant disorder caused by mutations in the heparan sulfate (HS) synthesizing enzymes EXT1 or EXT2. Thus, HME patients are HS-deficient and characterized by the presence of numerous benign cartilaginous tumors –exostoses- forming next to the growth plates of axial and appendicular skeletal elements, including long bones and ribs. However, exostoses have not been described in the craniofacial skeleton, despite the fact that it contains several endochondral structures. Hence, we focused on the cranial base and in particular its synchondroses. These structures contain dual mirror-image growth plates, responsible for antero-posterior cranial base elongation and are flanked by intracranial and sub-cranial perichondrium. Indeed, several exostosis-like masses formed along the sphenoidal and occipital synchondroses of conditional *Ext1*-deficient mice (*Ext1f/fl;Col2CreER)* injected with tamoxifen at P10. In the mutants, the occipital bone also was deformed, the cranial base was shorter and thinner, and the synchondrosis growth plates exhibited fewer resting and proliferative chondrocytes and an irregular columnar organization. These events were accompanied by deranged expression of typical growth plate chondrocyte markers including *ColII, ColX* and *MMP13* as well as reduced expression of two HS-rich proteoglycans: *Perlecan* and *Syndecan 3*. Using *Ext1*-deficient mice in a *Gli1LacZ* background, we found that altered Ihh signaling in growth plate and perichondrium was associated with exostosis initiation in mutant synchondroses and ribs. In addition, ectopic Ihh signaling was detected in resting chondrocytes in mutant synchondroses and ribs. Surprisingly, PTHrP signaling was found in perichondrium as well as exostosis chondrocytes at early stages present in the top distal layer. In that location, PTHrP may help early exostoses to acquire their mature growth plate-like organization. In sum, our data reveal that the skull is also affected by *Ext1* deficiency and displays large exostosis-like masses whose formation appears to be linked to aberrant HH and PTHrP signaling. In particularly, the establishment of an Ihh-PTHrP axis might be necessary for exostosis formation. We are currently re-examining radiographic skull scans from HME patients to determine whether analogous craniofacial skeletal defects are present.

Contributions of Wnt/β-catenin-responsive cells to articular and growth plate cartilage growth

Yu Usami[1], Aruni T. Gunawardena[1], Eiki Koyama[1], Rebekah S. Decker[1], Maurizio Pacifici[1], Motomi Enomoto-Iwamoto[1]
[1]The Children's Hospital of Philadelphia, Philadelphia, PA

INTRODUCTION: At the end of long bones, the epiphyses contain two specialized types of cartilage: growth plate and articular cartilage. The growth plate is essential for the longitudinal growth of bone, while articular cartilage supports joint function by providing resilience and smooth movement to the joint. It still remains unclear which progenitor cells contribute to articular cartilage and growth plate during long bone development and growth and whether the cells are distinct or not. The Wnt/β-catenin signaling pathway is one of the pivotal pathways for skeletal formation. Both excessive activation and inactivation of Wnt/β-catenin signaling cause deformity of the articular cartilage and growth plate, indicating the importance of spatiotemporal control of Wnt/β-catenin signaling in the cells forming these cartilages. The purpose of this study was to determine location and fate of cells responsive to Wnt/β-catenin signaling in the epiphyses during postnatal growth.

METHODS: All animal experiment procedures were approved by the Institutional Animal Care and Use Committee of the Children's Hospital of Philadelphia. *Mice:* *Axin2CreERT2* mice were mated with *Rosa26-ZsGreen* that harbor Cre-inducible green fluorescence protein (GFP) to generate *Axin2CreERT2;ZsGreen* mice. The similar compound mice have been used to detect Wnt/β-catenin-responsive cells. The *Axin2CreERT2* mouse harbors CreER under the control of *Axin2* promoter that is a target of Wnt/β-catenin signaling. Thus, in the *Axin2CreERT2;ZsGreen* mouse, tamoxifen activates Cre-inducible GFP reporter (ZsGreen) expression in the cells where Wnt/β-catenin signaling is active. *Fate mapping:* The *Axin2CreERT2;ZsGreen* mice (n=3) received an injection of tamoxifen (Tx) into peritoneum at postnatal day (P) 6, P20 or P42 (20 μg/mouse for P6; 200 μg/mouse for P20 and 42) and the mice were euthanized to harvest the knee joints 3, 7, or 14 days after Tx injection. The harvested knee joints were fixed with 4% buffered paraformaldehyde over night (4 °C). After decalcification and processing, 4μm sagittal frozen sections or paraffin sections of the proximal tibia were made.

RESULTS: Three days after Tx injection at P6, we detected GFP-positive cells in three distinct regions of the tibia epiphysis: (1) the border between articular cartilage and growth plate adjacent of the groove of Ranvier (Ranvier's Groove); (2) the posterior and anterior surface areas of articular cartilage and (3) the plateau of articular cartilage. The GFP-labeled cells were expanded from 3 to 14 days after Tx injection with differential patterns among these three regions. The GFP-positive cells adjacent the groove of Ranvier broadly expanded toward growth plate and articular cartilage. In the posterior and anterior surface areas of articular cartilage, the number of GFP-positive cells also increased, but the labeled cells were densely packed in the surface layers. In contrast, the GFP-positive cells in the plateau had become broadly distributed over the entire articular cartilage. To determine whether and where Wnt/β-catenin-responsive cells reside at later stages, we performed short labeling by Tx injection at P20 and P42. GFP-positive cells were mainly detected near the groove of Ranvier and the posterior and anterior surface of articular cartilage at the all time points. In the tibial plateau, a small number of GFP-positive cells were found in the middle zone but not in the superficial layer.

DISCUSSION: The findings in this study indicate that Wnt/β-catenin-responsive cells are located in specific areas in the epiphysis and contribute to growth of articular cartilage and growth plate in distinct spatio-temporal manners. The Wnt-responsive cells were detected in the area near the groove of Ranvier at the all time points examined. It has been shown that experimental or traumatic defects in the groove of Ranvier cause growth disturbance. Furthermore, inactivation of Wnt/β-catenin signaling severely impairs growth plate organization and function. Thus, the Wnt/β-catenin-responsive cell population in this area may exert an important role in supporting growth plate function from an early postnatal stage until adult stages. We have previously reported that transient activation of Wnt/β-catenin signaling increases the thickness of articular cartilage with an increase in number of articular chondrocytes. Our data indicate that Wnt-responsive cells are located in the transitional zone in tibial plateau and the anterior and posterior surface layers of articular cartilage. Thus, these regions would be therapeutic targets for stimulation of articular cartilage repair.

Single Cell Imaging to Probe Early Stem Cell Chondrogenesis in Hydrogels

Sebastián L. Vega, Michelle Kwon, Jason A. Burdick
Department of Bioengineering, University of Pennsylvania, Philadelphia, PA 19104

Introduction: Due to limitations in the natural healing capacity of cartilage and given the increasing incidence of osteoarthritis, there exists a growing demand for cell-based therapies for cartilage repair. Tissue engineering, and particularly those approaches based on autologous mesenchymal stem cells (MSCs), is evolving as a clinically relevant technique to promote cartilage regeneration. Our laboratory recently reported that hydrogels functionalized with an N-cadherin (N-cad) peptide, a key factor in mediating cell-cell interactions during the early stages of chondrogenesis, resulted in an upregulation of genes preceding chondrogenesis within the first 3 days of culture [1]. We hypothesize that the N-cad peptide initiates WNT/β-catenin signaling leading to β-catenin (βcat) shuttling from the cytosol to the nucleus and the subsequent transcription of genes necessary for chondrogenesis [2]. To further probe the role of our N-cad mimetic peptide on βcat signaling, we utilized confocal imaging to determine the nuclear/cytosolic presence of βcat in single MSCs encapsulated in hydrogels with N-cad mimetic peptide (**N-cad**), inactive peptide (**Null**), or a 1:1 mix of N-cad and Null peptides (**50:50**) (**Fig 1a**).

Materials and Methods: *Cell Culture:* Human MSCs expanded to passage 3 in growth media were used from the same donor in all experiments. *Hydrogel Encapsulation:* MSCs (5 million/ml) were photoencapsulated into 1.5% (w/v) methacrylated hyaluronic acid (MeHA) hydrogels with light (365 nm, 2 mW/cm^2, 10 min) in the presence of 0.05% (v/v) photoinitiator (I2959, Ciba). MeHA was functionalized with N-cad mimetic (Ac-HAVDIGGGC) or inactive scramble (Ac-AGVGDHIGC) peptides via Michael-type addition reactions. MSC-laden hydrogels were cultured in chondrogenic media supplemented with 10 ng/ml TGF-β3. *Immunostaining:* Prior to antibody incubation, MSCs were fixed, permeabilized, and blocked with 3% NGS. Primary βcat antibody (abcam, 1:100) was added overnight at 4°C, followed by secondary antibody (life technologies Alexa Fluor 488, 1:200) for 2 h at room temperature. *Imaging and 3-D Reconstructions:* MSC-laden hydrogels were imaged with a 20x objective using a Leica SP8 inverted confocal microscope. Using this setup, xy-plane cross-sections were acquired (thickness ~150 μm, step-size 0.69 μm) and reconstructed using Volocity 3-D Image Analysis Software. *Single cell analysis:* For each cell, the nuclear and cytosolic domains were determined by intensity-based thresholding of DAPI and actin stains, respectively. Volume rendering of the actin channel was used to calculate cell volume (Cell V) and cell shape index (Cell Roundness). To quantify βcat signaling, intensity-based thresholding was used to determine the ratio (βcat Ratio) between the volume of βcat in the nucleus and cytosol normalized to the volumes of the nuclear and cytosolic domains (**Fig 1b**). At least 40 cells were analyzed per group. * denotes statistical significance ($p<0.01$).

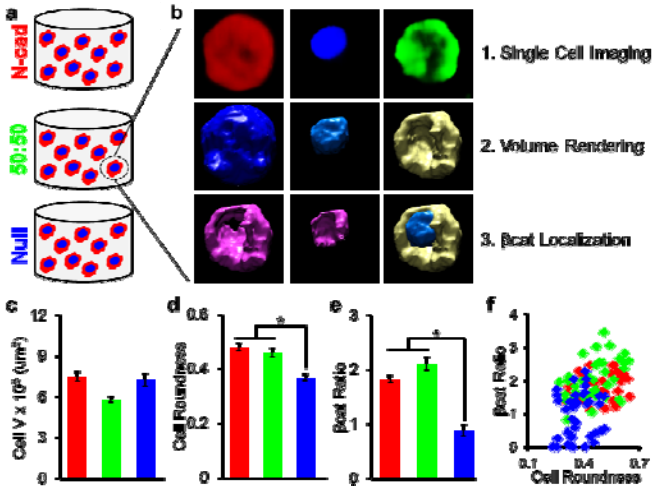

Results: There were no statistical differences in Cell V between the three culture conditions (**Fig 1c**). However, there was an increase in Cell Roundness and βcat Ratio for MSCs cultured in the N-cad and 50:50 groups (**Fig 1d, 1e**). This is particularly interesting because N-cad mediated βcat signaling supports our hypothesis, and mature chondrocytes adopt a round morphology. To ascertain whether there is a relationship between βcat signaling and cell roundness, we plotted βcat Ratio vs. Cell Roundness, and found three distinct populations as well as a positive correlation between both metrics (**Fig 1f**).

Conclusions: This study shows the utility of single cell 3-D imaging-based techniques towards advancing our understanding of N-cad mediated chondrogenesis. Our findings suggest that N-cad mimetic peptides recapitulate microenvironments of early chondrogenesis resulting in an increase of cell roundness and βcat signaling. Current focus is on building upon these findings by investigating the role of N-cad peptides on long-term matrix production.

References: (1) Liming B et al., PNAS, 2013, vol. 110, pp. 10117-10122; (2) Ma B et al., Calcif Tissue Int, 2013, vol. 92, pp. 399-411.

Pathophysiological Role of ADAM8 (A Disintegrin And Metalloproteinase 8) in intervertebral disc degeneration

Yejia Zhang, Miersalijiang Yasen, Robert Mauck, Maurizio Pacifici, Lachlan Smith, D. Greg Anderson, Dessislava Z. Markova, Motomi Enomoto-Iwamoto

INTRODUCTION: Chronic back pain related to intervertebral disc (IVD) degeneration is a significant problem, costing billions in the U.S. alone. Despite the staggering disease burden, there is no current effective treatment to retard IVD degeneration and reduce associated pain because the etiology of IVD degeneration remains unclear. IVD degeneration is characterized by increased extracellular matrix degradation and a variety of cellular responses. ADAM8 (A Disintegrin And Metalloproteinase 8) is a membrane-anchored proteinase and involved in cell-matrix and cell-cell interactions in physiological and pathological processes. Our results lead to the hypothesis that ADAM8 is a key enzyme in the degenerative cascade in IVD tissues and represents a major, novel and potentially far-reaching step ahead in understanding disease etiology.

METHODS: To examine expression and distribution of ADAM8 in IVD, degenerative annulus fibrosus and nucleus pulposus tissues were collected from patients undergoing surgery for back pain with appropriate institutional review board (IRB) approval. Degree of IVD degeneration was determined by MRI (grade V being the most degenerative). Distribution of ADAM8 in the IVD tissues was analyzed by immunostaining. ADAM8 and its specific proteolytic product, fibronectin fragments (FN-f (VRAA271), were quantified by Western blotting (n=3-4 each grade). To examine the role of ADAM8 in IVD degeneration, we performed gain-of-function experiments in mice. Mature human ADAM8 ectodomain was generated in HEK293T cell line (BioZyme, Apex, NC), labeled with the infrared dye (IRDye, Li-Cor Biosciences) and injected into the wild type mouse tail IVD. The ADAM8 or vehicle-injected IVD tissue was harvested 1-4 weeks after injection and subjected to histological inspection and immunostaining with an antibody to VDPIEN (neoepitope of cleaved aggrcan, a generous gift from Dr. J. Mort). We have also performed loss-of-function experiments in mice. The ADAM8 gene-inactivation mutant mice that harbor a point mutation, replacing the Glutamic acid at position 330 with a Glutamine ($ADAM8_{E330Q/E330Q}$ mice, generously provided by Dr. Anne Marie Malfait) was used to examine requirement of ADAM8 for IVD. We dissected IVDs from wild type and the $ADAM8_{E330Q/E330Q}$ mice at 9 months of age and examined the neoepitope of the fibronectin fragment (FN-f) (VRAA271) by Western blotting. Aggrecan cleavage was examined by immunostaining.

RESULTS: Immunostaining demonstrated that ADAM8 was expressed in human IVD tissues. Both ADAM8 and its proteolytic products (fibronectin fragments) were increased with IVD degeneration. These findings establish the clinical significance of ADAM8 in IVD degeneration. We observed that disorganized chondrocyte proliferation in IVDs was much more evident in the ADAM8-injected IVDs than in the PBS-injected IVDs in wild type mice. ADAM8-injected IVDs showed higher immunoreactivity to the antibody against the neoepitope of cleaved aggrecan, compared with the PBS-injected IVDs. These findings suggest that the ADAM8 proteolytic domain stimulates IVD degeneration.

There was no apparent developmental defect in the $ADAM8_{E330Q/E330Q}$ mouse IVD. Fibronectin neoepitope $VRAA_{271}$ resulting from ADAM8 cleavage was not observed in the IVDs of $ADAM8_{E330Q/E330Q}$ mice but was present in wild type control mice, suggesting that ADAM8 is required for production of FN-f (VRAA271). Immunostaining study showed that wild type IVDs contained cleaved aggrecan (the neoepitope VDIPEN) in the nucleus pulposus. Such a phenotype was not detected in the ADAM8 mutant IVDs, indicating that inactivation of ADAM8 function suppresses aggrecan degradation in IVD.

SIGNIFICANCE: The findings outlined above implicate ADAM8 as a critical mediator in IVD degeneration and support our central hypothesis that an excessive increase in ADAM8 proteolytic activity induces fibronectin cleavage and subsequent IVD degeneration, and that inhibition of ADAM8 could represent a therapeutic tool to delay or even halt the degenerative cascade in the IVD.

Alpha 5 Integrin Mediates Osteoarthritic Changes in Mouse Knee Joints

Maria E. Candela[1], Chao Wang[2], Aruni T. Gunawardna[1], Kairui Zhang[1,3], Leslie Cantley[1], Ling Qin[4], Lin Han[2], Motomi Enomoto-Iwamoto[1]
[1]Children's Hospital of Philadelphia, Philadelphia, PA, [2]Drexel University, Philadelphia, PA, United States, [3]Southern Medical University, Guangzhou, China, [4]University of Pennsylvania, Philadelphia, PA

Disclosure: None

INTRODUCTION: Osteoarthritis (OA) is one of the most common skeletal diseases and involves pathological changes in synovial joint components including articular cartilage and synovium. The Importance of articular superficial layer in OA has been of focus since the initial change in OA is irregularity of articular cartilage surface. α5 integrin, a major fibronectin receptor is dominantly expressed in articular cartilage superficial layer and synovium. It has been demonstrated to play roles in synovial joint development and in the regulation of chondrocyte survival and matrix degradation in articular cartilage. Therefore, we hypothesized that α5 integrin signaling is involved in synovial joint development and pathogenesis of OA. To test this, we generated conditional knock out mice lacking α5 integrin expression specifically in synovial joints, cartilage or limb skeletal cells, and analyzed limb development and pathological and biomechanical changes of knee joints after OA surgery.

METHODS: All animal experiment procedures were approved by the Institutional Animal Care and Use Committee of the Children's Hospital of Philadelphia. Transgenic mice: 5 integrin was conditionally knocked out from the synovial joints, cartilage or limb skeletal cells by generation of the compound transgenic mouse, *GDF5Cre;α5fl/-*, *Col2CreER;α5fl/fl or Prrx1-Cre;α5fl/fl* mouse, respectively. Prrx1-Cre;α5fl/fl and α5fl/fl were subjected to radiological and histological inspection at 8-weeks of age. *GDF5Cre;5fl/-* and control *5fl/fl*, or *5fl/-* mice received OA surgery. *Col2CreER;α5fl/fl* or the control mice received tamoxifen injection (100μg/mouse) at P5 and P7 followed by OA surgery. OA surgery: Under anesthesia, we transected the medial collateral ligament in the right knee in both α5 integrin CKO (n=5) and control littermates (n=5-9) at 3-months of age and also removed microsurgically their medial meniscus. Knees were collected and examined by histological and histochemical means 1 month after surgery. Histological evaluation of osteoarthritic changes: The extent of changes in medial tibial plateau and medial femoral condyle of articular cartilage was examined using OARSI scoring systems. The extent of changes in the synovium was examined according to the following scale: 0, normal (synovial lining 1-3 cells thick); 1, mild inflammation (synovial lining 4 or 5 cells thick, increased cellularity); 2, moderate inflammation (synovial lining 6-8 cells thick and/or increase in cellularity); and 3, severe inflammation (synovial lining >9 cells thick and dense cellularity). Nanoindentation: Atomic Force Microscopy (AFM)-based nanoindentation was performed on the surfaces of medial condyle cartilage using a borosilicate colloidal spherical tip ($R \approx 5$ μm, nominal spring constant $k \approx$ 7.4 N/m, AIO-TL tip C, NanoAndMore) and a Dimension Icon AFM (BrukerNano), following previously established procedures [1]. *Statistics:* Student's t-tests or two-way factorial ANOVA followed by Bonferroni post-hoc multiple comparison tests were used to identify the differences. The threshold for significance for all tests was set as $p<0.05$.

RESULTS: The *GDF5Cre;α5fl*/- and *Prrx-1Cre;α5f/f* mice were born normally and had an overall appearance similar to the control mice. Histological analysis of the knee joints of the GDF5Cre;α5fl/- mice did not show significant abnormalities in the structure of synovial joints including articular cartilage. Next we compared the osteoarthritic changes between GDF5Cre;α5fl/- and the control mice after hemisectomy of the medial meniscus in the knee joint. Interestingly, we observed significantly milder histological osteoarthritic changes in the tibial medial plateaus of the α5 CKO (*GDF5Cre;α5fl/-*) mice than those in the control mice, which was evaluated by OARSI score method (Fig. 1A). The α5 CKO articular cartilage in the OA surgery side showed significantly higher effective indentation modulus, *Eind* (in MPa) than the control (p=0.0482, Fig 2). In addition, for the mice without surgery, average of the *Eind* of the α5 CKO articular cartilage was found to be marginally higher than the control (p-0.0563, Fig.2). The α5 CKO group contained a smaller number of TUNEL-positive cells than the control group, while the expression levels of MMP13 were similar between these two groups. In addition, we found significant change in the synovium structure of control mice compared with α5 CKO mice. Histological analysis of control mice knee joint showed hyperplasia of synovium compared to α5 CKO mice (Fig. 1B). Moreover the margin of medial tibia in control mice showed the presence of ectopic cartilage (osteophytes), while α5 CKO mice did not (Fig. 3). When the *Col2CreER;α5fl/fl* mice were subjected to OA surgery after tamoxifen injection (P5), they did not reveal resistance to OA changes compared to the control mice.

DISCUSSION: These findings indicate that α5 integrin may not be essential for synovial joint development, but participates in induction of cell apoptosis and osteoarthritic changes in articular cartilage, and stimulation of synovitis. The difference in the results between the GDF5Cre;α5fl/- mice and the *Col2CreER;α5fl/fl* mice suggest that α5 integrin in synovium but not in articular cartilage triggers OA response. Up-regulation of α5 integrin has been reported in osteoarthritic cartilage in human. Thus α5 integrin can be a therapeutic target for OA treatment.

SIGNIFICANCE: Osteoarthritis is the most common joint disease and causes clinical symptoms including pain and stiffness. The results provide important insights into the mechanisms of early stages in osteoarthritis and will pave the way toward the development of new and effective therapeutic drugs to prevent or ameliorate trauma-induced and aging-related OA.

REFERENCES: [1] Batista et al., *Matrix Biol.* 38, 84-90 (2014).

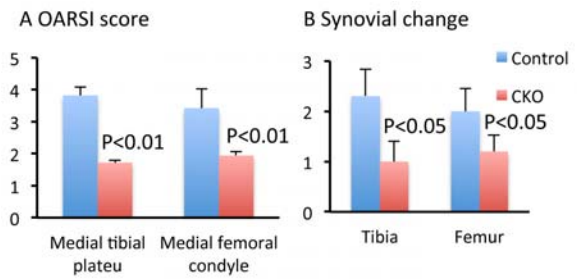

Figure 1. Scoring of OA phenotype in the control and the α5 integrin CKO (*GDF5Cre;α5fl/-*) mice. The osteoarthritic changes in articular cartilage (A) and synovium (B) were significantly milder in the CKO (*GDF5Cre;α5fl/-*) mice compared to those in the control mice.

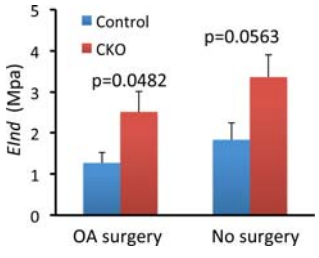

Figure 2. Effective indentation module, *Eind* of the control and α5 CKO (*GDF5Cre;α5fl/-*) articular cartilage at 4 weeks after OA surgery (OA surgery) and without surgery (No surgery). (Student t-test, α=0.05)

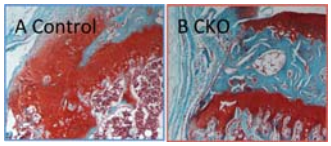

Figure 3. Osteopyte formation in the medial distal tibiae.of the control (A) and α5 CKO (*GDF5Cre;α5fl/-*) (B).

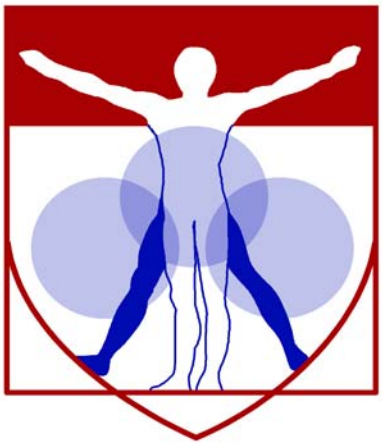

PENN

CENTER for
MUSCULOSKELETAL
DISORDERS

Imaging Abstracts

Low-Magnitude Mechanical Stimulation to Improve Musculoskeletal Deficits in End-Stage Renal Disease Patients

Kelly A. Borges, Chamith S. Rajapakse, Wenli Sun, Elizabeth A. Kobe, Mary B. Leonard, Felix W. Wehrli

Purpose: To investigate musculoskeletal deficiencies in end-stage renal disease and potential of daily exposure to mechanical stimulation as a non-pharmacologic means to improve bone quality in hemodialysis patients.

Materials and Methods: This study was approved by our institutional review board. Informed consent was obtained from all screened participants. Thirty patients on maintenance hemodialysis were randomized to daily 20-min standing on either an active low magnitude mechanical stimulation (LMMS) or a placebo device. Analysis at baseline and completion of the 6-month intervention included DXA (hip and spine bone mineral density (BMD), and fat and lean body mass index), peripheral quantitative CT (tibia trabecular and cortical BMD; lower limb muscle density, muscle and subcutaneous fat cross-sectional area), and MRI (tibia and fibula stiffness, trabecular thickness, bone volume fraction, plate-to-rod ratio, and cortical porosity).
Results: At baseline, significant musculoskeletal deficits were observed in the dialysis patients compared to the reference data. Intention to treat analysis did not show any significant changes in outcomes associated with LMMS, possibly due to variability in adherence (0-100%) across participants. When considering participants with greater than the median adherence (70%) of the active LMMS group, distal tibia stiffness, trabecular density, and plate-to-rod ratio increased 5.3% (p=0.02), 2.3% (p=0.034), and 6.5% (p=0.004), respectively. No significant changes were observed in the placebo group and in non-distal tibia locations for either group.

Conclusion: Daily exposure to LMMS could potentially be used to overcome some of the significant musculoskeletal deficits associated with end-stage renal disease.

Reproduction Differentially Affects Cortical and Trabecular Bone and Alters Cortical Bone Stiffness and Trabecular Structure towards a Male Phenotype

Chantal de Bakker, Youwen Yang, Chih-Chiang Chang, Allison Altman, Wei-Ju Tseng, X. Sherry Liu
Department of Orthopaedic Surgery, University of Pennsylvania, Philadelphia, PA, USA

Introduction: Pregnancy and lactation have been shown to result in significant maternal bone loss, which does not fully recover after weaning [1,2]. However, multiple clinical studies have found that reproductive history has no adverse effects on future osteoporosis risk [3]. As a way to explain this paradox, we hypothesized that prior to the onset of reproduction, females have more bone than needed in order to form a "buffer" for future bone loss that may occur as a result of pregnancy and lactation. We also expected that, since males do not undergo pregnancy and lactation, they do not need this additional "buffer" and should undergo minimal changes in bone structure throughout their adult life. Thus, this study investigated the impact of reproductive history and gender on the structural indices of rodent bone at multiple skeletal sites and at two different ages.

Methods: *6-month rats:* SD rats were divided into 3 groups: Reproductive (n=6), Virgin (n=6), and Male (n=9). Reproductive rats underwent 1 cycle of pregnancy and lactation and were allowed to recover for 6 weeks post-weaning. All rats were euthanized at age 6 months. Tibiae, femurs, and L4 vertebrae were harvested for *ex vivo* µCT scanning and 3-point bending. *15-month rats:* Rats belonged to 3 groups: Reproductive (n=7), Virgin (n=10), and Male (n=9). Reproductive rats underwent 3 repeated cycles of pregnancy, lactation, and weaning, and were euthanized ~3 months after the last weaning date. All rats were sacrificed between age 14-19 months, with an average age of ~15 months. Tibiae, femurs, and L4 vertebrae were harvested for *ex vivo* µCT scanning and 3-point bending. *Mouse study:* C57BL/6J (B6) and CD1 mice were used to assess the species- and strain-dependence of gender differences in bone structure. Male B6 (n=8), Female B6 (n=16), Male CD1 (n=8), and Female CD1 (n=12) mice received *in vivo* µCT scans of the distal femur and L4 vertebra at age 13-14 weeks. *Statistics:* 2-way ANOVA with Bonferroni corrections was used to compare age and group (in rats) and strain and gender (in mice). All animal experiments were approved by IACUC.

Results: Male and Reproductive rats had 47% and 44% lower trabecular bone volume fraction (BV/TV), respectively, than Virgin Females at the proximal tibia ($p<0.05$, Fig 1A). This was due to a reduced trabecular number (Tb.N), which was 48% lower in Males and 35% lower in Reproductive Females relative to Virgins ($p<0.05$).Male rats had 15% greater trabecular thickness (Tb.Th) than Virgin Females, but there was no difference in Tb.Th between Reproductive and Virgin Females. At L4, Male and Reproductive rats had 32% and 26% lower BV/TV, respectively, than Virgin Females ($p<0.05$, Fig 1B). Tb.N at L4 in Male and Reproductive rats was 21% and 18% lower than Virgin females, respectively ($p<0.05$). At both the tibia and L4, BV/TV and Tb.N were lower in 15-month rats than 6-month rats ($p<0.05$), while there was no effect of age on Tb.Th. At the femur midshaft, the polar moment of inertia (pMOI), a measure of bone's resistance to bending, was 146% greater in Male rats than either Female group ($p<0.05$, Fig 2). This was due to increased robustness of the bone, as male rats had 48% greater cortical area (Ct.Area), and 29% greater endosteal, and 40% greater periosteal perimeters than both Female groups. Femur midshaft cortical structure did not change with age in Female rats, but both Ct.Area and pMOI increased between ages 6 and 15 months in Males. 3-point bending indicated a 32% and 50% greater peak load in Male rats than Reproductive and Virgin Females, respectively ($p<0.05$).

Comparisons of trabecular bone between Male and Virgin Female B6 and CD1 mice showed different trends from rats: at the femur, BV/TV was 117% higher in Males than Females, whereas at L4, there was no significant difference based on gender (Fig 3). At both sites, Virgin Females had a lower Tb.N (38% at femur, 21% at L4), with elevated Tb.Th (7% at femur, 9% at L4) relative to Males ($p<0.05$). B6 mice had lower trabecular bone quality than CD1 at both sites ($p<0.05$).

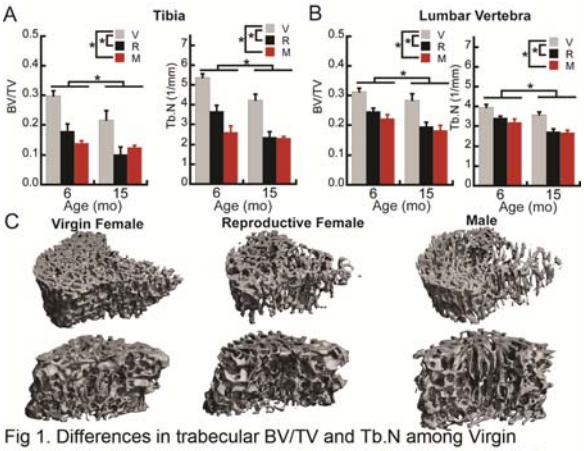

Fig 1. Differences in trabecular BV/TV and Tb.N among Virgin Female (V), Reproductive Female (R), and Male (M) rats at (A) the tibia, and (B) L4. *:$p<0.05$. (C) Representative renderings of trabecular bone at the tibia (top) and vertebra (bottom) of each group.

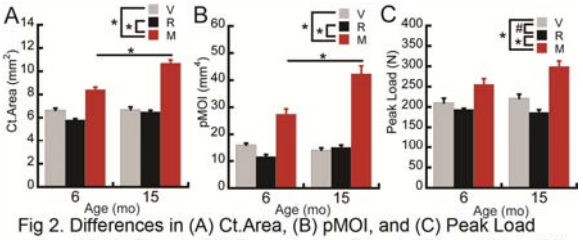

Fig 2. Differences in (A) Ct.Area, (B) pMOI, and (C) Peak Load among Virgin Female (V), Reproductive Female (R), and Male (M) rats. *: $p<0.05$, #: $p<0.1$.

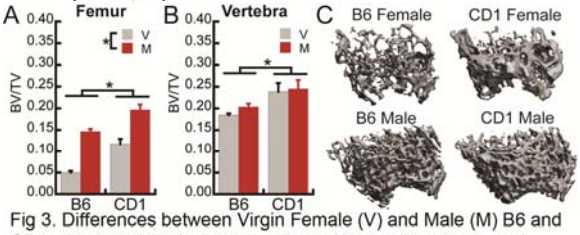

Fig 3. Differences between Virgin Female (V) and Male (M) B6 and CD1 mice in trabecular bone quality at (A) the distal femur and (B) the L4 vertebra. (C) Representative 3-D renderings of trabecular bone at the femur.

Discussion: Comparison between Male and Virgin Female rats indicates that Males have lower trabecular bone volume and inferior microarchitecture relative to Virgin Females at both the tibia and lumbar vertebra. This was similar to baseline differences between male and female rats found in loading studies [4]. However, the trabecular phenotype was highly similar between Males and Reproductive Females, indicating that gender-based differences in trabecular bone were abolished following female reproduction. Because the female skeleton serves as an important source of calcium for infant skeletal development/growth, these results suggest that the female skeleton may initially contain more trabecular bone than needed in order to ensure that an adequate trabecular structure remains after reproduction. In contrast to trabecular bone, the structural and mechanical properties of Male rat cortical bone at the femur midshaft were superior to those of both Virgin and Reproductive Females, due to Male rats' larger size. On the other hand, when comparing trabecular morphometry between Male and Virgin Female mice, the trends were opposite to those of rats, as Female mice showed inferior trabecular microarchitecture to Males. Previous findings have been highly strain-dependent: a study of B6 mice found similar results, whereas a study of BALB/c mice generally found greater trabecular volume in females [5,6]. The precise reason behind this variation is not fully understood and requires further investigation. The variance between gender difference in rats and mice also highlighted the importance of accounting for the effects of gender, reproductive history, species, and strain in bone research.

Significance: Clinical studies indicate no adverse effects of parity on future fracture risk, but the precise impact of the long-lasting, reproduction-associated changes in maternal bone is not fully understood. This study suggests that the female skeleton may initially contain excess trabecular bone to compensate for reproductive bone loss. Additionally, this study highlights the importance of accounting for effects of gender and reproductive history in bone research.

References: [1] Liu XS et al., *J Bone Miner Res.*, 2012; [2] Bowman BM and Miller SC, *Bone*, 1999; [3] Kovacs CS and Ralston SH., *Osteporos Int*, 2015; [4] Hefferan TE et al., *J Appl Physiol.*, 2003; [5]Glatt V et al., *J Bone Miner Res.*, 2007; [6] Willinghamm MD et al., *Calcif Tissue Int.*, 2010.

Acknowledgements: Funding: NIH/NIAMS P30AR050950, NIH/NIAMS R03-AR065145, NSF Graduate Student Research Fellowship.

Recapitulation of the Spectrum of Intervertebral Disc Degeneration in a Large Animal Model

Sarah E. Gullbrand,[1,2] Neil R. Malhotra,[1] Thomas P. Schaer,[1] Zosia Zawacki,[1] Andrew H. Milby,[1]
George R. Dodge,[1,2] Edward J. Vresilovic,[3] Dawn M. Elliott,[4] Robert L. Mauck,[1,2] Lachlan J. Smith,[1,2]
[1]University of Pennsylvania, Philadelphia, PA; [2]Philadelphia VA Medical Center, Philadelphia, PA
[3]Pennsylvania State University, Hershey, PA; [4]University of Delaware, Newark, DE

Disclosures: None

Introduction: Intervertebral disc degeneration is a progressive cascade that leads to structural and mechanical failure, and is frequently associated with low back pain. Patients present in a variety of degenerative states, classically defined by the Pfirrmann grading system based on qualitative interpretation of MRI imaging.[1] Current treatments focused on alleviating the symptoms of discogenic pain are limited as they do not restore disc mechanics or structure. As a result, there is considerable interest in developing biologic regenerative therapies to treat disc degeneration. For these therapies to be successful they must be tailored to the degenerative state of each disc. For example, they may include injection of stem cells, hydrogels or growth factors for mild to moderately degenerated discs, or engineered total disc replacements for severely degenerated discs.[2, 3] A critical aspect of evaluating and translating these regenerative approaches into clinical use is a size-relevant large animal model that recapitulates the spectrum of degeneration seen in humans. The objective of this study was to establish a goat model of intervertebral disc degeneration in which a gradient of degenerative changes, from mild to severe, could be reproducibly achieved, through mechanical (nucleotomy) or chemical (chemonucleolysis) perturbation.

Methods: With IACUC approval, 9 goats underwent a surgical procedure to induce degeneration of the lumbar intervertebral discs. Using an open, lateral, retroperitoneal transpsoatic approach, L1-2, L2-3 and L3-4 lumbar discs were randomized to receive either subtotal nucleotomy (n=5) or injection of 200µL of either 0.1U, 1U or 5U chondroitinase-ABC (ChABC) via a 22G spinal needle (n=5 per dose). The L4-L5 (n=5) disc received a sham saline injection, and the T13-L1 and L5-L6 discs served as intact controls. Lateral plain radiographs of the lumbar spine were obtained pre-operatively, immediately post-operatively, and at 1, 2, 4, 6, 8, 10 and 12 weeks post-operatively for quantification of disc height index (DHI). After 12 weeks, the animals were euthanized, and the lumbar spines harvested and imaged using a 3T MRI scanner. Images for quantitative T1ρ and T2 mapping[4] were obtained, as well as T2 weighted images for Pfirrmann grading. Correlations between quantitative MRI parameters and Pfirrmann grade were established by linear regression. Individual motion segments were then imaged using high resolution µCT to visualize and quantify morphologic changes to the vertebral bony endplate. Alcian blue (glycosaminoglycans) and picrosirius red (collagen) stained, mid-sagittal, paraffin processed sections were used to visualize degenerative changes. For quantitative outcome measures, statistically significant differences ($p<0.05$) were established via one or two-way ANOVAs with Bonferroni post-hoc tests.

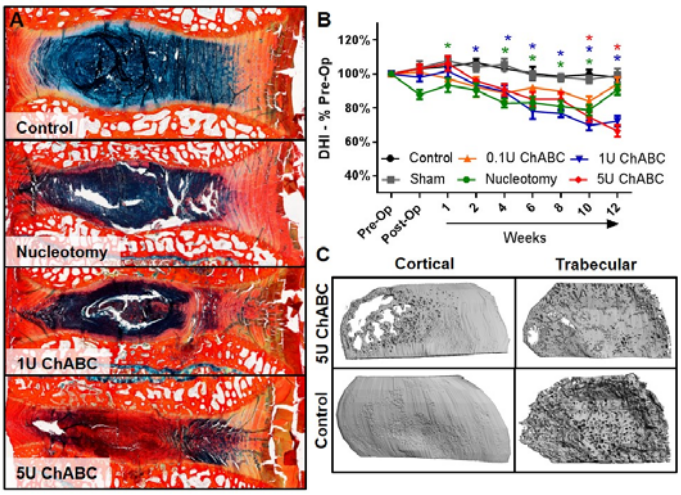

Figure 1. Nucleotomy and ChABC injection in the goat intervertebral disc precipitate a gradient of degenerative changes demonstrated by Alcian blue and picrosirius red stained histology (A), disc height index (*=$p<0.05$ compared to sham) (B) and (C) µCT of the vertebral boney endplate.

Results: Histological evaluation (Fig 1A) revealed advanced degenerative changes to the disc in the 5U ChABC group, with moderate changes in the nucleotomy and 1U groups. Discs injected with 1U or 5U of ChABC exhibited a progressive decrease in DHI, with 28% and 34% reductions in DHI in the 1U and 5U groups, respectively, after 12 weeks ($p<0.05$). Compared to the sham group, DHI was also significantly reduced in the 5U group at 10 weeks, and in the 1U group at 2, 4, 6, 8, and 10 weeks ($p<0.05$). Discs subjected to nucleotomy or injection of 0.1U ChABC also exhibited an initial decrease in DHI (significant at 1, 4, 6, 8 and 10 weeks), however, recovery of disc height to near pre-operative values was observed at 12 weeks in both groups (Fig 1B). DHI for control and sham injected discs was unchanged over 12 weeks. 3D µCT analysis (Fig 1C) demonstrated substantial cortical bone loss in the vertebral endplate of the 1U and 5U groups, and increased bone mineral density and trabecular thickness in the adjacent trabecular bone. T1ρ and T2 values in the nucleus pulposus (NP) were significantly lower in the 1U and 5U groups compared to sham and control discs (Fig 2A and B). NP T2 values were significantly lower in the nucleotomy group compared to sham. Alterations in T1ρ and T2 values correlated significantly ($r^2=0.63$ and $r^2=0.53$, respectively) with the significant increase in Pfirrmann grade from control (Fig 2C and D).

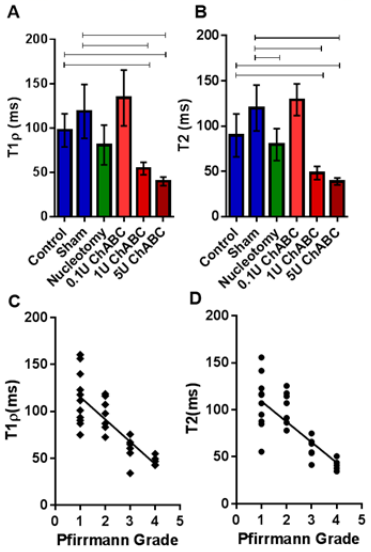

Figure 2. NP T1ρ (A) and T2 (B) were significantly lower in nucleotomy, 1U and 5U ChABC groups. Bars denote significance ($p<0.05$). NP T1ρ (C) and T2 (D) were significantly correlated with Pfirrmann grade ($p<0.05$).

Discussion: A large animal goat model of disc degeneration was established that presents with a gradient of degenerative changes, from mild to severe. This work advances previous caprine animal models of degeneration, which have achieved mainly mild degenerative changes.[3] Observed changes to both the disc and the bone in the adjacent vertebral endplate were consistent with the changes reported in human disc degeneration.[5,6] Over the 12 week study, nucleotomy and injection of low dose (0.1U) ChABC induced mild to moderate degenerative changes to the disc, as seen via disc height changes, quantitative MRI, and histology. Injection of higher doses (1U and 5U) ChABC induced moderate to severe disc degeneration.

Significance: In this study, we established a large animal model that replicates the spectrum of disc degeneration seen in humans and provides the basis for future studies of the biological pathways underlying disease progression. Moreover, this model can be used in the future to evaluate the therapeutic potential and safety of novel biological therapies designed to treat disc degeneration at a variety of stages.

References: [1]Pfirrmann+2001, [2]Sakai+2015, [3]Mizuno+2006, [4]Martin+2015, [4]Hoogendoorn+2008, [5]Rutges+2011, [6]Haefeli+2006

Acknowledgments: This work was supported by the Department of Veterans' Affairs.

Correlations Between Quantitative T2 and T1ρ MRI Parameters and Mechanics and Biochemical Content in a Rabbit Intervertebral Disc Degeneration Model

Sarah E. Gullbrand,[1,2] Beth G. Ashinsky,[1] John T. Martin,[1,2] Stephen Pickup,[1] Lachlan J. Smith,[1,2] Robert L. Mauck,[1,2] Harvey E. Smith[1,2]
[1]University of Pennsylvania, Philadelphia, PA [2]PhiladelphiaVA Medical Center, Philadelphia, PA

Disclosures: None

Introduction: For patients with low back pain, the diagnosis of degenerative changes to the intervertebral disc is largely limited to plain radiographs and qualitative assessment of magnetic resonance imaging (MRI). Improved diagnostic measures are necessary to enable early detection and treatment of disc degeneration. Quantitative MRI, such as T1ρ and T2 mapping, are thought to be sensitive to proteoglycan and water content, respectively, in cartilaginous tissues[1] and as such, may serve as powerful non-invasive diagnostic techniques to evaluate compositional and functional changes to the disc. The aim of this study was to correlate changes in mechanical and biochemical properties with MRI parameters in rabbit discs using an *in vitro* chymopapain digestion model.

Methods: Rabbit lumbar spinal motion segments without posterior elements were injected with 100 µL of saline (control, n=2) or chymopapain at 3 U/mL (n=4), 15 U/mL (n=4) or 100 U/mL (n=3) with a 27G needle. After injection, specimens were wrapped in saline-soaked gauze and maintained at room temperature overnight. T2 (TE=i*8.2 ms, i=1,2…16) and T1ρ (Spin Lock Time=i*10 ms, i=1,2…6) MRI sequences were obtained for each specimen at 4.7T using a custom coil.[2] Specimens were mechanically tested in tension-compression (20 cycles, +21N to -42N)[3], with displacement measured by optical tracking. The 20th cycle was fit to a sigmoid function to obtain the neutral zone (NZ) modulus, NZ range of motion (ROM), compressive modulus, compressive ROM, and total ROM.[4] The nucleus pulposus (NP) was manually removed, and water and GAG contents were quantified and normalized to total NP volume. Alcian blue (glycosaminoglycans) and picrosirius red (collagen) stained histological sections were used to visualize the effects of chymopapain digestion. Differences in quantitative outcome measures were established via one-way ANOVA with Bonferroni post-hoc tests ($p<0.05$). Univariate regressions were calculated for all combinations of measured variables in R (https://www.r-project.org/). A stepwise multiple linear regression was also performed to determine which mechanical and biochemical parameters contributed most to changes in NP T2 and T1ρ.

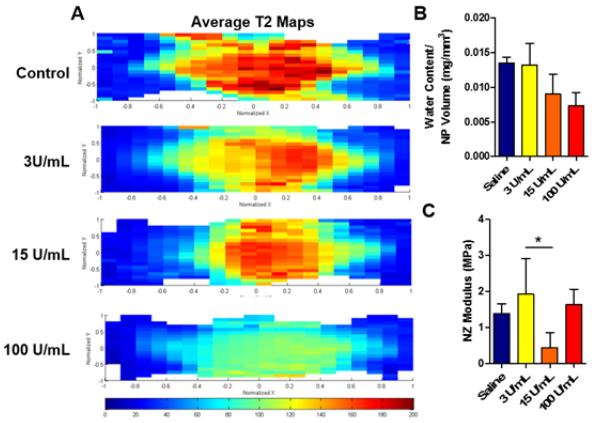

Figure 1. Average T2 (A) and water content (B) in the NP decreased with increasing chymopapain dosage. NZ modulus (C) significantly decreased in the 15 U/mL group compared to the 3 U/mL group.

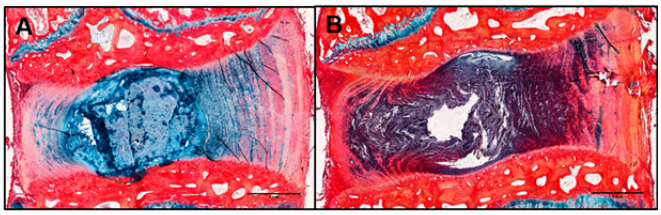

Figure 2. Alcian blue and picrosirius red stained histology sections of control disc (A) and a disc from the 3 U/mL group with the lowest NP T2 (B).

Results: NP T2 and T1ρ values decreased with increasing dose of chymopapain (Fig 1A). NZ modulus (Fig 1B) was significantly reduced in the 15 U/mL group compared to the 3 U/mL group. There was a trend toward reduced water content (Fig 1B) in the NP with increasing chymopapain dose ($p<0.1$). Histology (Fig 2) confirmed the loss of proteoglycans in the NP following chymopapain digest. Univariate regressions (Fig 3) indicated that NP T2 significantly correlated with NP water content ($r^2 = 0.74$), but only weakly to mechanical properties. T1ρ did not correlate to biochemical properties, but did correlate to NZ modulus ($r^2=0.52$). All mechanical properties were significantly and strongly correlated with one another. The stepwise multiple linear regression yielded a model with water content and NZ ROM as variables significantly impacting T2 (multiple r^2 = 0.61). Stepwise multiple regression did not identify variables other than NZ modulus that significantly contributed to T1ρ.

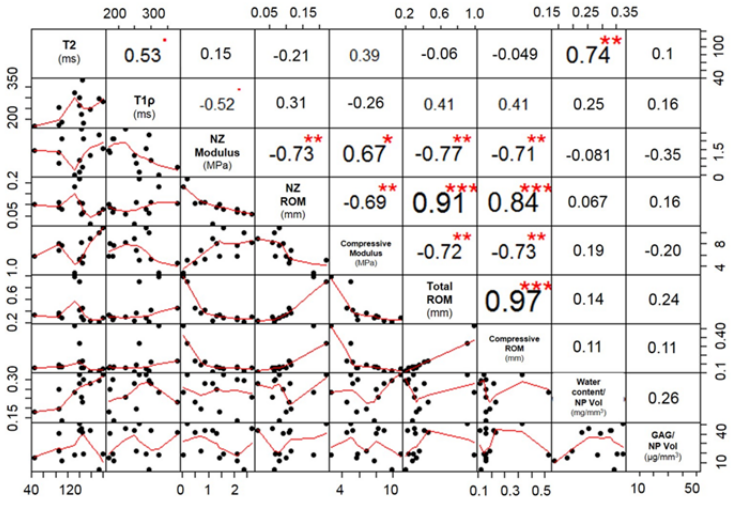

Figure 3. Univariate correlations (scatter plots below diagonal, r^2 values above diagonal) for all variables illustrate that T2 and T1ρ were most strongly correlated with water content and NZ modulus, respectively.

Discussion: These results indicate that quantitative MRI can detect changes in the mechanical and biochemical properties of the degenerating rabbit disc. This work builds on previous studies which have investigated the relationship between T2 and local disc tissue mechanics and T1ρ and biochemical content.[5,6] NP water and GAG content decreased with increasing dose of chymopapain, and the disc modulus was reduced and ROM increased for doses up to 15 U/mL. However, the opposite trend was observed in the 100 U/mL group, likely due to loss of NP pressure and an increased share of compressive loads supported by the annulus fibrosus. The quantitative T2 and T1ρ MRI parameters are sensitive to different aspects of disc composition and function – T2 was correlated with water content and NZ ROM, while T1ρ signal was most sensitive to NZ modulus.

Significance: Quantitative MRI techniques may offer a non-invasive methodology to evaluate functional and compositional changes to the intervertebral disc in both animal models of disc degeneration and regeneration and in human patients with low back pain.

References: [1]Li+2011, [2]Martin+2015,[4]Beckstein+2008, [4]Martin+2013 [5]Johannessen+ 2006, [6]Antoniou+2013

Acknowledgments: This work was supported by the Department of Veterans' Affairs (IK2 RX001476) and the Penn Center for Musculoskeletal Disorders (P30 AR050950).

Bone Deficits in Chronic Kidney Disease and the Effect of Renal Transplantation on Mechanical Competence

Elizabeth Kobe, C. S. Rajapakse, W. Sun, Michelle Slinger, Rhiannon Miller, Benjamin Newman, M. B. Leonard, and F. W. Wehrli

Abnormal vitamin D and mineral metabolism are a universal complication of advanced chronic kidney disease (CKD). Secondary hyperparathyroidism results in abnormal trabecular microarchitecture and cortical thinning. Renal transplantation (RTxp) corrects many of the risk factors for bone deficits; however, glucocorticoid therapy and persistently elevated PTH levels may further compromise strength. The objective of this study was to use MRI-based finite-element analysis to asses bone mechanical competence at the time of RTxp, compared with controls, and to examine changes after RTxp.

Sixty RTxp recipients (52% male, 32% preemptive), ages 20-60 years, were enrolled at transplantation and compared with 104 healthy controls (49% male), ages 19-60 years. MRI of the distal tibia was performed on a 1.5 Tesla scanner (Siemens Tim Trio, Erlangen, Germany) using a 2-channel surface coil at 0.137 mm x 0.137 mm x 0.410 mm voxel size. Trabecular bone parameters and stiffness of the whole section were computed on the basis of these images using digital topological and finite element analysis, respectively.

Within controls, bone volume fraction (BV/TV) was inversely associated with age ($p=0.001$) and greater in males ($p<0.001$). At baseline, Rtxp recipients had lower BV/TV, Tb.N, higher Tb.Sp, and lower stiffness, adjusted for age and sex ($p < 0.05$) (Figure 1). In CKD patients, from baseline to 6 months following renal transplantation, stiffness significantly decreased by 3% ($p=0.01$). During 6-12 and 12-24 months, stiffness increased by 4% and 1%, respectively, however these changes were not statistically significant.

Further analysis is needed to determine if trabecular and cortical bone compartments are differentially affected by CKD and renal transplantation.

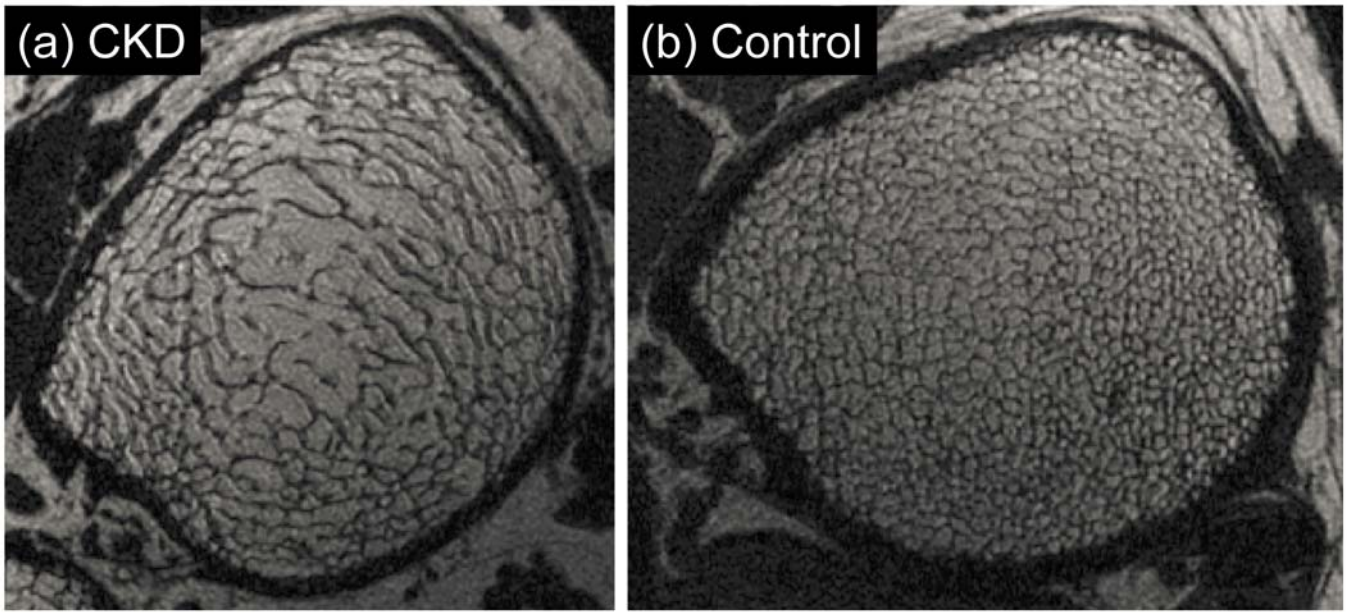

Figure 1: (a) Baseline MR image of the distal tibia metaphysis obtained from a 26-year old Caucasian female CKD patient and (b) a healthy control subject with the same age, race, and sex. Compared to the control, the CKD patient shows decreased Tb.N, increased Tb.Sp, and thinned cortex, which contribute to decreased stiffness, consistent with the overall baseline results from the study.

Effect of IL15Rα ablation on bone structural integrity.

Emanuele Loro, Manoj K. Mishra, Tejivir S. Khurana
Department of Physiology, Pennsylvania Muscle Institute, University of Pennsylvania School of Medicine, Philadelphia, PA, USA

Interleukin-15 (IL-15) and its primary binding partner IL-15 receptor α (IL-15Rα) are pro-inflammatory cytokines expressed in a wide variety of tissues and cell types. They also act as myokines secreted from muscle into the systemic circulation as IL-15/IL-15Rα complex in response to exercise. We and others have established a role for these molecules as determinants of muscle energy metabolism and contractile properties. Overexpression of muscle IL-15 and knockout of IL-15Rα share common positive effects on exercise capacity and resistance to diet-induced obesity. In addition, IL-15Rα knockout mice (IL-15Rα$^{-/-}$) have increased spontaneous activity and fatigue-resistant muscles. IL-15Rα gene SNPs have been associated with predictors of metabolic syndrome, endurance performance in elite athletes, and interestingly, with bone volume.

Contrasting reports exist in the literature on the effects of IL-15 on bone. Mice overexpressing muscle IL-15 have increased bone mineral content. On the other hand, IL-15 administration can stimulate osteoblast apoptosis in a dose-dependent manner, exerting deleterious effects on bone similar to those found in rheumatoid arthritis or periodontal disease.

This ongoing study aims to provide a better understanding of how systemic loss of IL-15Rα affects bone. To test these effects, we measured structural parameters in femurs from 13 weeks old control and IL-15Rα$^{-/-}$ mice under normal feeding and in-cage activity conditions at the PCMD biomechanical and imaging cores. Significant alterations were noted in a number of bone integrity indices. These included reduced femur flexural rigidity (1415 *vs* 1693 N-mm^2) and modulus (4.02 *vs* 4.57 GPa), as assessed by 3-point bending assays. Additionally, significant changes were noted by micro CT as tabulated below.

Bone	***Parameter***	***Control***	***IL15Rα$^{-/-}$***	***Unit***	***P***
Femur - Trabecular	Trab_Thickness (Tb.Th.)	0.045±0.002	0.040±0.002	mm	*
	Trab_Degree Anisotropy (DA)	1.410±0.055	1.557±0.048		*
	Degree Anisotropy_H2	0.252±0.009	0.286±0.008		*
	Bone surface (BS)	26.42±1.232	23.11±0.666	mm^2	*
	Bone surface/Bone volume	62.12±3.095	70.38±2.659	mm^2/mm^3	*
Femur – Midshaft	TMD	1200±4.046	1158±4.013	mg HA/cm^3	**

To test the effects of acute loss of IL-15Rα in cultured osteoblast in vitro, we have developed and are validating inducible shRNA vectors and CRISPR-based targeting constructs.

We believe that our studies will help further our understanding of the role of IL-15Rα on bone structure and function.

We acknowledge and thank the NIH/NIAMS supported Penn Center for Musculoskeletal Disorders (AR050950).

A Biphasic Tissue Engineered Osteochondral Construct Combining a Scaffold-free Cartilage Tissue Analog and a Woven PCL Scaffold: Feasibility in a Porcine Defect Model

George R. Dodge[1,2,3], Christian Pfeifer[1,2], Matthew B. Fisher[1,2], Gregory R. Meloni[1,2,3], Franklin T. Moutos[3,4], Patrick Diviney[1,2], Ryan A. Cocca[1], Robert L. Mauck[1,2,3], and Farshid Guilak[3,4]
[1]McKay Orthopaedic Research Laboratory, University of Pennsylvania, Philadelphia, PA, USA; [2]Translational Musculoskeletal Research Center, Philadelphia VA Medical Center, Philadelphia, PA, USA; [3]Collaborative Research Partner, Acute Cartilage Injury Program, AO Foundation, Davos, Switzerland; [4]Department of Orthopaedic Surgery, Duke University, Durham, NC, USA

Disclosures: FTM; GRD (none); CP (none); MBF (none); RLM (none); GRM (none); PD (none); RC (none); FG (Cytex Therapeutics, Inc.)

INTRODUCTION: Focal articular defects can lead to progressive cartilage degeneration and eventually osteoarthritis, which decreases joint function and quality of life. Surgical interventions, including microfracture, osteochondral transfer, and autologous chondrocyte implantation have been widely adopted in the clinic as a reparative strategy for the treatment of such defects. However, each of these methods has limitations, and so development of additional therapies will be important to advance functional repair. Tissue engineered and scaffold-based therapies have emerged as leading candidates for cartilage repair. This study developed a biphasic engineered osteochondral unit consisting of a scaffold-free cartilage tissue analog (CTA) atop a 3D woven poly(ε-caprolactone) (PCL) scaffold, and evaluated feasibility of cell delivery and biocompatibility of this construct in a large animal model of osteochondral repair.
METHODS: Utilizing an osteochondral defect model developed in our laboratory [1], surgical implantation was performed bilaterally using two, 6-month old, male juvenile Yucatan minipigs with IACUC approval. Initial *in vitro* experiments were carried out to determine the compatibility of chondrocytes with the PCL scaffold by seeding isolated porcine chondrocytes onto the PCL scaffolds and culturing them for 4 weeks. Confocal microscopy was performed to determine the extent to which the chondrocytes interacted with the PCL scaffold. In the surgical model, a 4mm biopsy punch was used to bilaterally create four defects per joint, each of which was either left empty as a negative control or replaced with a CTA generated in a specialized suspension culture model [2], a woven PCL scaffold alone (thickness of 0.75 mm) [3], or a biphasic construct consisting of a CTA and PCL scaffold that had been precultured together (Figure 1). To create CTAs, chondrocytes were incubated with cell-tracker red, seeded at high density (10^7 cells/well) in poly-HEMA coated 24-well plate (Costar, Corning), and cultured for 4 days to allow for self-aggregation. A PCL scaffold was then placed on top of the 4-day old CTA and both CTA controls and biphasic CTA/PCL constructs were cultured for an additional 3 months prior to implantation. A 4mm biopsy punch was used to trim the CTA and CTA/PCL construct prior to implantation. Constructs were press fit into prepared defects. Pigs were sacrificed after two and six weeks and gross morphology was assessed. Osteochondral segments were also harvested and imaged by confocal microscopy to visualize implanted cells. Next, microCT with contrast (Lugol's solution) and histological assessment (Alcian blue and Masson's trichrome staining) was performed to evaluate repair.

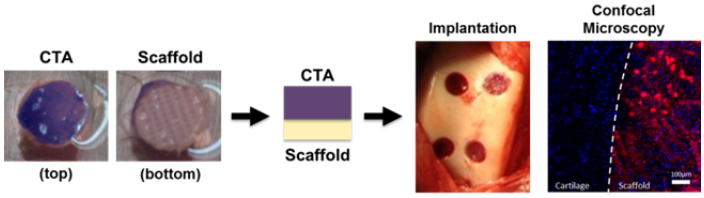

Figure 1. Schematic of our unique biphasic construct precultured *in vitro* and implanted *in vivo*. The CTA was impregnated with cell-tracker red to determine cell compatibility *in vivo*. After termination, the biphasic constructs were counterstained with Hoechst and imaged.

RESULTS: Confocal microscopy of the CTA and seeded chondrocyte CTA/PCL scaffold confirmed that chondrocytes infiltrated into the PCL scaffold and were clearly identified within the first 100 microns of the scaffold surface (Figure 1). In the animal model, gross appearance showed the presence of the scaffold with CTA, which was identified by tracker dye at two and six weeks (Figure 1). Gross imaging at the time of termination showed some degree of fill in all groups. MicroCT with contrast confirmed the successful placement and retention of the PCL scaffold at the defect site (Figure 2, right) and showed an increase in boney remodeling after six week *in vivo* (Figure 2, bottom), consistent with this defect model. MicroCT (Figure 2) and histology (Figure 3) showed increased articular surface congruity with scaffold placement. Both CTA and PCL scaffolds increased subchondral remodeling, while the empty defect appeared to have an attenuated remodeling response. The scaffold was intact after six weeks *in vivo*, with the fibers evident via microCT and histological assessment.

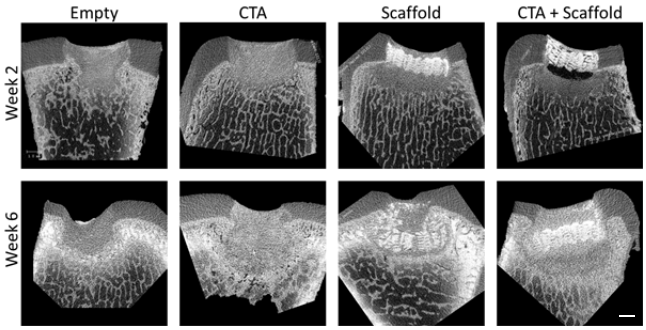

Figure 2. MicroCT with Lugol's contrast after 2 and 6 weeks of healing. At two weeks the CTA and scaffold demonstrated improved articular surface congruity with moderate boney remodeling. After six weeks there was an increased boney remodeling response. Scale bar = 1 mm.

DISCUSSION: In this feasibility study, two specialized tissue engineering approaches were combined to generate a biphasic CTA/PCL construct, where the woven scaffold served as a substrate that anchored the overlying CTA. The study demonstrates that both materials are excellent candidates for repairing focal osteochondral defects in a Yucatan minipig model. In particular, the integrated biphasic construct will allow for the different mechanical properties of cartilage and bone to be matched by the CTA and PCL scaffold, respectively [2,3]. The presence of delivered cells after six weeks indicates that the CTA is a suitable biological construct *in vivo*, and retention of the PCL scaffold over at least six weeks provides sufficient stability for native cells to begin integrating with the construct. There was a large boney remodeling response in all treatments, which is consistent with our previous studies in this juvenile model [1,4]. Ongoing studies are investigating longer time points and additional quantitative outcomes (including mechanics), as well as evaluating the inclusion of osteoconductive molecules within the PCL to promote boney anchorage of the construct.

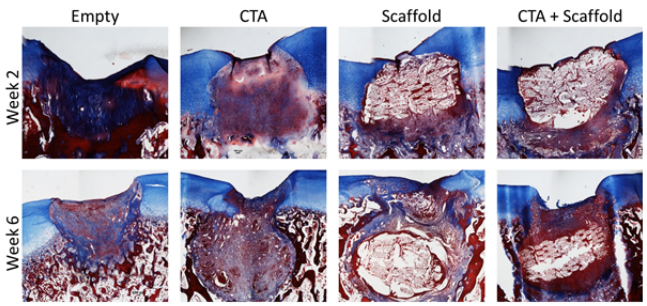

Figure 3. Masson's Trichrome staining after 2 and 6 weeks *in vivo*. PCL scaffold architecture was maintained while implantation invoked a subchondral remodeling response.

SIGNIFICANCE: This study demonstrated the feasibility of using a biphasic construct comprised of a cartilage tissue analog and a PCL scaffold for osteochondral defect repair in a clinically relevant large animal model.

REFERENCES: [1] Fisher+ Tissue Eng Part A. 2015; [2] Kim+ JOR 2011; [3] Moutos, Guilak Tissue Eng Part A. 2010; [4] Pfeifer+ ORS Annual Meeting 2015.

ACKNOWLEDGEMENTS: The work was supported in part by the AO Foundation, the Deutsche Forschungsgemeinschaft, and the NIH.

Pediatric bone density is influenced by physical activity and genetic variation at known bone density loci

Authors: Jonathan A. Mitchell, PhD[1]; Alessandra Chesi, PhD[2]; Okan Elci, PhD[3]; Shana E. McCormack, MD[4,5]; Sani M. Roy, MD[5]; Heidi J. Kalkwarf, PhD[6]; Joan M. Lappe, PhD[7]; Vicente Gilsanz, MD[8]; Sharon E. Oberfield, MD[9]; John A. Shepherd, PhD[10], Andrea Kelly, MD[4,5], Struan F.A. Grant, PhD[2,4,5*] and Babette S. Zemel, PhD[4, 11*]
*Equal contribution (Grant and Zemel)

Affiliations: [1]Department of Biostatistics and Epidemiology, Perelman School of Medicine, University of Pennsylvania, Philadelphia; [2]Divisions of Human Genetics and Endocrinology, Children's Hospital of Philadelphia, Philadelphia; [3]Biostatistics and Data Management Core, Children's Hospital of Philadelphia, Philadelphia; [4]Department of Pediatrics, Perelman School of Medicine, University of Pennsylvania, Philadelphia; [5]Division of Endocrinology and Diabetes, The Children's Hospital of Philadelphia, Philadelphia; [6]Division of General and Community Pediatrics, Cincinnati Children's Hospital Medical Center, Cincinnati; [7]Division of Endocrinology, Department of Medicine, Creighton University, Omaha; [8]Department of Radiology, Children's Hospital Los Angeles, Los Angeles; [9]Division of Pediatric Endocrinology, Diabetes, and Metabolism, Department of Pediatrics, Columbia University Medical Center, New York; [10]Department of Radiology, University of California San Francisco, San Francisco; [11]Division of Gastroenterology, Hepatology and Nutrition, The Children's Hospital of Philadelphia, Philadelphia;

Background
Osteoporosis is characterized by low bone mineral density (BMD) and can have its origins in early life. Both genetics and physical activity contribute to bone mineral density (BMD), but it is unknown if the benefits of physical activity on childhood bone accretion depend on genetic risk.
We aimed to determine if physical activity and overall BMD genetic risk score were associated with pediatric BMD, and if physical activity interacted with bone fragility genetic variants to influence BMD in childhood.

Methods
We leveraged the six-year prospective longitudinal study design of the 'Bone Mineral and Density in Childhood Study', comprised of European ancestry children (N=918, 52.4% female). Our outcome variables were femoral neck (FN), total hip (TH) and spine areal-BMD (aBMD) Z-scores, and total body less head (TBLH) bone mineral content (BMC) Z-score, estimated by dual energy X-ray absorptiometry. Hours spent in total, high, and low impact physical activity were self-reported. Single nucleotide polymorphisms (SNP), near 67 known BMD susceptibility loci, were genotyped and a genetic risk score calculated. Statistical interactions of physical activity with genetic risk score and each SNP were examined using linear mixed effects models, adjusted for age, Tanner stage, BMI and dietary calcium. We applied the Benjamini and Hochberg (BH) method to correct for the multiple testing when testing each SNP.

Results: Genetic risk score was negatively associated with bone Z-scores (e.g., TBLH-BMC Z-score: β=-0.02, P=4.9x10^{-6}). Total and high impact physical activity were positively associated with bone Z-scores (e.g., TBLH-BMC Z-score: β_{total}=0.02, P=3.3x10^{-4} and β_{high_impact}=0.05, P=4.0x10^{-10}). There was no evidence of physical activity-genetic risk score interactions. However, total physical activity interacted with rs2887571 (*ERC1/WNT5B*) to influence TBLH-BMC in males (P=7.1x10^{-5}), females (P=0.027), and both sexes combined (P=6.7x10^{-4}), where total physical activity associated with Z-score stability for non-risk G allele carriers and positively associated with Z-score for AA homozygotes (beta=0.03, P=8.2x10^{-6}). Furthermore, among risk A allele homozygotes, low impact physical activity associated with Z-score stability while high impact physical activity associated with higher TBLH-BMC Z-score (beta=0.08, P=2.7x10^{-9}).

Conclusions
The beneficial effect of physical activity on bone, especially of the high impact form, applies to children genetically predisposed to lower adult BMD.

Clinical and Radiographic Investigation of the relationship between mitral valve prolapse, systemic joint laxity and temporomandibular disorder – a cross-sectional national study in Taiwan

Authors: Yuh DY, Chang TH, Huang RY, Mupparapu M

Abstract:

Background: Temporomandibular disorder (TMD) is generally recognized as a multifactorial disease, comprising biological, behavioral, environmental, social, emotional, trauma, stress, parafunction and cognitive factors, alone or in combination.[1] Many studies have documented an association among mitral valve prolapse (MVP), systemic joint laxity (SJL), and hypermobility of temporomandibular joint which may induce by collagen distribution.[2,3,4] **Aim**: Investigation of the correlation between MVP, SJL and TMD. **Materials and Methods:** This study utilized the Taiwan Longitudinal Health Insurance Database 2005 (LHID2005) and 975,831 subjects were observed from 2004 to 2008 including 497,801 female and 478,030 male. The ICD-9-CM codes of TMD including 524.6, 524.60, 524.61, 524.62, 524.63, 524.69, 729.1, 830, 830.0 and 830.1 and divided into five groups (Table 1) according to Diagnostic Criteria for TMD (DC/TMD).[5] We looked at the utilization of imaging for the diagnosis of TMD, subluxation /muscle disorders and TMJ ankylosis (n= 2710) (Table 2). The ICD-9-CM codes of MVP: 394.0 and 424.0 (n=18,987); SJL: 728.4 and 728.5 (n=546) were utilized in this study. Furthermore, other frequently discussed risk factors such as facial trauma (the ICD-9-CM codes: mandibular fracture from 802.20 to 802.39 and maxillary fracture from 802.4 to 802.9); psychosis (the ICD-9-CM codes from 295 to 313, V6289 and V624) were also utilized in this study to adjust the variables. Finally, the logistic regression was performed to estimate the chances of TMD flare-up in subjects with MVP or SJL. **Results:** The results showed 674 subjects with TMD combined MVP; 23 subjects with TMD combined SJL; 15 subjects of MVP combined SJL; 2 subject with TMD, MVP and SJL (Fig. 2). The variables were analyzed in unspecific TMD and disc disorders models receptively (Table 3 and 4). **Summary:** This national cross-sectional study showed that MVP in subjects is associated 1.6 times more in subjects with unspecific TMD; no significant effect in disc disorders. Relatively subjects of SJL has 2.6 times chance to accompany unspecific TMD; 16.5 times chance to accompany disc disorders. TMD symptoms are considered with a peak in age range between 20 and 40 years. Females are predominantly affected by these disorders. Facial trauma and psychosis are the risk factors of TMD.

References:

1. Scrivani SJ, Keith DA, Kaban LB. Temporomandibular disorders. N Engl J Med. 2008; 359: 2693-705.
2. Chang TH, Yuh DY, Wu YT, Cheng WC, Lin FG, Shieh YS, Fu E, Huang RY. The association between temporomandibular disorders and joint hypermobility syndrome: a nationwide population-based study. Clin Oral Invest. 2015; 19(8): 2123-32.
3. Westling L, Holm S, Wallentin I. Temporomandibular joint dysfunction. Connective tissue variations in skin biopsy and mitral valve function. Oral Surg Oral Med Oral Pathol. 1992; 74: 709-18.
4. Nadeau C, Kuperstein AS, Mupparapu M, Stoopler ET. Temporomandibular disorder in a patient with pseudoxanthoma elasticum: a case report and review. Spec Care Dentist. 2013; 33(5): 255-9.
5. Schiffman E, Ohrbach R, Truelove E. Diagnostic Criteria for Temporomandibular Disorders (DC/TMD) for Clinical and Research Applications: Recommendations of the International RDC/TMD Consortium Network and Orofacial Pain Special Interest Group. J Oral Facial Pain Headache. 2014; 28(1): 6–27.

TMD Groups	US	Arthrography	CT	MR	Pan	Pan/Tomography	Total Images/ Group n	%
Unspecific TMD	4	12	59	91	1224	1068	2458/13199	18.62
Disc Disorders			1	3	23	60	87/202	40.07
Ankylosis			2	1	15	1	19/	26.76
Muscle disorders			2	3	32	53	90	53.25
Subluxation			5	3	24	24	56	2.82
Total	4	12	69	101	1318	1206	2710	17.33

Progression of Vertebral Bone Disease in Mucopolysaccharidosis VII Dogs from Birth to Skeletal Maturity

Sun H. Peck, Jennifer L. Kang, Joseph A. Chiaro, Neil R. Malhotra, Patricia O'Donnell, Mark E. Haskins, Margret L. Casal, Lachlan J. Smith

University of Pennsylvania, Philadelphia, PA

Disclosures: SHP (N), JLK (N), JAC (N), NRM (N), PO (N), MEH (4-BioMarin Pharmaceutical Inc.), MLC, (N), LJS (N)

Introduction: The mucopolysaccharidoses (MPS) are inherited lysosomal storage disorders characterized by mutations in hydrolases that degrade glycosaminoglycans (GAGs). GAGs accumulate in cells leading to multi-systemic clinical manifestations [1]. Many subtypes, including MPS VII (Sly Syndrome, beta-glucuronidase deficiency), exhibit severe skeletal abnormalities that are prevalent in the spine [2-4]. Previously, we showed the presence of cartilaginous lesions in MPS VII vertebrae that represent failed secondary ossification during postnatal development [4, 5] and contribute to progressive spinal deformity [6]. To effectively target and optimize timing for therapeutic intervention for vertebral bone disease in MPS VII, it is critical to first elucidate temporal patterns of disease manifestation during postnatal development. Therefore, the objective of this study was to establish the nature, timing, and progression of vertebral bone disease in MPS VII from birth to skeletal maturity, using the naturally-occurring canine disease model.

Methods: For this study, we used the naturally-occurring MPS VII canine model that mimics both the progression and pathological phenotype of the skeletal abnormalities found in human patients [7]. With IACUC approval, control and MPS VII dogs (n=1-5) were euthanized at 9, 14, 30, 42, 90, 180, and 365 days, and lumbar and thoracic vertebrae were excised. Progression of vertebral bone formation of primary and secondary ossification centers were analyzed using µCT. Bone formation in vertebral secondary ossification centers was visualized through reconstructed images of the regions cranial and caudal to the growth plates. To quantify trabecular bone content in the primary ossification centers, standard 3D morphometric analyses were performed and bone volume fraction (BV/TV) and bone mineral density (BMD) were determined [8]. For non-invasive assessment of bone formation, serum was collected at 90, 180, and 365 days-of-age and bone-specific alkaline phosphatase (BAP) activity was measured using an ELISA kit. Significance for 9 and 14-day BV/TV and BMD measurements (n=5 for each group) was established using 2-way analyses of variance and post-hoc Tukey's test ($p<0.05$). Significance for 30 and 42-day BV/TV and BMD measurements (n=2 for each group) were determined with unpaired t-test ($p<0.05$).

Results: Initiation of vertebral secondary ossification was markedly delayed in MPS VII animals compared to controls (Fig 1). While secondary ossification commenced by 14 days-of-age in controls, in MPS VII vertebrae, this did not occur until 30 days-of-age. Further, when it did commence, secondary ossification in MPS VII animals was highly irregular compared to the smooth, symmetrical phenotype in controls as seen from the axial images in Fig 1. Examining midsagittal cross-sectional images (Fig 2), bone formation in secondary ossification centers of the MPS VII animals was observed to cease progressing between 42 and 90 days-of-age. At 180 and 365 days-of-age, bone content in secondary ossification centers was greatly diminished compared to controls. Additionally, at 365 days, in control animals, growth plates were closed but remained open in MPS VII animals. Examining primary ossification centers, trabecular bone content was normal at early ages, but beyond 30 days, MPS VII vertebrae exhibited lower BV/TV and BMD (Fig 2, Figs 3A and B). Finally, serum BAP levels were lower in MPS VII animals at 90 and 180 days (during skeletal growth), but not at 365 days (skeletal maturity) (Fig 3C).

Discussion: This work establishes that vertebral bone disease in MPS VII manifests differently in primary and secondary ossification centers in a temporally-dependent manner, informing optimal targeting and timing for potential therapeutic interventions. Vertebral secondary ossification in MPS VII was found to be not only markedly delayed, but also highly non-uniform, suggesting that early developmental signals for bone formation are both impaired and spatially dysregulated. While primary ossification centers were not significantly affected at early ages, pathological changes (lower trabecular BV/TV and BMD) in MPS VII animals were evident at older ages. Lower serum BAP activity levels in MPS VII animals at 90 and 180 days may indicate reduced osteoblast activity during skeletal growth. Results also suggest that serum BAP may be a robust, non-invasive diagnostic tool for assessing bone disease progression in MPS patients.

Significance: MPS VII is associated with severe skeletal disease for which there are currently no treatments. This study contributes to identification of optimal therapeutic windows for targeting bone disease in MPS VII and suggests a new diagnostic tool for assessing bone disease in MPS patients.

References: [1] Neufeld+ 2001. [2] Dickerman+ Spine, 2004. [3] White. Rheu, 2011. [4] Smith+ Mol Gen & Met, 2012. [5] Smith+ J Orthop Res, 2010. [6] de Kremer+ Am J Med Genet, 1992. [7] Haskins+ Pediat Res, 1984. [8] Chiaro+ Bone, 2013.

Acknowledgments: Funding sources: NIH; Penn Center for Musculoskeletal Disorders; National MPS Society. The authors thank Ms. Caitlin Fitzgerald and Ms. Therese Langan for animal care.

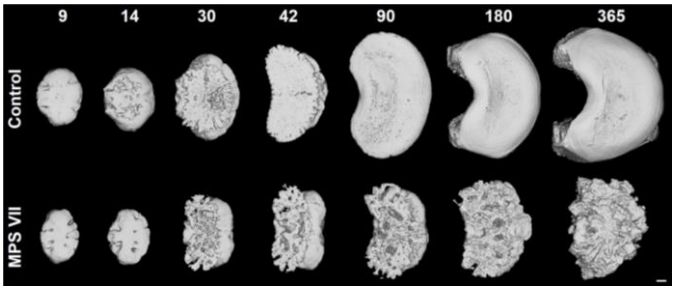

Figure 1. Representative axial µCT images showing delayed, incomplete, and non-uniform progression of secondary ossification in MPS VII vertebrae compared to controls. Numbers indicate postnatal days-of-age. Scale=1mm.

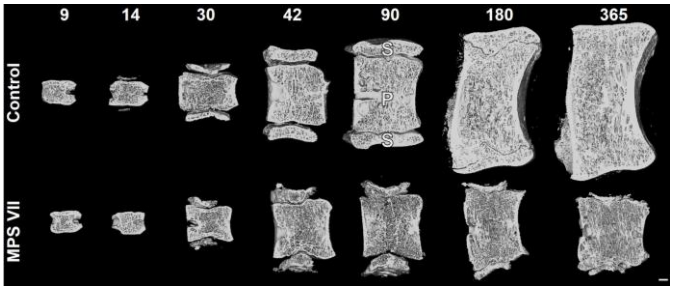

Figure 2. Representative midsagittal µCT images showing lower trabecular bone content in MPS VII vertebral primary ossification centers at older ages compared to controls. Numbers indicate postnatal days-of-age. Scale=1mm. S: Secondary ossification center; P: Primary ossification center.

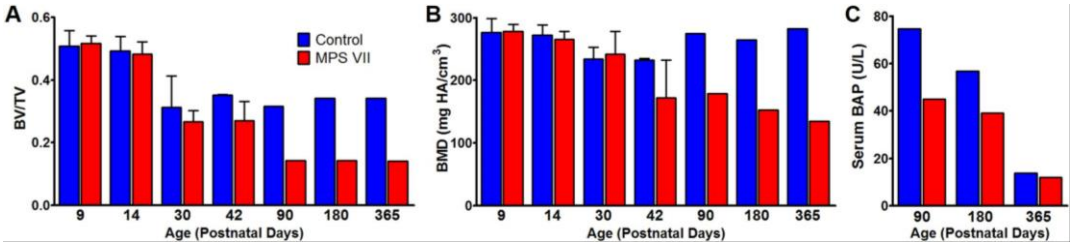

Figure 3. A. Bone volume fraction (BV/TV) and **B.** Bone mineral density (BMD) for control and MPS VII vertebral primary ossification center trabecular bone from birth to skeletal maturity. **C.** Serum bone alkaline phosphatase (BAP) activity for control and MPS VII animals at older ages. 9 days (n=5), 14 days (n=5), 30 days (n=2), 42 days (n=2), 90 days (n=1), 180 days (n=1), and 365 days (n=1).

High-resolution 3D gagCEST Imaging of *In Vivo* Human Knee Cartilage at 7T MRI

Guruprasad Krishnamoorthy, **Ravi Nanga**, Puneet Bagga, Hari Hariharan, Ravinder Reddy

Center for Magnetic Resonance and Optical Imaging, Department of Radiology, Hospital of the University of Pennsylvania

ABSTRACT:

Osteoarthritis (OA) is a degenerative disease affecting molecular composition of cartilage of Knee. Early detection of OA is critical for preventing the progression and reversing the course of the disease when the cost of the treatment is low and treatment success rate is much higher. Early stage of OA is associated with the loss of Glycosaminoglycan which are side chains of Proteoglycan (PG) molecules from the Extracellular Matrix of cartilage. Currently available non-invasive methods to measure PG have limitations in either specificity or sensitivity / spatial resolution. A recently developed method known as Chemical Exchange Saturation Transfer imaging of Glycosaminoglycan (gagCEST) images PG non-invasively. While this method is highly specific to GAG, current implementation of this method is based on single slice, time intensive and not conducive for routine evaluation of patients. In this study, a novel 3D / multi-slice gagCEST imaging technique is developed to image GAG of human knee cartilages in a practically achievable scan time at 7T MRI. Asymptomatic healthy volunteers and elderly subjects with knee pain have been scanned and intra subject reproducibility was determined with Intra-class correlation of 0.95.

Characterization Of Biological Interaction between Steroid and Palvarotene

Sayantani Sinha[1], Kenta Uchibe[1], Usami Yu[1], Haruna Shimizu[1], Maurizio Pacifici[1] and Masahiro Iwamoto[1]

[1] Translational Research Program In Pediatric Orthopedics, The Children's Hospital of Philadelphia, Philadelphia, Pennsylvania

Heterotopic Ossification (HO) is a multifaceted pathological condition that leads to the formation of excess endochondral bone at extraskeletal sites. Fibrodysplasia Ossificans Progressivia (FOP) is a severe form of HO caused by mutations in ALK2 and is characterized by intermittent flare-ups. Prednisone is thus used as a standard-of-care anti-inflammatory agent for FOP patients since there is no effective treatment to prevent HO itself. Previous studies from our group showed that the retinoic acid receptor gamma agonist Palovarotene inhibited HO in injury and genetic mouse models. Though promising, those studies did not determine whether a combination therapy involving Palovarotene plus prednisone may be more effective or whether the two drugs would actually negatively impact each other. To this end, we used our standard HO model in which rhBMP-2 mixed in Matrigel is implanted subcutaneously in 8 weeks old CD-1 female mice, eliciting HO in about 2 weeks. Freshly implanted mice were treated by gavage with pre-established doses of Palovarotene, prednisone or combination at different times/regimens. For comparison, companion mice received vehicle. Micro-CT scans showed that prednisone and dexamethasone given singly reduced HO, but co-treatment with Palovarotene was more effective. Early treatment appeared to be important for effectiveness of steroid action. To exclude non-specific systemic drug effects, mice were subjected to body weight measurements and blood analyses showed no obvious detrimental effects. To uncover mechanisms of drug action, we analyzed signaling pathways in mesenchymal progenitor cells in vitro. Cells were reverse-transfected with various reporter plasmids and quantified for activity with or without drug treatment. Treatment with dexamethasone increased glucocorticoid-response elements/GRE-Luc activity within 24hrs, while co-treatment with dexamethasone and palovarotene did not further increase or decrease GRE-Luc activity. Similar results were obtained with a retinoic acid receptor reporter plasmid (RARE) in response to palovarotene or in combination. Interestingly, co-treatment did result in appreciable decreases in NFkB activity. In sum, our data indicate that there is no major negative interactions of palovarotene and steroids against HO and a combination therapy may in fact offer alternative regimens, possibly making the therapy as effective and safe as possible for FOP patients.

Mapping of pain circuitry in early post-natal development using manganese-enhanced MRI

Authors: MM Sperry, BM Kandel, KE Bass, SR Das, PS Dhillon, JC Gee, GA Barr

Abstract:

Approximately 400,000 human infants are admitted to the neonatal intensive care unit in the United States every year, and undergo 10-20 or more medically essential but potentially painful procedures each day, often without analgesics. We know that the number of painful procedures in the human neonate is related to poorer outcomes but not how these painful procedures change brain function. Thus we have virtually no detailed understanding of the mechanisms by which the brain is engaged during pain early in life. Based on similarities in brain development between rat and human neonates, the goal of this study was to use MEMRI to map brain circuits that are activated following peripheral tissue injury in infant rats, at an age roughly equivalent to that of a human neonate. To characterize this circuitry, 12-day old rat pups were systemically injected with manganese chloride (75 mg/kg), a calcium analog able to pass through the blood brain barrier at this stage in development. Twenty-four hours later, half of the pups (n=19) were treated with formalin injected into the hindpaw and half were not (n=19). This injury model engages supraspinal pathways and has been used extensively in both developmental and adult studies as a model of inflammatory pain. To allow activation of multiple structures, pups survived for 7 hours prior to perfusion and brains were imaged for 8-10 hours *ex vivo*. T1 weighted 3D spin echo images were used to visualize the Mn uptake in the brain (Bruker Biospin). Images were normalized and smoothed to a previously established group template space (Advanced Normalization Tools) and intensity normalized to the visual cortex, a region unlikely to be affected by pain stimuli. Two methods of analysis were implemented to elucidate the pain circuits. Voxel and region-wise morphometric analysis showed statistically significant differences in several brain regions between the control and formalin-treated groups ($p < 0.001$, uncorrected for multiple comparisons). Using structural equation modeling (SEM) of anatomically defined circuits, and iterative addition and subtraction of anatomical components known to be involved in pain processing, two possible models that accounted for the maximum variance (comparative fit index, CRI > 0.90 and standardized root mean square residual, SRMR < 0.08) were identified. In these models the formalin-treated group exhibited a significant fit to the SEM, whereas the control group did not, suggesting that these pathways are involved in the pain perception circuitry, as activated by the formalin stimulus. These findings suggest that as young as 12 days of age, a painful injury activates both the sensory and affective components of pain.

Presentation preference: no preference
Theme: Development
Subtheme: Development of Motor, Sensory, and Limbic Systems
Topic: Sensory systems
Keywords: nociception, MEMRI, ontogeny, circuits

Supported by funds from the Battaglia Endowment and NIH T32EB009384.

Removal of bone marrow contributions for evaluating of bone water by near infrared (NIR) spectroscopy

Author list:
Hee Jin Yang [1], Mugdha V. Padalkar[1], Eric Greco[1], Michael Inspiryan[2], Chamith S. Rajapakse[2], Nancy Pleshko[1]
[1]Temple University, Philadelphia, PA, USA, [2]Univerity of Pennsylvania, Philadelphia, PA, USA

Abstract:
Bone fracture risk increases with age and disease state. Recent studies have pointed to factors other than bone mineral density that contribute to fragility, including bone water. Near infrared spectroscopic (NIRS) methods are being proposed for evaluation of water in bone at microscopic resolution. However, there are significant interfering absorbances from bone marrow that complicate the NIRS analysis. The current study investigates methodology to reduce the bone marrow contribution to NIR spectra. Methods: Bovine tibias were harvested from slaughtered 2-4 month old animals (Research 87, Boylston, MA) and stored in phosphate buffered saline (pH 7.4, Invitrogen, Carlsbad, CA) at -20°C until processing. Thawed tibias were cut into 500 um thick slices using a diamond wafering saw (Buehler Isomat 1000, Lake bluff, IL). NIR spectral images of the bone slices (~ 20 x 20 mm) were obtained using a Perkin Elmer Spotlight 400 imaging spectrometer (Shelton, CT). NIRS images were collected in transmission mode from 4000 to 7800 cm^{-1} at 64 cm^{-1} spectral resolution and 50 um pixel resolution with 2 co-added scans. Each image took approximately an hour. The bone slices were placed between two glass slides to avoid water loss during imaging. After NIRS imaging, the slices were washed in an ultrasonicator (Emerson Industrial Automation, Danbury, CT) for 30 minutes at 45°C with 1% tergazyme solution, followed by gentle washing of the slices in DI water, and then NIRS data collection. NIRS images were analyzed using ISYS 5.0 software (Malvern Instruments, Columbia, MD). The mean intensities of NIR absorbance peaks at 5792 cm^{-1} (arising from the fat component of bone marrow) and 4608 cm^{-1} (from the bone collagen matrix) were analyzed in second derivative spectra (Savitzky Golay, 3rd order polymer and 7 points of smoothing) images before and after sonication. Results: It was found that the overall fat absorbance was reduced by 35% after ultrasonication, and in the trabecular region of bone, it was reduced by 97%. There were no significant changes to the collagen absorbances. These results indicate that the ultrasonication methodology can be used to remove bone marrow from bone prior to NIRS imaging.

ULTRASOUND-GUIDED DRY NEEDLING ON HEALTHY RAT SUPRASPINATUS TENDON

[1]C.N. Riggin, [2]V. Khoury, [1]J.A. Gordon, [2]S.M. Schultz, [1]A.M. Pardes, [2]C.M. Sehgal, [1]L.J. Soslowsky
[1]McKay Orthopaedic Laboratory and [2]Department of Radiology, University of Pennsylvania, Philadelphia, USA

INTRODUCTION

Tendinopathy is a common clinical problem and conservative treatments are often ineffective. Recently, ultrasound-guided dry needling, or repeatedly introducing a needle into the abnormal tissue [1, 2] has been attempted, to disrupt pathological tissues, induce bleeding, and release factors to stimulate healing. However, a controlled laboratory model to study this potential therapy, as well as basic evidence supporting this practice is lacking [3]. Therefore, the objective of this study was to perform ultrasound-guided dry needling in healthy rat supraspinatus tendons to evaluate the acute vascular, biological, and mechanical response in the tendons, to understand the initial effects of dry needling. We hypothesized that dry needling would cause an early increase in blood flow, inflammation, cellularity, and matrix formation, and a decrease in material properties.

METHODS

32 Sprague-Dawley rats were used (IACUC approved). 22 underwent bilateral ultrasound-guided dry needling followed by sacrifice at days 1, 3 or 7 for histology (n=6) and mechanics (n=10). 10 healthy rats served as controls. Color Doppler ultrasound was performed 24 hours prior to needling, 5 and 24 hours after needling (n=6). The rotator cuff was visualized using a 14MHz probe. A 27G needle was inserted posteriorly and guided between the humeral head and acromion to penetrate the supraspinatus tendon 10 times along its length. Color Doppler images were acquired and analyzed for regional and local blood flow (color weighted fractional area (CWFA)). A one-way ANOVA with repeated measures and Bonferroni test were performed (*$p<0.05$). The right tendon was mechanically tested [4]. T-tests were performed (*$p<0.05$). The left tendon was stained for safranin-o (Saf-O), hematoxylin and eosin (H&E), interleukin-1β (IL-1β), tumor necrosis factor α (TNFα), and type III collagen. Images were graded by three blinded investigators for cell shape (1-spindle to 3-round), cellularity (1-low to 3-high), Saf-O staining (1-low to 3-high), and DAB staining (1-low to 4-high). A Kruskal-Wallis test and a Dunn's post hoc test were performed (*$p<0.05$).

RESULTS

The CWFA in local and regional areas were increased 5 hours-post dry needling (Fig 1A). There was an increase in cross sectional area and no change in max load (Fig 1B) or percent relaxation, but a decrease in maximum stress, insertion modulus (Fig 1C), midsubstance modulus, and stiffness. There was an increase in rounded cell shape (Fig 1D), IL-1β (Fig 1E), and type III collagen at day 1, an increase in cellularity at days 1 and 7, and an increase in glycosaminoglycans (GAG) content at days 3 and 7 (Fig. 1F).

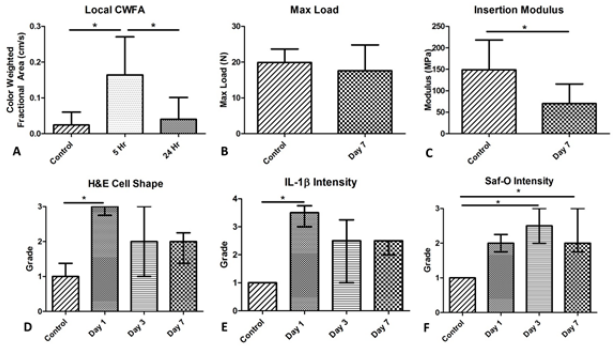

Figure 1: (A) Doppler imaging results demonstrate a local increase color weighted fractional area (CWFA) 5 hours after the dry needling procedure. (B, C) Mechanical evaluation of the supraspinatus tendon 7 days after needling demonstrated an increase in insertional modulus and no change in maximum load. (D-F) Histological evaluation demonstrates more rounded cell shape, increased inflammation, and increased GAG production after needling. Data presented as mean ± standard deviation with *$p<0.05$.

DISCUSSION

Dry needling the rat supraspinatus tendon caused an acute injury response as hypothesized. Increases in blood flow in the shoulder and in the needled tendon demonstrate systemic and local responses to this micro-damage. There was an early increase in cellularity with a more rounded cell shape. Increases in type III collagen and GAGs indicated the formation of granulation tissue. Additionally, the increase in inflammatory mediators is consistent with a previous study evaluating dry needling in injured rat tendons [5]. Mechanical properties confirm that micro-damage was induced in the tendon, causing an increase in the cross sectional area, a decrease in material properties, but no change in maximum load, supporting that this injury may not dispose the tendon to failure risk. This study demonstrated that the rat supraspinatus tendon can be dry needled consistently under ultrasound guidance, and that a controlled healing response can be elicited. Further studies will evaluate the effect of dry needling on pathologic tissue.

ACKNOWLEDGEMENTS

The authors thank B Kneeland, J Huegel, and P Bhatt. This study was funded by the NIH/NIAMS supported Penn Center for Musculoskeletal Disorders (P30 AR050950) and a NSF Graduate Research Fellowship.

REFERENCES

[1] Rha DW, et al, Clin Rehabil 2012. [2] Housner JA, et al. Clin J Sport Med 2010. [3] Chiavaras MM, et al, Semin Musculoskelet Radiol 2013. [4] Peltz CD, et al, J Orthop Res 2010. [5] Hammerman M, et al, J Appl Physiol 2014.

Bound Bone Water Density is a Surrogate Measurement of Organic Matrix Density

Alan C. Seifert, Cheng Li, Suzanne L. Wehrli, and Felix W. Wehrli
Laboratory for Structural NMR Imaging, Department of Radiology

Synopsis: Proton NMR signal in bone arises from pore water (T_2 > 1ms), bound water (T_2 ~ 400±100μs), and collagen (T_2 << 100μs). Pore water is hypothesized to scale with porosity, and bound water with collagen density. Here we measured single adiabatic inversion-recovery zero echo-time (SIR-ZTE) bound water density in 15 human cortical bone specimens at 9.4T, and found strong correlations with both gravimetric organic matrix density (R^2 = 0.74) and μCT porosity (R^2 = 0.73). SIR-ZTE is therefore suitable for measurement of matrix density in vivo.

Introduction: Proton NMR signal in bone arises from three pools: (1) T_2 > 1 ms, corresponding to free water within the Haversian and lacunocanalicular pore system, (2) T_2 ~ 400±100 μs, corresponding to motionally restricted water hydrogen-bonded to matrix collagen, and (3) T_2 << 100 μs, corresponding to highly immobilized ^{1}H nuclei in collagen [1]. These pools and their redistribution in response to increased porosity are diagrammed in a schematic T_2 spectrum (Fig. 1). Horch et al. [2] found the bound water pool in cortical bone, imaged using single adiabatic inversion recovery UTE imaging (SIR-UTE) for long-T_2 pore water-suppression, to correlate strongly with mechanical properties and short-T_2 bound water density by bi-exponential fitting of CPMG data. Cao et al. [3] also examined the correlation of long T_2-suppressed ^{1}H density to gravimetric matrix density in three porcine cortical specimens, and Ong et al. [4] found a negative correlation between porosity and bound water by ^{2}H IR. To provide a foundation for the use of ^{1}H SIR-zero TE (SIR-ZTE) imaging to measure matrix density (and, further, bone mineralization) in human cortical bone, we have examined a set of 15 specimens and compared bound water density with gravimetric matrix density and μCT porosity.

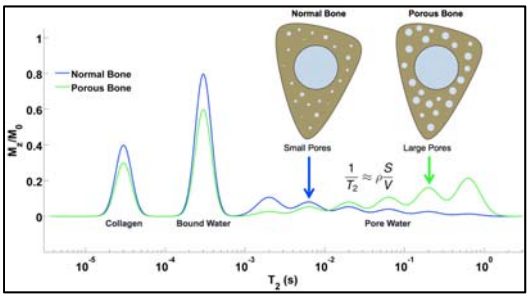

Fig. 1: Schematic T_2 spectrum of equilibrium ^{1}H signal in normal (blue) and porous (green) bones, showing the relative positions and sizes of collagen, collagen-bound water, and pore-resident water fractions. Porous bone has a smaller bound water fraction, and a larger pore water

Methods:

Specimens: 15 cylindrical samples of human cortical bone (8F, 27-97 y; 7M, 37-93 y) were cut from cadaveric human tibiae. The long axis of each cylindrical sample was perpendicular to the anatomic axis of the bone. Bone from donors with bone-demineralizing disorders was excluded.

MRI: Bones were imaged along with a reference phantom of 10 mM $MnCl_2$ in 90% D_2O/10% H_2O ([^{1}H] = 11.08 M) using an adiabatic inversion recovery-prepared version of a commercial ZTE pulse sequence on a 9.4T vertical-bore NMR spectrometer and micro-imaging scanner (Bruker, Billerica, MA). A 5-ms 5-kHz bandwidth adiabatic pulse inverts long-T_2 pore water magnetization while nulling short-T_2 bound water signal. After TI = 50 ms, readout gradients are ramped up, signal is excited with a 25.6-μs 60° RF pulse, and data are acquired at 100-kHz bandwidth 0.5-mm isotropic resolution. One half-projection is acquired following each inversion, with TR = 200 ms.

Analysis: The bone and reference phantom in each image were masked, and intensities were corrected for differences in relaxation times between bound bone water (T_1 = 480 ms, T_2* = 400 ms) and the reference phantom (T_1 = 13 ms, T_2* = 530 μs). Transverse relaxation during adiabatic and excitation RF pulses was simulated and incorporated, and signal intensities were converted to ^{1}H concentrations.

μCT: Bones were scanned on a Scanco μCT35 scanner (Scanco, Brüttisellen, Switzerland) at 18.5-μm isotropic resolution. Bones were masked by active snakes in ITK-SNAP [5], and pores were segmented by thresholding, yielding porosity as pore volume / total volume.

Gravimetry: The fully hydrated samples were weighed, dried at 105° C for 110 hr to remove all bound and pore water, re-weighed, ashed at 600° C for 30 hr to burn off all organic matrix, and weighed again. Organic matrix density was quantified as the difference between dry and ash masses divided by total volume measured by μCT.

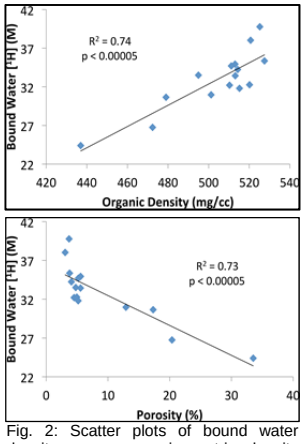

Fig. 2: Scatter plots of bound water density versus organic matrix density

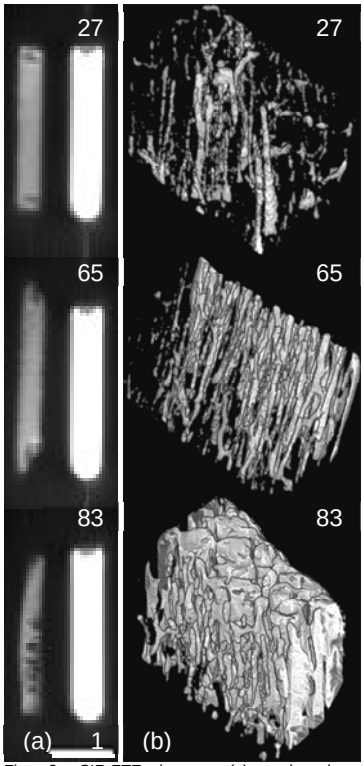

Fig. 3: SIR-ZTE images (a) and volume renderings (b) of pore spaces of bones from 27 y/o, 65 y/o, and 83 y/o females, demonstrating the range of porosities (3.7%, 5.6%, and 33.5%, respectively). In panel (a), bones are on the left

Results: Bound water ^{1}H concentration by SIR-ZTE is correlated positively with organic density (R^2 = 0.74) and negatively with μCT porosity (R^2 = 0.73) (Fig. 2). Bound water is also correlated with gravimetric mineral density (R^2 = 0.72), which is, in turn, also strongly correlated with matrix density (R^2 = 0.91). Organic density and porosity are also strongly associated (R^2 = 0.91). Pore-space volume renderings of bone differing substantially in porosity are shown in Fig. 3. Pore volume fraction and pore water concentration increase proportionally, and pore water T_2 also increases as individual pores enlarge and the contribution of surface relaxation to T_2 is diminished.

Discussion and Conclusions: The strong correlation of long T_2-suppressed ^{1}H density in cortical bone to matrix density and porosity further supports the potential of this method as a surrogate for matrix density. The association between gravimetric matrix and mineral densities shows that mineralization, in the absence of demineralizing disorders, is constant over a wide range of ages. As ^{1}H SIR-UTE has already been applied in vivo [2], this entirely non-invasive SIR-ZTE method may provide detailed insight into bone chemistry and composition in human subjects.

References: [1] Horch RA. MRM 2010;64:680-7. [2] Horch RA. MRM 2012;68(6):1774-84. [3] Cao H. MRM 2008;60(6):1433-43. [4] Ong HH. JBMR 2012;27(12):2573-81. [5] Yushkevich PA. Neuroimage 2006;31(3):1116-28.

Acknowledgements: NIH R01 AR50068, F31 AG042289, UL1TR000003, and Institution's ITMAT.

Performance of Bi-Component T_2* Fitting of Bound and Pore Bone Water Fractions is Dependent on Field Strength

Alan C. Seifert, Suzanne L. Wehrli, and Felix W. Wehrli

Synopsis: Discrimination between bound and pore bone water is vital for quantification of bone matrix density and porosity. The two main approaches are T_2-selective magnetization preparation and bi-exponential T_2* fitting. T_2* of pore water, however, is shortened by field gradients arising from the difference in susceptibility between water and bone. We scanned human cortical bone specimens at 4 field strengths, and validated bi-exponential fitting against μCT porosity and gravimetrically-determined matrix density. Our results indicate that T_2* bi-exponential fitting of FIDs may be a suitable method for quantifying bound and pore water fractions at 1.5T, but may fail at higher field strengths.

Introduction: ^{1}H NMR signal in bone arises from three pools: free water in pores, motionally restricted water bound to matrix, and immobilized ^{1}H nuclei in the collagen molecules themselves. Discrimination between these pools is vital for quantification of bone matrix density via bound water, and for surrogate measures of porosity via pore water. Fortunately, these pools are distinguishable based on T_2 [1]. The two main approaches to differentiation are T_2-selective magnetization preparation [2] and bi-exponential T_2* fitting [3]. As shown in Figure 1, however, T_2* of pore water is shortened by strong internal field gradients arising from the difference in susceptibility between water and bone tissue (□□□~ 2.5 ppm SI), complicating separation of bound and pore water, particularly at higher field strengths. An example T_2-T_2* 2D spectrum also illustrating this effect at 9.4T is shown in Fig. 2. To assess the viability of T_2* bi-component fitting as a method for quantifying bound and pore water fractions, we have scanned a set of human cortical bone specimens at 4 field strengths, and validated bi-exponential fitting of the resulting FIDs against μCT porosity and gravimetrically determined matrix density.

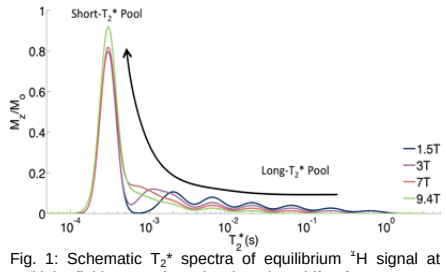

Fig. 1: Schematic T_2* spectra of equilibrium ^{1}H signal at multiple field strengths, showing the shift of pore water signal from the long-T_2* pool to the short-T_2* pool. This shortening of pore water T_2* due to stronger internal magnetic field gradients within pores, complicates

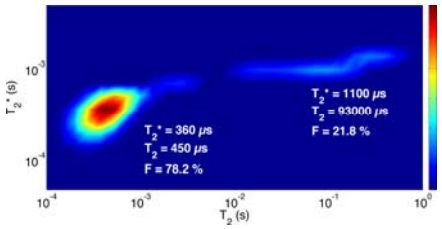

Fig. 2: T_2-T_2* 2D relaxation spectrum at 9.4T (generated using the MERA software package [4]) of a bone specimen taken from a 37 y/o male donor. Two pools, corresponding to bound and pore water, are clearly separated in the T_2 dimension, but much less so in T_2*. This effect is more severe at higher B_0.

Methods:

Specimens: 15 cylindrical samples of human cortical bone (8F, 27-97 y; 7M, 37-93 y) were cut from tibial specimens. The long axis of the cylinder was perpendicular to the anatomic axis of the bone, so this axis can be oriented parallel to B_0 in a solenoidal RF coil.

NMR: 1.5T, 3T, and 7T scanning was performed using custom ^{1}H-free solenoidal RF coils (10 mm diameter, 25 mm length) in whole-body human MRI scanners (Siemens, Erlangen, Germany). Each bone was scanned using a saturation-recovery (SR) FID pulse sequence [5] of the form [90°-SPOIL]$_{12}$-T_{SR}-90°-ACQ. RF pulse duration was 100 μs for saturation pulses and 20 μs for excitation pulses, and readout bandwidth was 250 kHz. 12 T_{SR}s were arrayed exponentially from 3 ms to 6 s. 9.4T scanning was performed on an NMR spectrometer (Bruker, Billerica, MA) using a 5-mm BBI probe with a 1-axis gradient and an SR-FID pulse sequence. 90° pulses were 19-20 μs in duration, and all other parameters were identical to those used at lower fields.

Analysis: Reconstruction and fitting was performed in Matlab (Mathworks, Natick, MA). For T_2* bi-exponential fitting, a sum of two decaying exponentials, $f(t) = ae^{\frac{-t}{b}} + ce^{\frac{-t}{d}} + e$, was fitted to the FID after the longest T_{SR} = 6 s by non-linear least squares. Short-T_2* fraction and relaxation time are given by a/(a+c) and b, respectively; long-T_2* parameters are c/(a+c) and d. Two-dimensional T_1-T_2* bi-component fitting, which should improve accuracy [6], was also performed by fitting $f(T_{SR}, t) = g(1 - e^{\frac{-T_{SR}}{h}})e^{\frac{-t}{k}} + m(1 - e^{\frac{-T_{SR}}{n}})e^{\frac{-t}{p}} + q$ to SR-FID data arrays. Pool fractions are given by g/(g+m) and m/(g+m), T_1s by h and n, and T_2*s by k and p, for short- and long-T_2* fractions, respectively. For validation, bones were scanned by μCT (Scanco, Brüttisellen, Switzerland) at 18.5-μm isotropic resolution, and total and pore volumes were calculated. The fully hydrated samples were then weighed, dried at 105° C for 110 h to remove all bound and pore water, re-weighed, ashed at 600° C for 30 h to burn off all organic matrix, and weighed again [7]. Matrix density was quantified as the difference between dry and ash masses divided by total volume.

	Short		Long	
	Fraction (%)	T_2* (μs)	Fraction (%)	T_2* (μs)
1.5T	69.6±12.7	400±120	30.4±12.7	4100±1200
3T	68.1±21.9	390±120	32.0±21.9	4400±8600
7T	82.3±14.0	370±80	17.7±14.0	1300±420
9.4T	55.1±28.7	300±150	44.9±28.7	890±530

Table 1: Fitted T_2* (by 1D T_2* bi-exponential fitting of FID data) and T_2 (by 2D T_1-T_2 bi-exponential fitting of SR-CPMG data) pool sizes and relaxation times.

Results: Average FID pool fractions and relaxation times are given in Table 1, and correlations of short-T_2* fractions at four field strengths with organic matrix density calculated from gravimetry are shown in Fig. 3. At 1.5T, short-T_2* fraction is strongly correlated with matrix density (R^2 = 0.63). At 3T, less than 50% of the variance in short-T_2* fraction is explained by matrix density (R^2 = 0.44). The correlation is weaker still at 7T (R^2 = 0.31), and non-existent at 9.4T. Correlations of short-T_2* fractions with porosity are similar to those with matrix density (R^2 = 0.70, 0.50, 0.40, 0.02 at 1.5, 3, 7, and 9.4 T, respectively). Addition of the T_1 dimension yielded marginally stronger correlations with matrix density at low B_0 (R^2 = 0.80, 0.61, 0.16, 0.02) and porosity (R^2 = 0.84, 0.76, 0.25, 0.10).

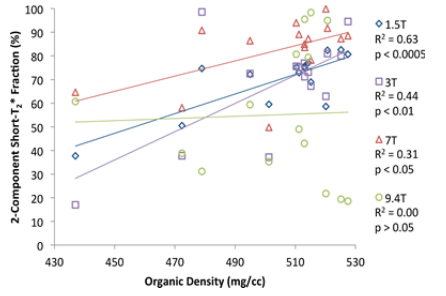

Fig. 3: Scatter plot and correlations of the short-T_2* signal fraction obtained by bi-exponential fitting of FIDs at four B_0 field strengths versus the organic matrix density measured by gravimetry and μCT. Performance of T_2* bi-exponential fitting is dramatically reduced as B_0 increases.

Discussion and Conclusions: Our results indicate that T_2* bi-exponential fitting of FIDs may be a suitable method for quantifying bound and pore water fractions at 1.5T, but may fail at higher field strengths. At 3T and higher, oscillations appear in the magnitude FID data, presumably due to the contribution of fat [8], which complicate fitting of a bi-exponential function. If FIDs exhibiting these oscillations are identified and excluded (5 out of 15, predominantly elderly females), the short-T_2* fractions derived from the remaining FIDs become strongly correlated with matrix density at 1.5T (R^2 = 0.83) and 3T (R^2 = 0.78), and moderately at 7T (R^2 = 0.61), though a subject-dependent 33% failure rate, disproportionately affecting the elderly females most likely to be studied with this method, may not be acceptable. In practice, this susceptibility-induced shortening of T_2* and oscillations due to off-resonance signal contribution may pose significant challenges to accurate quantification of bound and pore water fractions via bi-component T_2* fitting.

References: [1] Horch RA. MRM 2010;64:680-7. [2] Horch RA. MRM 2012:68;1774-84. [3] Nyman JS. Bone 2008;42(1):193-9. [4] Does M. http://www.vuiis.vanderbilt.edu/ ~doesmd/MERA/MERA_Toolbox.html. [5] Seifert AC. NMR Biomed 2013;26:1158-66. [6] Celik H. JMR 2013;236:134-9. [7] Anumula S. Bone 2008;42(2):405-13. [8] Diaz E. NMR Biomed 2011;25:161-8. **Acknowledgements:** NIH R01 AR50068, F31 AG042289, UL1TR000003, and Institution's ITMAT.

Comparison of Relaxation-Based NMR Methods for Quantifying Bound and Pore Water Fractions

Alan C. Seifert, Suzanne L. Wehrli, and Felix W. Wehrli

Synopsis: Increased cortical porosity is a major cause of the impaired strength of osteoporotic bone. MicroCT and gravimetry are accepted methods for validation of porosity and matrix density, but involve long scan times and destruction of specimens, respectively. In this work, we compare several NMR methods for quantification of bound and pore water (biomarkers for matrix density and porosity, respectively). T_2 fitting of CPMG data at 9.4T outperforms T_2* fitting of FIDs at 3T, while ^{2}H IR at 9.4T performs approximately as well as T_2* fitting. Incorporation of a second T_1 dimension yields improved fidelity for both T_2 and T_2* fitting.

Introduction: Increased cortical porosity is a major cause of the impaired strength of osteoporotic bone. Micro-computed tomography (μCT) is a gold-standard method for quantification of cortical porosity [1], but this method requires long scan times, and segmentation of pores is sensitive to user input. Gravimetry, in which the masses of water, organic matter, and mineral are determined by drying and ashing the bone, is a widely accepted validation method [2], but results in destruction of the specimen. In this work, we compare several NMR methods for quantifying bound and pore water, which are biomarkers for matrix density and porosity, respectively: (1) 1D T_2* [3,4] and (2) 2D T_1-T_2* [5] bi-component fitting at 3T, (3) 1D T_2 [6] and (4) 2D T_1-T_2 bi-component fitting at 9.4T, and (5) ^{2}H inversion-recovery (IR) at 9.4T [7]. These methods have the advantage of being non-destructive, relatively quick, and less dependent on user input.

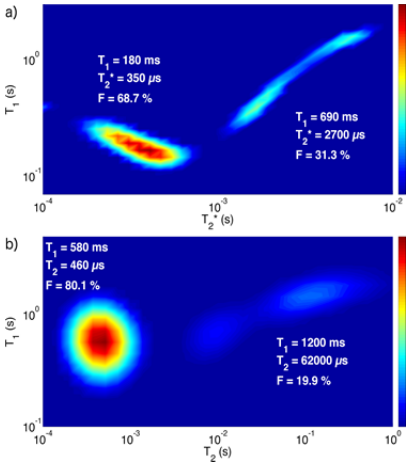

Fig. 1: a) T_1-T_2* 2D relaxation spectrum at 3T and b) T_1-T_2 spectrum at 9.4T (generated using the MERA software package [9]) of a bone specimen taken from a 37 y/o male donor. The two pools, corresponding to bound and pore water, are separated by several orders of magnitude in the T_2 dimension, but by much less in T_2*. Addition of the T_1 dimension slightly improves results relative to 1D T_2 or T_2*

Methods:

Specimens: 15 cylindrical samples of human cortical bone (8F, 27-97 y; 7M, 37-93 y) were cut from tibial specimens. The long axis of each cylinder was perpendicular to the anatomic axis of the bone, so this axis can be oriented parallel to B_0 in a solenoidal RF coil.

NMR: Bone samples were scanned in a 3T human MRI scanner (Siemens, Erlangen, Germany) using a saturation-recovery (SR)-FID pulse sequence [8] of the form [90°-SPOIL]$_{12}$-T_{SR}-90°-ACQ. Readout bandwidth was 250 kHz, and 12 T_{SR}s were arrayed exponentially from 3 ms to 6 s. Samples were then scanned in a 9.4T NMR spectrometer (Bruker, Billerica, MA) using both a SR-FID sequence and a SR-CPMG sequence of the form [90°-SPOIL]$_{12}$-T_{SR}-90°-[TE/2-180°-TE/2]$_n$-ACQ. Echo spacing was 200 μs with the loop iterator n arrayed logarithmically from 0 to 5000, and all other parameters were identical to those used at lower fields. Finally, labile protons were exchanged with ^{2}H by immersion in 99.9% D_2O-PBS for six days, and the D_2O-exchanged bones were scanned using ^{2}H IR with pulse durations t_{90}/t_{180} = 30/60 μs. A ^{2}H spectrum consists of a narrow central peak with T_1 = 200±40 ms corresponding to free D_2O in pores, flanked by a doublet with T_1 = 11±2 ms arising from D_2O whose motion is anisotropically restricted due to interaction with matrix collagen [7]. The integral of the spectrum with the narrow pore water peak nulled by inversion-recovery divided by the integral of the fully relaxed spectrum yields bound water fraction. Scan times for these five methods were: 1D T_2*, 3 min; 2D T_1-T_2*, 6 min; 1D T_2, 4 min; 2D T_1-T_2, 29 min; and ^{2}H IR, 21 min.

Analysis: Reconstruction and fitting were performed in Matlab (Mathworks, Natick, MA). For $T_2^{(*)}$ bi-exponential fitting, a sum of two decaying exponentials, $f(t) = ae^{\frac{-t}{b}} + ce^{\frac{-t}{d}} + e$, was fitted to the CPMG echo train (or FID) after the longest T_{SR} = 6 s by non-linear least squares. Two-dimensional T_1-$T_2^{(*)}$ bi-component fitting, which should improve accuracy [5], was performed by fitting $f(T_{SR}, t) = g(1 - e^{\frac{-T_{SR}}{h}})e^{\frac{-t}{k}} + m(1 - e^{\frac{-T_{SR}}{n}})e^{\frac{-t}{p}} + q$ to SR-CPMG (or SR-FID) data arrays.

μCT: Bones were scanned on a Scanco μCT35 scanner (Scanco, Brüttisellen, Switzerland) at 18.5-μm isotropic resolution. Bone exteriors were masked by active snakes in ITK-SNAP [10], and pores were segmented by thresholding. Porosity was calculated as pore volume / total volume.

Gravimetry: The fully hydrated samples were then weighed, dried at 105° C for 110 hr to remove all bound and pore water, re-weighed, ashed at 600° C for 30 hr to burn off all organic matrix, and weighed again. Organic matrix density was quantified as the difference between dry and ash masses divided by total volume measured by μCT.

	μCT Porosity	Organic Density	9.4T 2H IR Bound Fraction	3T 1D T2* Short-T2* Fraction	3T 2D T1-T2* Short-T2* Fraction	9.4T 1D T2 Short-T2 Fraction
9.4T 2D T1-T2 Short-T2 Fraction	0.90	0.89	0.66	0.50	0.74	1.00
9.4T 1D T2 Short-T2 Fraction	0.87	0.88	0.67	0.49	0.72	
3T 2D T1-T2* Short-T2* Fraction	0.76	0.61	0.51	0.26		
3T 1D T2* Short-T2* Fraction	0.50	0.44	0.46			
9.4T 2H IR Bound Fraction	0.50	0.46				
Organic Density	0.91					

Table 1: Matrix of R^2 values between parameters. Color indicates the strength of the correlation, from green (strong) to

Results: Two example 2D relaxation spectra, generated by non-negative least squares, are shown in Fig. 1. Pore water is distributed across a broad range of relaxation times; this presumably reflects a large distribution of pore sizes and orientations within cortical bone. A T_1-T_2* spectrum (Fig. 1a) shows the two components separated by a factor of 8, while a T_1-T_2 spectrum (Fig. 1b) shows the components separated by over two orders of magnitude (also note the difference in x-axis limits between panels a and b). A correlation matrix (Table 1) provides the strengths of the correlations between the various NMR and validation measurements. T_2 fitting of CPMG data at 9.4T is found to outperform T_2* fitting of FID data at 3T, while ^{2}H IR at 9.4T performs approximately as well as 1D T_2* fitting. Addition of the T_1 dimension yields improved fidelity for both T_2 and T_2* fitting.

Discussion and Conclusions: Success of bi-exponential fitting generally improves as the separation of the time constants of the two pools increases. Because the T_2* of pore water is substantially shortened by dephasing due to internal magnetic field gradients arising from the susceptibility difference between water and bone (□□□~ 2.5 ppm SI), T_2* bi-component fitting of FIDs is at a disadvantage compared to T_2 fitting of CPMG echoes. Surprisingly, ^{2}H IR, which relies on the large T_1 difference between bound and free D_2O, was found to perform less well than T_2 bi-component analysis. This may be due to a distribution of T_1 values within the pore D_2O pool, rendering it impossible to fully null this component. These results show that bi-component fitting of CPMG echo amplitudes is a reliable method for quantification of bound and pore water, while other methods should be used with caution.

References: [1] Borah B. JBMR 2009;25(1):41-7. [2] Anumula S. Bone 2008;42(2):405-13. [3] Nyman JS. Bone 2008;42(1):193-9. [4] Biswas R. Bone 2012;50(3):749-55. [5] Celik H. JMR 2013;236:134-9. [6] Horch RA. MRM 2010;64(3):680-7. [7] Ong HH. JBMR 2012;27(12):2573-81. [8] Seifert AC. NMR Biomed 2013;26:1158-66. [9] Does M. http://www.vuiis.vanderbilt.edu/ ~doesmd/MERA/MERA_Toolbox.html. [10] Yushkevich PA. Neuroimage 2006;31(3):1116-28.

Acknowledgements: NIH R01 AR50068, F31 AG042289, UL1TR000003, and Institution's ITMAT.

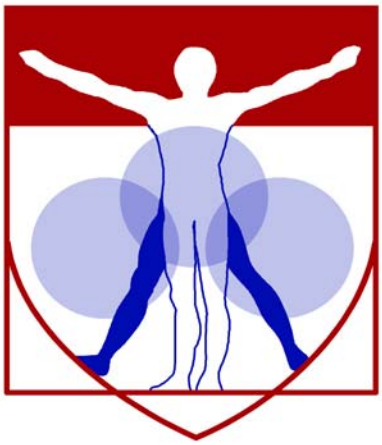

PENN

CENTER for

MUSCULOSKELETAL

DISORDERS

Molecular Profiling Posters

Painful cervical facet joint injury alters spinal dorsal horn excitatory and inhibitory synapse numbers and astrocytic GLT-1 that is sustained

Meagan E. Ita, Nathan D. Crosby, Ben A. Bulka, Beth A. Winkelstein

The spinal facet joints are a common source of pain. Traumatic facet joint injury in the cervical spine can induce a host of spinal responses characteristic of central sensitization that are also associated with persistent pain. Although spinal hyperexcitability, glial activation and excitatory synaptogenesis have been reported at day 7 after painful facet trauma, it is unknown whether such spinal modifications remain at later times. This study investigated the relationships between pain, spinal synapse numbers, and spinal astrocytic expression of the glutamate transporter, GLT-1, 14 days after facet trauma. Male Holtzman rats underwent either a facet joint stretch or sham surgery (n=5/group); mechanical hyperalgesia was measured for 14 days. At day 14, immunohistochemistry measured co-localization of the pre-synaptic structural protein, bassoon, with each of the excitatory post-synaptic marker, homer1, or the inhibitory post-synaptic marker, gephyrin, separately to quantify excitatory and inhibitory synapses in the dorsal horn. GLT-1 was also co-localized with and normalized to GFAP to quantify astrocytic GLT-1. Hyperalgesia was induced after injury ($p<0.001$). Painful injury induced a significant increase ($p<0.047$) in the number of excitatory synapses in the dorsal horn and a significant decrease ($p<0.003$) in the number of inhibitory synapses. Both total GLT-1 expression and astrocytic GLT-1 ($p<0.047$) increased in the dorsal horn after painful injury. Further, when normalizing astrocytic GLT-1 to total GFAP expression, there is still an increase ($p=0.039$), suggesting that the increase in co-localized GLT-1 and GFAP is not simply due to increased GFAP immunoreactivity after painful injury. The shift in synapse distribution after injury supports the notion that structural plasticity in the spinal cord is sustained after painful facet trauma and likely contributes to the maintenance of joint pain. The increased astrocytic activation is consistent with other reports, whereas the increase in spinal GLT-1 is opposite prior work with this model showing decreases at day 7 in spinal GLT-1 using western blot. However, intrathecal inhibition of GLT-1 has been reported to attenuate neuropathic and inflammatory pain, suggesting that increased GLT-1 in the current findings may contribute to pain. Additional work is needed to define the mechanistic role of GLT-1 in maintaining joint-mediated pain, as well as the relationships between astrocytic responses and synaptogenesis. Nonetheless, these findings implicate long-term modifications of spinal plasticity in pain maintenance after even a transient joint trauma that produces chronic pain.

Failed Vertebral Bone Formation in Mucopolysaccharidosis VII is Associated with Aberrant Sox9 Regulation and Altered Wnt Signaling

Sun H. Peck[1], Eileen M. Shore[1], Neil R. Malhotra[1], George R. Dodge[1], Margret L. Casal[1], Maurizio Pacifici[2], Mark E. Haskins[1], Lachlan J. Smith[1]

[1]Univeristy of Pennsylvania, Philadelphia, PA; [2]Children's Hospital of Philadelphia, Philadelphia, PA

Introduction: Mucopolysaccharidosis (MPS) VII is a lysosomal storage disorder defined by deficient β-glucuronidase activity that results in abnormal accumulation of glycosaminoglycans [1, 2]. MPS VII presents with severe spine disease associated with failed vertebral cartilage-to-bone conversion during postnatal growth [3]. Progressive kyphoscoliosis significantly increases mortality [4, 5]. Our objective was to establish the molecular basis of failed vertebral endochondral bone formation in MPS VII using the naturally-occurring canine model, which exhibits a similar disease phenotype to humans [6]. Our specific aims were to identify 1) the stage of failed chondrocyte differentiation in MPS VII vertebral epiphyses and 2) dysregulation of relevant biological pathways using whole-transcriptome sequencing (RNA-Seq).

Methods: Previously, we identified the developmental window when failed vertebral bone formation first manifests (between 9 and 14-days of age) in MPS VII dogs [7]. For this study, we collected vertebral epiphyseal tissue from unaffected control and MPS VII dogs at both ages (n=5, all groups) and measured mRNA levels of chondrocyte differentiation markers using qPCR, Sox9 protein levels using immunoblotting, and global gene expression using RNA-Seq.

Results: SOX9 mRNA was downregulated at 14 days compared to 9 days in both control and MPS VII dogs, but Sox9 protein expression decreased only in controls (Fig A, B). Expected mRNA increases for subsequent differentiation stage markers (RUNX2, PTH1R, MEF2C, COL10A1) at 14 days were seen only in controls. RNA-Seq identified many more differentially expressed genes between control and MPS VII tissue at 14 days as compared to 9 days. Wnt/β-catenin signaling was the top dysregulated bone formation pathway at both 9 and 14 days, with 14 and 54 pathway-associated genes significantly differentially expressed, respectively. RNA-Seq revealed significant downregulation of key inhibitory elements and activating signaling molecules of this pathway at both ages in MPS VII compared to controls, with differences more pronounced at 14 days compared to 9 days-of-age (Fig C).

Discussion: Our data suggest that both unaffected and MPS VII chondrocytes receive regulatory signals to exit the proliferative stage as indicated by downregulation of SOX9 mRNA at 14 days. However, aberrant persistence of Sox9 protein in conjunction with low expression of late-differentiation stage markers in MPS VII suggests that aberrant Sox9 protein processing may contribute to abnormal chondrocyte differentiation. Downregulation of both inhibitory and activating molecules in the Wnt pathway suggests MPS VII cells experience decreased Wnt signaling but are unable upregulate compensatory responses. These results provide the basis for further mechanistic investigations of bone disease in MPS and implicate the Wnt/β-catenin pathway as a potential therapeutic target.

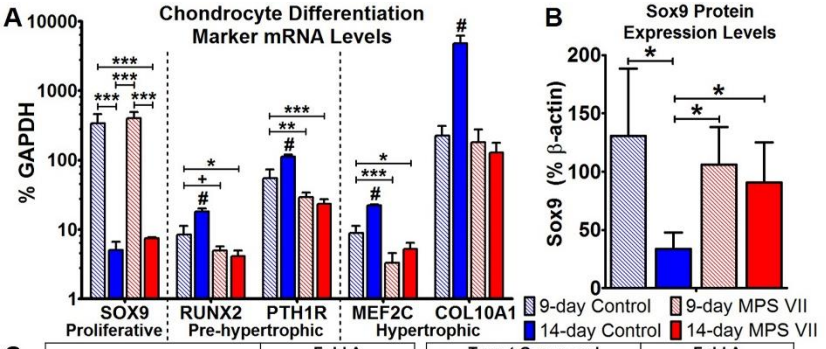

C

Antagonists and Inhibitors	Fold Δ 9-days	Fold Δ 14-days
WIF1	-2.9	-38.4
SOST	NC	-5.6
DKK1	NC	1.6
DKK2	NC	-5.0
DKK3	2.1	3.2
WNT5A	-2.1	-2.7

Target Genes and Activators	Fold Δ 9-days	Fold Δ 14-days
CTNNB1 (β-Catenin)	NC	-1.4
WNT2B	NC	-3.6
WNT4	NC	-3.8
LEF1	NC	-1.9
TCF7	NC	-4.2
WLS	-1.3	-1.7

Figure. A) mRNA expression levels of chondrocyte differentiation markers in vertebral epiphyseal cartilage of unaffected control and MPS VII dogs at 9 and 14-days of age. **B)** Sox9 protein levels in vertebral epiphyseal cartilage of control and MPS VII dogs at 9 and 14-days of age. **C)** Gene expression fold changes (all $p<0.05$) of key antagonists and activators of Wnt/β-catenin pathway in MPS VII vertebral epiphyseal chondrocytes compared to controls at 9 and 14 days, identified by RNA-Seq. (Green: downregulated in MPS VII; Red: upregulated in MPS VII; NC: no significant change). (N=5 for all groups. Statistical analyses with 2-way ANOVA and post-hoc Tukey's test. #$p<0.001$ for 14-day controls compared to all other groups, ***$p<0.001$, **$p<0.01$, *$p<0.05$, +$p<0.1$.)

References:

1. Sly, W.S., et al., J Pediatr, 1973. **82**(2): p. 249-57.
2. Vogler, C., et al., Mod Pathol, 1994. **7**(1): p. 132-7.
3. Smith, L.J., et al., Molecular Genetics & Metabolism, 2012. **107**(1-2): p. 153-60.
4. Pizzutillo, P.D., et al., J Pediatr Orthop, 1989. **9**(1): p. 76-8.
5. de Kremer, R.D., et al., Am J Med Genet, 1992. **44**(2): p. 145-52.
6. Haskins, M.E., et al., 1984. **18**: p. 980-984.
7. Peck, S.H., et al. *Orthopaedic Research Society Transactions*. 2015. Las Vegas.

Acknowledgments: The authors thank Dr. John Tobias for bioinformatics support, and Ms. Patricia O'Donnell, Ms. Caitlin Fitzgerald, and Ms. Therese Langan for animal care.

Impaired Wnt Signaling Contributes to Delayed Chondrocyte Differentiation in Mucopolysaccharidosis VII Dogs

Sun H. Peck[1], Eileen M. Shore[1], Neil R. Malhotra[1], John W. Tobias[1], Maurizio Pacifici[2], Mark E. Haskins[1], Lachlan J. Smith[1]

[1]University of Pennsylvania, Philadelphia, PA; [2]The Children's Hospital of Philadelphia, Philadelphia, PA

Disclosures: SHP (N), EMS (N), NRM (N), JWT (N), MP (N), MEH (4-BioMarin Pharmaceutical Inc.), LJS (N)

Introduction: Mucopolysaccharidosis (MPS) VII is a lysosomal storage disorder characterized by mutations in the β-glucuronidase (GUSB) gene. Impaired GUSB enzyme activity leads to the incomplete digestion and progressive accumulation of heparan, chondroitin, and dermatan sulfate glycosaminoglycan (GAG) byproducts [1]. MPS VII presents with severe skeletal manifestations, which are particularly prevalent in the spine. Vertebral dysplasia due to failed cartilage-to-bone conversion during postnatal development leads to kyphoscoliosis and spinal cord compression, significantly reducing patient quality of life and life expectancy [2, 3]. Using the naturally-occurring canine model, we previously identified the developmental stage (between 9 and 14 days-of-age) when failed vertebral bone formation first manifests in MPS VII [4] and subsequently found that resident chondrocytes in the vertebral epiphyseal cartilage fail to undergo hypertrophic differentiation (Fig 1). GAGs perform crucial roles in the distribution and availability of many secreted signaling molecules that regulate chondrocyte differentiation [5, 6]. We hypothesized that aberrant GAG accumulation in MPS VII epiphyseal cartilage disrupts these signaling pathways, preventing initiation of chondrocyte differentiation at the appropriate developmental stage. Our objectives in this study were to 1) establish pathways that fail to activate in MPS VII epiphyseal cartilage using whole-transcriptome sequencing (RNA-Seq) and 2) examine cellular responses to related secreted growth factors using a cartilage explant model.

Methods: With IACUC approval, vertebral epiphyseal cartilage from unaffected control and MPS VII dogs was collected postmortem at 9 and 14 days (n=5 all groups, schematic, Fig 1B). High quality total RNA (RIN>7) was extracted from each sample, and RNA-Seq libraries were prepared using the TruSeq mRNA stranded kit (Illumina; San Diego, CA). Paired-end, 100-base pair sequencing was performed (Illumina HiSeq 2500) and results mapped to the canine genome. Differential gene expression between all groups was determined with DESeq2 [7], with litter as a covariate and adjusted for false discovery rate (significance, $p<0.05$). Differential mRNA expression was confirmed using qPCR, and nuclear β-catenin protein levels were measured via Western blots and densitometry. For explant culture studies, vertebral epiphyseal cartilage explants from 9 day control (n=4) and MPS VII (n=2) animals were cultured for 1, 3, or 7 days in serum-free medium (α-mem, 0.1% BSA, 1% PSF) in the presence or absence of 500 ng/mL Wnt3a (R&D, Minneapolis, MN). Following culture, RNA was isolated from explants and SOX9 mRNA expression was determined using qPCR. Significance ($p<0.05$) was established with 2-way analyses of variance and post-hoc Tukey's tests (RNA-Seq confirmatory mRNA and protein expression) or unpaired t-tests (cell culture mRNA expression).

Results: Principal component analysis (PCA) of global gene expression from RNA-Seq showed distinct clustering of each sample group (Fig 2A), indicating clear effects of both age and disease state between all groups. A total of 411 and 1104 genes were significantly differentially expressed with a fold-change greater than 2 between control and MPS VII at 9 and 14 days, respectively. The Wnt/β-catenin pathway was identified as the top dysregulated bone formation pathway at both ages with 14 and 54 pathway-associated genes differentially expressed at 9 and 14 days, respectively. Specifically, there was significantly lower expression of both key inhibitory elements and activating molecules in MPS VII compared to controls, verified by qPCR (Fig 2B). Immunoblots showed significantly higher levels of nuclear β-catenin protein at 14 compared to 9 days in controls but no change in MPS VII (Fig 2C). Control explants treated with Wnt3a exhibited a significant decrease in SOX9 mRNA after 1 and 3 days. After 3 and 7 days, untreated control explants also exhibited a significant decrease in SOX9 expression (Fig 3). In contrast, MPS VII explants exhibited no significant response to Wnt3a at day 1, but did exhibit significant decreases in SOX9 mRNA after 3 and 7 days of treatment. Unlike untreated controls, untreated MPS VII explants did not show decreased SOX9 expression after 3 or 7 days.

Discussion: Wnt/β-catenin signaling regulates both the timing and rate of chondrocyte differentiation during endochondral ossification [8, 9]. Our results demonstrate that in MPS VII epiphyseal cartilage, Wnt/β-catenin signaling does not activate at the appropriate developmental stage to initiate and sustain chondrocyte differentiation. Lower expression of both inhibitory and activating molecules in the Wnt pathway suggests that MPS VII chondrocytes experience decreased Wnt signaling but are unable to upregulate compensatory responses. Sustained low levels of nuclear β-catenin protein expression from 9 to 14 days in MPS VII is consistent with this mechanism. Wnt3a is the prototypical activator of Wnt/β-catenin signaling, potentiating chondrocyte maturation and subsequent bone formation [10]. Downregulation of SOX9 expression is necessary for chondrocytes to proceed from proliferation to hypertrophy [11]. Control explants (with healthy chondrocytes) treated with Wnt3a exhibited an immediate decrease in SOX9; further, with increasing culture time, untreated control explants exhibited decreased SOX9, suggesting an intrinsic propensity of healthy cells to mature towards hypertrophy even in the absence of exogenous signals. In contrast, MPS VII explants exhibited a delayed response to Wnt3a treatment, and in the absence of Wnt3a continued to express high levels of SOX9 after 3 and 7 days, suggesting an intrinsic inability of diseased cells to both respond to exogenous signals and transition from proliferation to hypertrophy. These results provide the basis for further mechanistic investigations of skeletal disease in MPS VII and identify the Wnt/β-catenin pathway as a potential therapeutic target.

Significance: MPS VII is associated with severe skeletal disease for which there are currently no effective treatments. This study identifies the Wnt/β-catenin pathway as a promising target for therapeutic intervention in MPS VII.

References: [1] Sly+ J Pediatr, 1973. [2] Pizzutillo+ J Pediatr Orthop, 1989. [3] de Kremer+ Am J Med Genet, 1992. [4] Peck+ ORS Trans, 2015. [5] Cortes+ Development, 2009. [6] Jochmann+ Matrix Biol, 2014. [7] Love+ Genome Bio, 2014. [8] Enomoto-Iwamoto+ Dev Bio, 2002. [9] Tamamura+ J Biol Chem, 2005. [10] Parr+ Development, 1993. [11] Dy+ Dev Cell, 2012.

Acknowledgments: Funding sources: NIH; Penn Center for Musculoskeletal Disorders; National MPS Society. The authors thank Dr. Margret Casal, Ms. Patricia O'Donnell, Ms. Caitlin Fitzgerald, and Ms. Therese Langan for animal care.

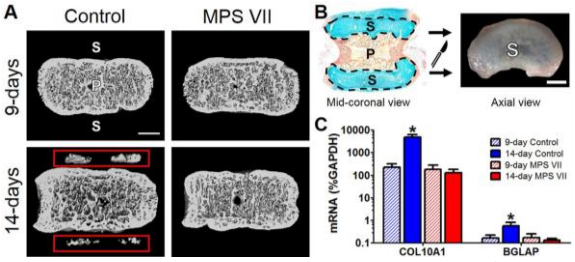

Figure 1. Representative mid-coronal microCT images of T7 vertebrae. Red boxes: bone formation in secondary ossification centers in 14-day control animals. **B.** Schematic of vertebral epiphyseal cartilage excision (mid-coronal ABPR-stained histological section). **C.** mRNA levels of COL10A1 (hypertrophic marker) and BGLAP (bone marker) in vertebral epiphyseal cartilage at 9 and 14 days-of-age. N=5; scale=1mm; *p<0.05 vs all. S: Secondary and P: Primary ossification center.

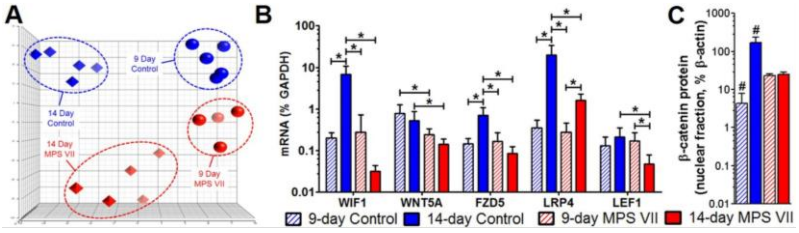

Figure 2. A. RNA-Seq PCA plot. **B.** mRNA levels of Wnt/β-catenin signaling pathway genes measured by qPCR. **C.** Nuclear β-catenin protein expression in control and MPS VII vertebral epiphyseal chondrocytes. N=5; *p<0.05; #p<0.05 vs all.

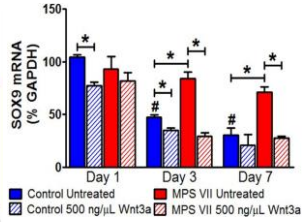

Figure 3. SOX9 mRNA for control (n=4) and MPS VII (n=2) explants with Wnt3A treatment after 1, 3 and 7 days. *p<0.05, #p<0.05 vs day 1.

Whole-Transcriptome Profiling of Notochord-Derived Cells during Embryonic Nucleus Pulposus Formation

Sun H. Peck[1], Kendra K. McKee[2], Neil R. Malhotra[1], John W. Tobias[1], Robert L. Mauck[1], Brian D. Harfe[2], Lachlan J. Smith[1]

[1]University of Pennsylvania, Philadelphia, PA; [2]University of Florida, Gainesville, FL

Disclosures: SHP (N), KKM (N), NMR (N), JWT (N), RLM (N), BDH (N), LJS (N)

Introduction: Intervertebral disc degeneration is implicated as a major cause of low back pain [1], necessitating new therapeutic strategies that alleviate symptoms as well as restore disc structure and mechanical function. The earliest degenerative changes occur in the central nucleus pulposus (NP), where altered composition initiates a cascade that compromises mechanical function and culminates in structural failure. An impediment to the development of cell-based strategies for NP repair is the unique developmental origin of the NP, as NP cells are derived from the notochord and not the mesenchyme [2-4]. Improved understanding of embryonic NP formation may enable recapitulation of developmental signals that might drive therapeutic cell types, such as mesenchymal stem cells, towards an NP cell-like phenotype to optimize adult disc regeneration. The objective of this study was to establish changes in global mRNA expression profiles of resident cells as the notochord transforms into the NP using whole-transcriptome sequencing (RNA-Seq), focusing on signaling pathways that regulate patterning, growth, differentiation, structural extracellular matrix (ECM) molecules, and putative NP cell-specific markers.

Methods: For these studies (IACUC approved), we used the Shh-cre;ROSA:YFP mouse model [3], which takes advantage of the fact that all notochordal cells express the morphogen Sonic Hedgehog (SHH), while the cells of the surrounding mesenchyme do not. In this model, SHH-expressing cells also express YFP, enabling isolation of pure populations of notochord-derived cells at any developmental stage. Two key developmental stages were examined: embryonic day 12.5 (E12.5, immediately prior to initiation of the notochord to NP transformation) and postnatal day 0 (P0, fully formed NP) (Figs 1A, B). Each biological replicate (n=4, both groups) consisted of pooled embryos or pups (~6) from one litter. E12.5 RNA was extracted from isolated notochords, and P0 RNA was extracted from YFP-positive cells isolated using fluorescence-assisted cell sorting (Fig 1C). High quality total RNA (RIN>7) was isolated from each sample and RNA-Seq libraries prepared using the TotalScript Kit (Illumina; San Diego, CA). Single-end, 100-base sequencing was performed (Illumina HiSeq 2500) and results aligned to the mouse genome. Differential gene expression was established using DESeq2 [5] with significance as $p<0.05$.

Results: Principal component analysis (PCA) revealed clear differences in global mRNA abundance between E12.5 and P0 (Fig 2). There were >4600 genes significantly differentially expressed with fold-changes greater than 2. There was significantly higher mRNA abundance of ECM structural genes, including proteoglycans (aggrecan (ACAN); brevican (BCAN); biglycan (BGN); decorin (DCN)) and collagens (COL1A1, COL6A1, COL10A1), at P0 compared to E12.5 (Fig 3A). Examining signaling pathways known to regulate skeletal patterning, growth, and differentiation, there was significantly lower mRNA abundance of Shh pathway activators including ligand (SHH), receptors (Patched1 (PTCH1); Smoothened (SMO)), and transcription factors (GLI1, 2, 3) (Fig 3B). A large number of genes associated with the TGF-β pathway were also differentially expressed at P0 compared to E12.5, including 11.2 and 3.9-fold increases in TGFB1 and TGFBR2, respectively (Fig 3C). Furthermore, many genes of the Wnt signaling pathway were differentially expressed at P0, including pathway ligands such as WNT7B, modulators such as SFRPs (secreted frizzled-related proteins), and downstream target genes, AXIN2, CD44, and MYC (Fig 3D). Finally, we examined differential expression of molecules considered to be specific markers of the NP cell phenotype [6]. Many such markers exhibited stable expression across the E12.5 to P0 developmental window, including brachyury (T), keratins 8 and 18 (KRT8, KRT18), and hypoxia-induced factor (HIF1A). Others exhibited significant changes in expression from E12.5 to P0, including keratin 19 (KRT19, 2.9-fold increase), carbonic anhydrase 3 (CAR3, 8.3-fold increase), carbonic anhydrase 12 (CAR12, 4.6-fold decrease), and vimentin (VIM, 5.7-fold increase).

Discussion: The large number of differentially expressed genes at P0 compared to E12.5 is not surprising given the substantial morphological changes occurring in this developmental window. Changing expression levels of ECM and signaling molecules likely reflect a switch from patterning (altered Shh and Wnt signaling) to growth (increased TGF-β signaling and ECM) as the NP develops into a functional, load-bearing tissue. TGF-β signaling has previously been identified as critical for disc development [7], and our findings support those results. Differential expression of many Shh and Wnt pathway genes supports the changing role of these pathways at the intersection of the embryonic and postnatal phases of development [8]. Analysis of putative NP markers [6] also showed significant differential expression at P0 when compared to E12.5. Ongoing work will validate these RNA-Seq results and establish the effects of targeted activation or inactivation of these signaling molecules on embryonic disc formation and postnatal growth. NP markers found to exhibit stable expression throughout embryonic development may be the most faithful indicators of a cell's notochordal origin, although the importance of many of these markers in the context of adult function and regenerative therapeutics remains to be fully elucidated. Our long term goal is to establish and recapitulate the specific developmental signals required for embryonic NP formation in order to improve cell-based therapeutic strategies for disc regeneration.

Significance: Low back pain associated with intervertebral disc degeneration is a significant global health issue. The results from this study will inform the development of improved cell-based therapeutics for disc regeneration.

References: [1] Andersson. Lancet, 1999. [2] Smith+ Dis Model Mech, 2011. [3] Choi+ Dev Dyn, 2008. [4] McCann+ Dis Model Mech, 2012. [5] Love+ Genome Bio, 2014. [6] Risbud+ J Orthop Res, 2015. [7] Sohn+ BMC Dev Biol, 2010. [8] Winkler+ PLoS ONE, 2014.

Acknowledgements: NIH, Penn Center for Musculoskeletal Disorders, Department of Veteran's Affairs.

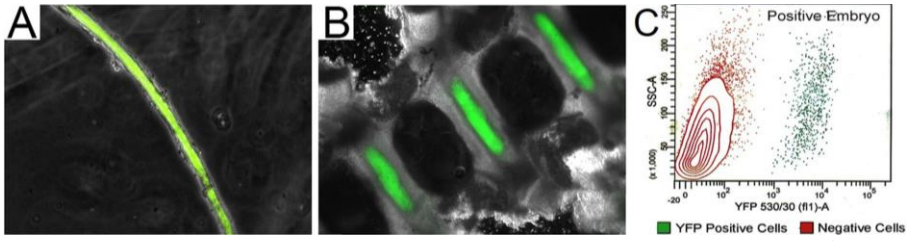

Figure 1. A. E12.5 YFP-positive notochord. **B.** P0 spine with YFP-positive NP. **C.** FACS plot of isolated YFP-positive notochord-derived cells.

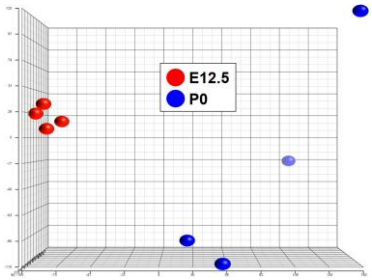

Figure 2. RNA-Seq PCA plot. N=4.

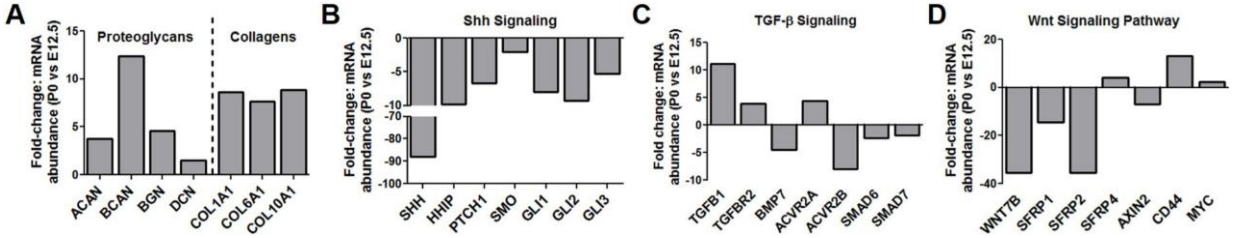

Figure 3. Fold-change in mRNA expression of P0 vs E12.5 cells. A. ECM structural genes. **B.** Shh pathway genes. **C.** TGF-β pathway genes. **D.** Wnt pathway genes. N=4; all $p<0.05$.

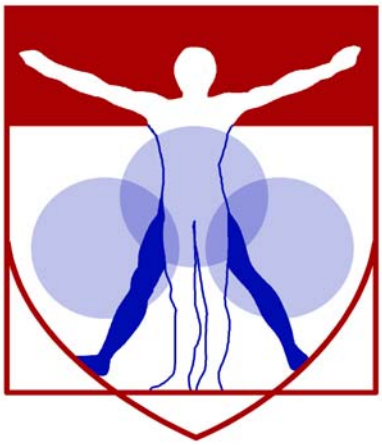

PENN

CENTER for
MUSCULOSKELETAL
DISORDERS

Miscellaneous Abstracts

Optimizing Manipulation of Septal Cartilage for Reconstructive Rhinoplasty Applications

Robert M. Brody MD[1,2], Robert Lyman, Ivy Gandy, Bhavana Mohanraj[1], Gregory R. Meloni[1], Oren Friedman MD[2], George R. Dodge PhD[1]
[1]McKay Orthopaedic Research Laboratory, University of Pennsylvania, Philadelphia, PA, USA;
[2]Department of Otorhinolaryngology – Head & Neck Surgery, University of Pennsylvania, Philadelphia, PA, USA

DISCLOSURES: No disclosures for any author.

INTRODUCTION: The surgical repair of traumatic, congenital, cosmetic, and oncologic nasal deformities often requires significant cartilage augmentation to reconstruct a functionally and aesthetically acceptable nose [1]. With decreased inflammatory reactions and extrusion rates when compared to allograft or synthetic materials, cartilage autografts are the preferred material in providing structural support and bulk to improve aesthetic appearance. These grafts are harvested from the nasal septum during septoplasty or from the auricle of the external ear. In order to fit a specific defect with a unique contour, these grafts must be mechanically manipulated to overcome their inherent rigidity and non-deformability. These crushing injuries and sharp dissection may induce chondrocyte death and leeching of extracellular matrix (ECM), resulting in variable degrees of autograft stability and resorption, directly impacting cosmetic and functional outcomes [2-4]. Although there is an extensive amount of information regarding injury of articular cartilage in the orthopaedic literature, knowledge regarding the chondrocyte homeostasis and mechanisms of injury within hyaline and elastic cartilages of the head and neck is limited. Herein, using manipulative approaches that are clinically relevant, we describe the specific changes that occur within nasal septal cartilage explants after they have been manipulated by various blunt and sharp injuries.

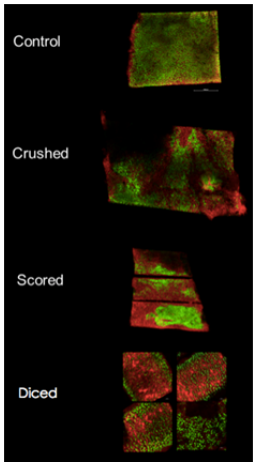

Figure 1: Live/Dead Assay of human nasal septal cartilage 48 hours after injury.

METHODS: Initial investigations were performed on specimens of discarded human nasal septal cartilage was performed. This specimen was split into 4 samples: a control sample that remained uninjured, a scored sample with partial thickness incisions along its surface, a diced sample consisting of 1mm cubes, and a crushed sample using the Cottle Cartilage Crusher (Surgipro Inc.). These samples were maintained in tissue culture for 48 hours. A Live/Dead assay (Live/Dead Viability/Cytotoxicity Kit, Life Technologies, NY) was then performed on these samples. Following this, four bovine nasal snouts were obtained. The cartilaginous nasal septum was excised from each snout and subsequently split into five experimental conditions: control, crushed, scored, diced, shaved. These cartilaginous samples were then maintained in tissue culture for up to nine days with sampling outcomes at 2 and 9 days. Portions of tissuse was either fixed in 4% PFA or digested in Proteinase-K for GAG and DNA assessments or gene expression analysis, . Histologic analysis performed using the Safranin-O/Fast Green stain to identify changes in glycosaminoglycan (GAG) representative of proteoglycan loss. DNA content was measured in the digested samples using the PicoGreen assay and GAG content in the media was assessed using the DMMB assay and normalized by DNA content, as an indicator of ECM degradation. Genes expression representing ECM and catabolism and cell stress were evaluated.

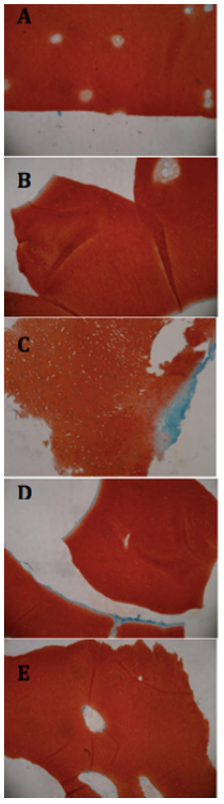

Figure 2: Safranin-0 /Fast Green at 2x magnification. Control (a), scored (b), crushed (c), diced (d), shaved (e)

RESULTS:

During our initial pilot study of human nasal septal cartilage, the Live/Dead assay showed diffuse cell death in areas adjacent to fracture (crushing) or sharp dissection (scored and diced) (Fig 1). There are gross changes seen in each manipulated cartilage sample after nine days in tissue culture (Fig 2) including curvature of the scored and shaved pieces over time. Additionally, crushing and shaved injuries resulted in a marked increase in GAG release to the media as compared to scoring and dicing injuries (Fig 3). Safranin O/Fast Green staining showed diffuse decreased staining in crushed samples indicating loss of GAG.

DISCUSSION:

In this study, matrix release and chondrocyte viability are differentially affected by the modality of injury in cartilage explants. The differences observed may be due to the amount of surface area exposed as a result of injury, as increasing the exposed surface area seems to trend with greater GAG release and cell death. These changes may are indicative of absorption and breakdown of an autograph which will lead to higher rates of cosmetic deformities and a lack of functional stability in vivo. Further evaluation of chondrocyte phenotype and cell stress markers will enhance our understanding of the effects of mechanical manipulation of cartilage and can be applied to areas outside of facial surgery including otologic and airway surgery.

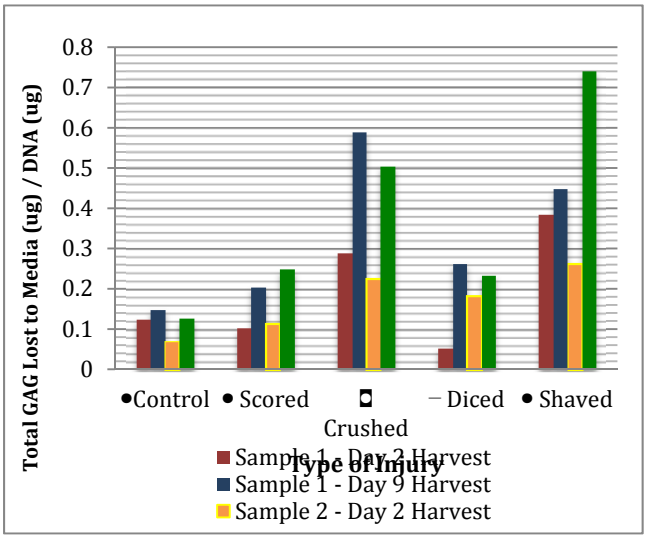

Figure 3: GAG content lost to media over 2-day incubation period and 9-day incubation period.

SIGNIFICANCE:

This study demonstrates that mechanical manipulation of septal cartilage differentially affects matrix release and chondrocyte viability which may ultimately impact function in clinical repair of nasal deformities.

REFERENCES:

[1]Cannady+ Facial Plast Surg Clin N Am. 2009; [2] Cakmak+ Arch Facial Plast Surg. 2005; [3] Lattyak Arch Facial Plast Surg. 2003; [4] Ale de Souza+ Arch Facial Plast Surg. 2008

ACKNOWLEDGEMENTS: This study was funded in part by the American Academy of Facial Plastics Leslie Bernstein Grant Resident Research Grant and the Penn Center for Musculoskeletal Diseases.

Injectable hydrogel delivery system for cells and growth factors to enhance vascularization

Minna H. Chen, Jason A. Burdick

Decreased blood flow to the extremities due to atherosclerosis is characteristic of peripheral artery disease, which affects millions of aging Americans and can result in a significant decline in quality of life. Growth factor and cell therapies have been shown in pre-clinical models to enhance vascularization and improve perfusion. However, targeted growth factor and cell delivery is important. We describe an injectable hydrogel of hyaluronic acid modified with adamantane and β-cyclodextrin groups for improved retention of cells at the injection site, which combined with hyaluronic acid and heparin microgels can control release of platelet derived growth factor (PDGF). Prior work has shown that delivery of endothelial progenitor cells with this hydrogel results in enhanced vasculogenesis compared to delivery of hydrogel or cells alone. Future work will evaluate the cell and growth factor combination therapy described in a mouse model of hind limb ischemia.

A New Mouse Model to Study Skeletal Muscle Stem Cell Heterogeneity

Christopher Greer, Elisia D. Tichy, Nicholas Oyster, and Foteini Mourkioti
McKay Orthopedic Research Laboratory, University of Pennsylvania, Philadelphia PA

Satellite cells are adult skeletal muscle stem cells that mediate skeletal muscle regeneration in response to both acute injury and chronic degenerative states. Isolation of satellite cells is critical for dissecting the signaling pathways responsible for mediating the regenerative potential of these cells, as well as the pathways that inhibit their regenerative potential in diseased states. Traditional satellite cell isolation methods rely on both negative and positive selection of cells expressing various cell surface markers. However, because the satellite cell population is extremely heterogeneous with respect to expression of the various cell surface markers used to isolate them, this method results in the exclusion of various satellite cell sub-populations that fail to meet the selection criteria. Because Pax7 is expressed by >99% of all sublaminal satellite cells, we've generated a novel transgenic mouse line in which EGFP is driven by a Pax7 promoter and therefore allows for isolation of the entire satellite cell population. With this mouse, we have identified distinct satellite cell sub-populations based on the EGFP expression level and we demonstrate that the relative abundance of each population decreases with age. Here, we present the characterization of this transgenic mouse line and we will further validate the relative regenerative potential of each satellite cell sub-population following transplantation into the mdx/mTR muscular dystrophy mouse model.

Differential Effects of Growth Factors on Neonatal and Adult Achilles Tenocytes

Huegel J; Mauck RL; Soslowsky LJ; Kuntz AF
McKay Orthopaedic Research Laboratory, University of Pennsylvania, Philadelphia, PA
andrew.kuntz@uphs.med.upenn.edu

INTRODUCTION: Tendon tears in adults are a common orthopaedic problem and often fail to heal even after surgical repair. Neonatal healing is superior to adult healing across multiple tissue types [1], and immunohistochemical studies in tendons have shown age-related differences in matrix composition and growth factor expression [2-4]. However, it is not known whether adult cells have an innate inability to synthesize matrix and initiate a successful repair, or whether the adult wound environment lacks sufficient presentation of growth factor stimuli to affect repair. During the repair process, several growth factors act as cues to initiate and regulate cellular responses such as cell proliferation and extracellular matrix production. Therefore, we hypothesized that neonatal tendon cells would be more responsive than adult cells to two growth factors that are upregulated during tendon healing [5]: transforming growth factor β3 (TGFβ3) and basic fibroblast growth factor (bFGF).

METHODS: Achilles tendons were harvested from postnatal day 3 (P3, neonatal) and five month old (adult) male Sprague-Dawley rats. Tendons were finely diced and placed in culture dishes with Dulbecco's modified Eagles medium (DMEM) supplemented with 10% fetal bovine serum (FBS) and antibiotics. Cells migrated out of the tissue and were expanded to confluence. To evaluate age and growth factor effects on tenocyte migration, a transwell assay (8 micron, Millipore) was performed with 3 concentrations [6-9] of TGFβ3 and bFGF. Cells were plated at 2 x 10^5 cells/ml and incubated for 6 hours with the specified factor in serum-free DMEM. Migration towards growth factor supplemented media was normalized to cell migration towards serum-free DMEM. To evaluate proliferative effects of growth factors, cells were plated at 5000 cells per well in a 96 well plate and treated with either TGFβ3 or bFGF in phenol-free DMEM supplemented with 2.5% FBS. MTT assays (Life Technologies) were performed on days 3 and 6. To quantify the effect of growth factors on collagen production, a Sircol collagen assay (Biocolor) was performed. Cells were plated in 12 well dishes at 1 x 10^5 cells per well and treated with TGFβ3 or bFGF in DMEM supplemented with 2.5% FBS. After 6 days, aliquots of media were complexed with Sircol dye reagent and analyzed colorimetrically. 2-way ANOVA with repeated measures with follow-up t-tests between groups at each time point were performed with statistical significance set at $p<0.05$ and trends at $p<0.1$.

RESULTS:
Tenocyte Proliferation: After three days, all concentrations of growth factors induced a significant increase in proliferation in adult cells, whereas neonatal cells only trended towards greater proliferation (Fig 1). After six days, adult cells continued to respond to bFGF but not to TGFβ3 (Fig 1). Higher concentrations of both bFGF and TGFβ3 induced significantly more neonatal cell proliferation than control cultures.
Tenocyte Migration: At 6 hours, all concentrations of bFGF and TGFβ3 induced greater migration than serum-free media (Fig 2). Similar to the proliferative response, a greater number of neonatal cells migrated towards 10% FBS supplemented media than adult cells. *Collagen production:* In adult cells, TGFβ3 increased collagen production compared to basal media (Fig 3). In contrast, neonatal cells were more responsive to bFGF. Most interestingly, neonatal cells produced greater than two-fold more collagen than adult cells at baseline conditions (2.5% FBS in DMEM). When treated with 10% FBS, both types of cells produced a quantity of collagen above the detectable range of the assay.

DISCUSSION: During tendon healing, growth factor cues stimulate cell proliferation and migration to the site of injury, as well as collagen deposition and reorganization. Our data show that both neonatal and adult tenocytes respond to exogenous growth factors, though the pattern of response differs based on cell age. Adult cells proliferated and migrated similarly to neonatal cells in response to growth factors, suggesting that these cells are capable of responding to stimuli to initiate a healing response. Along with previously reported differences in growth factor expression during aging, the data support the concept that these cells may simply lack growth factor stimuli in their environment. Tissue engineered approaches to tendon healing often include the addition of a growth factor to enhance healing [10]. This *in vitro* data supports the value of growth factor treatments in adult tendons.

While some commonalities in response were noted, major differences between neonatal and adult cells were also delineated. First, neonatal cells responded more robustly to FBS than adult cells. FBS contains a combination of factors including bFGF and TGFβ as well as other factors known to enhance tendon healing such as vascular endothelial growth factor (VEGF) and platelet derived growth factor (PDGF). This combination of factors may be more representative of a biological healing response, where a combination of factors may yield an overall synergistic effect. The increased response in neonatal cells suggests that younger cells have a greater capacity to respond to such a combination of factors than adult cells. Indeed, results suggest that neonatal cells are capable of producing greater than five times more collagen than adult cells over the same period of time. Because the production and reorganization of collagen is vital to the regeneration of such a load-bearing tissue, this result may be the primary distinction between young and old tissue healing. However, the addition of the

highest concentration of TGFβ did increase collagen production in adult cells by two-fold over control treatment, suggesting that stimulation of collagen production in older tissue is feasible. Future studies will establish the type and quality of collagen production after *in vivo* delivery of growth factors to injured tendons in order to determine the optimal dose and delivery timeline.

Significance: The poor intrinsic healing capacity of adults predisposes surgical repair of tendons to potential failure, while fetal and neonatal tissues provide a more robust healing response and can achieve mechanical properties closer to that of uninjured tissue. This study demonstrated that adult tenocytes respond similarly to neonatal cells in some aspects of the healing response, particularly in the response to pro-mitotic and pro-migratory factors, though neonatal cells showed an overall higher level of collagen biosynthesis. More broadly, this study supports the targeted use of exogenous growth factors in tissue-engineered tendon repair approaches in adults.

References: [1] Favata M et al. J Orthop Res. 24, 2006. [2] Smith RKW et al. Mat Biol 16, 1997. [3] Goodman SA et al. Biorheology 41(5), 2004. [4] Galatz L et al. J Orthop Res. 25, 2007. [5] Molloy T et al. Sports Med. 33(5), 2003. [6] Letson AK et al. Clin Orthop Relat Res. 308, 1995. [7] Fukui N et al. Rev Rheum Engl Ed. 65(6), 1998. [8] Manning CN et al. J Orthop Res. 29 (7), 2011. [9] Kashigawi K et al. Scand J Plast Reconstr Surg Hand Surg. 38, 2004. [10] Longo UG et al. Br Med Bull. 98(1), 2010.

Acknowledgements: This study was supported by the University of Pennsylvania Institute on Aging. We thank Jennica Tucker and Ben Freedman for dissection assistance.

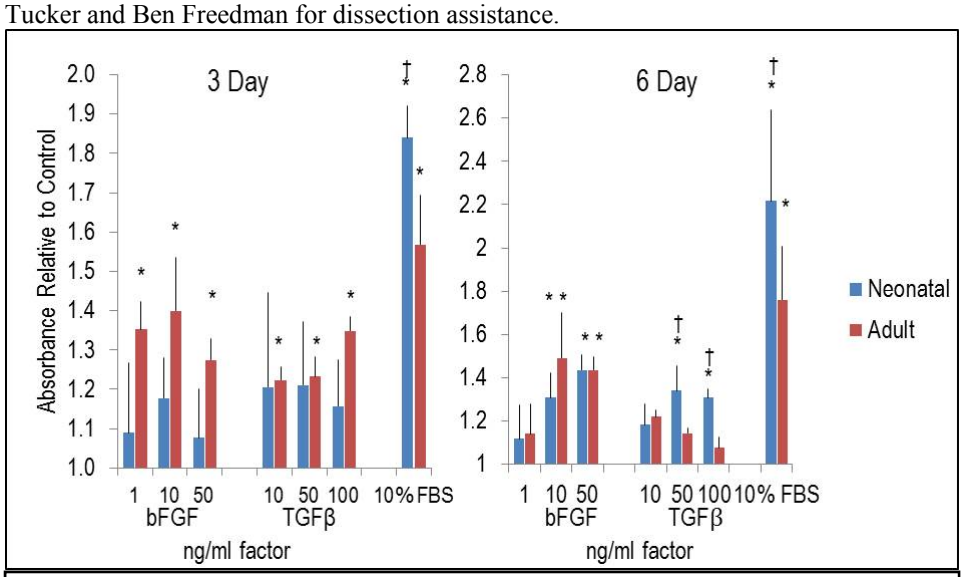

Figure 1. MTT proliferation after 3 and 6 days of growth factor treatment. bFGF and TGFβ induce a mitogenic response early in adult cells, but the response is only sustained by bFGF treatment. Neonatal cells are slower to respond. Asterisks indicate significant differences from control treatments ($p<0.05$). Crosses indicate significant differences between cell types ($p<0.05$).

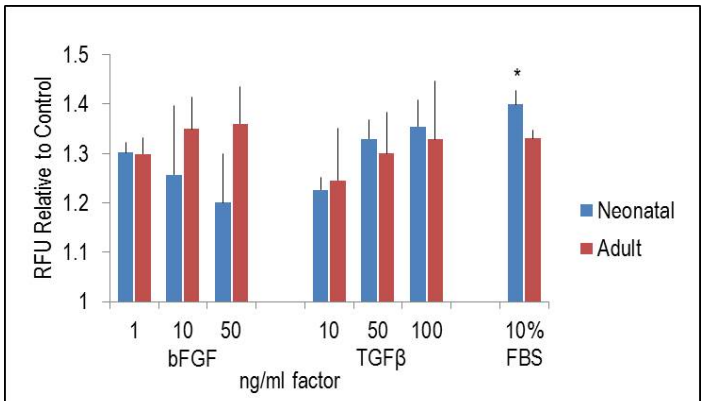

Figure 2. Transwell migration assay. bFGF and TGFβ act as chemotactic agents for every concentration of both factors, with no significant differences between cell types. Asterisks indicate significant differences from control treatments ($p<0.05$).

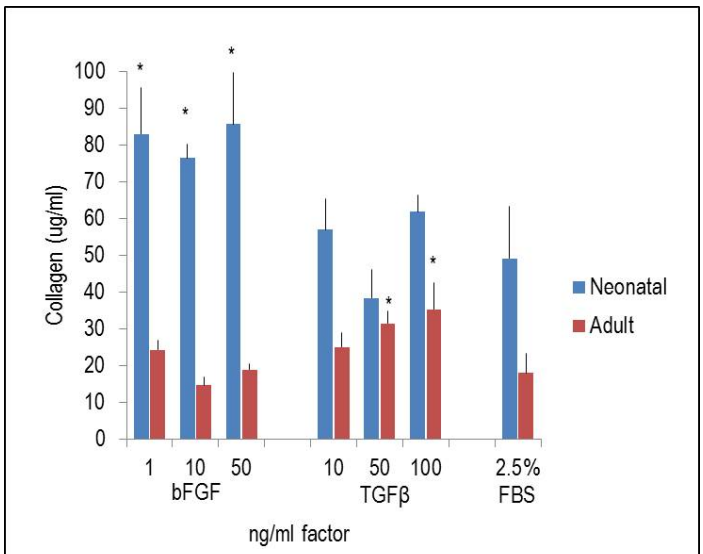

Figure 3. Sircol collagen quantification assay. bFGF induced collagen production in neonatal cells while adult cells were more responsive to TGFβ. Overall, neonatal cells responded more significantly to all treatments including basal media. Asterisks indicate significant differences from control treatments ($p<0.05$). All neonatal groups were significantly higher than adult groups.

Micro-Scale Chondrocyte-Seeded 'Noodle-Like' Constructs to Promote Cartilage Repair with Microfracture

Minwook Kim[1,2], Jason A. Burdick[2], Robert L. Mauck[+1,2]
[1]McKay Orthopaedic Laboratory, Department of Orthopaedic Surgery and [2]Department of Bioengineering, University of Pennsylvania, Philadelphia, PA

Disclosures: Minwook Kim (Y), Jason A. Burdick (Y), Robert L. Mauck (Y)

INTRODUCTION: Chondrocytes (CH) and mesenchymal stem cells (MSC) are commonly used cell sources for cartilage repair. CHs are stable and superior to MSCs in producing functional matrix, but are limited in number and lose their phenotype upon extensive passaging. Conversely, MSCs can be readily expanded and undergo chondrogenesis, but this capacity is attenuated with aging [1]. This is in part why microfracture procedures, which enable MSC entry into a cartilage lesion from the underlying marrow, are contra-indicated in older patients. To overcome this limitation, various studies have employed CH/MSC co-culture systems, and have shown that a small pool of healthy/young CHs can rejuvenate a larger pool of infirm/old MSCs when the two cell types are placed in close proximity to one another [2]. While an interesting finding, this co-culture effect is not altogether clinically relevant, as most studies are performed in larger, cylindrically shaped formats [3]. These constructs not only have the disadvantage of heterogeneous matrix accumulation due to limitations in nutrient transport (making scale-up a challenge), but also would require the ex vivo expansion of two cell types (CH and MSCs), rather than just CHs (as is currently done for ACI procedures). To overcome these obstacles, we set out to create a new micro-scaled tissue engineered platform that takes advantage of co-culture effects while at the same time having the potential for clinical use. Specifically, we designed a CH-seeded micro-scale noodle-shaped construct (micro-noodle) that can be readily implemented in the context of microfracture, allowing bone marrow derived MSCs entering the wound site to percolate into a micro-scaled CH-seeded gel fiber weave. Here, we report on the fabrication of these micro-noodles, investigate their chondro-inductive capacity in an environment mimicking microfracture (MSC-seeded fibrin glue), and evaluate them in an in vitro chondral defect model.

METHODS: Adult porcine MSCs and chondrocytes (CH) were obtained from bone marrow and articular cartilage, and expanded through passage 1-2. In the first study, CHs (red) were labeled using CellTracker and encapsulated at 20×10^6 cells in 1% w/v hyaluronic acid (HA) (Lifecore Biomedical) [4]. Micro-scale noodle-shaped constructs (micro-noodles) were fabricated using a custom-built micro-bore tubing system **(Fig. 1A)**. Cell seeded HA was extruded into a tygon microbore tube, exposed to UV light for 3 minutes to crosslink the gel, and then extruded from the tube. Formed micro-noodles (Ø 0.25 × 70 mm) were cultured in a defined medium with TGF (CM+; 10ng/mL) for 14 days. Cell viability and micro-noodle morphology were evaluated by confocal microscopy, and glycosaminoglycan (GAG) and hydroxyproline contents were measured. In a second study, to mimic the microfracture environment, micro-noodles were mixed with MSCs (CH:MSC ratio = 1:4) in fibrin glue for an additional 14 days (Tisseel, Baxter) [5] **(Fig. 2A)**. Paraffin sections (8μm) were stained with Alcian Blue for proteoglycans (PG) and immunostained for COL I, COL II and chondroitin sulfate (CS). In a final study, to determine whether this technology could be deployed in a chondral defect, micro-noodles were directly injected upon formation into a cartilage defect in an osteochondral unit. The full thickness defect (Ø 4 mm) was then filled with MSCs in fibrin glue (CH:MSC ratio = 1:4) and the entire unit cultured for 28 days in CM+ **(Fig. 3A)**, followed by Safranin-O/fast green staining. These were compared to minced cartilage, with the defect prepared and filled similarly. Significance was determined by two-way ANOVA with Tukey's post hoc ($p<0.05$).

RESULTS: **[Study 1]** Chondrocytes remained viable within micro-noodles, which curled into a random weave and opacified with culture duration **(Fig. 1B)**. The actin cytoskeleton in CHs in micro-noodles was cortical on day 0 **(Fig. 1C)**, but transitioned to a more fibrillar structure as cells divided and aggregated with one another by day 5 **(Fig. 1D)**. GAG content in micro-noodles (86 μg GAG) was similar to that of a standard cylindrical construct of the same volume at day 14 (85 μg GAG; Ø 4.78 × 2.25 mm; data not shown). After 56 days in culture, micro-noodles formed robust matrix that was homogeneous distributed throughout the diameter **(Fig. 1E)**. **[Study 2]** HA micro-noodles pre-cultured for 14 days and combined with MSC-seeded fibrin glue improved chondrogenesis at sites adjacent to the noodles, while fibrin constructs with only MSCs showed little matrix formation, primarily in the periphery. Composites with micro-noodles showed dense PG, Col I, and Col II deposition **(Fig. 2B-G)**. **[Study 3]** When placed in a chondral defect in in vitro organ culture, cells and/or tissues from all groups filled the defect and remained in place **(Fig. 3B-D)**. Micro-noodles that were directly injected were evident within the base of the defect and produced intense safranin O positive matrix staining (**Fig. 3B**, arrows).

DISCUSSION: In this study, we developed micro-scale CH-seeded noodle-shaped constructs that can be combined with current microfracture procedures. The small size of these constructs allowed for efficient nutrient transport, resulting in homogeneous matrix formation throughout the diameter when cultured in vitro. The small size and flexibility of these micro-noodles also makes them suitable for filling various defect sizes and shapes. When first formed, CHs appear as distinct rounded cells (with cortical actin), but rapidly reorganize to form a thin and tough 3D structure that can be manipulated with forceps. Pre-cultured CH-seeded micro-noodles improved MSC chondrogenesis when these two elements were co-cultured in fibrin glue. These micro-noodles could thus be incorporated within bone marrow/marrow concentrate and implanted to improve cartilage repair. Likewise, when the micro-noodles were directly injected into a chondral defect that was filled with MSC-laden fibrin glue, micro-noodles remained in place and deposited cartilage-like matrix. Current studies are aimed at further scaling down the diameter of these micro-noodles and optimizing their ease of use during surgical procedures. Together, these findings show that micro-noodle CH-seeded constructs are a clinically relevant tool that may be used to capitalize on CH/MSC interactions to improve cartilage repair; these micro-noodles are now being evaluated in a large animal cartilage defect model in conjunction with microfracture.

SIGNIFICANCE: CH-seeded micro-scale noodle-shaped constructs are a novel development that takes advantage of co-culture methods in a clinically relevant manner and holds promise for use in the augmentation of current microfracture procedures.

REFERENCES: [1] Kim ORS 2014 [2] Fischer ArthRheum 2010 [3] Buschmann JOR 1992 [4] Burdick Biomacro 2005 [5] Veronesi Stem Cells Dev 2013
ACKNOWLEDGEMENTS: This work was supported by the NIH (R01 EB008722) and the Penn Center for Musculoskeletal Disorders.

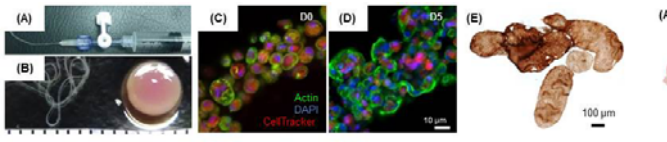

Fig 1. Fabrication of Micro-noodle. (A) Micro-noodle device (ID = 250 μm). (B) Micro-noodle and cylindrical construct after 14 days (marking = 1 mm). (C-D) Structure of micro-noodle under confocal microscopy at day 0 (C) and day 5 (D) (green = actin, blue = DAPI, red = chondrocytes (CellTracker), scale bar = 10 μm). (E) COL II staining at 56 days (scale bar = 100 μm; micro-noodle casted using a glass capillary (ID = 600 μm)).

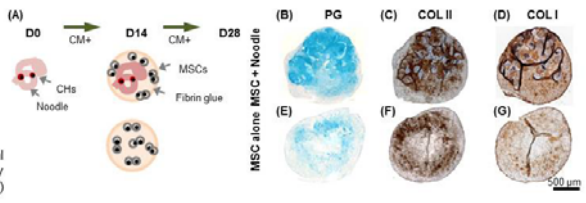

Fig 2. Influence of Micro-noodle in Fibrin glue in vitro (Bone marrow mimicking environment). (A) Schematic of micro-noodle and MSC/fibrin glue culture. (B-G) Histology of fibrin glue construct. (top = noodle/MSC/fibrin glue and bottom = MSC/fibrin glue). (B and E) Alcian blue, (C and F) COL II, (D and G) COL I staining (scale bar = 500 μm).

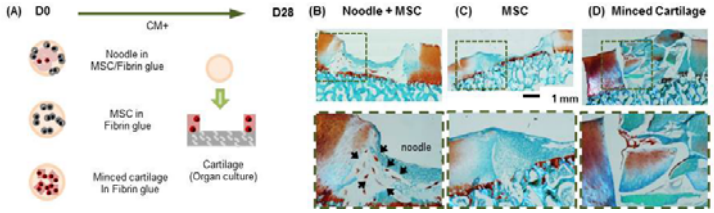

Fig 3. Defect Repair in Organ Culture. (Fibrin glue seeded with various combinations). (A) Schematic of organ culture. (B-D) Safranin-O/fast red staining of organ culture at 28 days. (top = full view of defect, bottom = zoomed view of dashed box at the top). (B) Micro-noodle in MSC/fibrin glue (red indicated by arrows = micro-noodles). (C) MSC/fibrin glue only. (D) Minced cartilage in fibrin glue (scale bar = 1 mm).

Influence of N-Cadherin Peptide Dose and Timing on MSC Chondrogenesis in 3D HA Hydrogels

Mi Kwon, Sebastián L. Vega, Robert L. Mauck, Jason A. Burdick.
University of Pennsylvania, Department of Bioengineering.

Introduction: In the condensation phase of chondrogenesis, stem cells aggregate via intercellular N-cadherin binding; however, this interaction is lost in hydrogel constructs, where cells are dispersed. We previously showed that mesenchymal stem cells (MSCs) encapsulated within hyaluronic acid (HA, an abundant matrix component in articular cartilage) hydrogels modified with N-Cadherin mimetic peptides (i.e., His-Ala-Val, HAV) underwent enhanced chondrogenesis and produced improved cartilaginous tissue when compared to unmodified hydrogels (see Bian et al, PNAS, 2013). However, there are still limitations to the use of MSCs in cartilage tissue engineering, such as population heterogeneity and incomplete differentiation, where not all MSCs commit to a chondrogenic lineage and may undergo hypertrophic differentiation when challenged. To further address this, we sought to investigate the dose and timing of the HAV sequence within engineered hydrogels. Notably, after condensation, N-cadherin interactions are lost *in vivo* by the activity of the cell-surface metalloprotease ADAM10; thus, continuous presentation of the HAV peptide may not be optimal for MSC chondrogenesis.

Materials and Methods: Methacrylated HA (MeHA, 30% modified) was synthesized through the reaction of HA with methacrylic anhydride and further functionalized via a Michael addition reaction of methacrylates on MeHA with thiols on cysteine containing peptides (solid phase peptide synthesis, Figure 1A). Human MSCs (Lonza) were encapsulated at a density of 20 million/mL in 1.5 wt% MeHA hydrogels (0.05 wt% Irgacure 2959, 2.0 mW/cm^2 UV light, 10 minutes). Constructs were cultured in the presence of 10 ng/mL TGF-β3 and analyzed for gene expression via qPCR (Type II collagen, aggrecan, Sox-9) and viability with Live/Dead staining. Ongoing studies are investigating long-term matrix production, mechanical function, and single cell analysis.

Results and Discussion: HA macromers were synthesized with a range of peptides containing stable and ADAM10 cleavable sequences, as well as scrambled controls. MSCs were viable within hydrogels. There was a positive concentration-dependent correlation between HAV presentation and type II collagen (a primary marker for chondrogenesis). In a separate study, MSCs encapsulated in functionalized MeHA with ADAM10-cleavable vs. non-cleavable peptides presenting the same HAV motif showed that at this time point, the cleavable peptide did not induce the same change in gene expression. However, further concentrations and timing can be explored regarding this sequence.

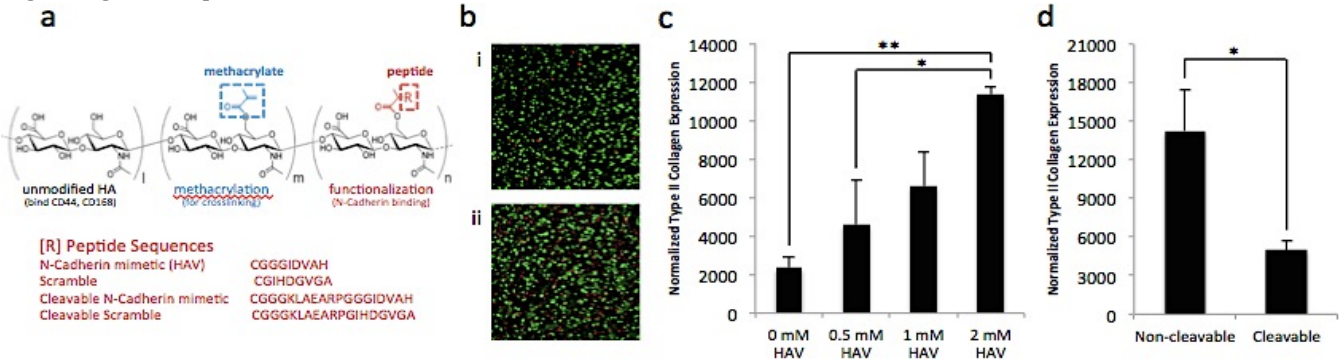

Figure 1. (a) Peptide-modified HA macromers. (b) Representative live/dead staining at (i) day 0 and (ii) day 2. (c) Type II Collagen expression in hydrogels with varying non-cleavable HAV peptide concentrations. (d) Type II Collagen expression in hydrogels with stable and cleavable HAV peptide (0.25 mM). All expression data quantified at day 3 and normalized to GAPDH and 2D monolayer control before encapsulation. *P<0.05, **P<0.01.

Conclusions: The concentration dependence on HAV of chondrogenic markers suggests that this differentiation is tunable by simply increasing the simulated developmentally relevant cell-cell contacts available. Furthermore, abolishment of type II collagen upregulation on this timescale with corresponding ADAM10-cleavable peptides confirms that cells are indeed able to regulate their microenvironment in this context and gives interesting insight into the temporal role of ADAM10 in this process. Studies with timepoints earlier and later than the one shown here and characterization with a wider range of peptide concentrations as well as mechanical and histological evaluations are ongoing.

Acknowledgements: This work was funded in part by NIH/NIAMS training grant T32-AR007132.

References: L. Bian, M. Guvendiren, R.L. Mauck, and J.A. Burdick. Hydrogels that mimic developmentally relevant matrix and N-Cadherin interactions enhance MSC chondrogenesis. PNAS (2013) 110:10117-10122.

Single-cell RNA FISH analysis of chondrocyte dedifferentiation challenges traditional definitions of phenotype

Claire M. McLeod[*,1,2], Allison J. Cote[*,1], Arjun Raj[#,1], Robert L. Mauck[#,1,2]
[1]University of Pennsylvania, Philadelphia PA, [2]Philadelphia VA Medical Center, Philadelphia, PA |[*,#]Equal contributions

Disclosures: Claire McLeod (N), Allison Cote (N), Arjun Raj (N), Robert Mauck (N).

Introduction: Aggrecan expression is a canonical feature of the differentiated chondrocyte phenotype, and is widely considered a leading indicator of cartilage-specific extracellular matrix deposition. However, we recently demonstrated that as mesenchymal stem cells (MSCs) undergo chondrogenesis, the expression of aggrecan and other standard markers of the differentiated phenotype do not strongly correlate with cartilage-like matrix accumulation at either the population or the single-cell level [1]. To reconcile this disconnect between aggrecan gene and protein expression with the traditional understanding of the chondrocyte phenotype, the objective of the current work was to use single cell techniques (single molecule RNA FISH) to monitor the absolute gene expression and matrix accumulation of primary chondrocytes. Specifically, we examined chondrocyte biology at the single cell level during two classical experiments: the de-differentiation of chondrocytes with serial passage in monolayer [2,3], and chondrocyte re-differentiation when expanded cells were returned to 3D culture [3].

Methods: Cell culture: Juvenile bovine chondrocytes were isolated from the articular cartilage of the trochlear groove via digestion with type II collagenase (0.5 mg/ml). Chondrocytes were expanded in basal media (DMEM + 10% FBS + 1x antibiotic-antimycotic) and serially passaged at a ratio of 1:10 when plates reached ~80% confluence. At each passage, chondrocytes were fixed for further analysis. At passages 0 and 5, chondrocytes were encapsulated in 2% agarose micro-gels (μgels) measuring 10 mm in diameter and ~400 μm in thickness, at a density of $2x10^6$ cells/mL. These μgels were cultured in basal media supplemented with 50 μg/mL ascorbate 2-phosphate, and fixed after 1 and 14 days. RNA FISH: Single molecule RNA FISH was performed as in [4]. Monolayer cultures and μgels were simultaneously stained with DAPI and oligonucleotide probes directed against aggrecan (ACAN) and GAPDH. From images, a custom MATLAB script was used to quantify absolute mRNA expression at the single cell level (n=39-113 cells/donor/condition). Matrix assessment: Extracellular matrix deposition was assessed via Alcian blue (pH 1) staining. Cell size: In monolayer, cell area was measured by tracing images of phalloidin-stained cells. For cells in suspension (after trypsinization during passaging), volume was computed from the cell radii measured by an automatic cell counter (n=274-543 cells/condition, Nexcelom Cellometer). Statistics: Normalized ACAN/GAPDH expression, area, and volume data were compared via one-way ANOVA with Tukey post-hoc tests. To compare single cell RNA counts, a generalized linear mixed model with a log-link function and by-donor random intercepts was constructed; passage and culture duration were considered fixed effects. Estimated means were compared using Satterthwaite-based t-distributions with simulated adjustment for multiple comparisons.

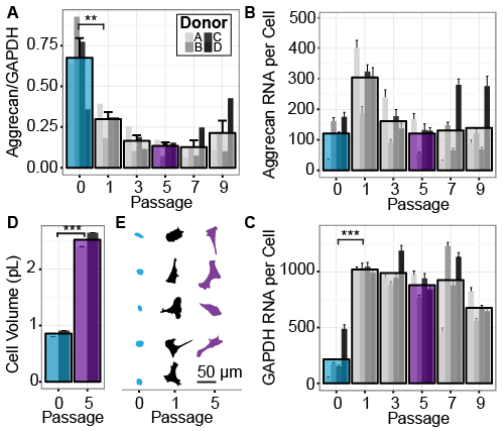

Fig.1: Chondrocyte dedifferentiation. **A)** Normalized aggrecan/GAPDH expression. Absolute aggrecan **(B)** and GAPDH **(C)** expression. **D)** Suspended cell volume. **E)** Cell morphology silhouettes. ** p<0.01, *** p<0.001

Results: For each condition examined, single cell aggrecan gene expression varied over 3 orders of magnitude (e.g. P0 monolayer: minimum = 0 ACAN mRNA, maximum = 809 ACAN mRNA). Consistent with the canonical understanding of chondrocyte de-differentiation, the normalized ACAN/GAPDH expression in individual chondrocytes decreased with passage (**Fig 1A**). However, this change was not due to a decrease in absolute ACAN copy number (**Fig 1B**). Rather, ACAN copy number showed a small increase from passage 0 (initial plating) to passage 1, before returning to passage 0 mean copy number at later passages. In contrast, there was a rapid increase in mean GAPDH copy number per cell over the first passage (~4 fold) that remained at these elevated levels through additional passages (**Fig 1C**). We also found that chondrocyte spread cell area generally increased with passage number (**Fig 1E**) and that the mean volume of suspended cells increased by ~3-fold between primary isolation (passage 0) and passage 5 (**Fig 1D**). To further explore how normalization may confound interpretation of gene expression changes, we forced the re-differentiation of culture-expanded chondrocytes that had lost their 'phenotype'. Consistent with classical studies, early passage chondrocytes produced matrix robustly upon encapsulation, while late passage (de-differentiated) chondrocytes showed a significant attenuation in matrix deposition (**Fig 2A**). RNA FISH showed that after 1 day of encapsulation, late passage chondrocytes expressed more ACAN and more GAPDH than early passage chondrocytes (**Fig 2C-D**). Over 14 days, mean ACAN levels were maintained in early passage cells, but decreased in late passage cells. In keeping with our findings in monolayer, the ACAN/GAPDH ratio in 3D was strongly influenced by changes in GAPDH (**Fig 2B-D**).

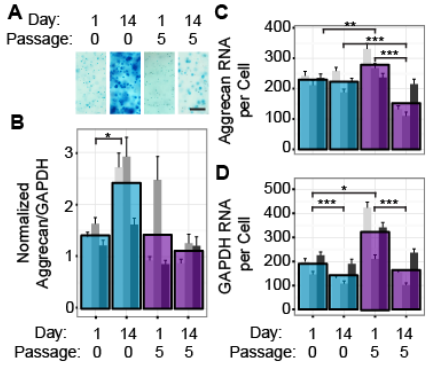

Fig. 2: Chondrocyte redifferentiation in 3D. **A)** Alcian blue staining. Scale= 200 μm. **B)** Normalized aggrecan/GAPDH expression. Absolute aggrecan **(C)** and GAPDH **(D)** expression. * p<0.05, ** p<0.01, *** p<0.001

Discussion: In this work, quantitative single cell analysis of gene expression provided novel findings related to the coordinate expression and function of chondrocytes. Taken together, these findings suggest that aggrecan expression does not decrease with chondrocyte de-differentiation and does not correlate with chondrocyte functional potential at the population level. Instead, normalization to housekeeping genes obscured relatively minor changes in aggrecan gene expression that occur during chondrocyte 'de-differentiation'. Previous studies from our group have shown that global transcription (including expression of GAPDH and many other abundant "house-keeping" genes) is regulated by cell size [4]. Here, cell enlargement with passage may be responsible for the increase in GAPDH expression. If aggrecan expression does not change, other elements of the cell must be responsible for shifting cell fate and altering the transcriptional focus of the cell. 'De-differentiation' and subsequent 're-differentiation' may be better characterized as a shift in cell focus rather than a loss in specific programmatic expression of marker genes. While it is not yet clear what cell-wide changes drive this process, future work utilizing transcriptomics may identify a more comprehensive set of markers that are predictive of differentiated cell function. Collectively, these findings challenge the traditional notion that aggrecan gene expression defines or is even strongly associated with the chondrocyte phenotype, and identify new directions in progenitor and cartilage cell biology to establish, enforce, and select subpopulations for therapeutic application.

Significance: Here, we show that aggrecan, a marker traditionally used to define the chondrocyte phenotype, is not downregulated with the loss of the differentiated phenotype, nor upregulated when a cartilage-like phenotype is induced through re-differentiation in 3D culture. Thus, absolute expression of this gene is only tenuously linked with the functional output of an individual cell.

References: [1] Cote+ Keystone Symposium, 2015. [2] Darling+ *JOR*, 2005. [3] Benya+ *Cell*, 1982. [4] Padovan-Merhar+ *Mol Cell*, 2015.

Acknowledgements: This work was supported by the NIH (DP2 OD008514, R01 EB008722, P30 AR050950) and the NSF (DGE-0822).

A Low-Cost Multi-Sensor Device for Unsupervised Large Animal Activity Monitoring

Feini Qu[1,2], Peter M. Gebhard[1], Christian G. Pfeifer[1,2], Emily L. Miedel[1], Robert L. Mauck[1,2]
[2]Translational Musculoskeletal Research Center, Philadelphia VA Medical Center, Philadelphia, PA

Introduction: Evaluating functional outcomes in musculoskeletal research is largely limited to subjective reporting. Quantitative, objective assessment of joint kinematics and gait traditionally involve specialized equipment such as force plates or optical markers that are difficult to implement in large animal studies and clinical research. To address this unmet need, we developed and validated a low-cost, battery-powered, multi-sensor apparatus that records animal activity. Furthermore, we describe a simple magnet-based method to enable simultaneous measurement of joint kinematics.

Methods: Device Hardware: The device consists of a plastic enclosure containing a 3.7 V polymer lithium ion battery, microcontroller board, radio board, sensor board, and data logger. The sensor board integrates a triple-axis accelerometer, gyroscope, and magnetometer. Device Validation: The device was validated in 3 ways with data sampling at 8 Hz for all tests. To detect changes in motion, the device was attached to a lead (65 cm length) and either swung in uniform circular motion at ~60 rpm or released from a set height to simulate a simple gravity pendulum, during which the angular velocity in the principal axis of rotation was recorded. To measure changes in angle, the device and a neodymium magnet were placed equidistant (15 cm) from a hinge joint. The device was kept stationary and the magnet moved to angles of 45, 90, 135, and 180º to simulate joint movement. Position was held for 5 s at each angle (n=3/group) and the magnetic field parallel to the magnetic dipole was recorded. Two magnets were tested: Weak (5/8" diameter, 1/5" thick) and Strong (1" diameter, 1/4" thick). Significance was assessed by two-way ANOVA with Bonferroni's post-hoc tests to compare magnetic field strength between groups ($p<0.05$). Animal Monitoring: To validate that the sensors could effectively capture and record activity in a large animal, the device was attached to a harness worn by a castrated male Yucatan minipig (26 kg) pre- and post-surgery (n=1) in an ongoing unrelated study involving bilateral arthrotomy of the stifle. Data was collected at 8 Hz for 30 min of unsupervised activity in a 4' x 6' pen on Day -1 (pre-operative) and post-operative Days 1, 2, and 7, with analgesics given for the first 5 days. Angular velocity (º/s) parallel to the dorsal plane (animal turning left or right) was recorded and the absolute values binned into 4 activity intensity levels: 0-5 (Rest), 5-50 (Low), 50-100 (Moderate), and >100 (High).

Results: A light-weight, palm-sized device capable of measuring acceleration, angular velocity, and magnetic field strength in three dimensions, as well as wirelessly transmitting the data in real time, was developed with off-the-shelf components that cost <$200. When swung in uniform circular motion at ~60 rpm, the device detected repetitive oscillatory changes in angular velocity at an average frequency of 1 Hz over a 17 s period. When released from a set height as a pendulum, characteristic damping oscillations were observed. The sensor detected changes in magnetic field strength when a magnet was positioned at various angles relative to a pivot point. Magnetic field values were significantly different between all angles for both Weak and Strong magnets, with an inverse power law relationship ($p<0.05$). As expected, the Strong magnet induced higher magnetic fields at each angle and was more sensitive to changes in position than the Weak magnet ($p<0.05$). Next, the device was used to monitor unsupervised large animal activity pre- and post-surgery. The device was worn by a Yucatan minipig and angular velocity in the dorsal plane was recorded. On Day -1 (pre-operative), the animal had full range of motion (ROM) and baseline assessment was characterized by Rest (49.6%) and Low (45.1%) intensity activity, punctuated by short periods of Moderate (4.9%) and High (0.4%) intensity activity. On Days 1 and 2 (post-operative), the animal was predominantly sedentary (96% Rest) and ambulated slowly with a stiff and limping gait (4% Low intensity activity). By Day 7, the animal had partially regained its baseline ROM and activity level, such that Low (24.3%) and Moderate (0.9%) intensity activity accounted for a quarter of the test period.

Discussion: Objective quantification of joint function is crucial for evaluating experimental treatments in translational models. Existing wearable animal monitors are generally accelerometer-based sensors that measure activity intensity. While devices capable of gait analysis do exist, they often employ multiple sensors and depend on species-dependent algorithms. Our low-cost, all-in-one device can provide information on joint kinematics in addition to basic activity level using a single sensor board. When worn by the research subject, the device wirelessly transmits data on acceleration, angular velocity, and magnetic field in 3D space, allowing for remote, real time visualization and analysis of unprovoked and unsupervised activity. Additionally, the ROM and frequency of joint flexion and extension can be derived by attaching a magnet distal to the articulating joint of interest and measuring changes in magnetic field strength. This method allows for species-independent, individualized assessment of joint kinematics using a single sensor. Simple and inexpensive, this device will facilitate the monitoring of animal and human subjects in orthopaedic research.

Injectable Polymeric Nanocomposites for Cartilage Tissue Engineering

Renata L. Sala, Michelle Kwon, Emerson R. Camargo, Jason A. Burdick

There is a need for new clinical therapies to treat patients with damaged cartilage tissues. Specifically, an injectable hydrogel that could be used to deliver stem cells to the damaged tissue site in a biocompatible and minimally invasive manner would be beneficial to the field. Towards this, poly (N-vinylcaprolactam) (PNVCL) is a biocompatible and thermosensitive biomaterial that can be used as an injectable hydrogel in non-invasive surgeries to repair cartilage tissues, since it undergoes a coil-globule transition in aqueous solution at a specific temperature (lower critical solution temperature) below body temperature. Combining this with mesoporous silica nanofibers and other polymers such as poly(vinyl acetate) (PVAc) improves the compressive strength, adhesion and cell growth properties of the formulation. Nanocomposites were prepared by the free radical polymerization of the precursor monomers in the presence of mesoporous SiO_2 nanofibers modified with methacrylate groups to promote the interaction between the organic/inorganic phases. Rheological characterization was performed to investigate how the mechanical properties of the PNVCL change in the presence of silica nanofibers and PVAc over temperature (from room temperature to 37°C). Higher storage and loss moduli were obtained in the presence of those components when compared to pure polymer in ranges suitable for soft tissue engineering. Additionally, at room temperature all materials were fluid, but when they reached 37°C, their loss modulus increased up to 450-fold, dependent on the polymer concentration, as seen in Fig.1a,b, which demonstrates that these nanocomposites can be applied as injectable biomaterials. The Alamar Blue (AB) assay was also employed to verify the nanocomposites' cytotoxicity through direct contact with Human MSCs (Lonza) to assess the cell viability after 1 and 3 days as shown in Fig.1c. All materials at different concentrations showed good biocompatibility and induced cell proliferation. After 1 day of incubation, the AB fluorescence intensities of cells grown in the presence of polymers were very similar to or higher when compared to control (cells cultured without polymers). Moreover, after 3 days of cell culture, higher fluorescence intensities were obtained, especially with more polymer. These outcomes suggest that PNVCL is a suitable biomaterial for investigation towards cartilage repair.

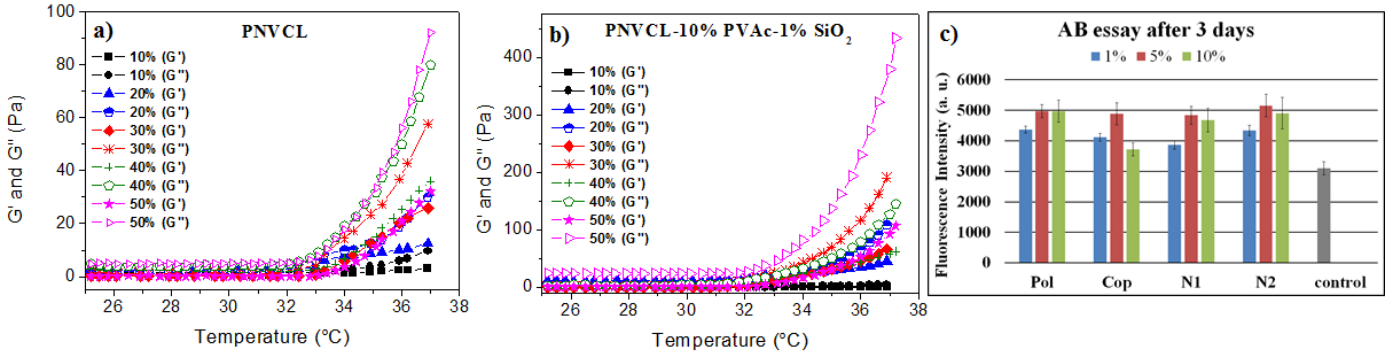

Figure 1. Storage and loss moduli of PNVCL (a) and as a nanocomposite with PVAc and 1% of SiO_2 nanofibers at different polymer concentrations (b). AB assay after 3 days (c) of cell culture in the presence of materials at different polymer concentrations; PNVCL (Pol), PNVCL-10% PVAc (Cop), PNVCL-1% SiO_2 (N1), PNVCL-10%PVAc-1% SiO_2 (N2).

Acknowledgements: This work was funded in part by the Brazilian agency São Paulo Research Foundation (FAPESP) (grant 2015/07185-1).

The Role of Telomeres in Duchenne Muscular Dystrophy-Associated Cardiac Muscle Failure

[1]Maryam Sharifi-Sanjani, [2]Patrick Robinson, [3]Ting Wang, [3]Liming Pei, [2]Benjamin L. Prosser, [1]Foteini Mourkioti
Perelman School of Medicine, [1]Department of Orthopaedic Surgery, [2]Department of Physiology, [3]Department of Pathology and Laboratory Medicine, University of Pennsylvania

Duchenne muscular dystrophy (DMD), a lethal X-linked recessive disease, is the most common myopathic disease in humans, affecting one in every 3500-liveborn males. Though DMD manifests severe muscular dystrophy, the leading cause of death is identified as cardiac muscle failure. Therapeutics, mostly focused on skeletal muscle, only relieve symptoms, and have multiple side effects. A conundrum has been that mdx mice, which share the same dystrophin deficiency as DMD patients, exhibit only mild muscle weakness in contrast to patients with DMD. Recently, we developed the novel mdx/mTR mouse model that lacks dystrophin (mdx) and has shorter telomeres (mTR) and like DMD patients, exhibit cardiac muscle dysfunction, and a markedly shortened lifespan. Although, the analysis of the cardiac phenotype of these mice showed telomere shortening and mitochondrial dysfunction, the molecular mechanisms contributing to these defects in dystrophic hearts are currently unknown. Telomeres are known to be protected via a capping mechanism that involves telomeric proteins. We recently found that telomeric proteins are attenuated in cardiac tissue from mdx/mTR mice. This finding was associated with attenuated mitochondrial fatty acid and oxidative phosphorylation of mdx/mTR mice cardiac muscle. Further, our studies demonstrate that mdx/mTR cardiac myocytes have increased level of reactive oxygen species and that anti-oxidant treated mdx/mTR mice exhibit enhanced telomere length. Together with previous reports suggesting a role for oxidative stress in telomere shortening and our recent studies demonstrating increased oxidative stress and mitochondrial dysfunction in mdx/mTR and its attenuation with antioxidant treatment, we will test the hypothesis that dystrophin deficiency during the continuous cardiac contraction induces mitochondrial defects, promoting cardiac susceptibility to oxidative stress and telomere shortening in cardiac myocytes; Telomere shortening, then, induces further mitochondrial compromise and added oxidative stress, which leads to additional telomere erosion and progression to lethal cardiac failure over time. These studies will transform the existing knowledge of cardiac DMD pathophysiology and will allow testing new of therapeutic approaches to improve the function or survival of dystrophin-defective cardiac muscle.

Gnas Inactivation Adversely Affects Cortical Bone Quality by Altering Osteoclast and Osteocyte Activity During Bone Remodeling

Girish Ramaswamy,[1,5] Hyunsoo Kim,[4] Deyu Zhang,[1,5], Yongwon Choi,[4] Frederick S Kaplan[1,2,5] Robert J. Pignolo,[1,2,5], Eileen M. Shore[1,3,5]
Department of [1]Orthopaedic Surgery, [2]Medicine, [3]Genetics, [4]Pathology and Laboratory Medicine, and the [5]Center for Research in FOP and Related Disorders, and, Perelman School of Medicine at the University of Pennsylvania, Philadelphia, PA

The *GNAS* gene encodes multiple transcripts, including the α-subunit of the stimulatory G-protein ($G_s\alpha$) of adenylyl cyclase, and shows genomic imprinting, with paternal but not maternal *GNAS* inactivation associated with Progressive Osseous Heteroplasia, a rare disorder of extraskeletal (heterotopic) ossification. We previously showed that paternal *Gnas* inactivation enhances osteoblastogenesis and inhibits adipogenesis. This study examined whether heterozygous *Gnas* inactivation also enhances bone formation during skeletal development and bone remodeling.

Trabecular BV/TV and architecture were unaffected in both *PatGnas*$^{+/-}$ and *MatGnas*$^{+/-}$ mice at all ages. However, compared to WT, 2-week-old *PatGnas*$^{+/-}$ and *MatGnas*$^{+/-}$ mice showed cortical BV/TV reduced by 15% and cortical thickness by 20% by μCT. At 3 and 9 months of age when bone remodeling occurs, *PatGnas*$^{+/-}$ showed persistent reductions in BV/TV and cortical thickness, while *MatGnas*$^{+/-}$ were similar to WT. Cortical porosity was elevated by ~10% in *PatGnas*$^{+/-}$ mice at all ages. Femurs from *PatGnas*$^{+/-}$ mice were weaker by >25% by 3-pt bending at all ages while *MatGnas*$^{+/-}$ femurs had reduced strength only at 2 weeks of age, consistent with μCT data.

TRAP staining revealed dramatically increased numbers of multi-nucleated endosteal osteoclasts in 9-month-old *PatGnas*$^{+/-}$ but not in *MatGnas*$^{+/-}$ mice. Differentiation of bone marrow macrophages (BMM) from *PatGnas*$^{+/-}$ mice formed more multi-nucleated osteoclasts and increased TRAP activity compared to WT BMMs indicating that $G_s\alpha$ regulates osteoclast differentiation. In addition, cortical bone from 9-month-old *PatGnas*$^{+/-}$ mice showed a higher fraction of TRAP+ osteocytes and elevated *Acp5*, *Sost* and *Pthrp* mRNA levels by qPCR. Osteoblast number and mineral apposition rate were similar between 2-week-old WT and *PatGnas*$^{+/-}$ mice supporting that changes in bone formation did not contribute to the cortical bone defects.

Overall our results indicate that paternal inheritance of *Gnas* inactivation in mice adversely affects cortical bone quality by altering osteoclast and osteocyte activity during bone remodeling. Studies are ongoing to investigate the effects of $G_s\alpha$ mutation on osteoclast progenitors and signaling mechanisms driving the differential effects between *PatGnas*$^{+/-}$ and *MatGnas*$^{+/-}$ mice. Thus *Gnas* regulates multiple cell types within the normal skeleton and extraskeletal tissues in age and inheritance dependent manners to impact skeletal development and heterotopic ossification.

Presented at the American Society for Bone and Mineral Research (ASBMR) Annual Meeting; Seattle, WA; October 2015
PCMD Symposium category: Miscellaneous

Targeted Ablation of Macrophages and Mast Cells Impairs Heterotopic Ossification in a Mouse Model of Fibrodysplasia Ossificans Progressiva

Michael R. Convente[1,2], EnJun Yang[3], Salin A. Chakkalakal[2], Deyu Zhang[2], Robert J. Caron[2], Daniel S. Perrien[5], Taku Kambayashi[3], Frederick S. Kaplan[2], Eileen M. Shore[1,2,4]
[1]Cell and Molecular Biology Graduate Group, [2]Department of Orthopaedic Surgery and Center for Research in FOP and Related Disorders, [3]Department of Immunology, [4]Department of Genetics, Perelman School of Medicine, University of Pennsylvania, Philadelphia, PA;
[5]Department of Orthopaedic Surgery and Rehabilitation, Vanderbilt University, Nashville, TN

Fibrodysplasia Ossificans Progressiva (FOP), a rare and disabling genetic disease characterized by progressive heterotopic ossification (HO), is caused by gain-of-function mutations (most commonly, R206H) in activin A receptor, ACVR1 (also known as ALK2), a bone morphogenetic protein (BMP) type I receptor, resulting in up-regulation of the BMP signaling pathway. BMP signaling amplifies inflammatory pathways, and work from our lab and others has documented the presence of immune cells at pre-osseous stages of HO formation. HO in FOP can be triggered by soft tissue injury, however the specific role of the immune system in FOP and development of HO remains poorly understood.

To investigate the immunological contribution during HO lesion formation, we examined the cellular and molecular response to tissue injury in a knock-in $Acvr1^{[R206H]FlEx/+}$ mouse FOP model. Following skeletal muscle injury, lesions form and progress through a series of catabolic and anabolic events that forms bone by 14 days. Strikingly, targeted ablation of macrophages via clodronate-encapsulated liposomes or mast cells via a double-transgenic mast cell-deficient $Acvr1^{R206H/+}$; $c\text{-}kit^{W\text{-}sh/W\text{-}sh}$ mouse each results in ~50% reduction of HO. Further, our preliminary data support an additive decrease in HO when both macrophages and mast cells are ablated. Examination of lesions at early and intermediate stages from $Acvr1^{R206H/+}$ mice shows increased immune cell invasion and protein expression of the inflammatory cytokines TNFα, IL-1β, and IL-6, predictive biomarkers for non-genetic trauma-induced HO, suggesting common inflammatory-mediated mechanisms during HO formation.

We also show that macrophages and mast cells express multiple type I and type II receptors from the TGF-β/BMP superfamily, including Acvr1/Alk2. BMP signaling, assayed by phosphorylated Smad1/5, is substantially up-regulated in $Acvr1^{R206H/+}$ mast cells and macrophages. Consistent with our *in vivo* data, mRNA expression of the pro-inflammatory cytokines TNFα and IL-6 is significantly elevated in mutant cells. Mast cell degranulation, a functional response to inflammatory stimulation, was also significantly increased in mast cells expressing $Alk2^{R206H}$.

Our study identifies key immune cells vital for HO development, as well as dysregulated inflammatory pathways caused by the FOP ACVR1 R206H mutation, providing novel cellular and molecular targets for prophylactic and therapeutic intervention in genetic and non-genetic forms of HO.

Presented at the American Society for Bone and Mineral Research (ASBMR) Annual Meeting and the Ninth Endocrine Fellows Foundation (EFF)/ASBMR Fellows Forum on Metabolic Bone Diseases; Seattle, WA; October 2015

Altered Collagen X At The Chondro-Osseous Junction Leads To Defects In B Lymphopoiesis

Elizabeth Sweeney, Ph.D., D. Roberts, M.S., O Jacenko, Ph.D.
University of Pennsylvania School of Veterinary Medicine, Philadelphia PA

During endochondral ossification (EO), hypertrophic cartilage blueprints define subsequent skeletal elements where hematopoietic marrows form. Although a link between altered endochondral skeletogenesis and aberrant hematopoiesis in the marrow was established by the skeleto-hematopoietic disease phenotype of mice transgenic (Tg) or null (KO) for collagen X, a hypertrophic cartilage-specific matrix protein, the necessary cellular and matrix components for hematopoiesis are still unknown. In the collagen X mice, skeletal disease manifestations involve both hypertrophic cartilage and trabecular bone, comprising the chondro-osseous junction (COJ); hematopoietic aberrations include marrow hypoplasia, altered B lymphocyte profile throughout life, and mis-expression of inflammatory and hematopoietic cytokines. Further, in vitro stimulation assays and in vivo parasite challenges confirmed impaired immune responses at all ages of collagen X Tg and KO mice. Here we show that the lymphopoietic defects observed in the collagen X mice resulted from an altered EO-derived COJ environment rather than from defects in hematopoietic progenitor cells. Furthermore, co-culture assays identified a cytokine defect in the trabecular osteoblasts of the COJ as the cause for aberrant B lymphopoiesis in these mice. Of note, many of the altered cytokines bind heparan sulfate proteoglycans (HSPGs), which are reduced or lacking in the COJ of the collagen X mice. Accordingly, B lymphopoiesis was rescued after IL-7 supplementation in vitro and in vivo. These data imply that EO-derived osteoblasts and associated matrix constituents may provide cytokine-rich niches for hematopoiesis, and that disruption of collagen X function causes changes in the HSPG/cytokine milieu at the COJ, leading to impaired lymphopoiesis and immunity. Support from NIH DK088334 to OJ and DK085227 to ES.

A novel molecular mechanism in dystrophic muscle stem cells

Elisia D. Tichy, Christopher Greer, Nicholas Oyster and Foteini Mourkioti
McKay Orthopaedic Research Laboratory, University of Pennsylvania, Philadelphia PA

Skeletal muscle diseases or myopathies result in loss of muscle mass, degeneration and functional weakness. Duchenne muscular dystrophy (DMD) is the most common recessive chronic muscle disorder that results from lack of dystrophin, a cytoskeletal protein that is essential for the stability of the skeletal muscle membrane. A conundrum has been that dystrophy knockout mice (mdx), which share the same dystrophin deficiency as DMD patients, exhibit only mild muscle weakness in contrast to patients. We reasoned that the ~8-fold difference in telomere length between mice and humans could account for this discrepancy and developed a new mdx mouse model with shortened telomeres (mdx/mTR). This dystrophic model exhibits all the pathological hallmarks of human DMD (Sacco, Mourkioti, Cell, 2010, Mourkioti, Nat. Cell Biol. 2013) and offers a useful tool to unravel the molecular mechanisms associated with injury in dystrophic muscles. We previously demonstrated that telomere shortening in muscle stem cells (MuSCs) is responsible for the failure to sustain the damage-repair cycle during regeneration (Sacco, Mourkioti, Cell 2010). Although these data support the notion that modulation or maintenance of MuSCs function might prevent or diminish destructive muscle processes in dystrophic muscles, the molecular mechanism(s) contributing to telomere shortening in dystrophic muscles is currently unknown. The identification of specific signaling pathways that affect MuSC function in relation to their telomere length may have therapeutic value for treating muscular dystrophies. In the current study, we will build upon our previous results in combination with our new unpublished molecular data on dystrophic MuSCs and test the hypothesis that during the progression of the dystrophic phenotype, the increased activity of a pleiotropic transcription factor contributes to the rapid telomere shortening of muscle stem cells and subsequent functional defects. The exploitation of downstream mediators in this pathway may lead to future targeted therapies for the treatment of DMD.

Radiculopathy induces spontaneous and reflex pain that is attenuated by meloxicam in a rat model of nerve root trauma

Christine L. Weisshaar, Blythe H. Philips, Beth A. Winkelstein

Department of Bioengineering, University of Pennsylvania, Philadelphia, PA
Department of Pathobiology, School of Veterinary Medicine, University of Pennsylvania, Philadelphia, PA

Many rodent pain studies use reflex testing with mechanical and thermal stimuli to evoke pain responses. Yet, these testing methods do not measure aspects of spontaneous pain, particularly in the early time period following injury. The rat grimace scale (RGS) quantifies spontaneous pain after inflammatory, visceral, incision, and orthopedic injuries, incorporating observational ratings based on positioning of the eyes, nose, whiskers, and ears. Nonsteroidal anti-inflammatory drugs (NSAIDs) are commonly used to relieve inflammatory and post-surgical pain in both human and veterinary patients. However, the effects of NSAIDs on spontaneous pain after radicular injury are unknown. The goal of this study was to evaluate if the NSAID, meloxicam, alters spontaneous and reflex pain responses in a rat model of cervical radiculopathy. Accordingly, spontaneous pain behavior was quantified using RGS, and mechanical hyperalgesia was measured by reflex testing on the forepaw, after a transient C7 right dorsal nerve root compression (NRC; n=7). A separate group received meloxicam (2mg/kg in 1ml saline) subcutaneously immediately prior to application of the root compression (NRC+meloxicam; n=7). As controls, another group underwent surgery but no compression (sham; n=7). RGS was measured at baseline (before injury), and 3, 6, 24 and 48 hours after injury; ipsilateral forepaw mechanical hyperalgesia was assessed at baseline, and days 1, 3, 5, and 7. The RGS scores of NRC at 6 hours are significantly higher than those for NRC+meloxicam ($p=0.012$) and sham ($p=0.041$). Yet, by 24 hours, the RGS scores for all groups return to baseline, and are not different from each other. Meloxicam also significantly ($p<0.001$) attenuates mechanical hyperalgesia at days 1, 3, and 5 compared to a compression without treatment. Interestingly, despite the fact that RGS scores for all groups returned to baseline by 24 hours, overall mechanical hyperalgesia is significantly reduced by meloxicam treatment ($p<0.001$). Together, these results suggest that pre-treatment with an NSAID reduces both spontaneous and reflex pain behaviors in the early stages of radicular pain and longer-term reflex pain. However, the first 6 hours after injury, and in pain development, may be a critical window in which to capture elements of spontaneous pain by RGS after neuropathic injury. Although additional studies are needed to evaluate long-term spontaneous pain after radicular injury, these findings provide a better understanding of spontaneous pain in a rodent model of radiculopathy and may also offer a foundation for more effective timing in the treatment for radicular pain.

Presentation preference: poster only

Disclosures of contributed support: The project described was supported by the Catherine D. Sharpe Foundation.

CD226 ligation protects against EAE by promoting IL-10 expression via regulation of $CD4^+$ T cells differentiation

Authors: Rong Zhang[1.2.4]*, Hanyu Zeng[1]*, Yun Zhang[1]*, Kun Chen[3], Chunmei Zhang[1], Chaojun Song[1], Liang Fang[1], Ran Zhuang[1], Zhuwei Xu[1], Kun Yang[1], Boquan Jin[1], Songtao Shi[4], Qintao Wang[2], Lihua Chen[1]
[*] These authors contributed equally to this work.

Names of the institutions:
1 Department of Immunology, the Fourth Military Medical University, Xi'an 710032, P,R, China. 2 State Key Laboratory of Military Stomatology, Department of Periodontology, School of Stomatology, the Fourth Military Medical University, Xi'an 710032, P,R, China. 3 Department of Neurobiology, the Fourth Military Medical University, Xi'an 710032, P,R, China. 4 Department of Anatomy and Cell Biology, University of Pennsylvania, School of Dental Medicine, Philadelphia, PA.

Abstract

Rationale : $CD4^+$ T lymphocytes, especially Th1 and Th17 were proved to be associated in the induction and treatment of experimental autoimmune encephalomyelitis (EAE), the well accepted model of multiple sclerosis. CD226, also known as DNAX accessory molecule-1 (DNAM-1) or platelet and T cell activation antigen 1 (PTA1), is proved to be a therapeutic target in amelioration of EAE. However, the mechanisms underlying how CD226 exerts its impact on EAE still needs to be further elucidated. Our previous studies showed that CD226 mAb LeoA1 could efficiently promote the production of IL-10, a cytokine with immunoregulatory properties and also an important role in EAE recovery. Therefore, we investigated whether CD226 mAb mediated regulation of EAE via the alteration of IL-10 expression levels and the differentiation of Th subsets.

Materials and Methods: Cytokines expression in the culture supernatants and the mice serum was measured by ELISA. The differentiation of Th subsets was determined by Intracellular cytokine staining using flow cytometry. Human $CD4^+$ T cells and mice $CD4^+$ T cells were purified using negative selection by specific kits and then submitted to specific conditions to allow In vitro T cell differentiation assays. Real-time quantitative RT-PCR was used to calculate the mRNA expression of related cytokines and transcriptional. factors. EAE mice was induced conventionally. Clinical score and histological analysis were used to assess the pathology and recovery of EAE.

Results: In this study, we found that CD226 ligation efficiently inhibited the production of Th1 and Th17 associated cytokines but led to a significant increase of IL-10 expression level which came at least partly from iTregs in PBMC or MLC system. Furthermore, LeoA1 treatment significantly facilitated the iTreg differentiation while suppressing the differentiation of Th1 and Th17 on both mRNA and protein levels. CD226 pAb in vivo administration effectively reduced the onset of mice EAE by inhibiting the differentiation of Th1/Th17 but promoting the IL-10-secreting $CD4^+$ T cells. More importantly, knockout of CD226 in mice showed the similar effects on EAE as in mice administrated with CD226 pAb in vivo.

Conclusions: This study therefore reveals the critical role of CD226 in the pathogenesis and treatment of EAE by reciprocally regulating IL-10-secreting iTregs and Th1/Th17 generation. Our findings thus provide hitherto unrecognized mechanism of CD226 targeted therapy of EAE.
Clinical significance: Our data suggest manipulating IL-10 and its relative signaling pathway could be a feasible therapeutic strategy to improve the efficacy of CD226 associated treatment of human autoimmune diseases and disorders.

Overexpression of Human Interleukin (IL)-8 in Mouse Intervertebral Disc Tissue to Model Patients with Back Pain

Tian Z, Enomoto-Iwamoto M, Xiu Y, Markova D, Anderson DG, Qin L, Chen Y, Huang J, Chen D and Zhang Y

Introduction: The etiology of axial back pain has been intensively investigated. We have previously shown that inflammatory mediators found in annulus fibrosus (AF) tissues from patients with discogenic back pain are likely produced by intervertebral disc (IVD) cells, and may play a key role in back pain. Among the chemokines identified, IL-8 is the most inducible in vitro: following IL-1β stimulation, IL-8 mRNA expression increased over 20,000 fold in NP and AF cells, while protein released increased by over 1,000 fold. To investigate the molecular mechanism of IL-8 signaling in the development of disc degeneration *in vivo*, we have generated a conditional IL-8 transgenic (Tg) mouse model. Our aim was to demonstrate that IVD cells produce interleukins that may, at least in part, be responsible for pain generation.

Methods. Tissue culture studies: IVDs from human spine segments (donor age range 21-75y), procured by the Gift of Hope Human Donor and Tissue Network of Illinois, were used with an approved IRB protocol. IVDs were dissected and AF and nucleus pulposus (NP) were separated. Cells were isolated by sequential enzymatic digestion of disc tissue and plated in 12- or 24-well plates. NP and AF cells were cultured in monolayer, with DMEM/F12 medium with 10% or 20% FBS, until they reached confluency. Cells were then serum-starved for 24 hours and subsequently stimulated with IL-1β (10 ng/mL) for 24 hours. IL-8 gene expression was analyzed using real-time PCR. IL-8 protein in the conditioned media was analyzed using enzyme-linked immunosorbent assay (ELISA). Cytokine array analysis: AF tissues were collected from patients undergoing spinal surgeries at Thomas Jefferson University, with an approved IRB protocol. Detailed discography scores and MRI grades were also recorded. Protein was extracted from the tissue and used to probe human cytokine array membranes. Cytokine profiles of painful and non-painful IVDs of the same MRI grades were compared. Transgenic mouse generation: pCALL2 plasmid was used to construct human IL-8 transgene. pCALL2-IL-8 mice were then bred with GDF5-Cre mouse (generously provided by David Kinsley, Stanford University) to conditionally express the transgene in cartilage and intervertebral disc tissues. Transgene expression was confirmed with PCR and IL-8 ELISA. Mouse behavioral testing was performed with Laboras (laboratory animal behavior observation, registration and analysis system, Metris®), a fully automatic and non-invasive system, to record more than 18 spontaneous behaviors.

Results. Following IL-1β stimulation, IL-8 gene expression increased 26,541 fold in NP cells (n=4, p=0.0083) and 22,429 fold in AF cells (n=4, p=0.0105). IL-8 protein released by the NP cells in response to IL-1β treatment also increased, from 31pg/ml to 74,056pg/ml, a 2,388 fold increase (n=4, p=0.0004). Similarly, IL-8 protein released by the AF cells increased, from 53pg/ml to 94,540pg/ml, a 1,784 fold increase (n=4, p=0.0055). IL-8 protein concentration in the AF tissues from patients with axial back pain is 1.8 fold of that in patients undergoing surgery for reasons other than back pain (e.g., scoliosis). But, due to the large individual variation, the difference is not statistically significant (p= 0.19). At 12 weeks of age, male Tg mice with IL-8 over-expression induced by breeding with GDF5-Cre mice showed a trend of decrease in ambulation and grooming (n=7, P=0.08), while female mouse behavior did not differ significantly.

Conclusion. We have shown that cultured IVD cells produce a massive amount of IL-8 in response to IL-1β stimulation, and generated a Tg mouse line to overexpress IL-8. We have preliminary evidence that male mice ambulate and groom less than negative controls. We will continue to characterize mouse behavior with a larger sample number, and will examine inflammatory cell infiltration and joint and spine tissue morphology.

Allogeneic Articular Chondrocytes Embedded in Hydrogels to Restore Intervertebral Disc Structure

Chee A; Mauck RL; Smith LJ; Smith HE; Malhotra NR; He TC; An HS, Zhang Y

INTRODUCTION:

Back pain is a common clinical problem that has an enormous socio-economic impact in today's aging population. According to the United States Bone and Joint Decade report, the estimated annual direct medical costs for all spine related conditions exceed $100 billion per year in the US. As an alternative to the surgical removal of the diseased disc, invasive fusion or artificial disc replacement, biological therapies that promote matrix repair and restore physiological function may be a future treatment option for disc degeneration.

With aging, progressive loss of the extracellular matrix of the intervertebral disc occurs; cells undergo senescence or apoptosis, leading to disc degeneration. Transplanting cells which would repopulate the disc and provide growth signals to resident cells by paracrine effects may be effective in reversing moderate to severe disc degeneration and reducing back pain. Because the disc tissue is relatively immuno-privileged, allogeneic articular chondrocytes may be used instead of autologous articular chondrocytes, thus avoiding an additional surgery on the same patient. An advantage of transplanting allogeneic articular chondrocytes into the disc is that they have a chondrogenic phenotype which is similar to that of the disc cells.

This study investigated the use of infrared, fluorescent and enzymatic methods for tracking allogeneic articular chondrocytes injected into the degenerating rabbit disc.

METHODS:

After approval from the Institutional Animal Care and Use Committee was obtained, articular cartilage was harvested from the knees of euthanized young rabbits via sequential enzymatic digestion, and was cultured in vitro. To track cells using fluorescence microscopy and enzymatic methods, chondrocytes were transduced with recombinant adenovirus expressing red fluorescent protein (RFP) and beta-galactosidase (β-gal) (Ad-RFP-β-gal). To track the cells after injection into the discs, the cells were labeled with Cellvue infrared dye (LI-COR Biosciences) according to the manufacturer's instructions.

New Zealand White rabbit surgeries were performed using a retroperitoneal approach to the lumbar spine. Three lumbar discs were injured by puncture with an 18G needle as previously described. Four weeks later, eight µl of transfected/labeled chondrocytes were injected into injured discs at a concentration of $1x10^7$ cells/ml. At two weeks and eight weeks post injection, the rabbits were sacrificed and the lumbar spines were harvested. Specimens were imaged with a LI-COR infrared scanner to detect location and distribution of infrared dye-labeled cells. The discs were then sectioned and a ß-gal assay was performed to detect functional ß-gal activity. Specimens were also imaged with confocal microscopy to detect RFP expression. Macrophage infiltration and IL-8 gene expression were examined with immunostaining or real-time PCR.

RESULTS:

i)Allogeneic ACs survive in degenerate rabbit IVDs. Articular chondrocytes labeled with infrared dye were detected in the degenerating IVDs at both 2 and 8 weeks after injection. The intensity of infrared dye did not differ when compared between the 2- and 8-week time points. ii) ***Allogeneic rabbit ACs transduced with Ad-RFP-β-gal continue to express transgenes post-injection.*** At 2 and 8 weeks post injection, discs stained positively for β-gal activity, thereby confirming the production of the reporter protein. Similarly, NP tissues contained RFP at 2 and 8 weeks post injection. Discs injected with chondrocytes transduced with Ad-hBMP-7 show more hBMP-7 expression at 2 weeks compared with 8 weeks post injection. No immune cells were detected by histology at either time point. iii) ***AC injection reduces inflammation in the injured IVD.*** IL-8 gene expression, as a marker of acute inflammation, was assessed in IVDs injected with ACs and compared with those injected with saline. IL-8 gene expression in discs injected with chondrocytes did not differ from intact discs ($p>0.05$, $n=11$), while those injected with saline increased 50-fold ($n=4$, $p=0.028$).

DISCUSSION:

These studies demonstrated that transplanted cells labeled with infrared dye survived in the rabbit discs for up to 8 weeks. Transplanted cell presence and viability were further confirmed by transducing the chondrocytes with recombinant adenovirus Ad-RFP-β-gal. These studies confirmed that RFP and β-gal activity were still present in the cells injected into the disc, further suggesting that the cells may have remained viable. This study suggests that allogeneic cells may achieve long term survival in the relatively immuno-privileged environment in the disc, thus providing a valuable source for cell therapy.

We have further shown the cyto-compatibility and maturation of N,N,N',N'-tetramethylethylenediamine (TEMED)/ ammonium persulfate (APS) crosslinked chondrocyte-Seeded HA Hydrogels. Finally, we have shown that biomechanics of a triple-interpenetrating-network (TIN) hydrogel are similar to human NP. Thus, future directions include comparing the effects of hydrogels as a vehicle for maintaining transplanted articular chondrocyte survival and whether they elicit an acute host inflammatory response in a rabbit IVD-injury model, and determining the therapeutic effect of young articular chondrocytes delivered to the injured mature rabbit IVDs.

SIGNIFICANCE: Three cell tracking methods have been utilized to demonstrate that cells injected into the discs remain viable in vivo for an extended period of time. These studies will help to lay the groundwork for using cell therapy to treat disc degeneration.

Ground Reaction Forces Are More Sensitive Gait Measures Than Temporal Parameters in Rodents Following Rotator Cuff Injury

Pardes AM, Freedman BR, Soslowsky LJ
McKay Orthopaedic Laboratory, University of Pennsylvania, Philadelphia, PA
soslowsk@upenn.edu

Disclosures: Pardes AM (N), Freedman BR (N), Soslowsky LJ (5; Orthofix, DJO)

Introduction: Musculoskeletal conditions affect 1 out of every 7 Americans, costing our society an estimated $254 billion yearly [1]. While tissue level animal studies provide valuable insight into the causes and treatment of musculoskeletal injuries and diseases, interpretation of the clinical and translational importance of such studies can be aided with a quantitative measure of resulting limb/joint function in live animals [2,3]. Several human and animal gait analysis studies have observed decreases in temporal parameters (e.g., stance time - how long the foot remains in contact with the ground in a single step) that seem to correspond with decreases in kinetic gait parameters (e.g., vertical ground reaction force). However, the relationship between temporal properties and ground reaction forces during locomotion has not been investigated [2,4,5]. This information is critical given the relative ease and low cost of measuring temporal parameters compared to the more complicated kinetic parameters. Therefore, the objective of this study was to compare the sensitivity of temporal versus kinetic parameters in response to functional changes using a validated gait and force-plate analysis system in rodent models following rotator cuff injury [2]. We hypothesized that temporal and kinetic parameters would correlate and be equally sensitive measures of rodent gait.

Methods: The data used in this study were obtained from our previous studies using rat rotator cuff injury models [3,6,7]. In one study, 28 animals underwent unilateral detachment of the supraspinatus only (SO) or supraspinatus and infraspinatus (SI) rotator cuff tendons and ambulatory measurements were collected preoperatively and at 3, 7, 14, 28, 42, and 56 days post-operatively. To create a more comprehensive and general model, data from the SO and SI groups were combined and used for the correlation and regression analysis in the current study as these groups demonstrated significant differences in shoulder function measured by kinetic gait parameters, as well as tendon and cartilage mechanical and histological properties [3]. Data from two other studies were used to assess the efficacy of the regression model created from the SO and SI data. In one study, 18 animals underwent unilateral detachment of the supraspinatus, infraspinatus, and biceps (SIB) tendons and ambulatory measures were collected identically to the SO and SI groups. In the other study, 20 animals underwent unilateral detachment of the supraspinatus tendon and repair with (RW) or repair without (RWO) post-operative analgesics and ambulatory measurements were collected at 2, 4, 6, 14, and 28 days following surgery. *Correlation analysis:* Pearson's correlation coefficients were calculated between temporal parameters (i.e., braking, propulsion, and stance times) and kinetic parameters (i.e., vertical, braking, and propulsion forces). *Kinetic and temporal parameter sensitivity:* The total number of significant differences in kinetic parameters alone between SO & SI, SIB & baseline, and RW & RWO was compared to the subset of significant differences identified simultaneously in corresponding temporal-kinetic pairs (i.e., vertical force & stance time, braking force & braking time, propulsion force & propulsion time) for each pair of experimental groups. Comparisons between kinetic and temporal parameters were also performed for uninjured and injured (SO and SI, combined) animals at 3, 7, and 14 days. *Regression modeling:* Step-wise backward elimination linear regression analysis was performed on the combined SO/SI data set to select the best temporal variables for predicting kinetic gait parameters. Resulting equations were then used to predict vertical, braking, and propulsion forces for all groups. The total number of known significant differences in experimental ground reaction forces between groups was compared to the number of significant differences identified by predicted kinetic parameters for these groups. *Statistical analysis:* Correlation coefficients and two-tailed p-values were calculated using bivariate Pearson correlation. Comparisons between groups for temporal and kinetic parameters were made using two-tailed t-tests. Significance was set at $p<0.05$ for all tests (SPSS v20.0).

Table 1 – Kinetic & Temporal Parameter Correlation Coefficients.
Significance key: * ($p<0.05$), ** ($p<0.01$), *** ($p<0.001$)

	Stance Time	Braking Time	Propulsion Time
Vertical Force	0.85***	0.91***	0.53*
Braking Force	0.55*	0.84***	0.84***
Propulsion Force	0.41*	0.77**	0.76**

Results: *Correlation analysis*: Numerous significant correlations between kinetic, spatial, and temporal parameters were identified (Table 1). As expected, corresponding temporal-kinetic pairs were significantly correlated. *Kinetic and temporal parameter sensitivity*: Known functional differences between groups were successfully identified by temporal parameters at rates of 20%, 29%, and 0% for SO vs. SI, SIB vs. baseline, and RW vs. RWO, respectively (data not shown). Overall, temporal parameters were better able to identify significant functional differences at early time points when the percent difference in kinetic parameters was greatest between experimental groups (Figure 1). *Regression modeling*: Stance and propulsion time were identified as the best variables for predicting vertical, braking, and propulsion force through backward elimination (data not shown). When the regression equations were used to predict ground reaction forces, they successfully predicted 70% of the known significant differences in kinetic parameters between SI and SO (Figure 2). When predicting data sets not used to create the model, the regression equations were less successful at predicting differences in ground reaction forces between groups as expected, especially when these differences were smaller in magnitude. Specifically, the model was able to predict 57% of known significant differences in kinetic parameters between uninjured animals and animals with a three-tendon tear (SIB), whereas it was able to predict 0% of known significant differences in ground reaction forces between animals with or without post-surgical pain relief (RW, RWO).

Discussion: Temporal parameters were consistently less sensitive than ground reaction forces in detecting functional differences in rat gait despite the significant correlations observed between these metrics. While the regression model developed to predict kinetic parameters did aid in identifying significant functional changes compared to temporal parameters alone, only differences that were large in magnitude, such as between injured and uninjured animals, were able to be detected with greater than 50% probability. Therefore, while gait analysis systems without force plates can be efficient and often feature fully automated analyses, they may only be adequate for use when large changes are expected. This agrees with previous rodent studies that found more pronounced differences in ground reaction forces than temporal parameters when evaluating changes in gait [8-9]. Future work may include analyzing other commonly injured joints such as the ankle.

Significance: This study supports the use of ground reaction force quantification as a more sensitive metric of limb/joint function than temporal gait parameters.

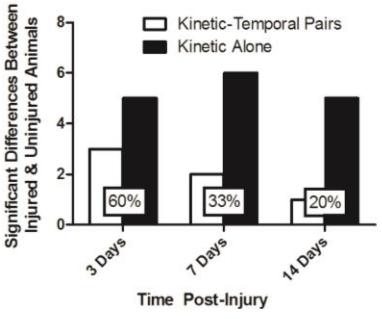

Figure 1 – Sensitivity of Kinetic vs. Temporal Gait Parameters. The total number of significant differences observed between injured (SI, SO) and control animals in kinetic parameters (ground reaction forces) (black bars) was compared to the subset of differences identified simultaneously in corresponding kinetic-temporal pairs (e.g., braking force & time) (white bars) at 3, 7, and 14 days post-op.

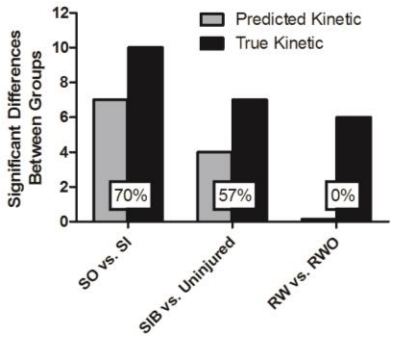

Figure 2 – Kinetic Parameter Predictability. Regression modeling was used to predict ground reaction forces from stance & propulsion times for in-model (SI, SO), and out-of-model (SIB, RW, RWO) data sets. Significant differences between groups in predicted kinetic parameters (gray bars) were compared to known significant differences in true kinetic parameters (black bars).

References: [1] Praemer A et al. American Academy of Orthopaedic Surgeons, 1999. [2] Sarver JJ et al. J Biomech, 2010. [3] Reuther KE et al. J Orthop Res, 2014. [4] Hsu JE et al. J Orthop Res, 2011. [5] Shih LY et al. Foot Ankle, 1993. [6] Thomas SJ et al. Clin Orthop Relat Res, 2014. [7] Caro AC et al. J Am Assoc Lab Anim Sci, 2014. [8] Schmitt D et al. J Exp Zool A Ecol Genet Physiol, 2010. [9] Allen KD et al. Arth Rheum Ther, 2012.

Acknowledgements: The authors thank Joseph Sarver, Katie Reuther, Steve Thomas, and Adam Caro for assistance and the NIH/NIAMS for funding.

Aberrant Glycosaminoglycan Accumulation and Sulfation in Epiphyseal Cartilage in Mucopolysaccharidosis VII

Sun H. Peck, Jennifer L. Kang, George R. Dodge, Neil R. Malhotra, Mark E. Haskins, Lachlan J. Smith

University of Pennsylvania, Philadelphia, PA

Disclosures: SHP (N), JLK (N), GRD (N), NRM (N), MEH (4-BioMarin Pharmaceutical Inc.), LJS (N)

Introduction: The mucopolysaccharidoses (MPS) are a family of genetic, lysosomal storage diseases that are characterized by deficient activity of one of the 11 acid hydrolases responsible for degradation of glycosaminoglycans (GAGs). MPS VII is characterized by impaired β-glucuronidase activity, leading to the incomplete digestion and progressive accumulation of heparan, chondroitin, and dermatan sulfate GAG byproducts [1]. MPS VII presents with severe skeletal manifestations, which are particularly prevalent in the spine and include scoliosis, kyphosis, and spinal cord compression [2-4]. Previously, our lab established the presence of cartilaginous lesions in the vertebral bodies of MPS VII patients and dogs, which represent failed epiphyseal bone formation during postnatal development [5]. Using the naturally-occurring canine model, we identified the developmental window (between 9 and 14 days-of-age) when failed bone formation first manifests (Fig 1A), and showed that resident chondrocytes fail to undergo hypertrophic maturation. However, the links between chondrocyte dysfunction and aberrant GAG accumulation in MPS VII remain to be established. GAGs perform crucial roles in controlling the distribution and availability of many growth factors that regulate cell differentiation during endochondral ossification. The biological function of these GAGs, including binding to specific growth factors, is a function not only of their concentration, but also fine structure, including critical dependence on sulfation [6-8]. The objectives of this study were to 1) identify defects in GAG sulfation pathways in MPS VII epiphyseal cartilage using whole-transcriptome sequencing (RNA-Seq), 2) define the nature of GAG accumulation in MPS VII epiphyseal cartilage, and 3) validate an *in vitro* explant culture model for measuring GAG accumulation for future mechanistic studies of cellular dysfunction.

Methods: For this study, we used the naturally-occurring MPS VII canine model that mimics both the progression and pathological phenotype of the skeletal abnormalities found in human patients [9]. With IACUC approval, unaffected control and MPS VII dogs were euthanized at 9 and 14 days-of-age, and T12, L1, and L2 vertebrae were excised for analyses. *Whole-Transcriptome Sequencing:* Vertebral epiphyseal cartilage from T12 vertebrae of control and MPS VII dogs (n=5, all groups) was collected, total RNA extracted, and RNA-Seq libraries prepared (Illumina TruSeq mRNA stranded kit). Paired-end, 100-base pair sequencing was performed (Illumina HiSeq 2500) and results mapped to the canine genome. Differential gene expression for GAG metabolic pathways was determined with DESeq2 [10] (significance, $p<0.05$). *GAG Content and Disaccharide Composition:* Cranial and caudal vertebral epiphyseal cartilage from L1 vertebrae of control and MPS VII animals at 9 days-of-age (n=3, both groups) was excised, combined, and digested with collagenase until cells were released from the extracellular matrix. Digests were centrifuged to separate the supernatant (extracellular fraction) from the cell pellet (intracellular fraction). Total GAG content in each fraction was measured using the dimethylmethylene blue (DMMB) assay and normalized to total cell count. Disaccharide composition of chondroitin and dermatan sulfate (CS/DS) extracellular GAGs isolated as above from 9-day control and MPS VII epiphyseal cartilage (n=3, both groups) was determined using UPLC. Significant differences in GAG composition ($p<0.05$) were determined using unpaired t-tests. *Explant Culture*: Epiphyseal cartilage from L2 control (n=4) and MPS VII (n=2) vertebrae was cultured as explants for 5 days in serum-free medium (α-mem, 0.1% BSA, 1% PSF) and total GAG content in intracellular and extracellular fractions, and in media, was measured using the DMMB assay and normalized to total cell count, with significant differences between groups ($p<0.05$) established using unpaired t-tests.

Results: *Whole-Transcriptome Sequencing:* RNA-Seq principal component analysis (PCA) of global gene expression showed distinct clustering (Fig 1B), indicating clear effects of both age and disease state between all groups. At 9 days-of-age, there was significant differential mRNA abundance of key genes involved in GAG sulfation, and differences were even greater at 14 days-of-age (Fig 1C, D). *GAG Content and Disaccharide Composition:* Both intracellular and extracellular GAG content were significantly higher in MPS VII cartilage at 9 days (Fig 2A, B). There were also significant differences in CS/DS disaccharide composition between control and MPS VII vertebral epiphyseal extracellular GAGs, in both extent and position of sulfation (Fig 2C). *Explant Culture:* After 5 days in culture, MPS VII cartilage explants exhibited increased GAG content in both intracellular and extracellular fractions compared to controls, with intracellular GAG content significantly higher in MPS VII after 5 days of culture, while GAG content in controls remained stable over time (Fig 3A, B). Media GAG content after 5 days was also significantly higher for MPS VII compared to controls (Fig 3C).

Discussion: Results demonstrate that while tissue-level differences are not yet evident between control and MPS VII epiphyses at 9-days-age, molecular level abnormalities are present that may impact cell function and initiation of ossification. Differential expression of genes involved GAG sulfation indicates that there is broad dysregulation of GAG metabolic pathways in MPS VII that occurs secondary to the primary GUSB mutation. Elevated extracellular GAG content and abnormal GAG sulfation patterns in MPS VII cartilage may disrupt the signaling pathways that are necessary to initiate and sustain chondrocyte hypertrophic differentiation through altered growth factor binding and distribution. Elevated intracellular GAG content also likely contributes to cellular dysfunction by increasing cellular stress. Continued accumulation of GAGs in MPS VII explants over 5 days of *in vitro* culture suggest that resident cells remain metabolically active, validating this model for future mechanistic studies of abnormal GAG metabolism.

Significance: MPS VII is associated with severe skeletal disease for which there are no treatments. This study establishes the nature of aberrant GAG accumulation in MPS VII epiphyseal cartilage and identifies defects in GAG sulfation pathways, which likely contribute to cellular dysfunction and failed bone formation.

References: [1] Sly+ J Pediatr, 1973. [2] Pizzutillo+ J Pediatr Orthop, 1989. [3] de Kremer+ Am J Med Genet, 1992. [4] Yasin+ Spine, 2014. [5] Smith+ J Orthop Res, 2010. [6] Hacker+ Nat Rev Mol Cell Biol, 2005. [7] Matsuo+ Royal Soc London Trans, 2014. [8] Manton+ Stem Cells, 2007. [9] Haskins+ Pediat Res, 1984. [10] Love+ Genome Biol, 2014.

Acknowledgments: Funding sources: NIH; Penn Center for Musculoskeletal Disorders; National MPS Society. Animal care: Dr. Margret Casal, Ms. Patricia O'Donnell, Ms. Caitlin Fitzgerald, and Ms. Therese Langan. University of Georgia Complex Carbohydrate Research Core for assistance with GAG analyses.

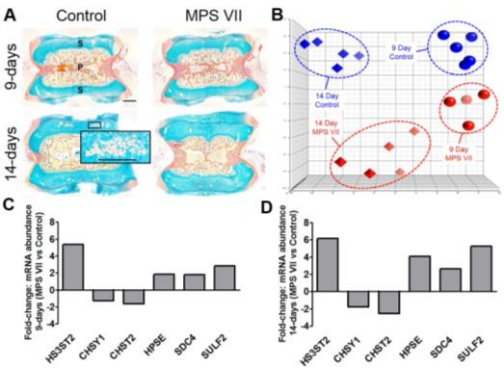

Figure 1. A. Representative mid-coronal ABPR-stained images of T11 vertebrae at 9 and 14 days-of-age. Inset: bone formation in secondary ossification centers in 14-day control animals. S: Secondary and P: Primary ossification center. **B.** RNA-Seq PCA plot. **C.** Fold-change of mRNA expression in MPS VII vertebral epiphyseal cartilage vs control at 9 days-of-age. **D.** Fold-change of mRNA expression in MPS VII vertebral epiphyseal cartilage vs control at 14 days-of-age. Scale=1mm; n=5; all $p<0.05$.

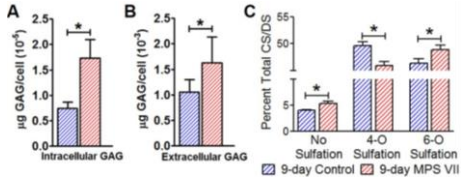

Figure 2. GAG analysis of 9-day vertebral epiphyseal cartilage. A. Intracellular GAG content. **B.** Extracellular GAG content. **C.** Extracellular GAG chondroitin and dermatan sulfate disaccharide composition. N=3; *$p<0.05$.

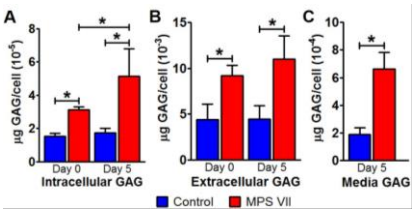

Figure 3. GAG content in epiphyseal cartilage explant model. **A.** Intracellular fraction. **B.** Extracellular fraction. **C.** Culture media, normalized to total cell count. Control (n=4), MPS VII (n=2); *$p<0.05$.

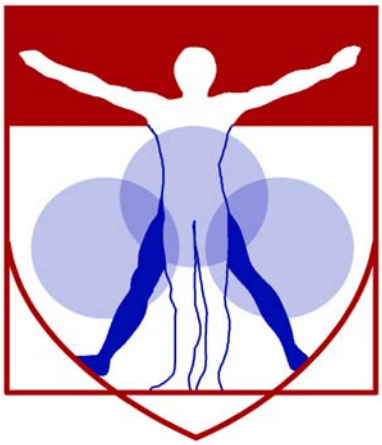

PENN

CENTER for

MUSCULOSKELETAL

DISORDERS

Notes